Design, fabrication and characterization of one dimensional photonic crystal devices

Shi, Xiaohua

Award date:
2007

Awarding institution:
University of Bath

Design, Fabrication and Characterization of One Dimensional Photonic Crystal Devices

Xiaohua Shi

A thesis submitted for the degree of Doctor of Philosophy

University of Bath

Department of Electronic & Electrical Engineering

December 2007

To my parents and my nephew.

If you find a path with no obstacles, it probably doesn't lead you anywhere.

—Frank. A. Clark

Acknowledgement

The work presented in this thesis would not have been possible without the love and sacrifice of my parents, who dedicated their lives to raise and educate me to be a happy and valuable person. I am also grateful for the kindly encouragement of my brother and sister-in-law that enable me to stand like a rock during the most difficult times and achieve what I had set out for, a PhD.

I would like to thank my supervisor Dr. Duncan Allsopp for providing me the opportunity to pursue research. His guidance has made it possible to achieve this feat. Furthermore, I would like to extend my gratitude to Dr. Federica Causa for her help and support throughout my PhD. My appreciation also goes to Dr. Wei Ding for the fruitful discussions and Dr. Tom Kehoe for the provision of technical insight into the technique of electron beam lithography. I am indebted to Dr. Antonio Moreno-Losana for sharing his clean room lab experiences.

I have benefited from the job provided by the Royal United Hospital, NHS Bath, which not only provided financial assistance but also helped me to meet with the local people and to appreciate the British culture. It also moulded me as a person with a keen understanding of real life and enriched my life-time experiences.

Last but not least, I owe a great deal of love and respect to my girl friend Shasha, for her love and support during the difficult times, which encouraged me to successfully accomplish the final goal.

Abstract

Photonic crystals (PhCs) are periodically structured electromagnetic media, generally characterised by not permitting light of defined ranges of frequency to propagate through the structure. These disallowed ranges of frequency are known as photonic band gaps. The intentional introduction of defects into the crystal gives rise to localized electromagnetic states that provide a mechanism for the control of the propagation of photons through PhCs.

In the case of one dimensional (1-D) PhCs, the introduction of a single defect into a finite PhC results in the formation of a resonant cavity structure, a so-called microcavity. The ease of fabrication and scope for integration make 1-D PhCs good candidates for the future applications of PhCs in light transmission systems and, as such, these structures are the focus of the research reported here. The aim of this thesis is to report a practical study of passive 1-D PhC devices and thereby extend the base of measurements that support and extend the results of theory and simulation.

Various types of 1-D PhC structures have been fabricated using electron beam lithography and inductively coupled plasma technologies in a clean-room environment. The fabricated structures in effect demonstrate a first or primitive level of integration of 1-D PhCs with another optical device, namely a ridge waveguide.

Measurements were performed by butt-coupling from a single mode fibre taper of the transmission characteristics of the resulting integrated waveguides, whilst a Side-band measurement method for very high resolution (0.2pm) microcavity characterisation was invented during the measurement process. A multiple wavelength transmission optical filter transmitting at the telecommunication wavelengths of 1310nm and 1550nm, and which could be used in a WDM system was demonstrated. The effect of introducing mode matching structures to minimize

the scattering loss and boost the quality factor value was investigated. Optimum positioning of the tapers produced a significant enhancement of Q. Finally, a narrow pass band filter constructed from coupled cavities was fabricated and characterised. A quasi-flat transmission peak with a pass band width of just 4nm was observed.

Publications

X. Shi, W. Ding and D. W. E. Allsopp, "Multiwavelength Transmission Microcavity in SOI Planar Ridge Waveguides," *Journal of Lightwave Technology*, Vol. 25, No. 8, pp. 2206-2212, 2007.

X. Shi, W. Ding and D. W. E. Allsopp, "SOI Ridge Waveguide Incorporating a Photonic Crystal Microcavity Multi-Channel Filter," *CLEO/QELS Conference*, Baltimore, Maryland, USA, May 10, 2007.

X. Shi and D. W. E. Allsopp, "Investigation of Tapering Effects on One Dimensional Photonic Crystal Microcavities," is under processing.

Contents

Chapter 1. Introduction

The discovery, invention and history of Photonic Crystals (PhC) and their subsequent developments in theory, fabrication and applications are reviewed in this chapter. Based on the understanding of fundamental theory and current research status of PhCs, the aims and objectives of this PhD project are then described.

1.1 History, Definition and General Overview of Photonic Crystal Structures

In 1887, Lord Rayleigh first discovered the peculiar reflective properties of a crystalline mineral with periodic "twinning" planes (across which the dielectric tensor undergoes a mirror flip). From this observation he realised there is a narrow band of wavelengths for which light propagation was prohibited through the planes [Joannopoulos 1995, Biswas 1995]. However, it was not until one hundred years later when John and Yablonovitch combined the theoretical tools of modern electromagnetism and solid state physics, in 1987, that research in photonic bandgaps became established and thrived [Yablonovitch 1987, John 1987, 1995]. This generalisation, which inspired the name "photonic crystal" for structures demonstrating photonic bandgaps, led to many subsequent developments in theory, fabrication and applications [Lourtioz 2005].

Photonic crystals are periodically structured electromagnetic media, generally possessing photonic band gaps, which are ranges of frequency for which light cannot propagate through the structure [Joannopoulos 1995]. Photonic crystals offer unique

ways to tailor light and the propagation of electromagnetic waves. In analogy to electrons in a crystal, electromagnetic waves propagating in a structure with a periodically modulated dielectric constant are organised into allowed photonic bands which are separated by gaps in the frequency spectrum where propagation is forbidden. For example, in an emission material, spontaneous emission is suppressed for photons of frequency lying in the photonic band gap, offering novel approaches to manipulating the electromagnetic field and creating high efficiency light-emitting structures [Martorell 1990, Ozbay 1994, Russell 1995]. Fig.1.1 shows the evolution of the periodic structures from one-dimension to three-dimensions, which are the foundations for the creation of photonic band gaps.

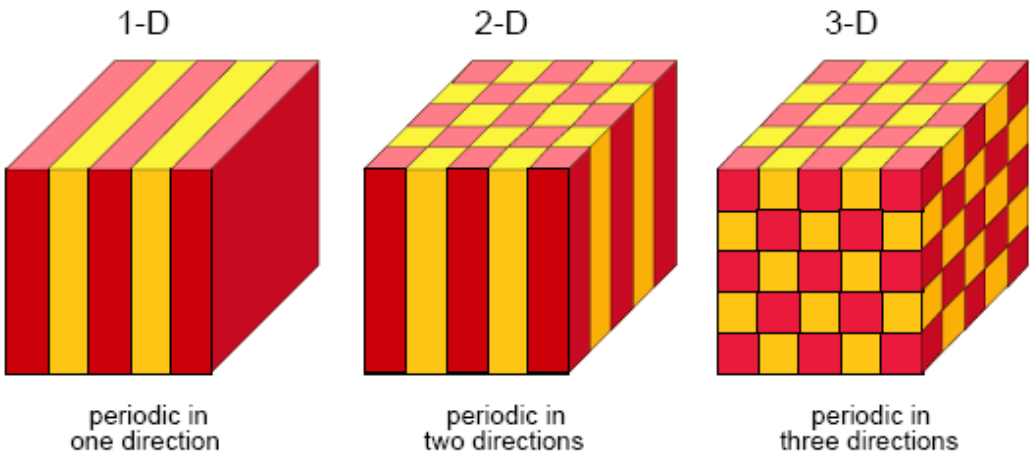

Fig.1.1, Schematic showing of the periodic structures
(Reprinted with permission from S. G. Johnson, *MIT MRS Chapter, IAP 2003*)

1.1.1 One Dimensional Photonic Crystals

The simplest possible photonic crystal, shown in Fig.1.1, is the one dimensional (1-D) structure. This consists of alternating layers of two types of material with different dielectric constants with each pair of layers being identical to the previous or next pair. The traditional approach to developing an understanding of this structure is to allow a plane wave to propagate through the material and to consider the multiple reflections and transmissions that take place at each interface, and the phase changes

that occur for plane waves propagating from layer to layer, and based on this concept, a matrix method has been introduced by Yeh to treat the phenomenon of electromagnetic waves propagating in layered media, which actually laid the very foundation for numerical research for 1-D PhCs [Yeh 1988].

As 1-D PhCs are the simplest photonic crystal structures and have the advantages of being easy to simulate and fabricate, they have attracted much interest both numerically and experimentally since the early days of research into PhCs. Notably, the formation of 1-D PhC integrated waveguide working as microcavities by etching holes in a ridge waveguide has been carried out by many researchers with Villeneuve and Foresi first reporting theoretical and experimental investigations [Villeneuve 1995(1,2), Foresi 1997]. More detailed research was performed by Zhang and Ripin on similar structures [Zhang 1996, Ripin 1999, 2000], and, more recently, Jugessur and Velha reported the incorporating of mode-matching features both within and outside the cavity region to enhance the quality factor and light throughput [Jugessur 2003, Velha 2006]. Apart from the holes etched in the waveguides to form the 1-D PhCs, multi-layer stacks [Chigrin 1999(1,2)] and waveguides incorporating rectangular grooves [Peyrade 2002] have also been studied. Lee reported the omnidirectional reflector and transmission filter optimized at a wavelength of 1.55μm formed by Si/SiO_2 multi-layer stacks [Lee 2002], similar work was also done by Patrini [Patrini 2002]. Taniyama has developed a numerical analysis of the reflectivity of electromagnetic waves for several one-dimensional photonic crystal structures [Taniyama 2002]. The literature references reported above inspired the work in this thesis at the beginning of this PhD project.

1.1.2 Two Dimensional Photonic Crystals

A two-dimensional photonic crystal is periodic along two of its axes and homogeneous along the third, as shown schematically in the middle part of Fig.1.1 [Joannopoulos 1995]. A typical specimen consisting of a square lattice of dielectric

columns is shown in Fig.1.2a. For certain values of column spacing, this type of crystal can have a photonic band gap in the *xy*-plane, as shown in Fig.1.2b [Joannopoulos 1995]. This figure describes the band gap formed by the two-dimensional PhC structure of Fig.1.2a in the form of a plot of the normalized frequency variation versus the wave vector. Inside this gap, no extended states are permitted and incident light is reflected. Notably, a two-dimensional photonic crystal can reflect light incident from any direction in the plane, with the band gap dependent on the periodicity and size of the variation of the dielectric constant in the direction of propagation.

After the identification of one-dimensional band gaps, it took a full century to add a second dimension, and three years to add the third. It should therefore come as no surprise that 2-D systems exhibit most of the important characteristics of photonic crystals, from nontrivial Brillouin-zones to topological sensitivity to a minimum index contrast, and can also be used to demonstrate most proposed photonic crystal devices [Lourtioz 2005].

Much experimental and theoretical work only considers in-plane propagation, which is the propagation normal to the cylinders that form the 2-D PhC. The key to understanding photonic crystals in two dimensions is to realise that the fields in 2-D can be divided into two polarizations by symmetry: *TM* (transverse magnetic), in which the magnetic field is in the *xy*-plane and the electric field is perpendicular; and *TE* (transverse electric), in which the electric field is in the plane and the magnetic field is perpendicular. Meade *et al* carried out a systematic theoretical investigation in order to identify a two-dimensional periodic dielectric structure that has a complete in-plane photonic band gap for both polarizations [Meade 1992]. The biggest in-plane band gap arises with a hexagonal lattice of low index holes in a high index background [Villeneuve 1992, Cassagne 1996], such structures have been fabricated in a wide variety of materials [Krauss 1994, 1996]. Jin *et al* fabricated three kinds of square metallodielectic 2-D photonic crystals [Jin 1999(2)], the first

photonic band gap was enlarged by a factor of 2 compared with dielectric photonic crystals, and they also investigated 2-D metallic photonic crystal in the THz range [Jin 1999(1)]. Inoue *et al* succeeded in fabricating a two-dimensional band structure with a near-infrared band gap based on a sample consisting of circular air rods constituting a triangular lattice [Inoue 1994]. Robertson *et al* [Robertson 1992] have measured band structure at microwave frequencies. Complete PBG's for individual polarization in the near infrared have been found by transmission measurements in micro-channel glass arrays [Inoue 1996, Rosenberg 1996] and GaAs structures [Krauss 1996]. A complete PBG at 5μm has been measured in macroporous silicon [Gruning 1996] with a lattice constant of 2.3μm and a hole depth of 75μm. This large aspect ratio was enabled by a special highly directional electrochemical etching process. A full photonic band-gap in the visible [Kitson 1996] has also been demonstrated for surface plasmon polariton modes.

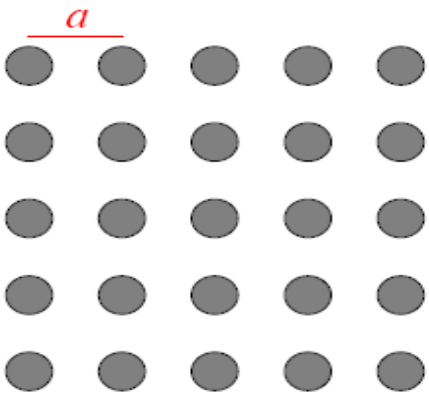

Fig.1.2a Cross-sectional view of the two-dimensional PhC consists of dielectric rods (ε=8.9) embedded in air (ε=1).

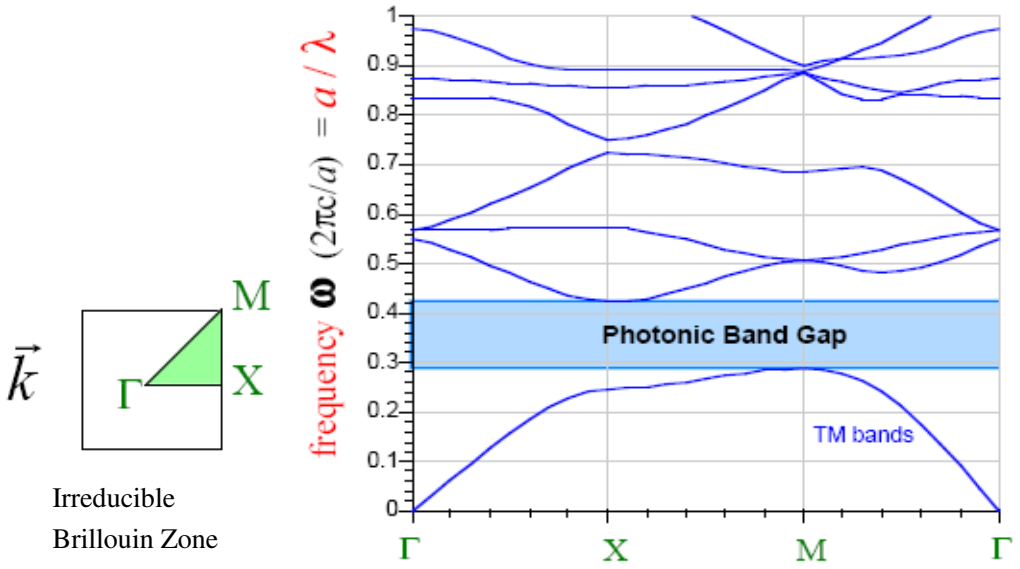

Fig.1.2b, the Photonic Band Gap created by the 2-D structure of Fig.1.2a under TM Polarisation, the left inset shows the Brillouin zone, with the irreducible zone shaded green. (Fig.1.2 a-b reprinted with the permission from S. G. Johnson, *MIT MRS Chapter,2003 IAP*)

1.1.3 Three Dimensional Photonic Crystals

The optical analogue of an ordinary crystal is a three-dimensional photonic crystal—a dielectric that is periodic along three axes, shown in Fig.1.1 3-D. Three dimensional photonic crystals were at the origin of the very notion of photonic crystal, and it is believed that only photonic crystals presenting a three-dimensional periodicity are capable of providing an omnidirectional band gap with the complete suppression of the radiative states in the corresponding frequency range [Ho 1990].

The first three dimensional PhC possessing a Photonic Band Gap was fabricated by

Yablonovitch *et al* [Yablonovitch 1991] at microwave frequencies and is known as "Yablonovite". The fabrication technique involved covering a slab of dielectric with a mask consisting of a triangular array of holes. Each hole is drilled through three times at an angle 35.26° away from the normal and spread 120° in azimuth. The relative size of the photonic band gap, i.e. the gap frequency divided by the mid-gap frequency, was found to be around 21%, which agrees well with theory [Chan 1996]. Cheng *et al* [Cheng 1993] have tried to recreate Yablonovotich's work at 1500nm operating wavelengths by using electron beam lithography to define the air channels but they were only able to create the first few layers of the structure. Several other 3-D designers offer complete 3-D PBG's [Souzuer 1993, Ho 1994, Fan 1994]. Of these, the woodpile structure is the smallest 3D PhC with an experimentally demonstrated 3-D PBG at wavelengths approaching 600μm [Ho 1994], and also structure achieved by stacking thin micro-machined silicon wafers [Ozbay 1994]. Another new approach is 3-D metallodielectric PhCs [Brown 1995] that involve the creation of a periodic lattice of isolated metallic regions within a dielectric host. These have been shown, theoretically [Fan 1996], to have enormous omni-directional band gaps approaching 80%.

1.1.4 Defect Introduction to the Periodic Structures

The key observation in the previous sections was that the periodicity of the crystal induced a gap into its band structure. No electromagnetic modes are allowed in the gap. But if this is indeed the case, the question arises of what happens when a photon (with frequency in the band gap) is sent onto the face of the crystal from outside. No real wave number exists for any mode at that frequency. Instead, the wave number is complex. In this case the modes are evanescent, decaying exponentially into the photonic crystal. Although these evanescent modes are genuine solutions of the eigen-value problem, they do not satisfy the translational symmetry boundary conditions of the crystal. There is no way to excite them in a perfect crystal of infinite extent. On the other hand, an imperfection or defect in an otherwise perfect

crystal could, in principle, sustain such a mode [Busch 1995, Ortowski 1995, Joannopoulos 1997(1,2), Jin 2001, Johnson 2001, Yamada 2001, Wang 2004].

By analogy with electronic dopants in semiconductors, intentional introduction of defects into the crystal gives rise to localized electromagnetic states such as those which occur in linear waveguides or filaments and point-like cavities [De La Rue 1995, Fan 1997, Lin 1998, Benisty 1999, Temelkuran 1999, Loncar 2000(1,2), Smith 2000, Olivier 2002]. The crystal can thus form a kind of perfect optical "insulator," which can confine light without loss around sharp bends, in lower-index media, and within wavelength-scale cavities, among other novel possibilities for control of electromagnetic phenomena [Mekis 1996, Baba 1999, Chutinan 2000(1,2), Tokushima 2000, Yamada 2002]. Fig.1.3 shows various types of defect inserted into 1-D, 2-D and 3-D structures. In 1-D, the defect can confine light to a single defect plane, in 2-D light can be localized at a linear defect, while in 3-D, light can be trapped at a single point in the crystal, known as the "cage of photon" [Yablonovitch 1991].

One class of imperfections involves changing the dielectric medium in some local region of the crystal, deep within its bulk. As a simple example, consider making a change to the isolated part by modifying its dielectric constant, modifying its size, or simply removing it from the crystal. A defect state does indeed appear in the photonic bad gap leading to a strongly localized state. By degrading a part from the lattice [Srinivasan 2003], a cavity is created which is effectively surrounded by reflecting walls. If the cavity has the proper size to support a mode in the band gap, then light cannot escape, resulting in pinning the mode to the defect [Srinivasan 2003]. In effect, a resonant cavity is formed.

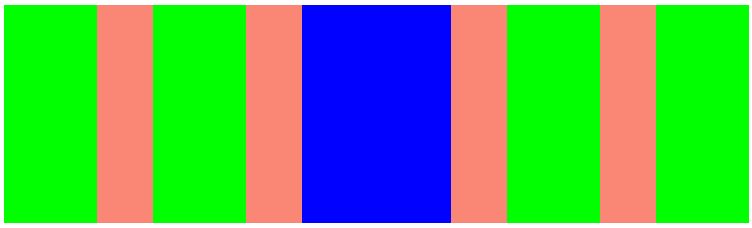

1-D defect

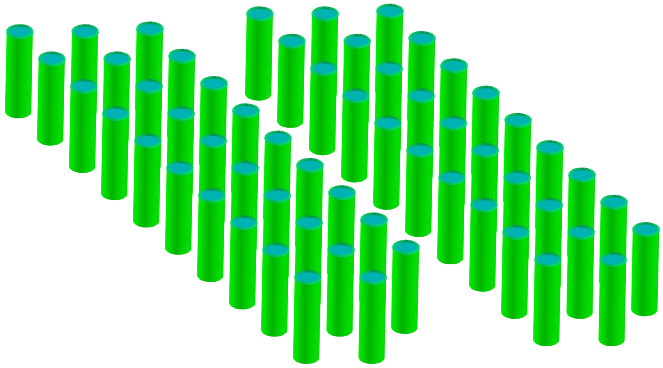

2-D Line Defect

3-D Cavity Defect

3-D Waveguide Defect

Fig.1.3 Defect introduction to the Photonic Crystal Structures

If the defect involves the removal of dielectric (an “air defect” as in the case of a vacancy in an atomic crystal lattice) then the cavity mode evolves from the dielectric band and can be made to sweep across the gap by adjusting the amount of dielectric removed [Knight 1998, Baba 2001]. Similarly, if the defect involves the addition of extra dielectric material (a “dielectric-defect”) then the cavity mode drops from the air band [Painter 1999]. In both cases, the defect state can be tuned to lie anywhere in the gap as shown in Fig.1.4.

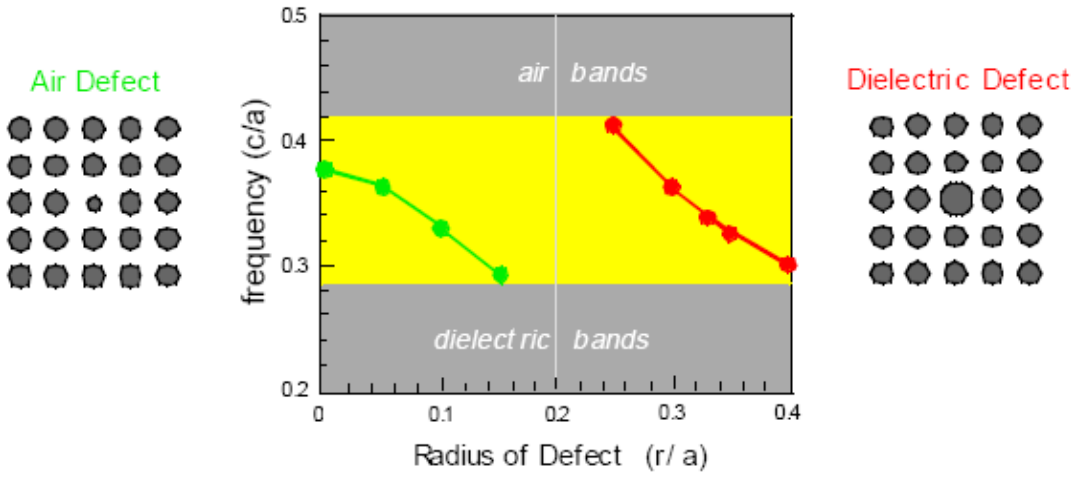

Fig.1.4 Tunable cavity modes
(reprinted with the permission from S. G. Johnson, *MIT MRS Chapter,2003 IAP*)

This flexibility in tuning defects makes photonic crystals a very attractive medium for the design of novel types of filters, couplers and even laser microcavities involving a high Q, single-mode, bridge configuration etc.

Point-like defects can be used to trap light [Srinivasan 2003]. By using line defects, light can be guided from one location to another [Johnson 2000]. The basic idea is to carve a waveguide out of an otherwise-perfect photonic crystal. Light that propagates in the waveguide with a frequency within the band gap of the crystal is confined to, and can be directed along, the waveguide. This is a truly novel mechanism for the guiding of light. Traditionally, light is guided within dielectric waveguides, such as optical fibre cables, which rely exclusively in effect on total internal reflection. However, if an optical fibre bends in a tight curve, the angle of incidence is too large for total internal reflection to occur and light can escape as the condition for total internal reflection is violated. Typically, the minimum bend radius in a planar light-wave circuit consisting of conventional rectangular ridge waveguides is several millimetres (mm) [Earnshaw 1999]. Photonic crystals, on the other hand, continue to confine light even around tight corners. Fig.1.5 demonstrates the effect [Mekis 1996]. As a consequence, the guided wave interconnects in a planar lightwave circuit may be much more compact when fabricated from photonic crystal defect waveguides

[Chen 1999, Temelkuran 1999, Chutinan 2000(1,2), Fan 2001]. Once light is induced to travel along the waveguide, it is prevented from propagating in any other direction by the band gaps in the corresponding periodic media [Fan 2002]. The primary source of loss can only be reflection back out of the waveguide input.

1.2 Applications of Photonic Bandgap Structures

Owing to their unique ability for controlling photon transmission, PhCs are predicted to have many applications in future optical and photonic systems, stimulating much work aimed at demonstrating practical devices, including the work presented in this thesis.

One very promising application of PhCs is aimed at improving the performance of waveguides [Villeneuve 1995(1,2), Konotop 1995, Mekis 1996, Foresi 1997, Baba 1999, Smith 2000, Loncar 2000(1,2)]. For example, a large enhancement of optical nonlinearity can be achieved more easily by use of the high local field of a localized photonic state at a defect in a 1-D PhC structure, because optical nonlinearities have a power law dependence on the amplitude of the optical field [Hattori 1996 1997, Tsurumachi 1999(1), Soljacic 2002 2003]; since the local light intensity can be made very high at a defect, by making use of a localized photonic-defect mode, the optical nonlinearity of the material at the defect can be effectively enhanced by many orders of magnitude. A photonic crystal waveguide is basically a PhC with a linear defect, which allows the propagation of light in a specific direction. Fig.1.5 shows the simulated transmission result of a 90 degree 2-D PhC waveguide [Mekis 1996]. Further, PhC waveguides in principle provide a superior guiding mechanism with respect to dielectric or metallic waveguides since their photonic band-gap (PBG) properties make them ideally lossless [Liu 1995, Labilloy 1997, Jin 1999(3) 2001, Zhang 2000, Smith 2000 2001, Rattier 2001, Olivier 2001(1,2), Wang 2004]. Indeed, a straight PhC waveguide is actually a system with a discrete periodicity along the

waveguide axis, in which the 1-D periodic potential given by the PhC may produce mode coupling whenever the Bragg condition is fulfilled. One can easily create a waveguide by removing a row of air holes or embedding dielectric waveguides into photonic crystal slabs [Mekis 1996, Baba 1999, Lau 2002].

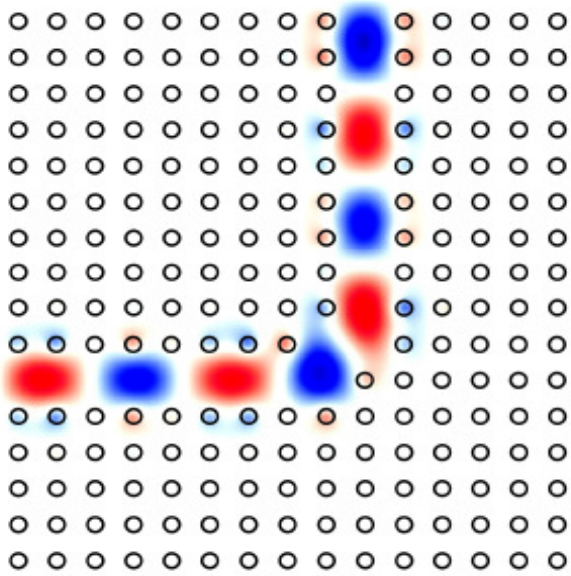

Fig.1.5 Lossless sharp bending waveguide created by creating a 90 degree defect on a 2-D PhC (A. Mekis, J.C. Chen, I. Kurland, S. Fan and J.D. Joannopoulos, "High Transmission through sharp bends in Photonic Crystal Waveguides," *Phys. Rev. Lett.* Vol. 77, pp. 3787-3790, 1996.)

Another seemingly straightforward application of PhCs is to make resonant microcavities. Theoretically, PhCs could trap light without loss in the intentionally fabricated defects, resulting in strong light localization to yield high quality factor and small volume microcavities [Yablonovitch 1991, Leung 1997, Srinivasan 2003]. Also, by inserting the PhC structures into conventional waveguides, optical filters with special transmission results can be made [Fan 1998, Soljacic 2003, Lousse 2004]; devices based on these systems can be made to be small in volume, have a nearly instantaneous response, and consume very small amount of power.

Until recently, perhaps the most successful application of PhCs was the so-called "Photonic Crystal Fibres (PCF)," [Birks 1995, Pechstedt 1995, Knight 1998, Cregan 1999, Russell 2003(1,2)]. Fig.1.6 shows the SEM images of the fabricated holey-core

PCF and the transmitted intensity of such optical fibres [Cregan 1999].

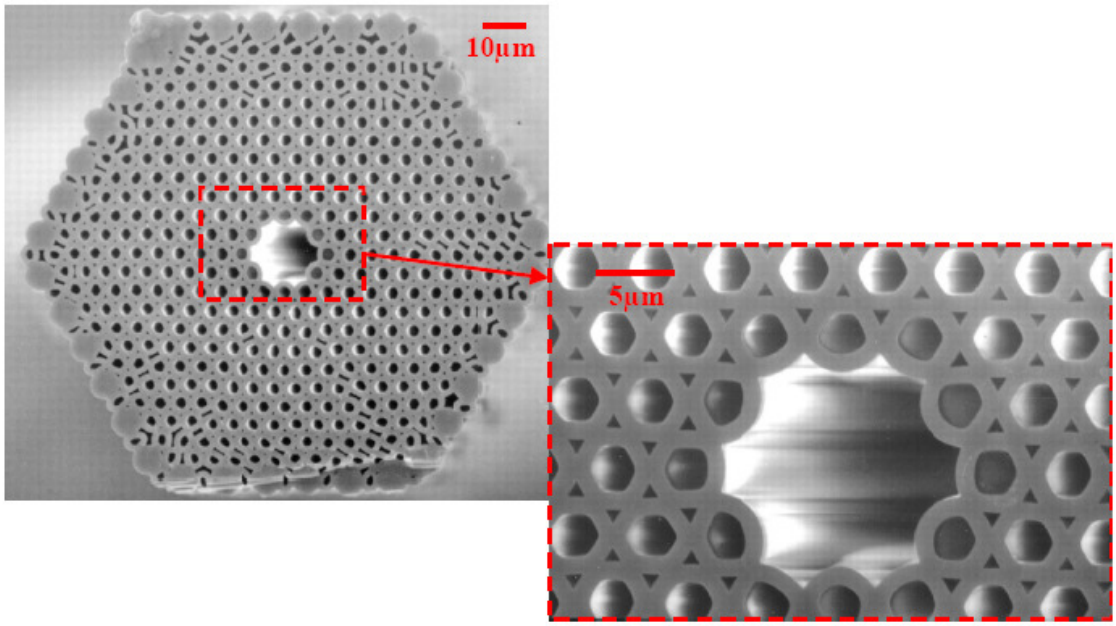

Fig.1.6a SEM image of the cross section of the fabricated holey-core Photonic Crystal Fibre
[R. F. Cregan, *et al.,Science*, 285, 1573, 1999]

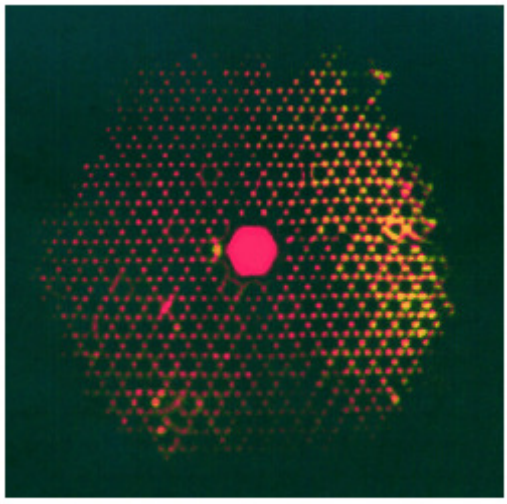

Fig.1.6b The transmitted intensity of the PCF after about 3cm
[R. F. Cregan, *et al.,Science*, 285, 1573, 1999]

Eventually, it is worthwhile mentioning that 1-D PhC structures are highly promising candidates for applications involving resonant behaviour, 1-D PhC structures with a defect layer can be considered as Fabry-Perot etalons or microcavities, and the work in this project is based upon 1-D PhCs. 1-D PhC structured devices can be fabricated easily by stacking thin films with different refractive indices together [Laude 1999, Tsurumachi 1999(1,2), Lee 2002], in particular quarter-wave stacks of two dielectrics with different refractive indices, which have long been used for mirrors or optical filters, are good examples of 1-D PhCs. They can have a wide photonic band gap centred on the frequency where Bragg reflection takes place. By placing a structural defect at the centre of the stack, a photonic-defect state that localized around the defect is created. Recently, much work has focused on forming such kind of 1-D PhCs in silicon rib or ridge waveguides in order to investigate their scope as a basis for future highly integrated low cost optical circuits [Ohtera 1999, Kosaka 2000].

In summary, due to their unique ability for manipulating photon transmission, it is reasonable to expect that PhCs will play a significant role in future photonic and optical applications. These advances will be accompanied by better understanding of the properties of such structures and also the improvements in fabrication technologies.

1.3 Aims and Objections of the PhD project

The great advances in the theory of PhCs in the last two decades have stimulated major research into the practical demonstration of their unique properties. However, in the case of PhC's sensitive to the technologically important ultra-violet, visible and near-infrared wavelength ranges, the immense difficulty of reproducible fabrication of structures containing features or elements substantially smaller than 1μm has inhibited or slowed the development of practical PhC devices.

In this PhD project, the design, fabrication and characterisation of one dimensional photonic crystal structure devices integrated in silicon-on-insulator (SOI) planar ridge waveguides have been carried out in order to explore the possible practical applications of PhCs to integrated optical circuits and enhance the optical performances of light transmission manipulation of such structures, notably a range of microcavity devices,. The emphasis of the device work has been on novel filters having potential application in 1550nm wavelength WDM optical communication networks. The aims here are to establish and demonstrate a simple and versatile fabrication technology to research the practical applications of novel microcavity concepts [Lan 2001(2) 2002(2), Lalanne 2003 2004, Beggs 2004, Lee 2005].

The fabrication process starts with the creation of silicon ridge waveguides based on a SOI wafer, which is defined by photolithography and dry-etching technology. Gold markers were then deposited on the wafer surface for later alignment by thermal evaporation. Finally, the PhC patterns were created by electron beam lithography (EBL) in the electron beam resist layer and then transferred to silicon by dry-etching.

For very fine characterisation of the quality factor value of optical microcavities, a novel measurement method has also been devised.

By precisely tuning the construction and dimension of the 1-D PhC structures, their transmission properties can be affected, to yield the real promising applications of 1-D PhCs and, as stated, this is the core aim of this project. By replacing the homogeneous cavity construction with double cavities of the normal 1-D PhC, a multi-wavelengh-transmission optical filter can be realized [Lee 2005]. Boosting up the Q value of the microcavity and transmittance value of the whole waveguide has been a problem which has inhibited the progress in 1-D PhCs for long time. The incorporation of mode matching structures or tapers between the ridge waveguide and the PhC mirrors of the microcavity and between the PhC mirrors and the cavity section itself has been investigated in a systematic way [Lalanne 2003 2004]. Finally, based on the tight requirement of a WDM system operating to the ITU standard, a coupled cavity structure has been investigated as an ideal candidate to form a band-pass optical filter based on 1-D PhCs [Lan 2001(2) 2002(2), Beggs 2004].

1.4 Organisation of the rest of the thesis

The rest of the thesis is organised as below:

Chapter 2 presents the theoretical background and preliminary simulation results of 1-D PhC microcavity transmission properties.

Chapter 3 describes the fabrication processes developed in this work in order to create 1-D PhC devices integrated into ridge waveguides.

Chapter 4 describes the measurement methods, in particular, a new side-band measurement method for characterising the quality factor of PhC microcavity filters.

Chapter 5 describes the creation of a multi-transmission optical filter based on multi-layered cavity 1-D PhCs.

Chapter 6 focuses on experimental investigation of the effects of mode matching tapers on the transmittance and quality factor of 1-D PhC optical filters.

Chapter 7 describes the study of band-pass optical filters based on coupled microcavites.

Chapter 8 presents the conclusions of the whole thesis and describes the expectations for further work in this area.

Chapter 2. Design and Simulation of the One Dimensional Photonic Crystal Micro-Cavity Structures

2.1 Introduction

This chapter describes the basic physics theory of one dimensional photonic crystals and the transmission of optical waves in layered media. The refractive indices of Si, air and SiO_2 are defined in the beginning, and as a first-step, the Kronig-Penny model is reviewed as a rigorous model for one dimensional periodically layered dielectric media.

Next, the Transfer Matrix Method (TMM) is developed and its uses in calculating the band gaps of the non-defect PhCs and the transmission properties of defects introduced PhC structures are presented.

This simulation work explored the effect of the refractive indices variation, the thickness of each layer and the number of layers on the formation of band gaps and on resonant transmissions in 1-D PhC microcavities. The obtained band gap was compared with the simulation result based on the Kronig-Penny model, and the structure parameters defined from the simulated transmission spectra laid the foundation for the following fabrication work.

2.2 Refractive Indices of silicon, air and SiO_2 and the Kronig-Penny Model

2.2.1 Refractive Indices of silicon, air and SiO_2

The refractive index value of silicon in this thesis was cited from the "Handbook of Optical Constants of Solids," [Edward 1985], where Edward combined the index of refraction values of silicon from a number of investigators [Edward 1985, 1998] and tabulated the values. Since the near IR and IR wavelength ranges are the most interested wavelengths in this work, and both dispersion and absorption of silicon are very weak in this range [Adachi 1988], the refractive index of silicon (expressed as $n + ki$), used in this thesis is under the condition of n = constant and k =0 with the imaginary part has been ignored.

The real n value in this thesis is derived from the Herzberger dispersion formula [Herzberger 1962]

$$n = A + BL + CL^2 + D\lambda^2 + E\lambda^4 \tag{2.1}$$

where $L = 1/(\lambda^2 - 0.028)$ with the wavelength λ in micrometers and 0.028 is the square of the mean asymptote for the short-wavelength abrupt rise in index for 14 materials (silicon included) [Herzberger 1962]. For the 184 data points, from 1.12 to 588μm, the coefficients are $A = 3.41906$, $B = 1.23172\times10^{-1}$, $C = 2.65456\times10^{-2}$, $D = -2.66511\times10^{-8}$, and $E = 5.45852\times10^{-14}$. The quality of the fit of reported indices to the dispersion formula is good with differences in the third and fourth decimal places. The pertinent temperature is 26°C, which is the temperature when the devices were measured.

While 1.55μm is the most interested wavelength in this project, the calculated n at

this wavelength from Eq. 2.1 is 3.4756, and 3.4 is used as the refractive index value of Si in this thesis for consistency.

1 is used as the refractive index of air in this thesis.

The refractive index of SiO_2 (crystalline quartz) was cited from Ghosh' work [Ghosh 1999], whilst the listed refractive index value in IR range is around 1.5277, a reduced effective value of 1.46 was used in the following simulations for consistency.

2.2.2 the Kronig-Penny Model

It is well known that when electrons move through a periodic lattice, allowed and forbidden energy bands are obtained. Such behaviour can be shown straightforwardly for an ideal rectangular potential in one dimension periodic, known as the Kronig-Penney model [Khorasani 2002]. The same model is applicable to the case of optical radiation if the electron waves are replaced by electromagnetic waves and the lattice periodicity structure is replaced by a periodic refractive index pattern [Ojha 2003]. One should expect allowed and forbidden bands of frequencies instead of energies. This is shown here in order to demonstrate the basic premise of photonic crystal structures.

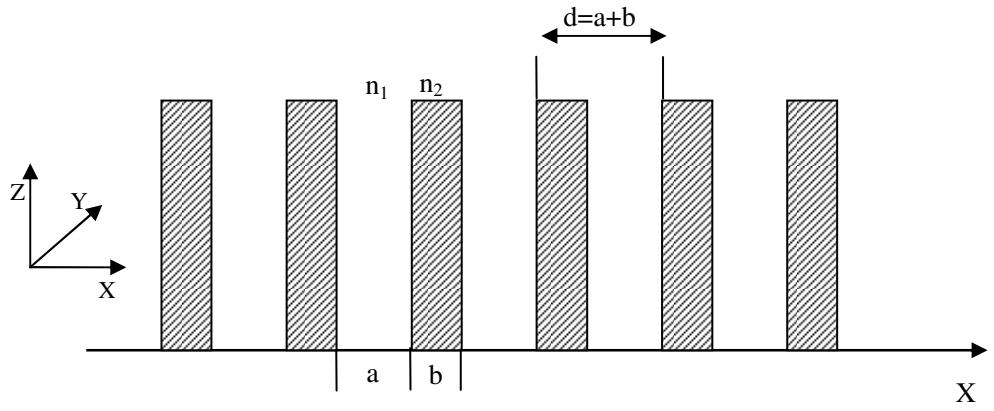

Fig.2.1 Periodic variation of the refractive index profile in the form of a rectangular structure.

Fig.2.1 shows a periodic step function for the refractive index variation with distance of the form

$$n(x) = \begin{cases} n_1, & 0 \le x \le a \\ n_2, & -b \le x \le 0 \end{cases} \tag{2.2}$$

where $n_1(x+td) = n_1$ and $n_2 = (x+td) = n_2$. Here t is the translation factor, which takes the values $t = 0, \pm 1, \pm 2, \pm 3, ...$ and $d = a + b$ is the period of the lattice with a and b being the width of the two media having refractive indices (n_1) and (n_2) respectively. In this case, the one-dimensional wave equation for the spatial part of the electromagnetic eigen mode $\psi_k(x)$ is given by

$$\frac{\partial^2 \psi_k(x)}{\partial x^2} + \frac{n^2(x)\omega_k^2}{c^2}\psi_k(x) = 0 \tag{2.3}$$

where $n(x)$ is given by Eq. (2.2). Using Eq.(2.2) in Eq.(2.3) yields

$$\frac{\partial^2 \psi_k(x)}{\partial x^2} + \frac{n_1^2\omega_k^2}{c^2}\psi_k(x) = 0; \qquad 0 \le x \le a \tag{2.4a}$$

$$\frac{\partial^2 \psi_k(x)}{\partial x^2} + \frac{n_2^2\omega_k^2}{c^2}\psi_k(x) = 0; \qquad -b \le x \le 0 \tag{2.4b}$$

Now, making use of Bloch's theorem, the wave function has the form $\psi_k = u_k(x)e^{ikx}$ and applying boundary conditions as given below

$$u_1(x)\big|_{x=0} = u_2(x)\big|_{x=0} \tag{2.5a}$$

$$u_1'(x)\Big|_{x=0} = u_2'(x)\Big|_{x=0} \tag{2.5b}$$

$$u_1(x)\big|_{x=a} = u_2(x)\big|_{x=-b} \tag{2.5c}$$

$$u_1'(x)\Big|_{x=a} = u_2'(x)\Big|_{x=-b} \tag{2.5d}$$

here four equations having four unknown constants. To obtain a nontrivial solution for the equations, the determinant of the coefficient of the unknown constants should be zero, which is given as

$$\begin{pmatrix} A_{11} & A_{12} & A_{13} & A_{14} \\ A_{21} & A_{22} & A_{23} & A_{24} \\ A_{31} & A_{32} & A_{33} & A_{34} \\ A_{41} & A_{42} & A_{43} & A_{44} \end{pmatrix} = 0 \tag{2.6}$$

where

$$A_{11} = A_{12} = A_{13} = A_{14} = 1;$$

$$A_{21} = i(\alpha - k), \quad A_{22} = i(\alpha + k), A_{23} = i(\beta - k), \quad A_{24} = -i(\beta + k);$$

$$A_{31} = e^{ia(\alpha - k)}, A_{32} = e^{-ia(\alpha + k)}, A_{33} = e^{-ib(\beta - k)}, A_{34} = e^{ib(\beta + k)};$$

$$A_{41} = i(\alpha - k)e^{ia(\alpha - k)}, \quad A_{42} = -i(\alpha - k)e^{-ia(\alpha + k)},$$

$$A_{43} = i(\beta - k)e^{-ib(\beta - k)}, \quad A_{44} = -i(\beta + k)e^{ib(\beta + k)},$$

$\alpha = (\frac{n_1 \omega_k}{c})$ and $\beta = (\frac{n_2 \omega_k}{c})$, k is the wave number related to frequency ω. On solving Eq. (2.6) one obtains the expression for the dispersion relation

$$k(\omega) = (\frac{1}{d}) \cos^{-1}\left[\cos(\frac{n_1 \omega a}{c}) \cos(\frac{n_2 \omega b}{c}) - \frac{1}{2}(\frac{n_1}{n_2} + \frac{n_2}{n_1}) \sin(\frac{n_1 \omega a}{c}) \sin(\frac{n_2 \omega b}{c}) \right] \tag{2.7}$$

where k is the wave number related to frequency ω.

Based on Eq. (2.7), a Matlab model has been developed to plot out k-- ω curves based on the Kronig-Penny model. Fig.2.2 demonstrates the evolution of photonic band gaps for three different multilayer structures which have been calculated with width $a = b = 100\,\text{nm}$. In Fig.2.2(a), $n_1 = n_2 = 1$, which means all of the layers have the same dielectric constant, so the media is completely homogeneous, no band-gap appears. In Fig.2.2(b), $n_1 = 1, n_2 = 1.5$, i.e. a small refractive index contrast, a small band gap emerges. Finally in Fig.2.2(c), $n_1 = 1, n_2 = 3.4$, i.e. a large refractive index contrast, large band-gaps appear in due wavelength positions. Since k repeats itself outside the Brillouin zone, the lines fold back into the zone when they reach the

edges. In Figs.2.2(b) and (c), gaps in frequency between the upper and lower branches of the lines—a frequency gap in which no mode, regardless of *k*, can exist in the crystal. Such a gap is called a photonic band gap, and as the dielectric contrast is increased, the gap widens considerably.

It is reasonable to conclude that in a one dimensional photonic crystal (PhC) a gap occurs between every set of bands at either the Brillouin zone's edge or its centre. Once any dielectric contrast occurs as in 1-D PhC, band gaps always appear. The smaller the contrast, the smaller the gaps, but the gaps open up as soon as $n_1 / n_2 \neq 1$. Furthermore, the bands above and below the gap can be distinguished by where the power of their modes lies—in the high ε regions, or in the low ε regions. Often the low ε regions are air regions. And for this reason, it is convenient to refer to the band *above* a photonic band gap as the "air band," and the band *below* the gap as the "dielectric band." The situation is analogous to the electronic band structure of semiconductors, in which the "conduction band" and the "valence band" surround the fundamental gap.

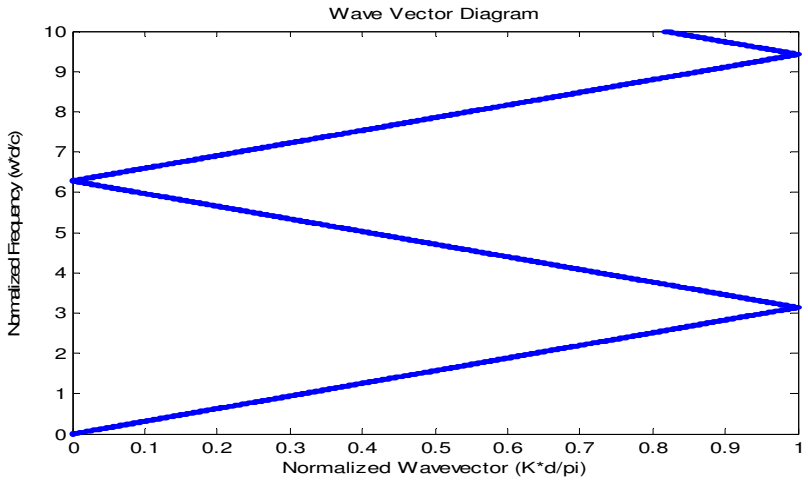

Fig.2.2 (a) n_1=n_2=1, no band-gap appears

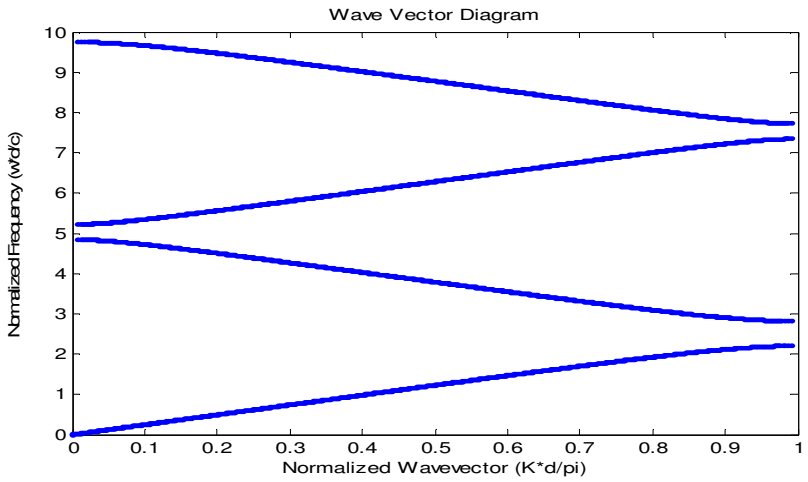

Fig.2.2 (b) n_1=1, n_2=1.5, narrow band-gap appears

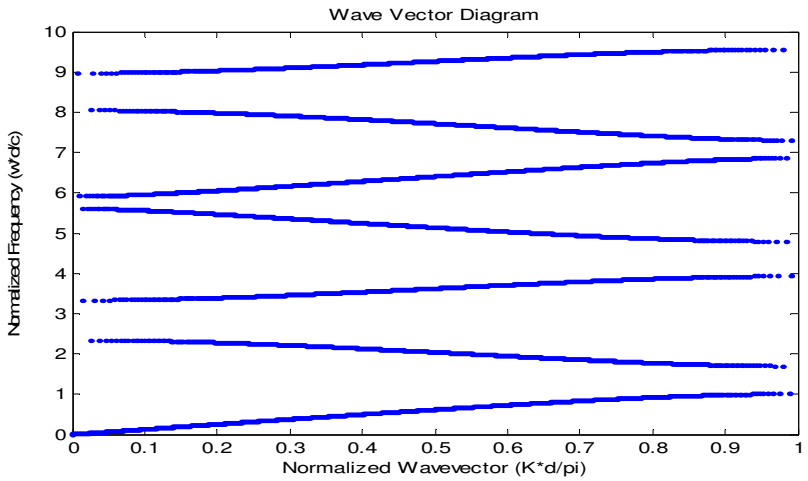

Fig.2.2(c) n_1=1, n_2=3.4, large band-gap appears

Fig.2.2 The photonic band for on-axis propagation, shown for three different dielectric contrasts.

2.3 Description of the Transfer Matrix Method

Yeh's work [Yeh 1988] guided the content of this section, as he systematically studied the theory of the propagation of optical waves in layered media and bridged the gap between theory and practice through the exploration of transfer matrix method (TMM) on real situations, and indeed, besides the name "photonic crystals", Yeh's theory dominates the numerical work in this chapter and even this thesis.

2.3.1 Transfer Matrix Formulation for a Thin Film

The problem of the reflection and transmission of electromagnetic radiation through a thin film is described here using the Transfer Matrix Method (TMM). TMM describes the relationship between the amplitude of a plane wave at the input side of thin film to that at the output side. Fig.2.3 shows the dielectric structure and defines the amplitudes ($A_1, A_2^{'}, A_2, A_3^{'}$) of the rightward travelling plane wave in each medium and the amplitudes ($B_1, B_2^{'}, B_2, B_3^{'}$) of the leftward propagating waves.

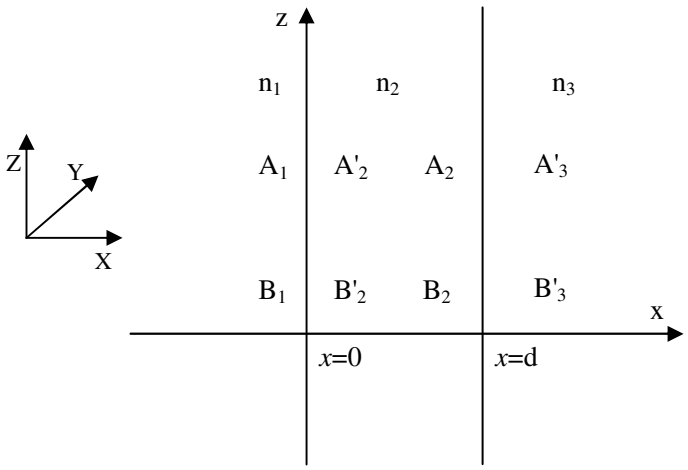

Fig.2.3 A thin layer of dielectric medium.

The refractive index variation along the propagation direction *x* is given by

$$n(x)=\begin{cases} n_1, & x<0 \\ n_2, & 0<x<d \\ n_3, & d<x \end{cases} \tag{2.8}$$

where $n_1, n_2,$ and n_3 are the refractive indices of layers 1, 2 and 3 and d is the thickness of the film. Since the whole medium is homogeneous in the z direction (i.e., $\partial n/\partial z = 0$), the electric field that satisfies Maxwell's equation has the form

$$E = E(x)e^{i(\omega t-\beta z)} \tag{2.9}$$

where β is the z component of the wave vector and ω is the angular frequency. In Eq.(2.9), it is assumed that the electromagnetic wave is propagating in the xz plane, and further assumed that the electric field is either an s wave (with E parallel to the y-axis), where y is the coordinate direction into the plane of the page, or a p wave (with the magnetic field vector parallel to the y-axis).

The total electric field $E(x)$ consists of a right-travelling wave and a left-travelling wave and can be written as

$$E(x) = R\cdot e^{-ik_x x} + L\cdot e^{ik_x x} \equiv A(x) + B(x) \tag{2.10}$$

where $\pm k_x$ are the x components of the wave vectors for left and right traveling waves and R and L are constants in each homogeneous layer. Let A(x) represent the amplitude of the right-travelling wave and B(x) be that of the left-travelling one. To illustrate the matrix method, the following definitions are now used

$$\begin{cases} A_1 = A(0^-) \\ B_1 = B(0^-) \\ A_2' = A(0^+) \end{cases}, \quad \begin{cases} B_2' = B(0^+) \\ A_2 = A(d^-) \\ B_2 = B(d^-) \end{cases}, \quad \begin{cases} A_3' = A(d^+) \\ B_3' = B(d^+) \end{cases} \tag{2.11}$$

where 0^- represents the left side of the interface between layer 1 and layer 2 at $x = 0,$ and 0^+ represents the right side of the same interface. Similarly, d^- and d^+ are defined for the interface between layer 2 and layer 3 at $x = d.$ Note E(x) for the s

wave is a continuous function of x. However, as a result of the decomposition of Eq.(2.9), A(x) and B(x) are no longer continuous at the interface. If the two amplitudes of E(x) are presented as column vectors, the column vectors shown in Fig.2.3 are related by

$$\begin{aligned}
\begin{pmatrix} A_1 \\ B_1 \end{pmatrix} &= D_1^{-1} D_2 \begin{pmatrix} A_2' \\ B_2' \end{pmatrix} \equiv D_{12} \begin{pmatrix} A_2' \\ B_2' \end{pmatrix} \\
\begin{pmatrix} A_2' \\ B_2' \end{pmatrix} &= P_2 \begin{pmatrix} A_2 \\ B_2 \end{pmatrix} \equiv \begin{pmatrix} e^{i\phi_2} & 0 \\ 0 & e^{-i\phi_2} \end{pmatrix} \begin{pmatrix} A_2 \\ B_2 \end{pmatrix} \\
\begin{pmatrix} A_2 \\ B_2 \end{pmatrix} &= D_2^{-1} D_3 \begin{pmatrix} A_3' \\ B_3' \end{pmatrix} \equiv D_{23} \begin{pmatrix} A_3' \\ B_3' \end{pmatrix}
\end{aligned} \tag{2.12}$$

where D_1, D_2, and D_3 are the dynamical matrices given by

$$D_l = \begin{cases} \begin{pmatrix} 1 & 1 \\ n_l \cos\theta_l & -n_l \cos\theta_l \end{pmatrix} & \text{(s wave)} \\ \begin{pmatrix} \cos\theta_l & \cos\theta_l \\ n_l & -n_l \end{pmatrix} & \text{(p wave)} \end{cases} \tag{2.13}$$

where $l = 1,2,3$ and θ_l is the ray angle in each layer and is related to β and k_{lx} by

$$\beta = n_l \frac{\omega}{c} \sin\theta_l, \quad k_{lx} = n_l \frac{\omega}{c} \cos\theta_l \tag{2.14}$$

P_2 is the so-called propagation matrix, which accounts for propagation through the bulk of the layer, and ϕ_2 is given by

$$\phi_2 = k_{2x} d \tag{2.15}$$

The matrices D_{12} and D_{23} may be regarded as *transmission matrices* that link the amplitudes of the waves on the two sides of the interfaces and are given by

$$D_{12} = \begin{pmatrix} \frac{1}{2}(1+\frac{k_{2x}}{k_{1x}}) & \frac{1}{2}(1-\frac{k_{2x}}{k_{1x}}) \\ \frac{1}{2}(1-\frac{k_{2x}}{k_{1x}}) & \frac{1}{2}(1+\frac{k_{2x}}{k_{1x}}) \end{pmatrix} \qquad \text{for } s \text{ wave} \tag{2.16}$$

and

$$D_{12}=\begin{pmatrix}\frac{1}{2}(1+\frac{n_2{}^2k_{2x}}{n_1{}^2k_{1x}}) & \frac{1}{2}(1-\frac{n_2{}^2k_{2x}}{n_1{}^2k_{1x}})\\ \frac{1}{2}(1-\frac{n_2{}^2k_{2x}}{n_1{}^2k_{1x}}) & \frac{1}{2}(1+\frac{n_2{}^2k_{2x}}{n_1{}^2k_{1x}})\end{pmatrix} \quad \text{for } p \text{ wave} \tag{2.17}$$

The expression for D_{23} is similar to those of D_{12}, except that the subscript indices need to be replaced: 1 with 2 and 2 with 3. Equations (2.16) and (2.17) can be written formally as

$$D_{12}=\frac{1}{t_{12}}\begin{pmatrix}1 & r_{12}\\ r_{12} & 1\end{pmatrix} \tag{2.18}$$

where t_{12} and r_{12} are the Fresnel transmission and reflection coefficients, respectively, and are given by

$$r_{12}=\begin{cases}\dfrac{k_{1x}-k_{2x}}{k_{1x}+k_{2x}} & for\ \mathrm{s}\quad wave\\ \dfrac{n_1{}^2k_{1x}-n_2{}^2k_{2x}}{n_1{}^2k_{1x}+n_2{}^2k_{2x}} & for\ \mathrm{p}\quad wave\end{cases} \tag{2.19}$$

and

$$t_{12}=\begin{cases}\dfrac{2k_{2x}}{k_{1x}+k_{2x}} & for\ \mathrm{s}\quad wave\\ \dfrac{2n_2{}^2k_{2x}}{n_1{}^2k_{1x}+n_2{}^2k_{2x}} & for\ \mathrm{p}\quad wave\end{cases} \tag{2.20}$$

The amplitudes A_1, B_1 and A_3', B_3' are related by

$$\begin{pmatrix}A_1\\ B_1\end{pmatrix}=D_1{}^{-1}D_2P_2D_2{}^{-1}D_3\begin{pmatrix}A_3'\\ B_3'\end{pmatrix} \tag{2.21}$$

Note that the column vectors representing the plane-wave amplitudes in each layer are related by the product of a set of 2×2 matrices. Each side of an interface is represented by a dynamical matrix and the bulk of each layer is represented by a propagation matrix. Such a method can be extended to the case of multilayer structures.

2.3.2 2×2 Matrix Formulation for a Multilayer System

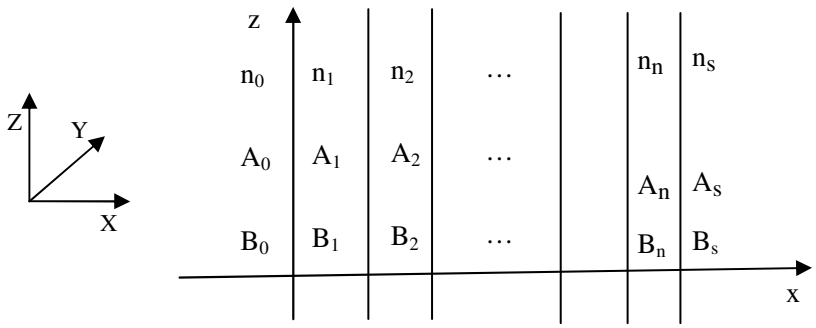

Fig.2.4 A multilayer dielectric medium

Referring to Fig.2.4, the case of multilayer structures is now considered. The dielectric structure is described by

$$n(x)=\begin{cases} n_0, & x<x_0 \\ n_1, & x_0<x<x_1 \\ n_2, & x_1<x<x_2 \\ \vdots & \\ n_N, & x_{N-1}<x<x_N \\ n_s, & x_N<x \end{cases} \tag{2.22}$$

where n_l is the refractive index of the *l*th layer, x_l is the position of the interface between the *l*th layer and the *(l+1)*th layer, n_s is the refractive index of the substrate, and n_0 is that of the medium preceding the stack.

The layer thicknesses d_l are related to the x_l values by

$$\begin{aligned} d_1 &= x_1 - x_0 \\ d_2 &= x_2 - x_1 \\ &\vdots \\ d_N &= x_N - x_{N-1} \end{aligned} \tag{2.23}$$

The electric field of a general plane-wave solution of the wave equation can still be written as

$$E = E(x)e^{i(\omega t-\beta z)} \tag{2.24}$$

where the electric field distribution $E(x)$ can be written as

$$E(x)=\begin{cases} A_0 e^{-ik_{0x}(x-x_0)}+B_0 e^{ik_{0x}(x-x_0)}, & x<x_0 \\ A_l e^{-ik_{lx}(x-x_l)}+B_l e^{ik_{lx}(x-x_l)}, & x_{l-1}<x<x_l \\ A_s^{'} e^{-ik_{sx}(x-x_N)}+B_s^{'} e^{ik_{sx}(x-x_N)}, & x_N<x \end{cases} \tag{2.25}$$

where k_{lx} is the *x* component of the wave vectors

$$k_{lx}=[(n_l\frac{\omega}{c})^2-\beta^2]^{1/2} \qquad (l=0,1,2,\cdots,N,s) \tag{2.26}$$

and is related to the ray angle θ_l by

$$k_{lx}=n_l\frac{\omega}{c}\cos\theta_l \tag{2.27}$$

According to Eqs. (2.10) and (2.11), A_l and B_l represent the amplitude of plane waves at interface $x=x_l$ Thus, we can write

$$\begin{aligned} &\begin{pmatrix} A_0 \\ B_0 \end{pmatrix}=D_0^{-1}D_1\begin{pmatrix} A_1 \\ B_1 \end{pmatrix} \\ &\begin{pmatrix} A_l \\ B_l \end{pmatrix}=P_1D_l^{-1}D_{l+1}\begin{pmatrix} A_{l+1} \\ B_{l+1} \end{pmatrix}, \qquad (l=1,2,\cdots,N) \end{aligned} \tag{2.28}$$

when $N+1$ represents *s*, $A_{N+1}=A_s^{'}$, $B_{N+1}=B_s^{'}$ and the matrices can be written as

$$D_l=\begin{pmatrix} 1 & 1 \\ n_l\cos\theta_l & -n_l\cos\theta_l \end{pmatrix} \quad \text{for } s \text{ wave} \tag{2.29}$$

and

$$D_l=\begin{pmatrix} \cos\theta_l & \cos\theta_l \\ n_l & -n_l \end{pmatrix} \qquad \text{for } p \text{ wave} \tag{2.30}$$

and

$$P_l = \begin{pmatrix} e^{i\phi l} & 0 \\ 0 & e^{-i\phi l} \end{pmatrix} \tag{2.31}$$

with

$$\phi_l = k_{lx} d_l \tag{2.32}$$

The relation between A_0, B_0 and $A_s^{'}, B_s^{'}$ can be written as

$$\begin{pmatrix} A_0 \\ B_0 \end{pmatrix} = \begin{pmatrix} M_{11} & M_{12} \\ M_{21} & M_{22} \end{pmatrix} \begin{pmatrix} A_s^{'} \\ B_s^{'} \end{pmatrix} \tag{2.33}$$

with the matrix given by

$$\begin{pmatrix} M_{11} & M_{12} \\ M_{21} & M_{22} \end{pmatrix} = D_0^{-1} \prod_{l=1}^{N} D_l P_l D_l^{-1} \cdot D_s \tag{2.34}$$

Here, one should recall that N is the number of layers, A_0 and B_0 are the amplitudes of the plane waves in medium 0 at $x = x_0$, and $A_s^{'}, B_s^{'}$ are the amplitudes of the plane waves in medium s at $x = x_N$.

2.3.3 Quarter-Wave Stack

To illustrate the use of the matrix method in the calculation of the reflection and transmission of a multilayer structure, layered media consisting of N pairs of alternating quarter-wavelength ($n_1 d_1 = n_2 d_2 = \frac{1}{4}\lambda$) with refractive indices n_1 and n_2 are created. Let n_0 be the index of refraction of the incident medium and n_s be the index of refraction of the substrate. The reflectance R at normal incidence can be obtained as follows: According to Eq.(2.28), the matrix is given by

$$\begin{pmatrix} M_{11} & M_{12} \\ M_{21} & M_{22} \end{pmatrix} = D_0^{-1}[D_1 P_1 D_1^{-1} D_2 P_2 D_2^{-1}]^N D_s \tag{2.35}$$

The propagation matrix for quarter-wave layers (with $\phi_l = \frac{1}{2}\pi$) is given by

$$P_{1,2} = \begin{pmatrix} i & 0 \\ 0 & i \end{pmatrix} \tag{2.36}$$

By using Eq.(2.21) for the dynamical matrices and assuming normal incidence, one obtains, after some matrix manipulation,

$$D_1 P_1 D_1^{-1} D_2 P_2 D_2^{-1} = \begin{pmatrix} -n_2/n_1 & 0 \\ 0 & -n_1/n_2 \end{pmatrix} \tag{2.37}$$

Carrying out the matrix multiplication in Eq.(2.37) the reflectance is

$$R = \left(\frac{1-(n_s/n_0)(n_1/n_2)^{2N}}{1+(n_s/n_0)(n_1/n_2)^{2N}}\right)^2 \tag{2.38}$$

Further descriptions of the TMM formation can be found in Appendix 1.

2.3.4 Designing Concept of the 1-D PhC Quarter-Wave Stack Microcavities

One dimensional photonic crystal structures in the form of quarter-wave stacks of two dielectrics with different refractive indices have long been used in photonics as mirrors or optical filters [Yeh 1988]. They can have a wide photonic band gap in the range of frequencies where Bragg reflection takes place. Placing a structure defect in the form of a layer of different thickness or third refractive index, or both, at the centre of the stack creates a photonic-defect around which an allowed localized mode of electromagnetic wave propagation occurs.

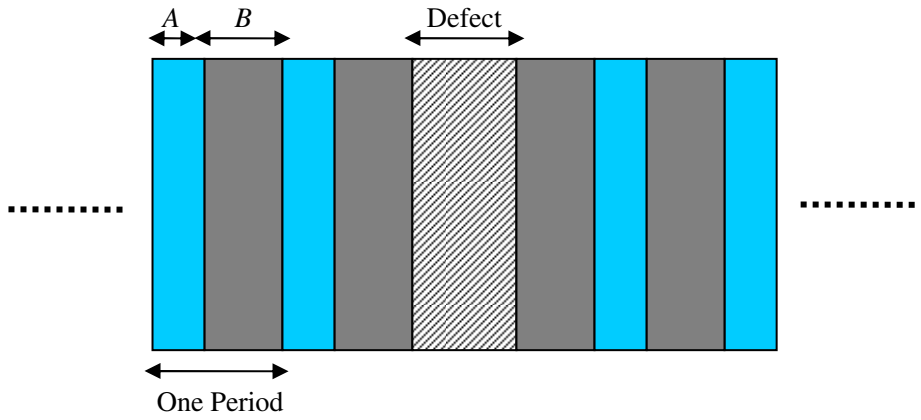

Fig.2.5 The assumed 1-D PhC structure with a defect layer.

Fig.2.5 depicts the assumed structure of the 1-D PhC with a defect layer. The structure is symmetrical, and the defect layer is sandwiched between two identical stacks of layers of high and low refractive indices on a substrate. Each stack is composed of *N* layers of low refractive index, *A* layers, and *N* layers of high refractive index, *B* layers. The refractive indices of the *A* and *B* layers are denoted n_A and n_B, and that of the defect layer is n_X. The physical thickness of the *A* and *B* layers are d_A and d_B, and that of the defect layer is d_X. In the case of a microcavity formed from quarter-wave stacks, the layer thicknesses must satisfy

$$n_A d_A = n_B d_B = \lambda / 4 , \tag{2.39a}$$

$$n_X d_X = \frac{s\lambda}{2} \qquad (s = 1,2,3\ldots) \tag{2.39b}$$

where λ is the centre wavelength of the incident light. In the case of $s = 1$ there is a single transmission peak induced by the successive forward and backward propagating reflections at the photonic-defect state, and this appears at the centre of the band gap (middle-gap position).

2.4 Simulation Results of the Band Gaps and Transmittances of the 1-D PhC Structures

In order to demonstrate some of the properties of 1-D PhC microcavities, the TMM described in the preceding section was applied to sets of Si/air and Si/SiO_2 multilayer structures. Although the TMM method is applicable only to multi-layer structures that are of infinite extent in the planes of the layers, the simulation results of the Si/air structures still informed the design of the SOI waveguide devices incorporating 1-D PhCs described in this work.

First, the equivalence of the Kronig-Penny model and the TMM for analyzing the behaviour of infinite 1-D PhC stacks is demonstrated. Fig.2.6 compares calculated results based on the Kronig-Penny model and TMM for a structure comprising a quarter wave stack which satisfies the equal optical length condition $n_A d_A = n_B d_B = \lambda/4$, $\lambda = 1550nm$ in this case, where the two layers are assumed to be Si and air. From the Kronig-Penny model the first band gap appears at the region of the normalised frequency of 1.3 to 2.8 equivalent to a wavelength range of 2422nm to 1124nm, which to within 0.5% agrees with the TMM result, from which the band gap ranges from 1130nm to 2430nm as shown in Fig.2.6(b).

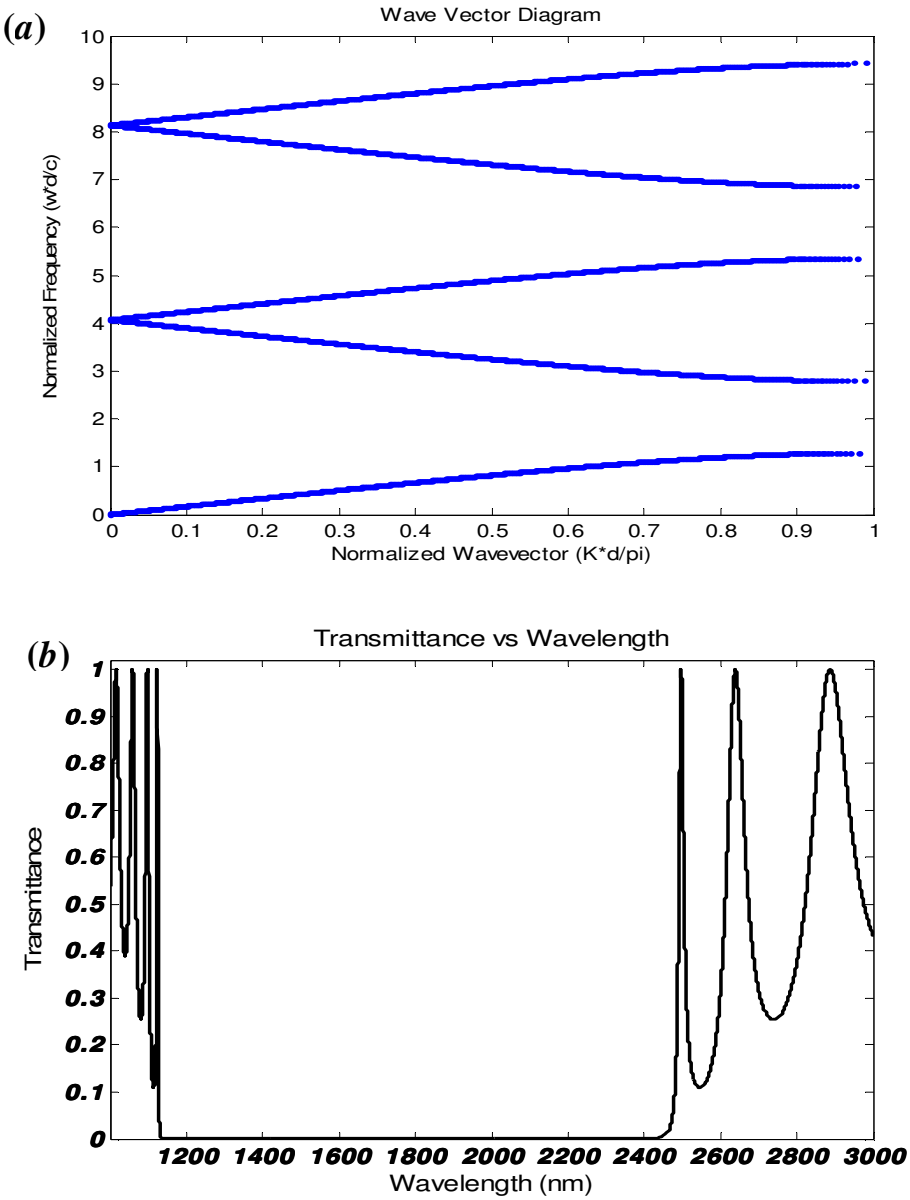

Fig.2.6 (a) Wave Vector Diagram of the band gap based on the Kronig-Penny Model; (b) TMM calculation of the band gap for a 1-D PhC comprising 10 periods of Si and air bilayers with the refractive indices to be 3.4 and 1, the thickness of each layer being 113.97nm and 387.50nm, respectively.

Next, the TMM was used to simulate the effects of incorporating defect layers. In both Si/air and Si/SiO_2 structures, it was assumed a defect layer was introduced by changing the width of one normal layer in the middle of the structure. In order to investigate the influence of each parameter, a Matlab program was developed based on the transfer matrices method, to calculate the band gap and the transmission peak of the structure. The 1-D PhC with a defect layer forms a microcavity where the light field of the resonant mode, or the defect mode, is localized around the defect layer.

The transmission and reflection can be explained as follows: The transmission spectra reflect the density of photon modes in the photonic crystals. In the region of the photonic band gap, the incident light beam does not have any modes to couple within the 1-D PhCs. Therefore, the light beam can not propagate into the crystal but is totally reflected back. However, by the introduction of the defect layer, a localized photonic state is created in the band gap region. In this case, the incident beam couples with the defect mode and is transmitted through the crystal. The response is represented by a sharp transmission peak as shown in the results reported in the following sub-sections. The position of the transmission peak can be controlled freely by changing the refractive index and/or the thickness of the defect layer.

The main factors which will affect the results are differences in the refractive indices of the materials used in the bilayers, the thickness of each layer, the number of pairs of layers in each of the 1-D PhC stacks, and the thickness and refractive index of the defect layer. Fig. 2.7 shows the proposed structure for simulation, light is assumed to be launched into the structure from a Si media with normal incidence and comes into a Si substrate in all cases.

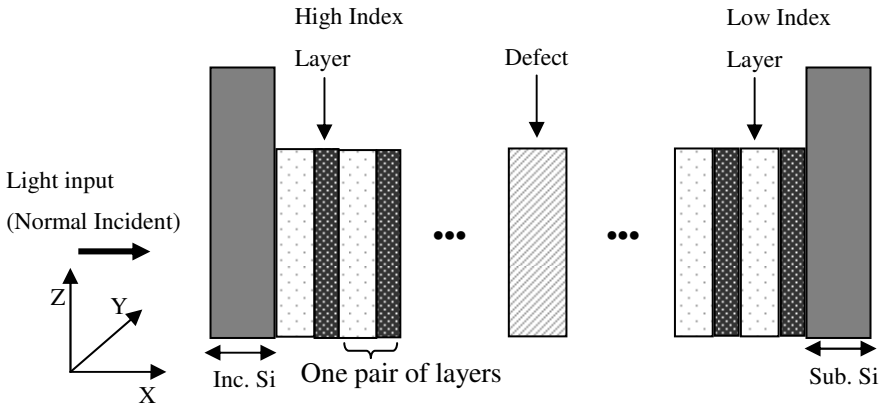

Fig.2.7 Schematic showing of the structure for simulation.

2.4.1 Low Index Layer of SiO_2

The first multilayer structure considered comprises SiO_2 filled low index gaps between quarter wavelength of Si layers with a Si defect layer. Table 2.1 shows the details of the parameters used for the calculation.

Layer	Material	Refractive Index	Thickness
1	SiO_2	1.46	265.41nm
2	Si	3.4	113.97nm
Defect	Si	3.4	227.94nm

Table 2.1 Parameters of quarter wavelength layers with SiO_2 low index gaps between Si high index layers and with double width of Si layer to be the defect.

The wavelength range for each simulation is from 1000nm to 3000nm, and the calculation step is 0.0001nm, detailed investigations of the resonances were also performed, while the designed resonance wavelength is 1550nm.

The simulation results are shown in Fig.2.8a-c, the x-coordinates of the resonances spectra have been slightly adjusted to have good views of the resonant behaviour. The quality factor values are calculated by the full width half maximum (FWHM) method,

$$Q = \frac{\lambda_0}{\Delta\lambda} \tag{2.40}$$

where $\Delta\lambda$ is the wavelength difference at half maximum position of the transmission peak and λ_0 is the resonant wavelength. Next the effect of having a low index defect layer was simulated. Table 2.2 shows the basic structure details when the defect layer is changed to be SiO_2.

Layer	Material	Refractive Index	Thickness
1	SiO_2	1.46	265.41nm
2	Si	3.4	113.97nm
Defect	SiO_2	1.46	530.82nm

Table 2.2 Parameters of a quarter wavelength stack comprising SiO_2 filled low index layers and Si high index layers and with double width of SiO_2 layer to be the defect.

The simulation results are shown in Fig.2.9a-c.

As can be seen from the spectra in Fig.2.8 and Fig.2.9, with the number of pairs of layers increase, the photonic band gap has a trend of becoming narrower and narrower and band gap edges are getting sharper. A big increase of quality factor value has been observed as the number of pairs of layers increases, this is due to the higher reflectivity of the Bragg mirrors as more periods are added. In all cases, the resonances occur at 1550nm as expected.

Comparing the Q values of the Si defect structures with the SiO_2 defect structures, for the same number of pairs of layers, a structure with Si defect has higher Q value than the one with SiO_2 defect, this can be explained by the fact that the actual mirror reflectivity depends on the refractive index of the cavity medium, i.e. the reflectivity of a quarter-wave stack depends on the refractive index of the medium where the beam is launched and a high index medium creates high reflectivity for the stacks, thus higher Q values are obtained for Si defect structures than SiO_2 defect structures for the same number of pairs of layers.

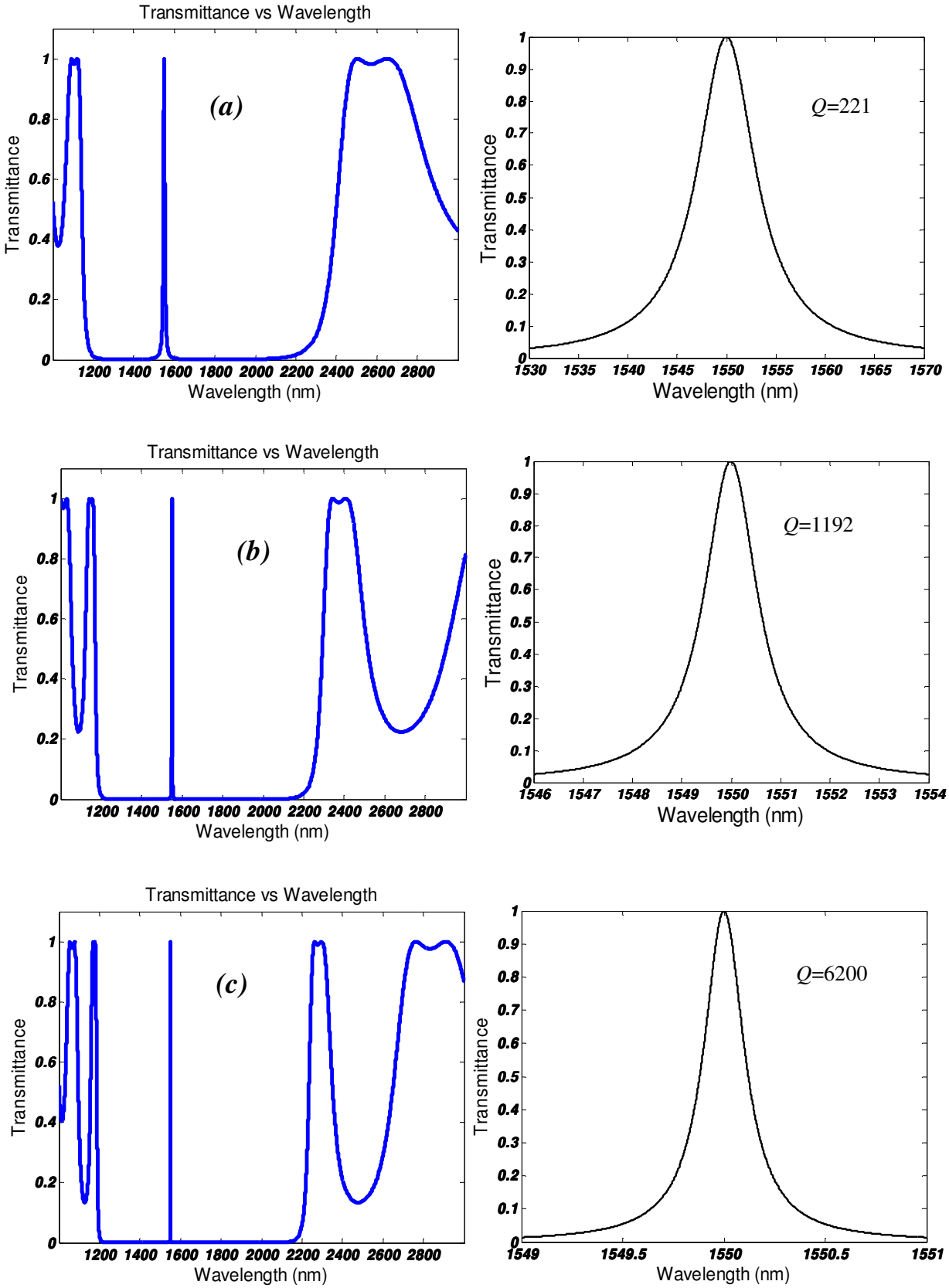

Fig.2.8 Transmittance versus wavelength characteristics of Si/SiO_2 with Si defect layer multilayer microcavities. (a) 6 pair of layers with Q value of 221; (b) 8 pair of layers with Q value of 1192; (c) 10 pair of layers with Q value of 6200.

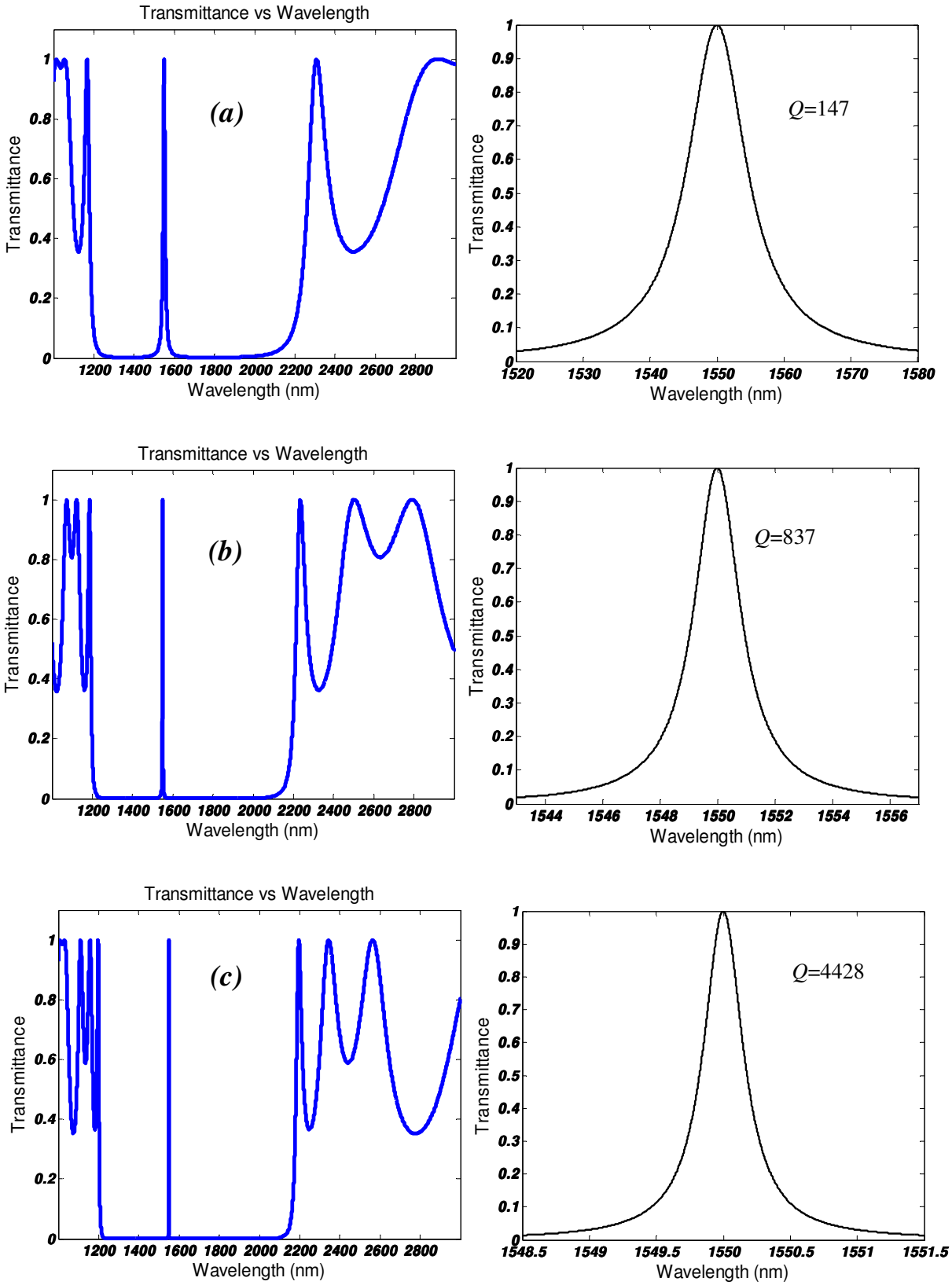

Fig.2.9 Transmittance versus wavelength characteristics of Si/SiO_2 multilayer microcavities with SiO_2 defect layers comprising (a) 6 pair of layers with Q value of 147 (b) 8 pair of layers with Q value of 837 (c) 10 pair of layers with Q value of 4428.

2.4.2 Low Index Layer of air

The second basic structure considered is a structure comprising quarter wavelength air filled low index gaps between quarter wavelength of Si layers, with the refractive index of air assumed to be 1. Such a basic structure more closely resembles the intended Si/air 1-D PhCs to be defined and fabricated into SOI ridge waveguides.

Two types of structures were simulated, first is the one with double width of air layer to be the defect layer. Table 2.3 shows the details of the whole structure and Fig.2.10a-c show the simulation results.

Layer	Material	Refractive Index	Thickness
1	air	1.0	387.50nm
2	Si	3.4	113.97nm
Defect	air	1.0	775.00nm

Table 2.3 Parameters of quarter wavelength stacks comprising air filled low index layers and Si high index layers and with double width of air layer to be the defect.

Second is the structure with double width of Si layer to be the defect layer. Table 2.4 shows the details of the whole structure and Fig.2.11a-c show the simulation results.

Layer	Material	Refractive Index	Thickness
1	air	1.0	387.50nm
2	Si	3.4	113.97nm
Defect	Si	3.4	227.94nm

Table 2.4 Parameters of quarter wavelength stacks of air filled low index layers and Si high index layers and with double width of Si layer to be the defect.

It also can be seen from the spectra in Fig.2.10 and Fig.2.11, with the number of pairs of layers increase, the photonic band gap has a trend of becoming narrower and narrower and band gap edges are getting sharper. A big increase of quality factor value has been observed as the number of pairs of layers increases as well compared to the Si/SiO_2 situation. And resonances of 1550nm have been observed in all the spectra.

And for the same number of pairs of layers, Q values of the Si defect structures are much higher than the air defect structures, this is due to the refractive index of Si is much higher than air, a high index cavity medium creates high reflectivity for the mirror stacks, thus higher Q values are obtained for Si defect structures than air defect structures for the same number of pairs of layers, which agrees with the results in the previous section of Si and SiO_2 defects situation.

It can also be further noticed for the same Si defect with same number of pairs of layers, Si/air mirror formations have higher Q values than Si/SiO_2 formations, the reason is higher refractive index contrast creates higher reflectivity to the mirrors, thus leads to higher Q values.

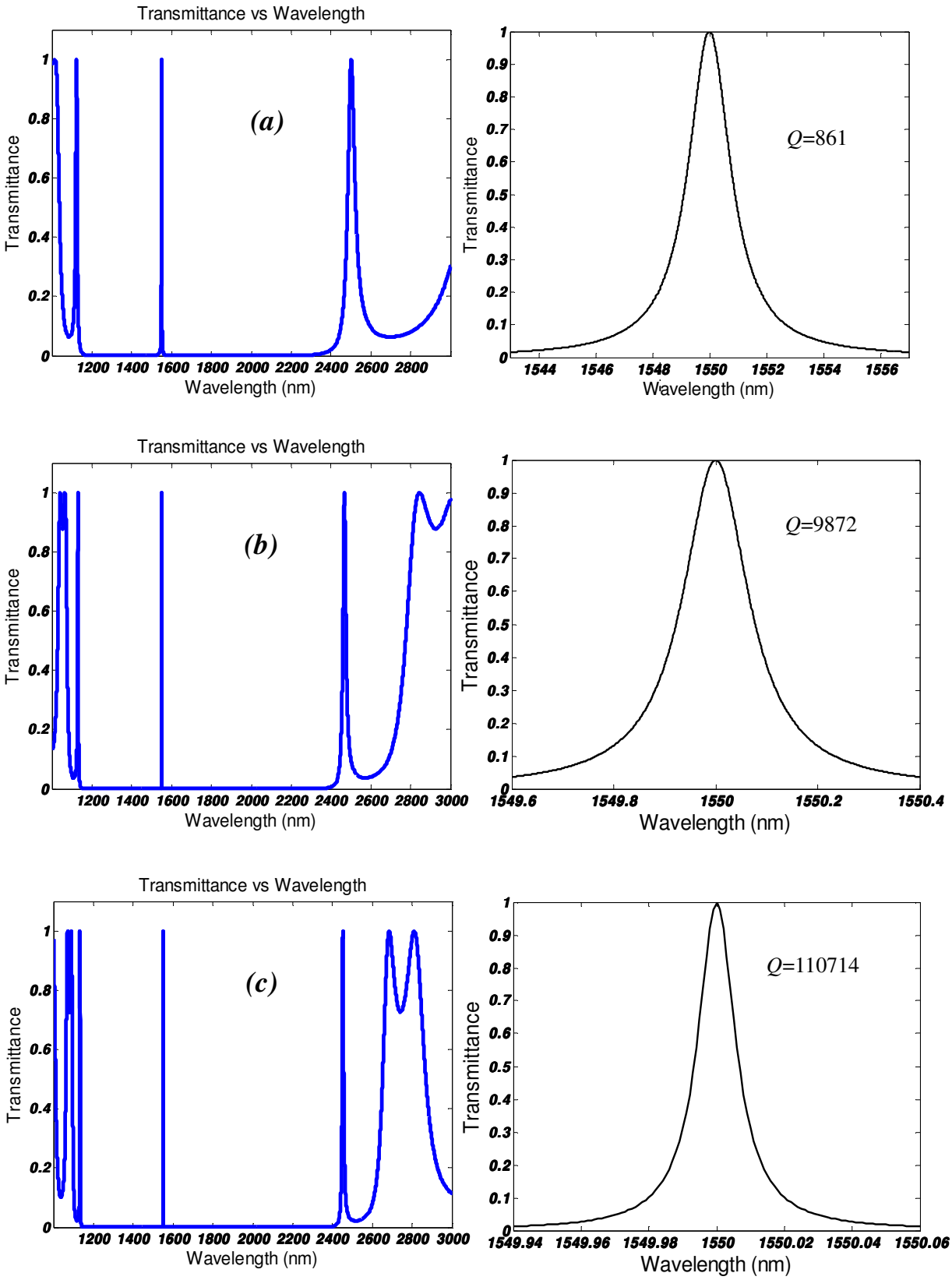

Fig.2.10 Transmittance versus wavelength characteristics of Si/air multilayer microcavities with air defect layers comprising (a) 6 pair of layers with Q value of 861 (b) 8 pair of layers with Q value of 9872 (c) 10 pair of layers with Q value of 110714.

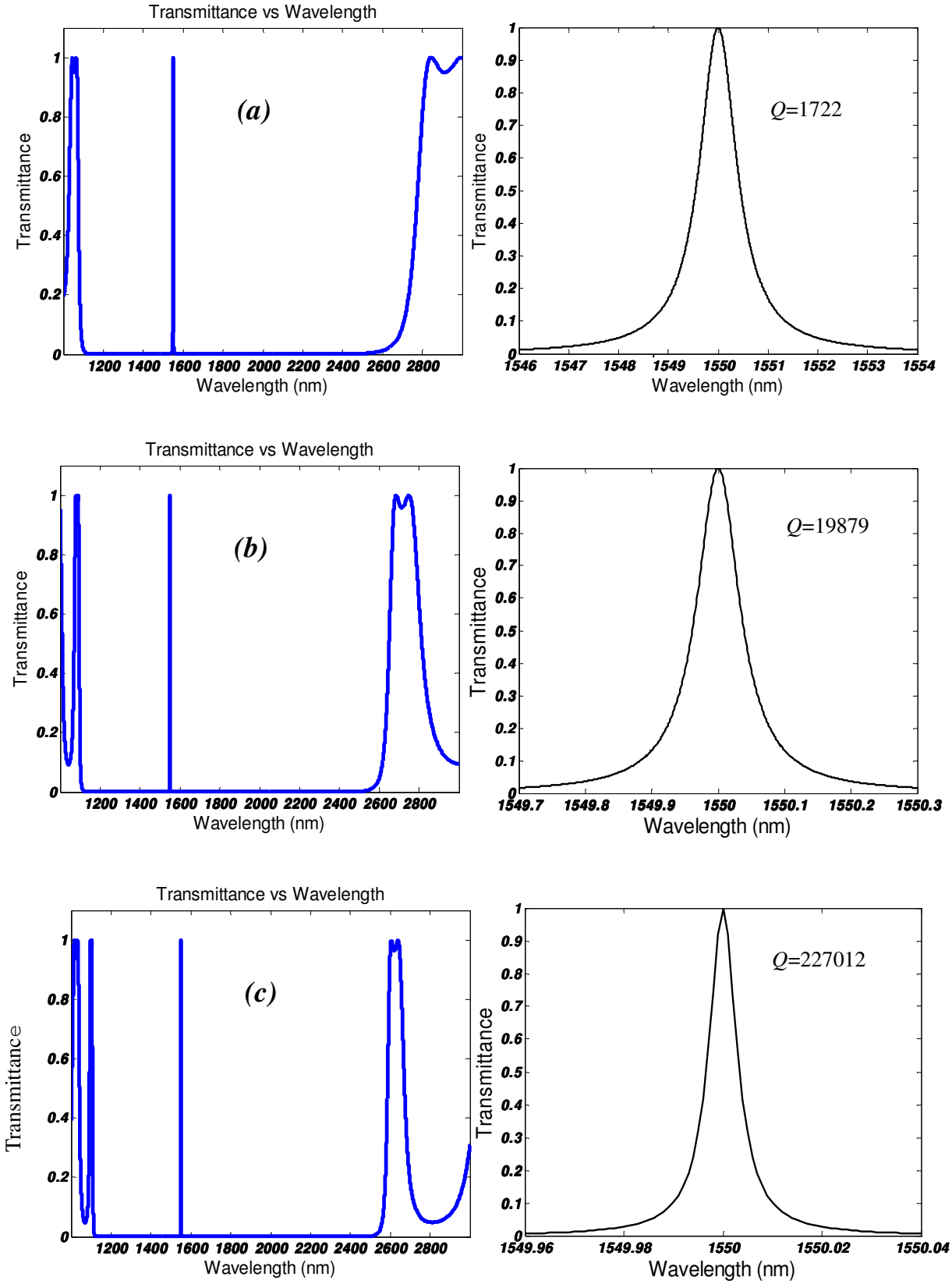

Fig.2.11 Transmittance versus wavelength characteristics of Si/air multilayer microcavities with Si defect layers comprising (a) 6 pair of layers with Q value of 1722 (b) 8 pair of layers with Q value of 19879 (c) 10 pair layers with Q value of 227012.

2.4.3 Conclusions of the Simulations

As can be seen from the above spectra, the photonic band gap has a trend of becoming narrower and narrower and the band gap edges get sharper and sharper as the number of pairs of layers increases, and also big rise of quality factor values is observed as the number of pair of layers increases, this is due to the higher reflectivity introduced by the added layers, and it can be seen that the position of the transmission peak is localized at the wavelength of 1550nm, in agreement with the design.

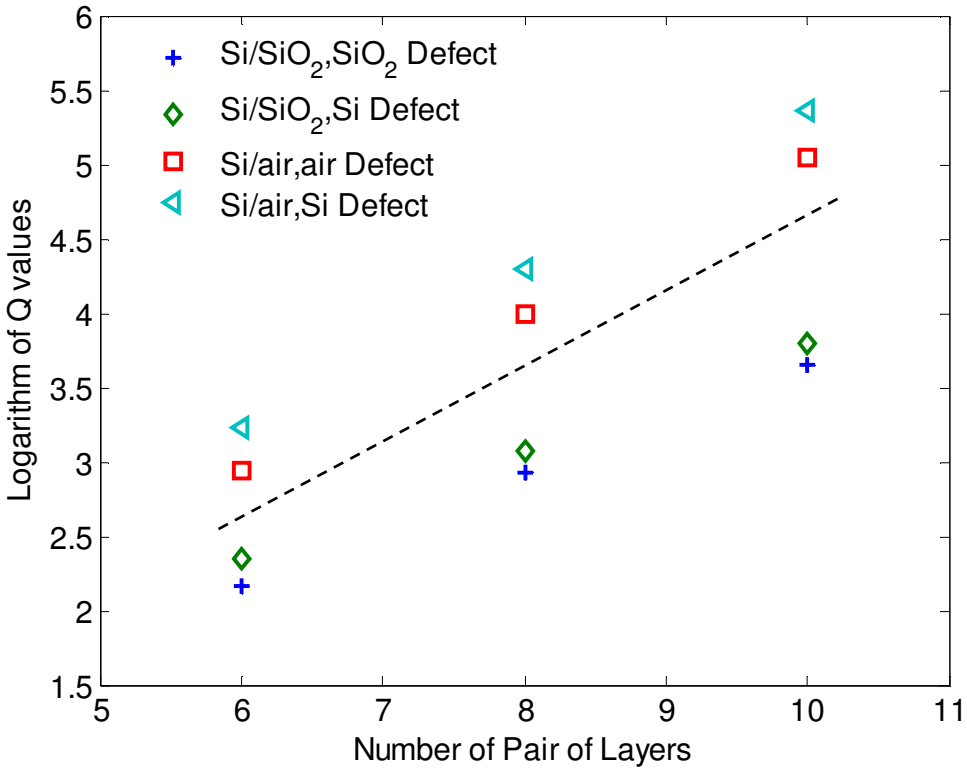

Fig.2.12 Logarithm of the obtained Q values versus number of pair of layers of different 1-D PhC structures; the dashed line is added to indicate the linear increase of the logarithm values.

For analyzing the quality factor values, Fig.2.12 shows the logarithm of the calculated Q values versus the number of pairs of layers, a clear linear trend of the logarithm values versus the number of pairs of layers can be observed, which indicates that in a limited periodic structure, Q values increase exponentially with the increase of the number of pairs of layers, due to the stronger reflectivity introduced

by the added layers. And for the same number of pair of layers also with the same defect material, Si/air structures have higher Q values than Si/SiO_2 structures, this is because higher refractive index contrast yields higher reflectivity for the mirrors. Further, it can also be noticed in Fig.2.12 that for the same Si/SiO_2 or Si/air structure, a higher index defect layer creates a higher Q value, this can be explained by the fact that the actual mirror reflectivity depends on the refractive index of the cavity medium, i.e. the reflectivity of a quarter-wave stack depends on the refractive index of the medium where the beam is launched and a high index medium creates high reflectivity for the stacks, so it can be concluded a high index defect layer is more effective than a low index defect layer in making a microcavity in order to obtain a high quality factor.

These calculated results inform that for practical PhC devices, in order to obtain high quality factor microcavity with small cavity volume, Si/air mirror formation with Si defect layer are desirable, the following fabrication works are based on such fundamental informations.

Chapter 3. Fabrication of the Photonic Crystal Structures

3.1 Introduction

The integration of PhC structures into Si ridge waveguides as a means of achieving highly integrated optical circuits has attracted much attention in experimental research into PhCs. This chapter describes the fabrication process of the Si waveguides and PhC nano-structures and builds up the fundamental technology for further exploration of various types of PhC structures in this PhD project.

Silicon-On-Insulator (SOI), owing to its cheap price and mature manipulation technologies, such as cleaning, etching and cleaving, was chosen in this project as the medium for fabricating the PhC devices. First, the waveguides were defined by photolithography and inductively coupled plasma (ICP) etching and designed to have bend with sinusoidal varying bends to avoid direct light coupling from input fibre to output fibre in the following measurement, next, electron beam lithography followed by further ICP etching were used to define the nano-structures. The samples were then thinned by mechanical polishing to a thickness of about 100 to 150μm to ensure good optical facets can be obtained in cleaving. The following sections of this chapter describe each of the fabrication steps in detail.

3.2 Preparation of Bending Waveguides on an SOI Chip.

In order to place the 1-D PhC structure into a waveguide, six bending ridge waveguides have been created on an SOI chip using conventional photolithography and dry etching technologies. Fig.3.1 shows the silicon ridge waveguide structure, including the intended dimensions, these being about 2.5μm wide and etched to a depth of about 200nm in a silicon layer of thickness 350nm.

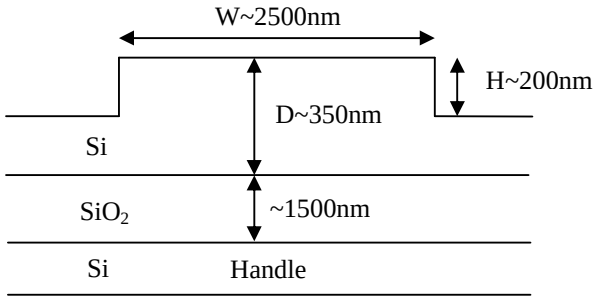

Fig.3.1 Side Elevation of the Waveguide.

The fabrication process of the waveguides is shown schematically in Fig.3.2(a-d).

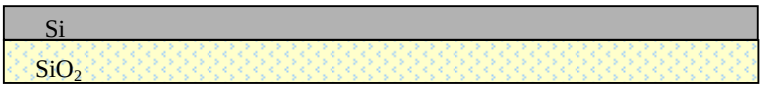

(*a*) An unprocessed SOI wafer.

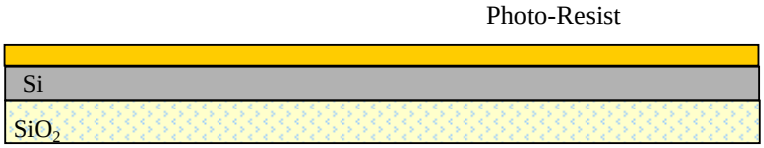

(*b*) After photo-resist coating.

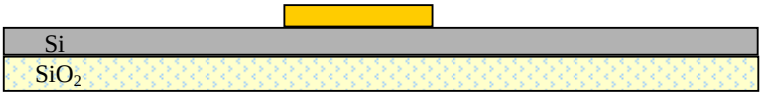

(c) After waveguide mask alignment and UV exposure and development.

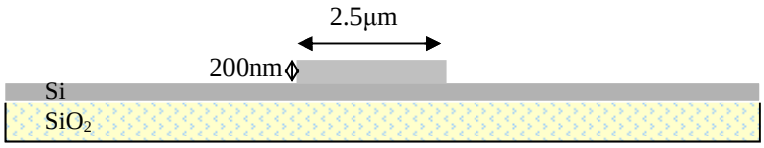

(*d*) After dry etching and removing remaining photo-resist.

Fig.3.2 (*a*) shows an unprocessed SOI wafer consisting with 350nm Si on the top and 1.5μm SiO_2 beneath; (*b*) shows the wafer after photo-resist coating; (*c*) shows after mask aligning, UV exposure and development, the shape of the waveguide left on the photo-resist; (*d*) is the side elevation of the Si waveguide after dry etching.

In order to create the tiny PhC structures in the right places of the waveguides by the electron beam lithography (EBL) technology, some alignment markers are required on the chip. For optimum alignment of the PhC structures to the underlying waveguides, these markers should be aligned with the waveguides. This marker area consisted of a large number of small squares (both with 16×16μm and 30×30μm), which are made from ~100nm thick gold deposited on 50 nm titanium by thermal evaporation. The Ti layer is used to give the gold good adhesion to the underlying Si.

Gold markers are required to give a clear target for sample viewing during the alignment process under SEM. Fig.3.3 shows the marker area, which was used for position alignment. In particular, the marker of Fig.3.4 was used for aligning the writing field before EBL exposure. The details of using the marker area and marker for alignment can be found in Appendix 2.

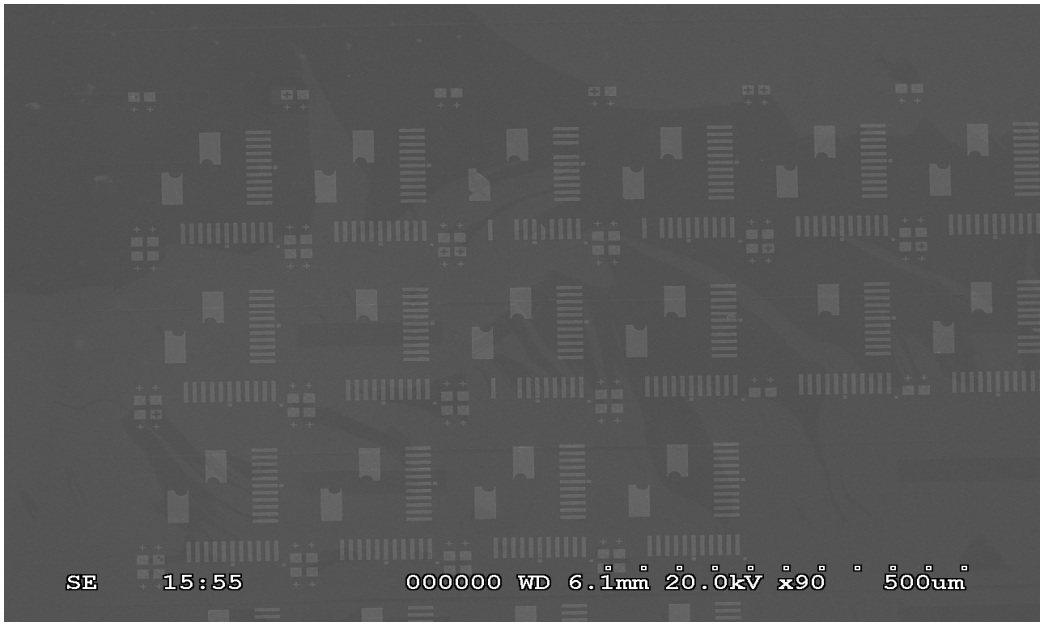

Fig. 3.3 SEM image of the Gold Marker area.

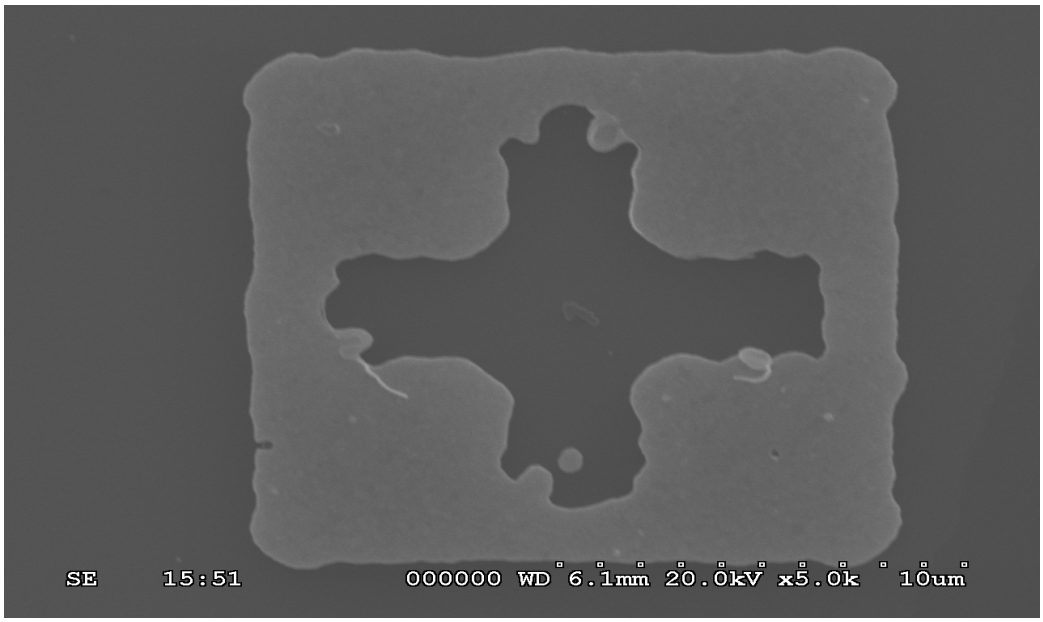

Fig. 3.4 SEM image of the 16×16μm Gold Marker, which was used for writing-field alignment.

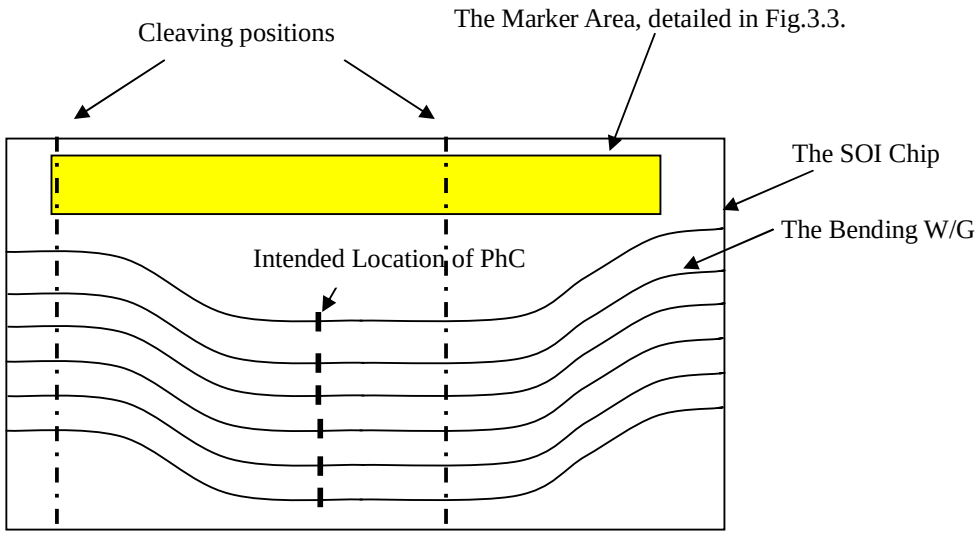

Fig. 3.5 Plan view of the six bending waveguides and the marker area on the chip.

Fig.3.5 shows schematically a plan view of the waveguides created and markers evaporated on the SOI chip. The black dashes across the waveguides indicate the intended locations of the PhC structures. For the sake of the final measurement, the PhC patterns are designed to sit in the near-centre, horizontal part of the waveguide. This enables the grooves in the PhC pattern to be perpendicular to the waveguide and eases cleaving of the sample.

3.3 Preparation of the Wafer for the Electron Beam Lithography

After this Ti/Au marker evaporation step, the chip is ready for defining the PhC structures by EBL. The next stage is further sample cleaning in solvents prior to spin coating with a resist sensitive to electron beam. In this work, it was polymethyl-methacrylate (PMMA).

For deep cleaning the chip, an ultrasonic bath was used. First, the chip was soaked in trichloroethane (TCE), acetone, and propan-2-ol (IPA) separately, then the beaker containing the chip and solvent was put in the ultrasonic bath for about 15 minutes

processing. This process may be repeated several times depending on the outcome of sample inspection for cleanliness under an optical microscope.

Once a clean chip surface is obtained, the chip is then spin-coated with dropped PMMA at 5000 rpm for 30s (ramp at 1000 rpm/s) and baked for 1 minute at 190^{o}C on a hot plate. The base of the chip is then wiped on a piece of tissue after taking it off the spinner chuck to remove any PMMA on the back face to ensure the chip is exactly level in the EBL system.

3.4. The Electron Beam Lithography Technology

Electron beam lithography (EBL) is a specialized technique for creating the extremely fine patterns required by the modern electronics industry for integrated circuits. Derived from the early scanning electron microscopes, the technique consists of scanning a beam of electrons across a surface covered with a resist film sensitive to electrons of the energy used, thus depositing energy in the desired pattern in the resist film. The process of forming the beam of electrons and scanning it across a surface is very similar to what happens inside an everyday television or CRT display, but EBL typically has three orders of magnitude of better resolution. The main attribute of the technology is that it is capable of very high resolution, almost to the atomic level. It is a flexible technique that can work with a variety of materials and an almost infinite number of patterns. However, it is slow, being one or more orders of magnitude slower than optical lithography; and it is expensive and complicated. Electron beam lithography tools can cost millions of dollars and require frequent servicing.

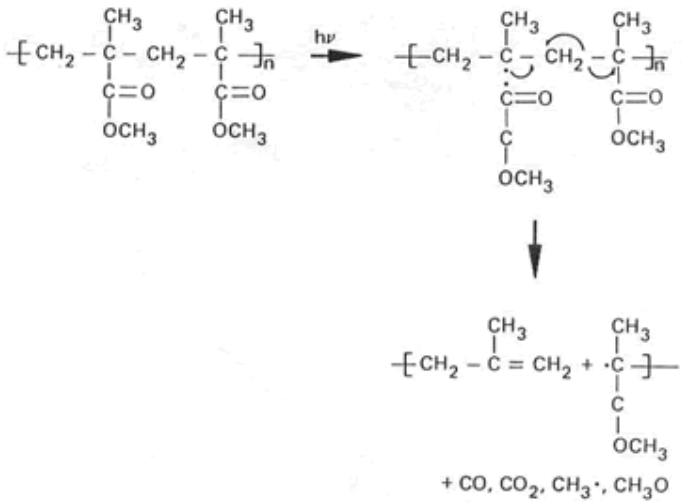

Fig. 3.6 Electron beam exposure breaking the polymer into fragments.

Electron beam exposure breaks the polymer component of the resist film into fragments (as shown in Fig. 3.6) that can be dissolved in a developer. In this work, 1:3 MIBK:IPA (MIBK is methyl isobutyl ketone and IPA is isopropyl alcohol) is used. The Raith and Hitachi EBL system in the nano-fabrication clean-room at the University of Bath is a universal lithography system which consists of a scan generator electronic (hardware) and a computer based operating software. The system has control in three major areas of scanning electron microscopes (SEM): beam blanker control, scan & signal control and stage control. Editing and pattern design is made simple with a GDSII internal editor. This allows users to build hierarchy patterns on different levels and designs with any dose level. Then pattern data can be generated with the simple CAD program included, or can be imported from a DXF (Auto CAD) file.

3.5 Creation of the PhC Structures

3.5.1 The Electron Beam Lithography Process

Firstly, the pre-prepared sample containing the bending ridge waveguides and gold alignment markers was loaded into the EBL chamber without coating PMMA. This operation is aimed at calibrating the PhC pattern positions with reference to the markers, since the positions and shapes of the latter will not now change. Three points from the markers were chosen to set up a so called *u*-*v* coordinate, which is independent from the physical construction of the chip surface, and these three points were recorded for the next step. From this newly created *u*-*v* coordinate system, the intended positions of the PhC patterns are now read and recorded. For details of this operation, please see Appendix 2.

Next, the chip was spin coated with PMMA and then re-inserted in the EBL chamber. Based on the calibration work and recorded positions of the markers and the intended positions of the PhC patterns, the EBL could now be driven to these positions automatically. Also, several steps including “Creating Positionlist”, creating the position coordinates of the pattern area, “Field Alignment”, aligning the write field, “Write-filed Corrections”, assigning a right write-field size to the software, “Dose Adjustment”, finding a proper exposure dose, and finally “Exposure” were performed stage by stage.

3.5.2 PMMA Resist Development

After exposure, the next step involves developing the resist. PMMA is far and away the most widely used e-beam resist, offering extremely high-resolution, ease of handling, excellent film characteristics, and wide process latitude. One of the primary attributes of PMMA is its simplicity. PMMA polymer dissolves in mixed solvents (Anisole safe solvent). Exposure causes scission of the polymer chains. The

exposed (lighter molecular weight) resist is then dissolved in the solvent developer.

The developer used is 1:3 by volume mixture MIBK : IPA. Experience showed it is best to prepare a fresh batch for important work, for such kinds of organic solvent can evaporate and change the concentration ratio of the developer. The temperature of the developer should be ~24°C and the development process should proceed for 5-30 seconds, after which the sample should be washed in pure IPA (iso-propyl-alcohol). Please also see Appendix 2 for the way of obtaining very fine nano-features through EBL.

For the PhC structure fabrication process, it was found that optimising the development time is very important, since both over developing or under developing will cause poor feature definition in the nano-structures. To find the optimum development time, process time was incremented in 5 seconds with inspection under an optical microscope after each step to assess the results. Final inspection must be in the EBL system itself operating in SEM mode. After many trials, 30 seconds was found to be the optimum developing time for the PhC structures described here.

3.5.3 Etching

After the sample has undergone EBL pattern definition and resist development, PhC patterns are etched into the ridge waveguide structure by inductively coupled plasma (ICP). The principle of ICP etching is shown in Fig.3.7. This is one of several drying etching methods for creating nano-structures and was chosen for the final etching step on the silicon chip, as it results in near vertical sidewalls [Collins 2006], as required to produce accurate structure definition in the PhC structures.

An inductively coupled plasma (ICP) is a very high temperature (7000-8000K) excitation source that efficiently dissociates, vaporises, excites, and ionises atoms.

ICP sources are used to excite atoms for atomic-emission spectroscopy and to ionise atoms for mass spectrometry.

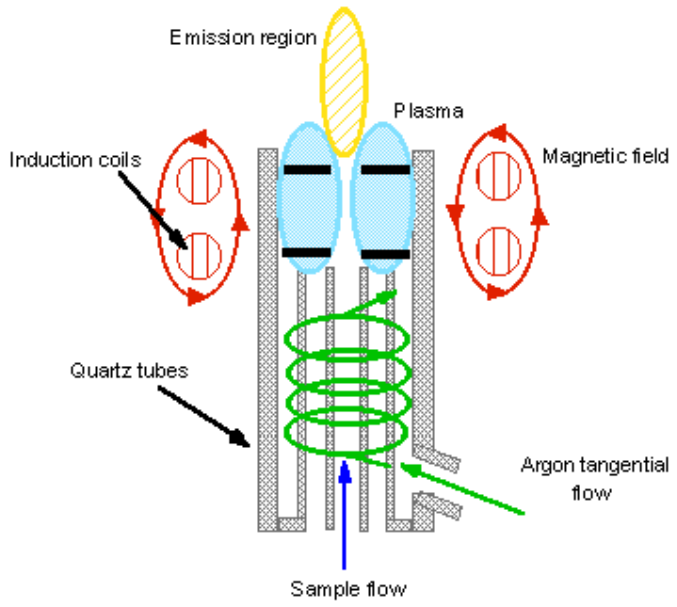

Fig. 3.7 Schematic show of the ICP equipment.

To obtain good etching by the ICP process, choosing an appropriate gas recipe and gas flow rate are very important. A literature survey [Peyrade 2002, Jugessur 2003, Chung 2004, Ji 2006] revealed the following gas recipe to be the best one for silicon etching: CHF_3─7sccm; SF_6─3sccm; RF─35; [Ji 2006] This recipe produces an etching rate of about 55nm/min for silicon.

To prevent the PMMA from etching under the plasma, use of the ICP power should be avoided. Etching trials were carried out in order to validate the process, notably the etch rate and PMMA mask durability. The initial experiment used a two minutes etching time using the plasma and gas flow conditions stated above. The etch depth was assessed using a surface profile-meter, from which was deduced that the etch rate of Si is 55nm/min and that of PMMA is 60nm/min. Since the coating thickness of the PMMA is about 200 nm and the requirement for the depth of the air gaps in the silicon is 150--200 nm in order for light transmission to satisfy approximately the calculations from the TMM model, it was concluded that PMMA can be used

directly for protecting the unexposed area.

After ICP etching, the final step of the whole fabrication process was put the chip into acetone solvent again for removing the residual PMMA. The finished sample is schematically shown in Fig. 3.8.

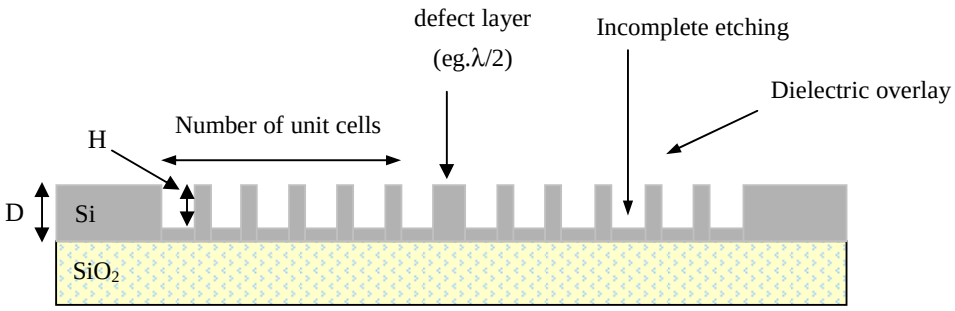

Fig. 3.8 Schematic side elevation of 1-D PhC waveguide.

3.5.4 SEM Images of the PhC Structures

The Si waveguides in the images shown in this section were etched by ion milling rather than ICP, done with the support of a technician at the beginning of the project. It is obvious that the roughness of the sidewalls of the waveguides shown here is more severe than in the sidewalls of the PhC pattern, and such a coarse etching could introduce severe scattering losses to the waveguides, although no waveguides etched by ICP and containing same PhC pattern were created for comparison. In later work, both the ridge waveguides and the PhC patterns were defined by ICP etching, with the result that side wall roughness of the waveguide ridge was much reduced.

Fig.3.9 shows an SEM micro-photograph of a completed structure under ×12000 magnification. The device comprises of six designed 387.50nm wide air gaps, and four designed 113.97nm wide Si sections including a 227.94nm wide centrally positioned defect layer of Si.

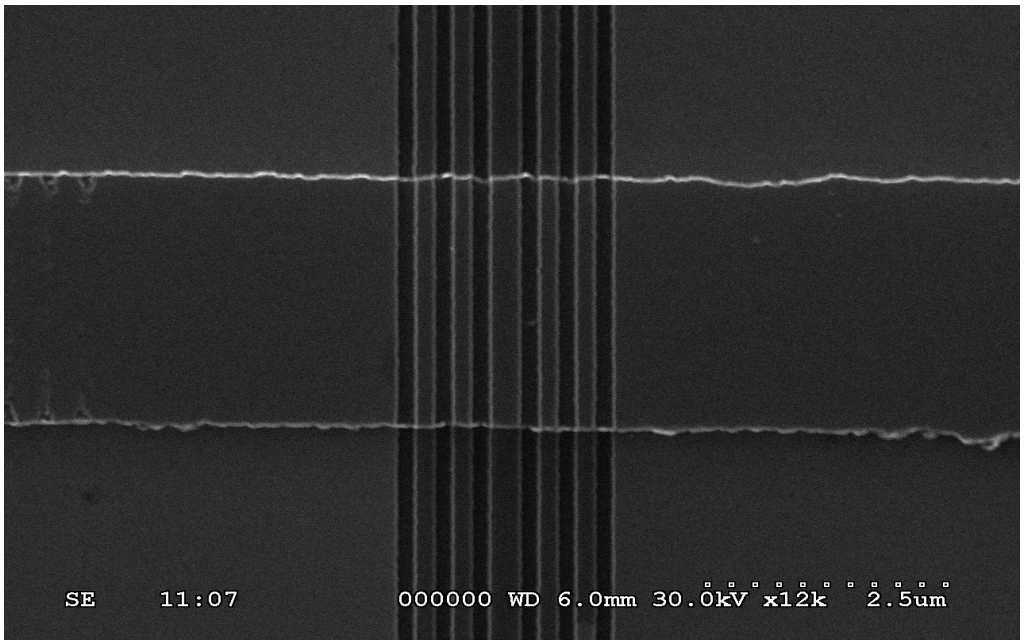

Fig.3.9 SEM image of the 1-D PhC microcavity comprising 6 bilayers of Si/air with the Si layer of the third period increased to form a defect. The image was taken at ×12000 magnification.

Fig.3.10 shows an SEM photograph of another waveguide microcavity. The structure consists 8 grooves of air at the designed size of 387.50nm and 6 sections of Si at the designed width of 113.97nm while in the middle of the structure is a designed width of 227.94nm Si defect layer.

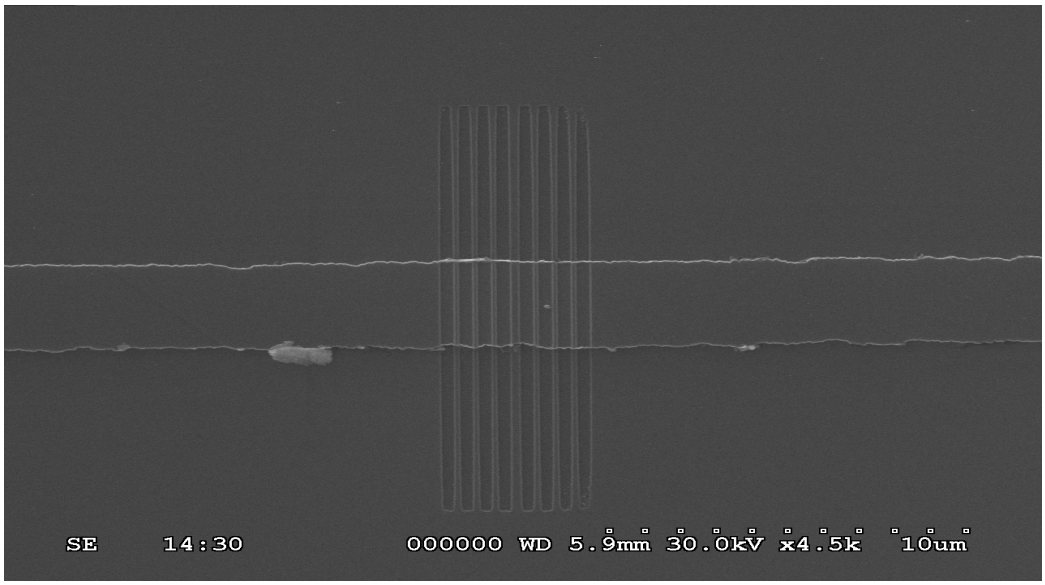

Fig.3.10 SEM image of the 1-D Si/air PhC structure of 8 bilayers under 4.5k magnification.

Fig.3.11 shows an SEM photograph of another fabricated PhC structure. This structure consists of 10 grooves of air at the designed size of 387.50nm and 8

sections of Si at the designed width of 113.97, while in the middle of the structure is a 227.94nm wide Si defect layer.

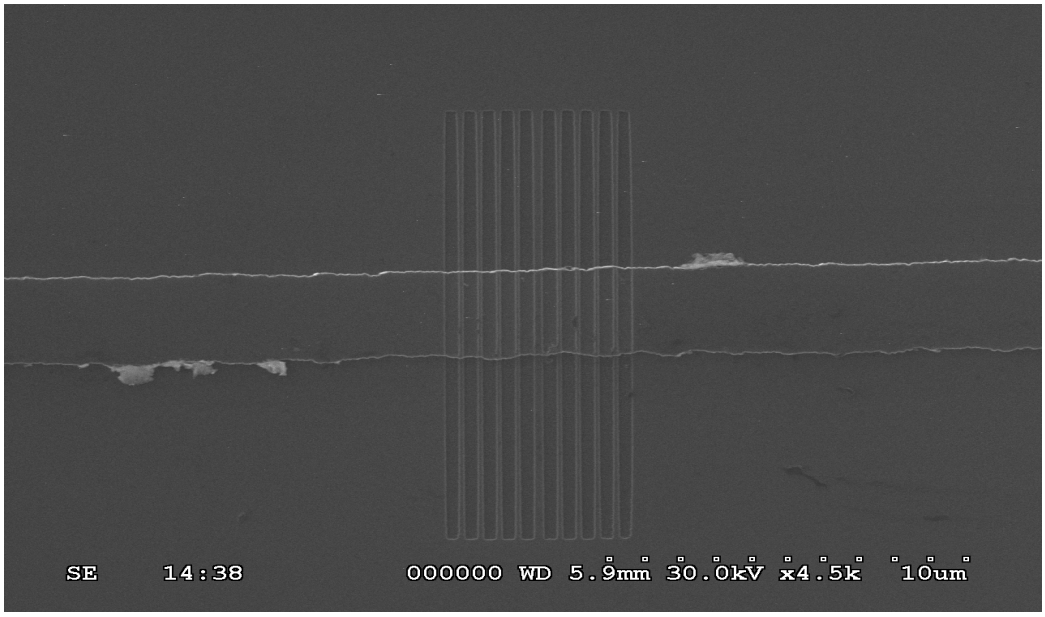

Fig. 3.11 SEM image of the 1-D PhC structure of 10 bilayers under 4.5k magnification.

Fig.3.12 shows the 6 bilayers PhC structure at the magnification of 25k. This high magnification image allows a clearer view of the sidewalls of the PhC structure. Unlike the waveguide ridge, the edges of the PhC layers are sharply defined, indicating that the side-walls etched by ICP are nearly vertical, as probably required for clearly demonstrating photonic crystal structure effects. Also from this highly magnified image, the dimensions of the Si and air layers could be estimated. The measured width of the air layer is about 380--400nm with the design width of 387.50nm, the measured width of the Si is about 130--150nm with the design width of 113.97nm, and the defect Si is about 210-240nm with the design width of 227.94nm. This 10-30nm deviation stands comparison with the state of the art in semiconductor based nano-fabrication using EBL.

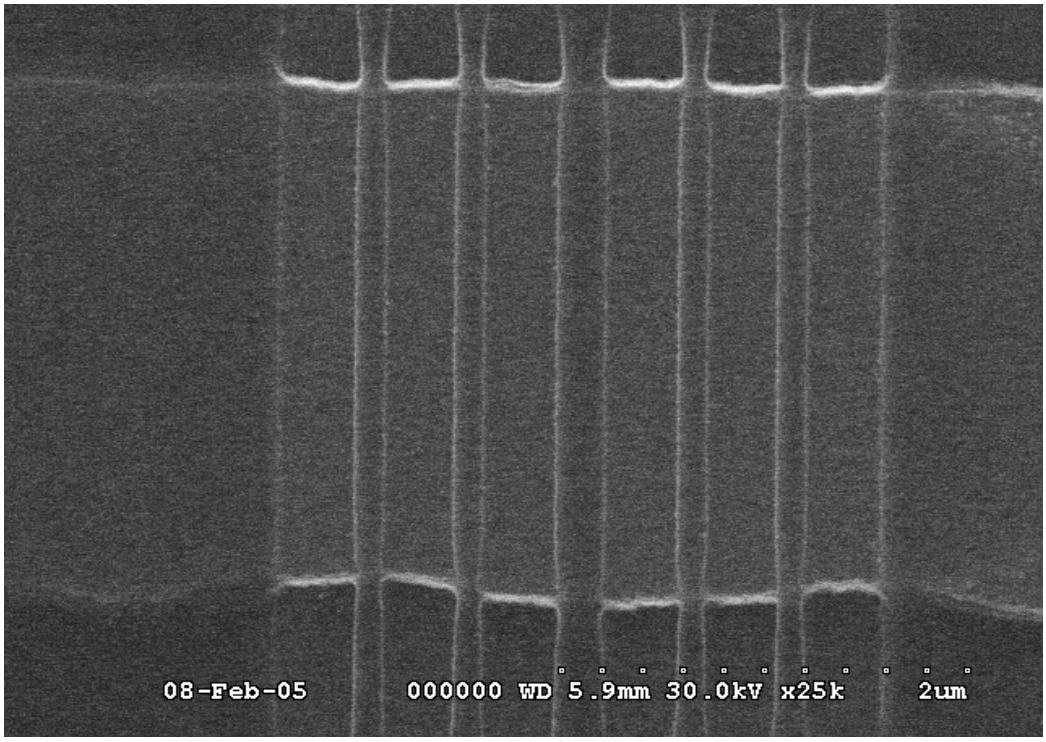

Fig. 3.12 SEM image of the 1-D PhC structure of 6 bilayers under 25k magnification.

TMM calculations have been performed based on these estimated dimensions, it is shown in Fig. 3.13 that such a dimension deviation will mainly shift the resonant wavelengths with the quality factor values remaining almost the same. Reduction of the layer width will shift the resonances to shorter wavelengths while accretion has a reverse effect.

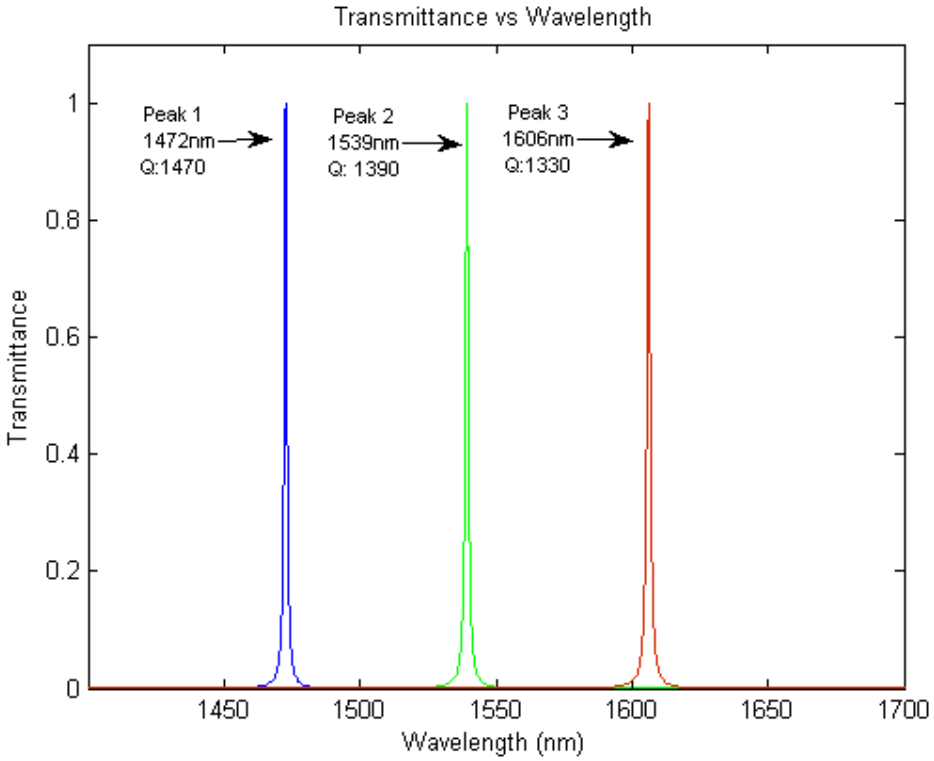

Fig. 3.13 Resonances of 6 bilayer Si/air stacks with Si defect. Peak 1, d_{Si} is 130nm, d_{air} is 380nm with d_{Defect} is 210nm; peak 2, d_{Si} is 140nm, d_{air} is 390nm with d_{Defect} is 220nm; peak 3, d_{Si} is 150nm, d_{air} is 400nm with d_{Defect} is 230nm.

Overall, the images in Figures 3.9 to 3.12 show that the PhC structures are created with high fidelity with the intended design in the Si waveguides, demonstrating the excellent process control achieved by EBL and ICP.

3.6 Thinning and Cleaving of the Sample

Since the butt-coupling method has been chosen for measuring the PhC integrated waveguides [Peyrade 2002], obtaining good optical facets on both sides of the waveguide is essential. Si is brittle and, if thin enough, will cleave along the (110) crystal lattice direction, thus creating smooth facets via which light can be coupled in and out of the ridge waveguide. To ensure accurate and clean cleaving close to the PhC structure, the sample first must be thinned by polishing. The chip was fixed by

wax with rear side up on to a metal mount and then polished with a mixture of water and lube. After a slow and careful process, the chip was thinned down to about 100μm for cleaving.

The cleaving was executed under a microscope by carefully cutting the waveguide. The chip was cut twice: one is in the middle and another is on the edge of the waveguide, while the active area containing the PhC structure was carefully protected and remained in the cleaved-off part.

3.7 Success Rate of the Sample Fabrication

From the description of the fabrication process in the above sections, it can be seen that the SOI wafers traveled a long and tough journey to finally become measurable samples, the inevitable damaging to the samples in cleaning, resist coating, exposing, etching, thinning and cleaving made that only about 10 to 20 percent of the fabricated samples finally have filtering responses.

3.8 Conclusions

In summary, a flexible procedure was developed for fabricating one dimensional PhC devices etched into SOI waveguides. Whilst the procedure depended on advanced techniques like EBL and ICP etching, these methods could be readily optimized to produce PhC devices with dimensions control close to the state of the art. The results of detailed optical characterization of various PhC structures are presented in the following chapters.

Chapter 4. Characterization of the Photonic Crystal Structure Integrated Waveguides

4.1 Introduction

The measurements were all based on a specially constructed system, which is composed of a computer controlled tunable diode laser source and power optical detector with a microscope aided nano-positioning system for extremely fine alignments. Light was coupled into and out of the waveguide samples using fibre butt coupling method. A number of fabricated samples were measured by the laser stepping method and the results generally compared well with the TMM calculation prediction.

Furthermore, a novel method for accurately measuring the quality factor of a microcavity was developed. This method could precisely determine the resonant wavelength and accurately evaluate the quality factor values of the microcavities. The improved spectral resolution of this new technique revealed that the Q of the 1-D PhC microcavity was 27% higher than estimated by stepping the wavelength of the tunable diode laser.

4.2 The measurement test bed

For the purpose of very fine optical measurement, an optical test bed was set up. This consists of an air bearing optical bench, an ANDO AQ4321D tunable external cavity diode laser source, two NanoMax TS 3-Axis flexure stages which give better than ±10nm positioning resolution and repeatability, and an HP 8153A Lightwave Multimeter. Further, a microscope, which had been specially modified, was fixed on the top of the air floating bench and used for preliminary alignment.

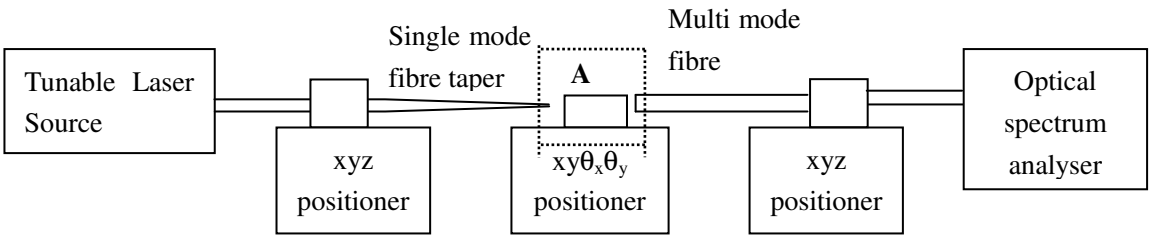

Fig. 4.1 Sketch of the Measurement Set up

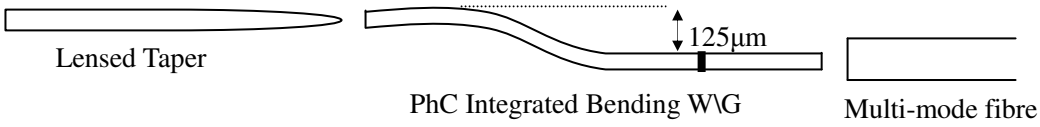

Fig. 4.2 Enlarged View of Area "A"

Fig. 4.1 Arrangement of the whole measurement station, where Fig. 4.2 gives an enlarged plan view of area "A" of Fig. 4.1, showing the light coupling and collection from the PhC integrated bending waveguide; the lensed taper could focus the light into a 2µm diameter spot with a working distance of 14µm, the output fibre was multimode with a 62.5µm diameter core.

The tuning range of the laser was limited to 1500nm—1620nm wavelength, with step of 0.01nm, therefore, the test bed is not capable of measuring all the band gaps of the PhCs, as these tend to exceed the tuning range of the laser. Instead, the purpose was to investigate in detail the resonant behaviour of a range of microcavity devices of the type shown in Figs 3.10-3.12. All the equipment, except the xyz-positioners, were computer controlled. A Labview code [Davies 2005] can give

a very fine step control of the tunable laser source, notably varying the wavelength, and read data from the multimeter. The obtained data were kept in .txt files for export to graph plotting software.

4.3 Fine Alignment with the NanoMax TS 3-Axis Flexure Stages

Because of the butt coupling method used for the measurement, the alignment became the critical step during the measurement process. In order to align optimally the light launching fibre taper and the power collection fibre to the ridge waveguide, extensive adjustment of the *x*, *y*, *z* coordinates of each fibre was required, as well as adjustment of the tilt of the sample itself.

The NanoMax-TS 3 axis flexure stage has *xyz* axes on each of the piezoelectric positioners that can be driven by open-loop control from a high voltage output amplifier to provide nanometric positioning on the three orthogonal axes. This *xyz* positioner is suited to the alignment of optical fibres, optical waveguides, optoelectronic packages and any other high resolution alignment or positioning application, including general purpose laboratory tasks. The power launching taper and the output receiving multimode fibre, the latter used for its large numerical aperture to enable easy alignment for maximum power detection, were both mounted on the two NanoMax stages. During the alignment process, the three axes were adjusted while observing the optical power meter display until maximum power throughput was achieved. Next, the chip was tilted about the *x* and *y* axes (which lie in a plane perpendicular to the paper with reference to Fig.4.1) to test for further increase in optical power throughput. Then the positions of the input and output coupling fibres were once more adjusted. This procedure took place iteratively until maximum optical power throughput resulted.

4.4 Results and Analysis

As indicated in Section 3.7, the rate of the samples having filter response is about 10 to 20 percent and nearly 40 wafers were fabricated at this preliminary stage; the quality factor values from the best performed waveguides are listed in Table 4.1. The wavelength resolution of the tunable laser enables the 3dB points of a low Q resonance to be measured to high accuracy. The uncertainty in the measurement of Q lays primarily the accuracy to which the resonant wavelength can be found. As Q values increase, the 0.01nm accuracy achievable with the tunable laser becomes insufficient to measure Q with accuracy better than two significant figures. This convention is adopted in Table 4.1(a), but underestimates the probable accuracy to which the lower Q values were measured.

The data in Tables 4.1 (a) offers approximate validation for the trends observed in the simulation results in Chapter 2. As the mirror number increases, the quality factor becomes higher due to the stronger reflection contributed by the Bragg mirrors, however, the measured Q values do not increase exponentially as the calculated Q values do. This is due primarily to the losses in the real geometry of the structures. Variations of the measured Q values can be noticed for each set of the structures, especially in the 8 bilayers structure, for example, a Q value of 854 was obtained, which is much smaller than average, one very possible reason for this is the inevitable structure parameter fluctuations introduced in fabrication. Further, the average of the measured Q values with 8 bilayers is higher than 10 bilayers, which suggests in practice, further increasing the number of the mirror layers does not straight lead to Q values increasing, this can be explained as that more fabrication complication, losses and also the measurement difficulties introduced by larger volume structures on the contrary limit their performances, and informs the differences between numerical and experimental works.

Number of Bilayers (All with Si Defect)	Calculated Q values from TMM	Measured Q values						Average of the measured Q values
6	1720	630	940	830	780	690	730	770
8	19900	850	1600	1100	1400	1900	1500	1400
10	227000	1100	1300	1400	1300	1400	1200	1300

Table 4.1(a) Calculated and Measured Q values of the fabricated 1-D PhC integrated waveguides.

Table 4.1 (b) shows the measured transmittance. With a trend of transmittance decreasing as the number of bilayers increasing can be observed, the data show in detail that increasing the number of bilayers from 6 to 8 causes the average T to drop from 0.49 to 0.42, a reduction of only ~14%, yet increasing the number of bilayers from 8 to 10 reduces the average T to 0.23, a drop of greater than 50%. The cause of the rapid drop of T with going from 8 to 10 bilayers is very possibly related to the greater fabrication difficulties yet causes structure deviations for large volume structures and also the greater losses introduced by the added layers in measurement.

Number of Bilayers (All with Si Defect)	Measured T						Average of the measured T
6	0.52	0.48	0.52	0.48	0.54	0.44	0.49
8	0.34	0.53	0.35	0.536	0.39	0.37	0.42
10	0.23	0.16	0.21	0.31	0.24	0.25	0.23

Table 4.1 (b) Measured T values of the fabricated 1-D PhC integrated waveguides.

Fig.4.3 shows the resonant part of the measured spectrum of an 8 bilayer 1-D PhC waveguide over the wavelength region of 1500nm to 1560 nm. The measurement was obtained with a wavelength step of 0.01 nm and is compared with the simulated result obtained with TMM.

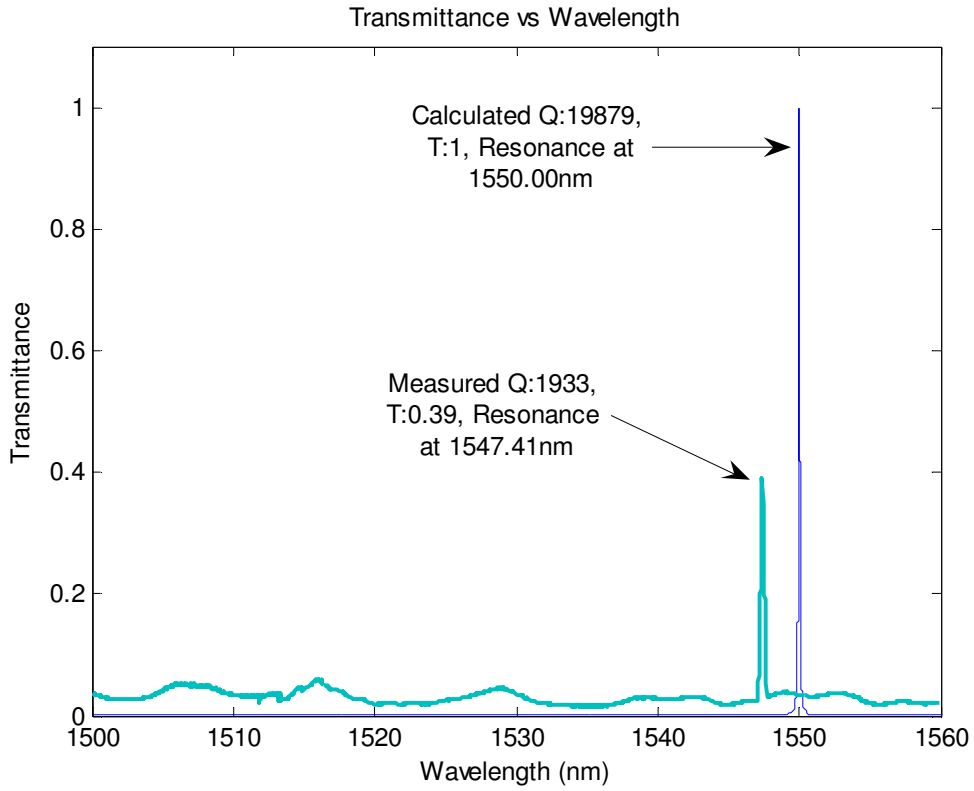

Fig. 4.3 The calculated and measured Transmission Spectrum of the 1-D PhC integrated waveguide of 8 bilayers with Si defect.

As can be observed from Fig.4.3, the resonant peak of the fabricated structure is observed at 1547.41nm wavelength, compared with a designed wavelength of 1550nm. The less than 3nm difference represents only a 0.2% error, demonstrating the high precision of the fabrication procedure. Further, this result implies that a design procedure based on the transfer matrix model at least accurately predicts the resonant wavelength. The validity of the application of TMM to the 1-D PhC is further discussed in Chapter 5. The error between the measured and designed resonant wavelength probably arises from the fact that the air gaps did not penetrate completely to the buried oxide layer. Consequently, the air fraction was lower than intended, making the width of the low index layer different by exactly one quarter of a wavelength, and the effective refractive index is actually higher than the value which was used in the TMM simulation. Additionally, fabrication fluctuations are of importance. A first issue is the non-vertical nature of the groove walls provided by some residual over-etch, under-etch, or a combination of the two. Another important issue is the lithographical error leading to a discrepancy between the designed slit

widths and the fabricated ones. The dimensions of the fabricated PhC structures, are in the 100nm range and have a width accuracy of 20nm, which is at the limit of the nano-fabrication facilities available (which are close to the state of the art). Overall, the close agreement between the measured and simulated wavelengths indicates acceptable fabrication tolerances during device processing.

The Quality Factor (Q Value) is normally used to assess the quality of the resonant cavity and provides a measure of the ratio of energy stored to energy dissipated in the cavity. The Q factor here is defined as the resonant frequency (centre frequency) f_0 divided by the bandwidth Δf or BW:

$$Q = \frac{f_0}{f_2 - f_1} = \frac{f_0}{\Delta f} = \frac{\lambda_0}{\Delta \lambda} \tag{4.1}$$

The bandwidth, BW or $\Delta f = f_2 - f_1$, is measured at full width half maximum (FWHM) of the resonance. From Fig.4.3 of the measurement of the resonance, a $\Delta\lambda$ value of 0.8nm has been obtained with the centre frequency at 1547nm, giving a Q value of 1933. This value of Q compares very favourably with measurements reported for other 1-D PhC waveguide structures [Foresi 1997, Jugessur 2003, Peyrade 2002]. Table 4.2 shows a comparison between measured Q values for 1-D PhC waveguide embedded microcavities and the results reported here. As can be observed from the data in Table 4.2, even without the inclusion of mode matching features the Q values reported exceed all but the highly optimised structures, including mode matching tapers, reported by Velha *et al* [Velha 2006]. For example, a Q value of 460 has been reported for resonant cavity filters formed by etching a row of air holes in an AlGaAs/GaAs epitaxial ridge waveguide [Jugessur 2003]. Further, the array of holes in the latter structure included extra holes designed to improve mode matching between the guided modes of the ridge waveguide and the Bloch modes of the PhC structure. In theory, the inclusion of such mode matching features will improve still further the Q values in the Si/air 1-D PhC waveguide filters of this research.

Reference	Material	Low index hole or groove	Number of periods in each side of the mirrors	Mode matching tapers	Q Value
Krauss	AlGaAs/GaAs	hole	4	Yes	2500
Jugessur	AlGaAs/GaAs	groove	4	Yes	460
Peyrade	Si/air	groove	4	None	110
			4 + taper	Yes	200
Ribolio	Si_3N_4/air	groove	4	Yes	105
Velha	Si/air	groove	2	Yes	1100
			3	Yes	2700
			4	Yes	8900
This work	Si/air	groove	3	None	630-940
			4	None	850-1900
			5	None	1100-1400

Table 4.2 Comparison of measured Q-values for 1-D PhC waveguide embedded microcavities.

The so called “radiation recycling” effect [Lalanne 2003] is used here as a possible explanation for the obtained quality factor values. Like for classical Fabry-Perot cavities [Yeh 1988], the radiation recycling model attributes the resonance to a phase-matching of the fundamental waveguide mode along one cavity cycle, but in addition, it encompasses a possible recycling of the radiated field. This recycling is taken into account within the model by introducing leaky modes in the cavity resonance mechanism, this representation is reasonable since leaky modes are powerful representations which are often sufficient for describing a portion of the total radiation field (in particular the portion close to the waveguide core) in many situations of practical interest [Snyder, 1983]. Fig. 4.4 (*a-c*) shows schematically the mode components and the coupling between them.

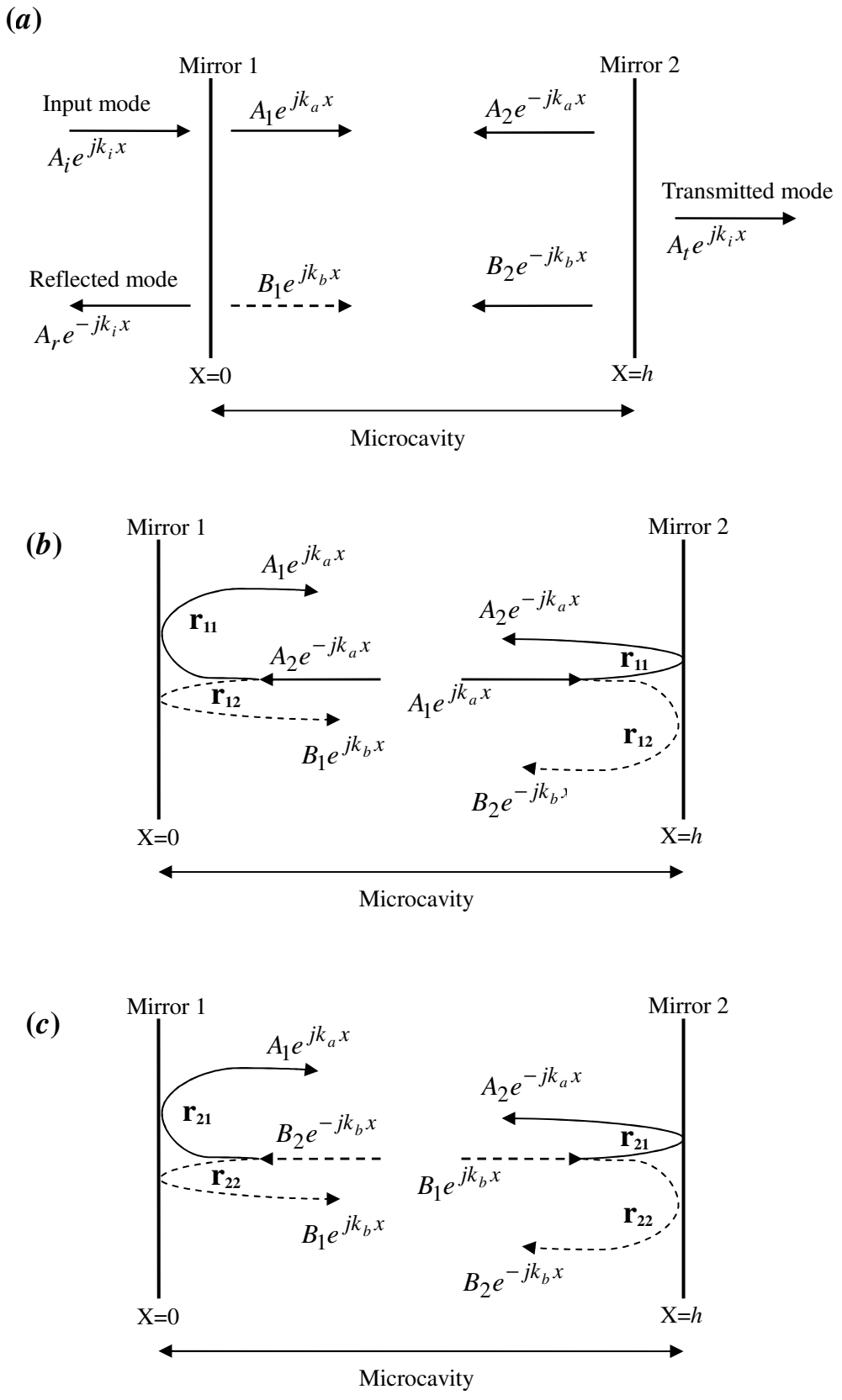

Fig.4.4 Schematic description of the radiation recycling.

At x = 0, according to the radiation recycling theory [Lalanne 2004], the input mode excites 1) a reflected mode $A_r e^{-jk_i x}$ and 2) a fundamental cavity mode comprising two counter propagating components: $A_1 e^{jk_a x}$ from left to right and $A_2 e^{-jk_a x}$ from right to left. While inside the cavity, there are two counter propagating parasitic evanescent or leaky modes, shown in Fig.4.4(a).

Power now couples from the components of the fundamental cavity mode via reflection-coupling, shown in Fig.4.4(b). It is assumed that the two mirrors are identical with r_{11} as the reflection coefficient of the cavity mode at the mirrors and r_{12} as the coupling coefficient between the cavity mode and the parasitic mode at the mirrors. In principle, two other coupling effects can occur at the mirrors: transfer of amplitude from the parasitic modes into the fundamental cavity mode, with coupling coefficient r_{21}.

It is intuitive that the coupling between B components to A components is just the reverse of the coupling from A components to B components; i.e.

$$r_{21} = r_{12} \qquad (4.2)$$

where $r_{21}(r_{12})$ is given by the overlap integral of the amplitudes of the A and B components evaluated at the mirrors. Also shown in Fig.4.4(c) is the direct coupling (reflection) between the leftward and rightward propagating parasitic modes. This occurs with coupling coefficient r_{22}.

Based on the effects illustrated in Fig.4.4, the amplitude of the rightward propagating component of the fundamental cavity mode at x = 0 is fed by three components: 1), the fraction of the input mode transmitted by mirror 1; i.e. $t_m A_i e^{jk_i x}\Big|_{x=0}$ where t_m is the transmission coefficient of a single mirror; 2), the fraction of the leftward propagating component of the fundamental cavity mode; i.e. $r_{11} A_2 e^{-jk_a x}\Big|_{x=0}$ and 3), the fraction of the leftward propagating parasitic mode coupled into the cavity mode

at mirror 1; i.e. $r_{12}B_2e^{-jk_bx}\Big|_{x=0}$. Therefore, at x = 0,

$$A_1 = t_m A_i + r_{11}A_2 + r_{12}B_2 \tag{4.3}$$

From Fig. 4.4(b), the amplitude of the rightward propagating parasitic wave at x = 0 is given by $B_1 = r_{12}A_2$. Finally at the input mirror, the amplitude of the externally reflected mode can be determined in terms of its component contributions. These are the reflection of the input mode; i.e. $r_{11}A_ie^{jk_ix}\Big|_{x=0}$ and the transmitted light from the leftward propagating component of the cavity mode; i.e. $t_mA_2e^{-jk_ax}\Big|_{x=0}$, therefore at x = 0,

$$A_r = r_cA_i = r_{11}A_i + t_mA_2 \tag{4.4}$$

where r_c is the reflection coefficient of the microcavity as a whole.

The complete set of cavity equations are obtained by field matching at the output mirror, i.e. at x = *h*. From Fig. 4.4, it can be seen that the leftward propagating component of the fundamental cavity mode, $A_2e^{-jk_ax}$, has a contribution $r_{11}A_1e^{jk_ax}\Big|_{x=h}$ from the rightward propagating component of the fundamental cavity mode and a contribution $r_{12}B_1e^{jk_bx}\Big|_{x=h}$ from the rightward propagating parasitic mode. Therefore

$$A_2e^{-j\Phi_1} = r_{11}A_1e^{j\Phi_1} + r_{12}B_1e^{j\Phi_2} \tag{4.5}$$

where $\Phi_1 = k_ah$ and $\Phi_2 = k_bh$.

From Fig. 4.4(b), the amplitude of the leftward propagating mode, which derives purely from reflection-coupling from $A_1e^{jk_ax}$ at the mirror at x = *h*, is given by

$$B_2e^{-j\Phi_2} = r_{12}A_1e^{j\Phi_1} \tag{4.6}$$

Finally, the transmitted wave, $A_te^{jk_ix}$, derives solely from the fraction of the rightward propagating component of the fundamental cavity mode transmitted by the output mirror, i.e.

$$A_t e^{jk_i(x-h)}\Big|_{x=h} = t_m A_1 e^{jk_a}\Big|_{x=h} \quad \text{or} \quad A_t = t_m A_1 e^{j\Phi_1} \tag{4.7}$$

Equations (4.3)-(4.7) can be manipulated to produce expressions for the reflection coefficient and transmission coefficient of the microcavity, denoted r_c and t_c, respectively. From Eq.(4.7), t_c can be written as

$$t_c = \frac{A_t}{A_i} = \frac{A_1}{A_i} t_m e^{j\Phi_1} \tag{4.8}$$

the ratio A_1 / A_i is obtained from Eq.(4.3) by writing A_2 and B_2 in terms of A_1. Using $B_1 = r_{12} A_2$ in Eq.(4.5) yields

$$A_2 = A_1 \frac{r_{11} e^{2j\Phi_1}}{1 - r_{12}^2 e^{j(\Phi_1+\Phi_2)}} = \frac{A_1 r_{11} e^{2j\Phi_1}}{\rho} \tag{4.9}$$

$$\text{where} \quad \rho = 1 - r_{12}^2 e^{j(\Phi_1+\Phi_2)} \tag{4.10}$$

Using (4.6) and (4.9) in (4.3) yields

$$t_m A_i = A_1 \{[1 - r_{12}^2 e^{j(\Phi_1+\Phi_2)}] - \frac{r_{11}^2 e^{2j\Phi_1}}{[1 - r_{12}^2 e^{j(\Phi_1+\Phi_2)}]}\} \tag{4.11a}$$

$$\text{or} \quad t_m A_i = \frac{A_1}{\rho}\{\rho^2 - r_{11}^2 e^{2j\Phi_1}\} \tag{4.11b}$$

Using (4.11b) in (4.8) results in

$$t_c = \frac{\rho t_m^2 e^{j\Phi_1}}{\rho^2 - r_{11}^2 e^{2j\Phi_1}} \tag{4.12}$$

where t_c, the transmission coefficient is defined. Eq. (4.4) defines the microcavity reflection coefficient. Putting Eq. (4.9) in Eq. (4.4) yields

$$r_c = r_{11}[1 + \frac{A_1}{A_i} \frac{t_m e^{2j\Phi_1}}{\rho}] \tag{4.13}$$

using (4.11) in (4.13) gives

$$r_c = r_{11}[1 + \frac{t_c e^{j\Phi_1}}{\rho}] \tag{4.14}$$

where r_c, the reflection coefficient is defined, and it can be noticed that apart from

r_{11}, an extra coefficient of $r_{11}\frac{t_c e^{j\Phi_1}}{\rho}$ has been obtained from the proposed radiation recycling mechanism, which is believed to have a positive impact on the Q value of the microcavity.

Radiation recycling involves mutual coupling between the fundamental cavity mode and any parasitic modes excited by reflection and/or scattering at the mirrors and subsequently supported by the cavity, such weak recycling takes place a great number of times and the Q value can be greatly enhanced. These parasitic modes can be leaky modes, as proposed by Lalanne *et al* [Lalanne 2004], or, if the basic waveguide is multimoded, they can be higher order cavity modes, or a combination of both.

4.5 A Novel Method for Characterizing the Q values of Optical Microcavities

From the simulation results in Chapter 2 and the measurement results in the previous section, high or very high Q values can be observed. It has also been reported that in optimised structures the theoretical Q can exceed 3×10^4 in 1-D PhC microcavities [Lalanne 2003]. Recently, 1-D PhC waveguide embedded PhC microcavities with mode matching tapers with measured Q values as high as 8900 have been reported [Velha 2006].

For characterising the Q values of the fabricated microcavities, the laser stepping method described in section 4.2 has been carried out for a long time and what are believed to be accurate Q values have been obtained in this way. However, for cavities with very high Q values, such a standard method has its limits: firstly, the

exact resonance wavelength can lie between adjacent minimum steps in the laser wavelength resulting in reduced values. Secondly, the normal wavelength stepping method requires a long measurement time to obtain enough data for signal averaging to reduce noise. To overcome the problems associated with the conventional measurement procedure, a novel, potentially high resolution measurement method is presented. The technique exploits the high spectral resolution that can be obtained using heterodyne detection of an amplitude-modulated electromagnetic wave. Fig.4.5 (a) illustrates the measurement system and the basic principle of the method. The technique exploits the systematic spectral broadening of a monochromatic electromagnetic wave, known as the carrier wave of frequency f_c when a sinusoidal amplitude modulation of frequency f_m ($<f_c$) is imposed on it. The resultant waveform has a time dependent amplitude variation of the form

$$[1+m\cos(2\pi f_m t)]A_c\cos(2\pi f_c t) = A_c\cos(2\pi f_c t) + \frac{mA_c}{2}\cos[2\pi(f_c - f_m)t] + \frac{mA_c}{2}\cos[2\pi(f_c + f_m)t] \tag{4.15}$$

where m is the ratio of the amplitude of the modulating waveform to the amplitude of the carrier and is known as the modulation index. The right hand side of Eq.(4.15) contains three spectral components at frequencies of $f_c - f_m$, f_c and $f_c + f_m$, with a known relationship between their amplitudes. Notably the amplitudes of the sidebands at frequency $f_c \pm f_m$ are equal. This is shown in inset (*a*) of Fig. 4.5. If a filter is imposed between the amplitude-modulated source and the detector acts in such a way that its impact in the sidebands is unequal, then the relative heights of the sidebands give a measure of the filter response over the frequency range $f_c \pm f_m$. This is shown schematically in inset (*b*) of Fig. 4.5. Since f_m can be varied continuously over a small frequency interval, the filter response in principle can be measured with extremely high precision. In practice, noise in the heterodyne detection system limits the minimum frequency step to 25MHz. This still represents a factor of five improvement in precision compared with minimum frequency step of even the best tunable diode laser source.

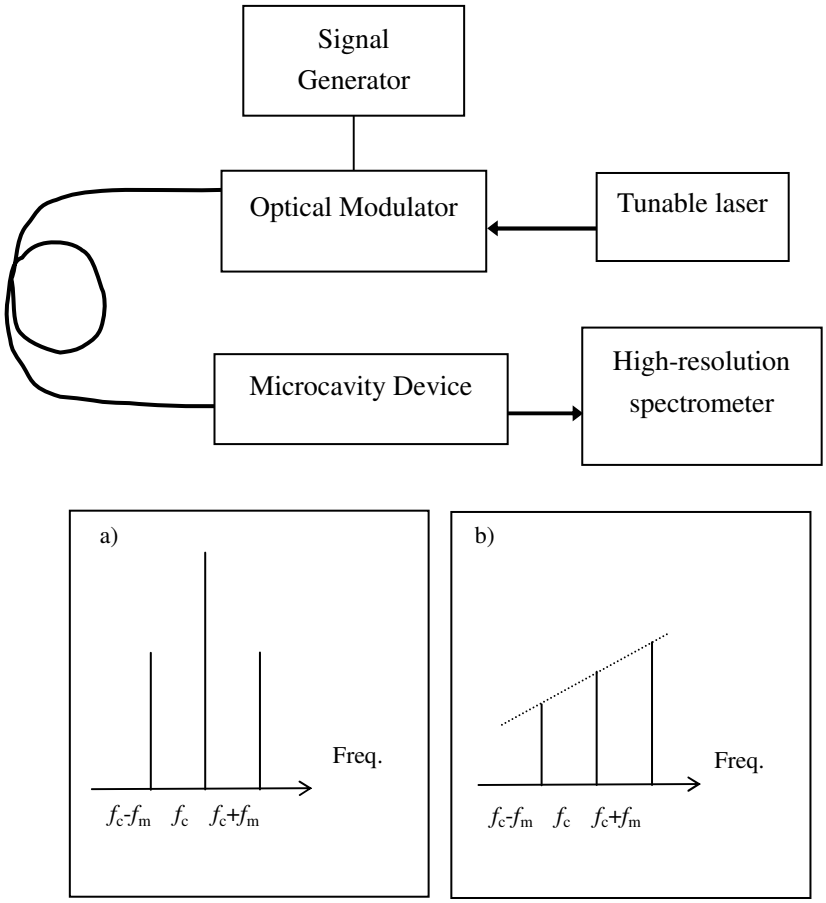

Fig.4.5 Upper: Measurement system. Insets: spectra of a light-wave amplitude-modulated by a sinusoidal voltage before (a) and after (b) filtering with the carrier tuned to lie on the up-slope of the filter response.

In the measurement system, the sinusoidal *rf* amplitude modulation is impressed on a light-wave carrier, generated by a tunable diode laser, using a chirp-free Mach-Zehnder optical modulator. The chirp free modulator prevents any parasitic frequency modulation from contributing to the variation in the amplitudes of the upper and lower sidebands. The modulated signal is then coupled into the PhC microcavity via a lensed tapered single mode fibre by the butt coupling method described in section 4.2. The carrier wave is then tuned to lie within the microcavity resonance so that the change in the relative amplitudes of the upper and lower sidebands with respect to the carrier provides an accurate measure of filter response as the frequency of the modulating *rf* signal is varied. The output optical signal from the PhC microcavity was fed into a commercial high-resolution spectrometer

(HRS), (Agilent 83453A). The HRS uses heterodyne detection, in which the signal from the PhC microcavity is mixed in a high bandwidth photodiode with a local oscillator generated by a second tunable laser.

Fig.4.6a shows a modulated laser source at the central wavelength of 1548.22270nm with rf signal of 30MHz prior to coupling the light into the microcavity. The two sidebands are separated from the main peak by about ±0.2pm. Fig.4.6b shows the effect of the microcavity filter.

a)

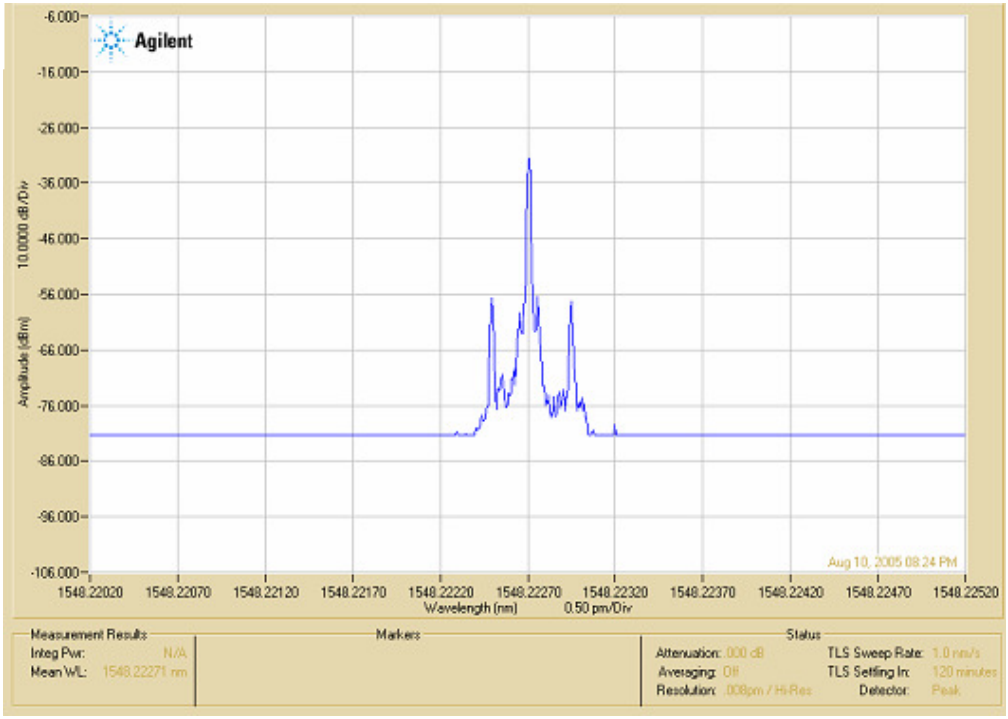

b)

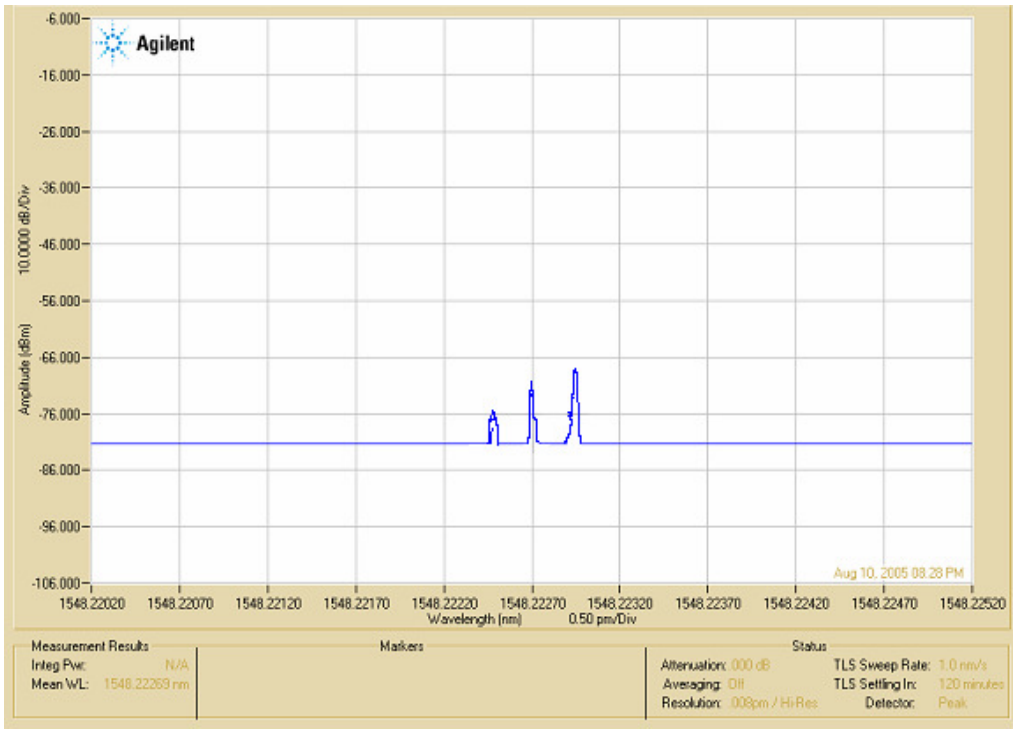

Fig.4.6 Spectrum of a 1548.2270nm lightwave carrier amplitude modulated by a 30MHz rf wave, (*a*) Prior to coupling into the microcavity, (*b*) After passing through the microcavity, the greater height of the upper sideband compared with the lower sideband shows that the wavelength of the carrier lies on the rising edge of the microcavity resonance. Each large division along the *x*-axis represents 0.5pm, whilst each large division along the *y*-axis represents -10dBm.

The microcavity used comprised eight bilayers and a defect layer of width 230nm. The influence of the PhC can clearly be seen, with the change in the intensity of the upper or lower sideband relative to that of the carrier wave giving a precise measurement of the filter response. Fig.4.7 presents enlarged views of the amplitude modulated signal resonances peaks after going through the microcavity for two different frequencies of the modulating *rf* signal.

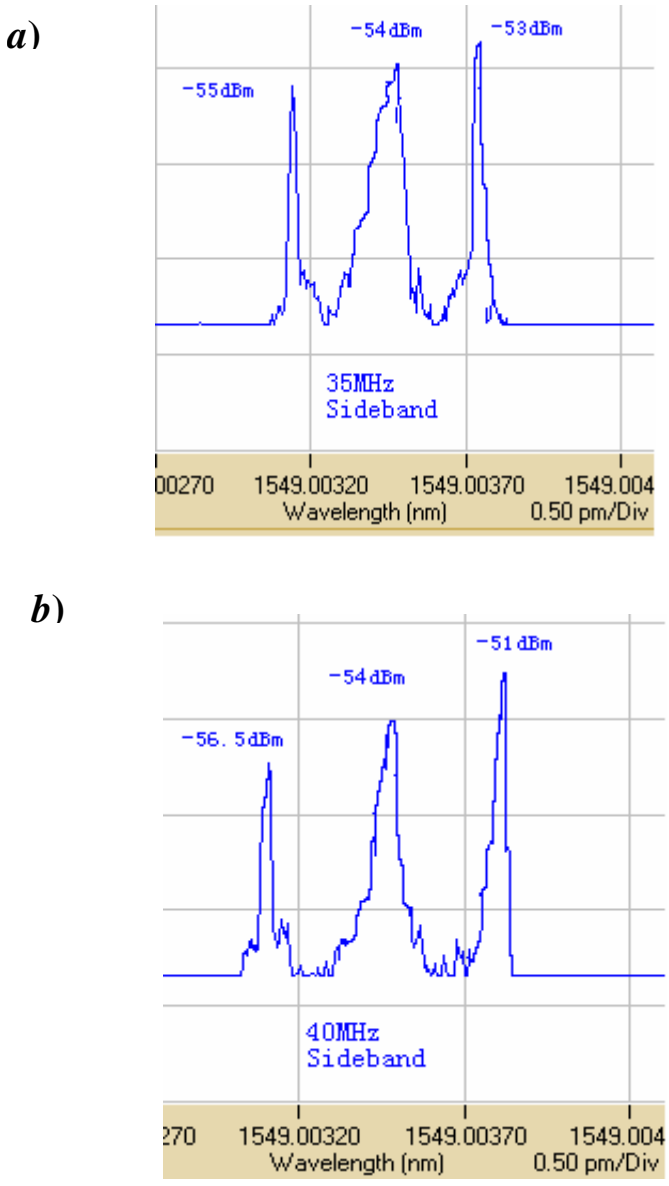

Fig.4.7 Enlarged view of the filtering effect of the microcavity on an amplitude modulated lightwave signal of wavelength 1549.00345nm. (a) a 35MHz *rf* signal and (b) a 40MHz *rf* signal.

Fig.4.8 shows a comparison of the response of the microcavity near resonance measured by the new method with that obtained by stepping the output wavelength of a continuous wave tunable diode laser and measuring the optical power output from the waveguide microcavity with a calibrated photodiode. The spectral resolution achieved by the new method was 0.2 pm, compared with a minimum wavelength step of only 1 pm attainable with the tunable diode laser, a fivefold improvement in precision. The sideband attenuation method precisely measures resonant wavelength at 1549.004 ± 0.0001nm, compared with an uncertainty of ~1 pm using the stepped unmodulated wavelength method. The transmittance, T, and quality factor, Q, of the 1-D PhC waveguide microcavity measured by the new method were 0.64 and 2093, respectively, compared with T=0.53 with an estimated Q of 1648 obtained from the conventional method of stepping an unmodulated tunable laser source.

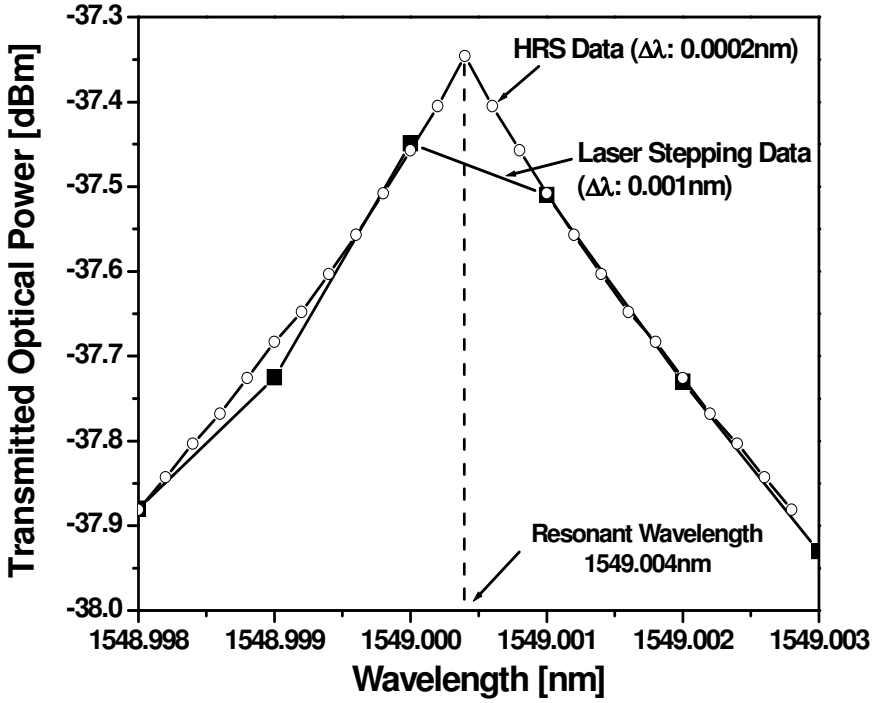

Fig.4.8 Comparison of the data obtained by the normal laser stepping method and the new side-band measurement method.

4.6 Summary of the Measurements

A butt-coupling measurement method with a conventional wavelength stepped tunable laser diode was executed as the main way for characterising the fabricated PhC structures. For this, a special test bed was set up with computer control of the laser and detector for recording the transmitted power versus stepped wavelength. All the successfully fabricated samples were measured by this method with resonance peaks observed close to those predicted by the TMM. A very high quality factor value of about 2000 was obtained. This value is believed to be very competitive according to a literature review. The measurement work validated the theoretical predication and simulation results of the band gap and resonance phenomenon present in defect containing 1-D PhCs, and solidly proved the viability of the fabrication technologies.

In addition, a novel method of accurately measuring the pass-band of high Q microcavities is also demonstrated in this chapter. This method is based on heterodyne detection of a chirp-free amplitude modulated optical signal. The filtering effect of the microcavity causes unequal attenuation of upper and lower sidebands of the same order when the optical carrier wave lies off resonance. The rapid variation of the rising and falling edges of the pass-band can be accurately traced by varying the frequency of the modulating signal rather than by stepping the wavelength of the tunable laser. The spectral resolution of the new method is limited by the minimum frequency spacing of the heterodyne detection system, this being 0.2pm compared with 1pm of the tunable laser used. The improved spectral resolution of the technique revealed that the Q of a 1-D PhC microcavity etched into a Si/SiO_2 multi- mode ridge waveguide was 27% higher than estimated using a stepped wavelength tunable unmodulated laser.

Chapter 5. Multi-transmission Optical Filter Based on a One Dimensional Photonic Crystal Structure

5.1 Introduction

In optical communications, fibre loss is referred to as signal attenuation or simply attenuation. Attenuation is an important property of an optical fibre because, together with signal distortion mechanisms, it determines the maximum transmission distance possible between a transmitter and a receiver (or an amplifier) before the signal power needs to be boosted to an appropriate level above the signal noise for high-fidelity reception. The degree of the attenuation depends on the wavelength of the light and on the fibre material. Fig. 5.1 shows a typical attenuation versus wavelength curve for a silica fibre. The loss of power is measured in decibels, and the loss within a cable is described in terms of decibels per kilometer (dB/km).

Fig. 5.1 shows that optical fibres have a large attenuation spike between 900 and 1200nm due to the fourth-order absorption peak from water molecules. Another spike from the third-order water absorption occurs between 1350nm and 1480nm for commonly fabricated fibres. Because of such absorption peaks, three transmission windows were defined initially. The *first window* ranges from 800 to 900nm, the *second window* is centred at 1310nm, and the *third window* ranges from 1480 to 1600nm. During these transmission windows, there are two standard wavelengths in use, 1310nm and 1550nm. 1310nm has been a standard for many years, only now

there is a trend towards using 1550nm brought about by the need to extend the distances between amplifiers [Keiser 2003].

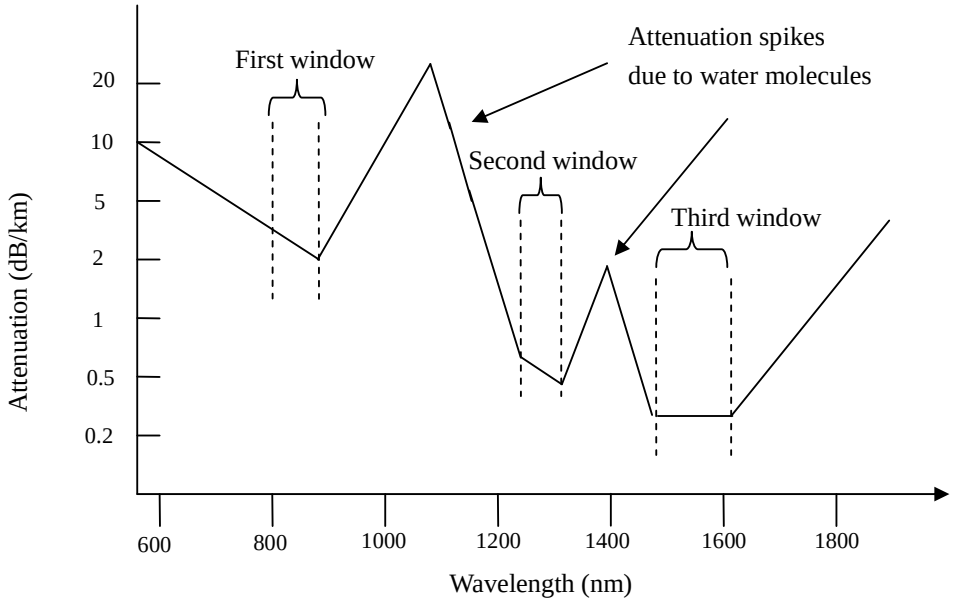

Fig. 5.1 A typical attenuation versus wavelength curve for a silica fibre.

Also in optical communications, the use of wavelength division multiplexing (WDM) offers a further boost in fibre transmission capacity. The basis of WDM is to use multiple light sources operating at slightly different wavelengths to transmit several independent information streams simultaneously over the same fibre. As stated above, 1310nm and 1550nm are the two most commonly used wavelengths in optical communications and transferring these two wavelengths simultaneously in the same optical fibre is broadly required in the WDM system [Keiser 2003]. Since planar waveguides are promising candidates for future highly integrated optical circuits, creating multi-transmission optical filters based on such structures will meet the challenge of future highly integrated WDM systems, especially for transferring the wavelength of 1310nm and 1550nm.

Recently, Lee *et al* demonstrated a novel technique for setting the resonant wavelengths of a multi-wavelength transmission microcavity [Lee 2005]; their

structure comprised multiple layers of Si-SiO_2 forming the mirrors of a microcavity with the homogeneous in-cavity material replaced by a Si-SiO_2 1-D PhC of a different period to that of the reflectors to create a structure of systematically varying periodicity. Lee *et al* used TMM to calculate the reflection spectra to obtain the resonant wavelengths, and then fabricated the structure by sputtering Si and SiO_2 alternately onto polished glass substrate; multiple-wavelength-transmissions were observed both in the calculated and measured spectra.

Lee's report inspired the work in this chapter, which, instead of creating the multi-wavelength filter in a film stack, the work of design and realization of such a multi-wavelength filter in a Si ridge waveguide devices have been done, which could promote the real application of such a structure in highly integrated optical circuits. Such filters could be used in a telecommunication network employing wavelength division multiplexing in which global control information is transmitted on one wavelength and data on several other wavelengths as shown schematically in Fig.5.2.

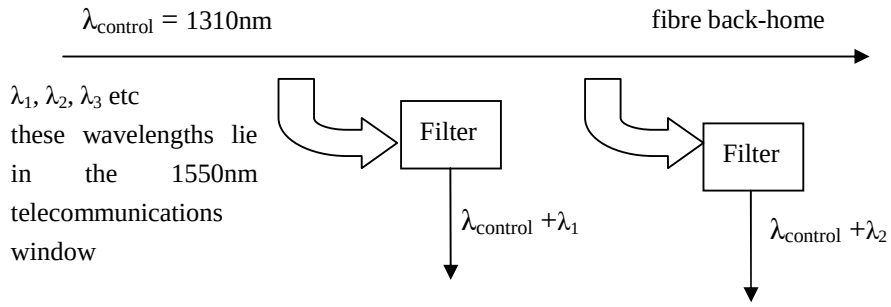

Fig.5.2 Schematic showing the practical application of the multi-wavelength filter, which could pass $\lambda_{control}$ plus just one of the wanted wavelength data channels.

Further in this chapter, a wave-vector diagram method is proposed as an additional way to predict the resonances, and good agreements have been obtained between the calculation from TMM, the prediction from the wave-vector diagram method and the measured results.

5.2 Preliminary Design Concepts

Lee *et al* [Lee 2005] created the Si/SiO_2 one-dimensional photonic crystal structures by inserting *N* pairs of Λ_B (as the defect region) in the middle of two sets of two pairs of Λ_A (as reflector region), schematically shown in Fig. 5.3.

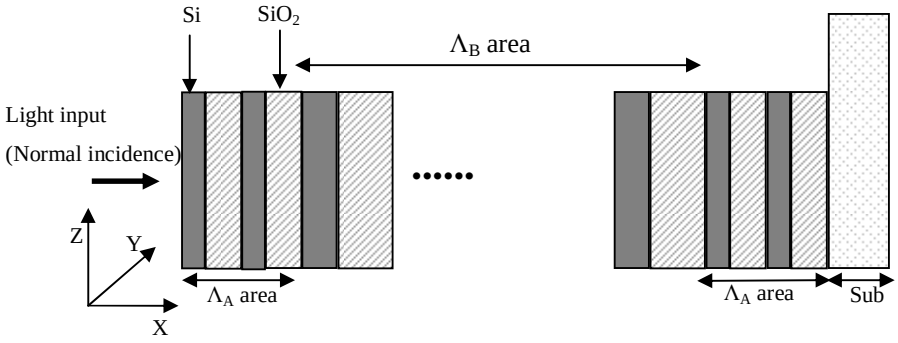

Fig.5.3 Schematic shown of the Si/SiO_2 1-D multi-transmission PhC structure reported by Lee *et al*. The *N* pairs of Λ_B was inserted into the middle of the four-pair Λ_A as the defect region, with the width of $\Lambda_B = 2\Lambda_A$.

As the structure to be fabricated in this chapter will have the same formation as in Fig. 5.3, but with SiO_2 replaced by air, TMM calculations are performed for predicting the multi-resonances using the information from Fig.5.3. The refractive index of Si in this simulation is chosen to be $n_{Si} = 3.4 + i0$ as explained in Chapter 2, with the refractive index of air to be $n_{air} = 1.0 + i0$. Initial simulations are performed by varying the number of Λ_B layers(N) with layer thicknesses satisfying the equal optical length condition $n_L d_L = n_H d_H = \lambda/4$, here λ is randomly chosen to be 1450nm for the purpose of demonstration. This wavelength yields $d_{AL} = d_{Aair} = 362.50$ nm with $d_{AH} = d_{ASi} = 106.62$ nm, which in turn yields $\Lambda_A = 469.12\,\text{nm}$ and $d_{BL} = 2d_{AL} = 725.00\,\text{nm}$, $d_{BH} = 2d_{AH} = 213.24\,\text{nm}$, with $\Lambda_B = 938.24\,\text{nm}$. Fig.5.4 shows the simulated transmittance spectrum of *N* = 1, 2, 4 and 8, respectively.

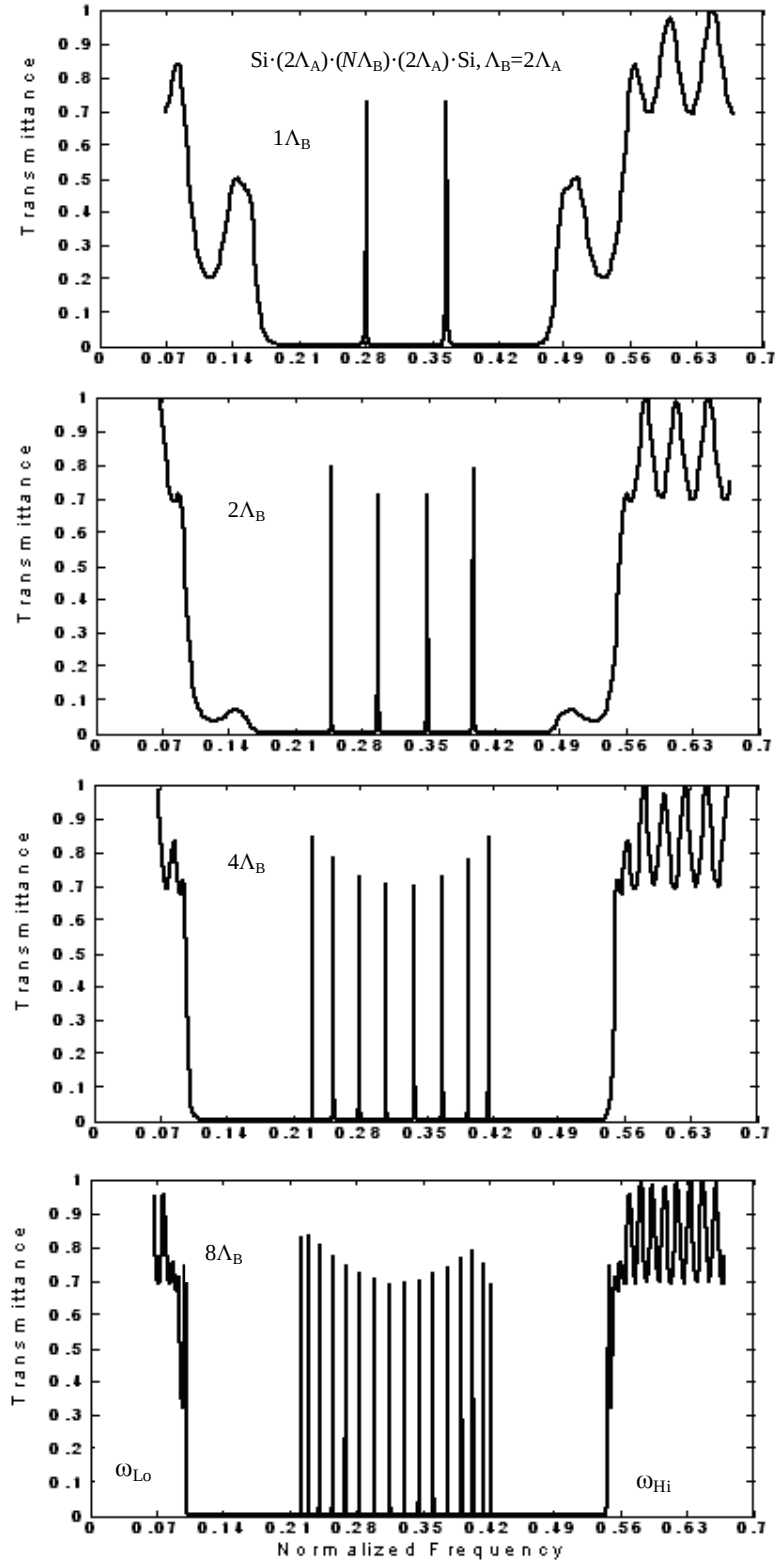

Fig.5.4, TMM calculated transmittance versus normalized frequency ($\omega=\Lambda_A/\lambda$) for the 1-D PhC described in Fig.5.3 with N = 1, 2, 4 and 8. The transmission peaks, as well as the photonic band gap, are symmetric with the mid-gap frequency ω_0 (~0.3235294) in the centre. Further, the number of the transmission peaks increases as a function of N according to $m=2N$.

As can be observed from the obtained transmittance spectra, the number of the transmission peaks m increases as N increases, in a function of $m = 2N$. The photonic band gap also becomes wider as N increases with the band gap edges getting sharper. The obtained transmission peak are evenly distributed on two sides of the centre normalized ω_0, while $\omega_0 = (\omega_{Lo} + \omega_{Hi})/2$, ω_{Lo} and ω_{Hi} are the lower and upper frequency edges as shown in Fig.5.4, respectively.

The work in this chapter focuses on fabricating multi-transmission optical filters transferring 1310nm and 1550 nm simultaneously towards highly integrated optical circuits to cater for the requirement from optical communication systems as stated in introduction. Based on the TMM calculation results in Fig.5.4 and the work reported from Lee *et al* [Lee 2005], multi-transmission peaks can be created as long as the homogeneous cavity region is replaced by a multi-layer structure, and the number of the resonances and the resonant frequencies (wavelengths) can be manipulated by changing the multi-layer cavity parameters. Further, it can be observed from Fig.5.4, the transmission peak number m equals twice the Λ_B layer numbers N, so for simultaneously transmitting two wavelengths (1310 and 1550nm in this chapter), $N \geq 1$ (N = 1, 2, 3, 4 ⋯⋯) will satisfy the requirement. However, for practical applications and fabrication simplicities, a large N is obviously not ideal as it will generate a large amount of transmission peaks and introduce fabrication complexities, here N = 1 and 2 are investigated by TMM for finding and optimizing the structure parameters which could satisfy the proposed requirements.

For N = 1, the 1-D Si/air PhC structure becomes the sketch shown in Fig.5.5, the incident and substrate materials are both assumed to be Si.

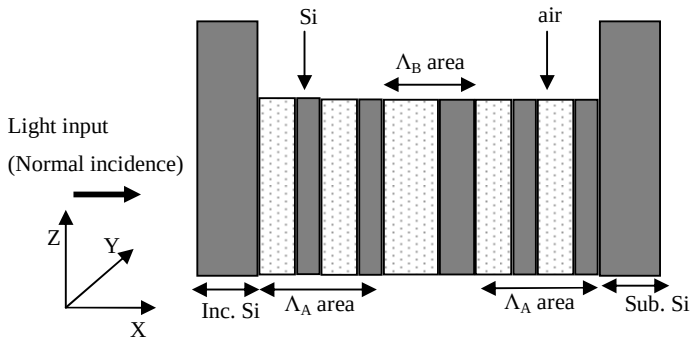

Fig.5.5 Schematic shown of the 1-D Si/air multi-layer cavity structure with the number of Λ_B layer to be 1, both the incident medium and substrate material are assumed to be Si.

$d_{AL} = d_{Aair} = 362.50$ nm with $d_{AH} = d_{ASi} = 106.61$ nm for Λ_A layer and $d_{BL} = d_{Bair} = 725.00$ nm with $d_{BH} = d_{BSi} = 213.22$ nm for Λ_B layer are used again for the simulation. The calculated transmittance spectrum in terms of normalized frequency is shown in Fig.5.6. As can be observed from Fig.5.6, the two resonant peaks appear at the frequencies of 0.281245 and 0.365812, respectively. Based on these two normalized frequencies and assuming 0.2812456 corresponds to 1550nm, Fig.5.7 shows a calculated transmittance versus wavelength spectra. This was obtained using the structure parameters formed from $\Lambda_{A1} = 1550 \times 0.2812456 = 435.93$ nm, while $d_{L1}(d_{air1}) + d_{H1}(d_{Si1}) = \Lambda_{A1}$ and $d_{L1}(d_{air1}) / d_{H1}(d_{Si1)} = n_{Si} / n_{air} = 3.4/1$, which yields $d_{L1} = 336.86$ nm and $d_{H1} = 99.08$ nm, as $\Lambda_{B1} = 2\Lambda_{A1}$ and N = 1. Resonances appear at 1192 and 1550nm, as that 1310 and 1550nm were expected, a big deviation of 118nm occurs at the wavelength of 1310nm. Such a big deviation indicates that for N = 1, a big adjustment is needed to obtain transmission peaks at 1310 and 1550nm; but for N = 2, much smaller adjustments are needed to achieve the requirement, further design and simulation work was carried for structures with N = 2 in the next section.

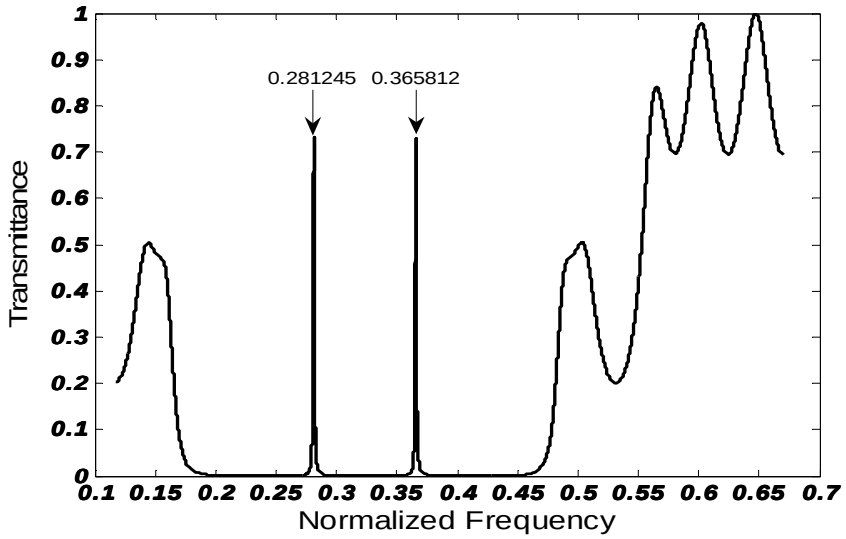

Fig.5.6 TMM calculated transmittance versus normalized frequency ($\omega=\Lambda_A/\lambda$) for the 1-D PhC structure described in Fig.5.5. Two resonant peaks are located at 0.281245 and 0.365812.

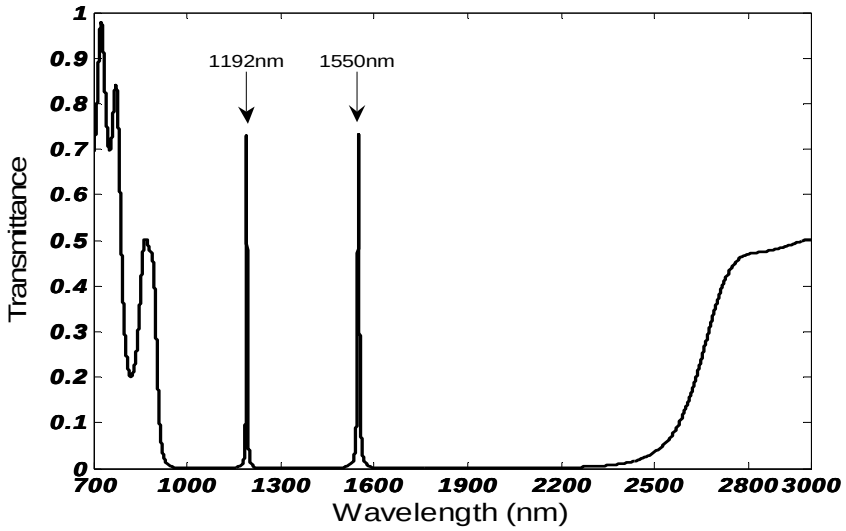

Fig.5.7, TMM calculated spectra of transmittance versus wavelength for the thicknesses of air layer to be 336.86nm and Si layer to be 99.08nm for A layers with N = 1 and $\Lambda_B=2\Lambda_A$. Two resonant peaks appear at 1192 and 1550nm.

5.3 Detailed Simulation for Multi-transmission of 1310 and 1550nm

From the discussion in section 5.2, it can be concluded that $m = 2N$ transmission peaks will be obtained as N is the number of Λ_B layer inserted in the middle of two pairs of Λ_A layers, and for $N = 1$, 1192 and 1550nm was obtained at the same time, which is big deviation from the required 1310 and 1550nm filter. In this section, a detailed simulation is carried out for $N = 2$ to search for the structure parameters which could transmit wavelengths of 1310 and 1550nm simultaneously. For $N = 2$, the 1-D PhC structure becomes the sketch shown in Fig.5.8.

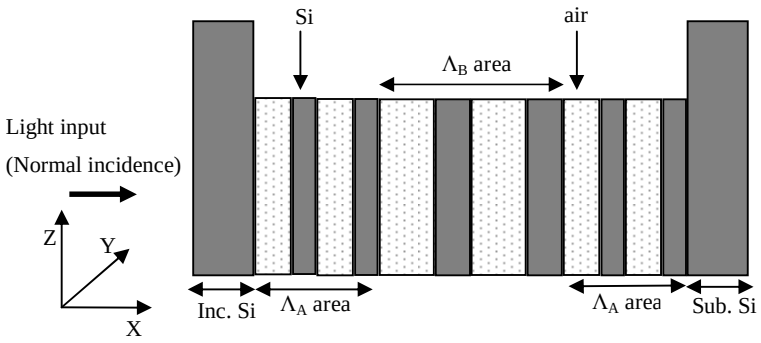

Fig.5.8 Schematic shown of the 1-D Si/air multi-layer cavity structure with the number of Λ_B layer to be 2, both the incident medium and substrate material are assumed to be Si.

The structure parameters of $d_{AL} = d_{Aair} = 362.50$ nm with $d_{AH} = d_{ASi} = 106.61$ nm for Λ_A layer and $d_{BL} = d_{Bair} = 725.00$ nm with $d_{BH} = d_{BSi} = 213.22$ nm for Λ_B layer in section 5.2 are used again as trial values for the simulations as $N = 2$, the obtained transmittance spectra is shown in Fig.5.9.

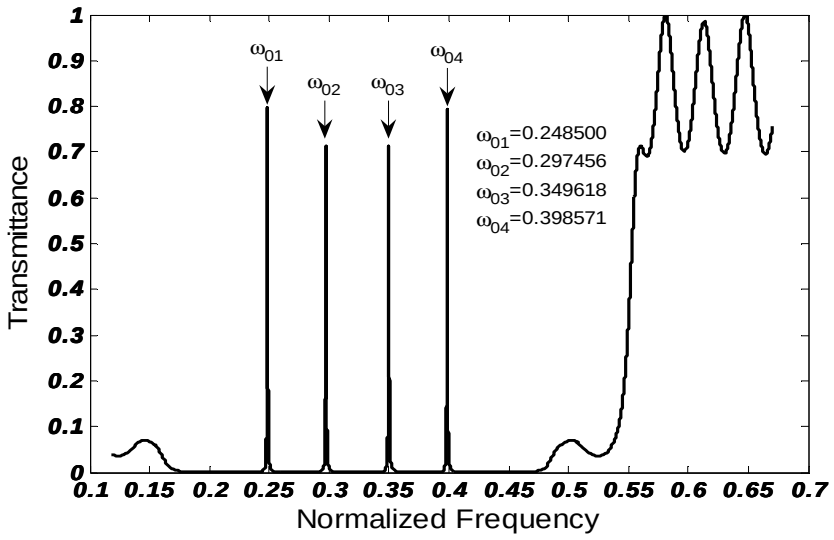

Fig.5.9 TMM calculated transmittance versus normalized frequency ($\omega=\Lambda_A/\lambda$) for the 1-D PhC structure described in Fig.5.8. Four resonant peaks appear at 0.248500, 0.297456, 0.349618 and 0.398571, respectively.

The normalized frequencies obtained in Fig.5.9 are used for predicting the structure parameters for transferring 1310 and 1550nm, as ω_{02} and ω_{03} correspond to the two middle wavelengths, the width of layers can be calculated as

$\Lambda_{A2} = 1550 \times 0.297456 = 461.06\,\text{nm}$, and

$d_{Aair} + d_{ASi} = \Lambda_A, \quad n_{air} d_{Aair} = n_{Si} d_{ASi}, \; n_{air} = 1, n_{Si} = 3.4,$

for A layer: $d_{Aair2} = 356.27\,\text{nm}, \; d_{ASi2} = 104.79\,\text{nm},$

since $\Lambda_B = 2\Lambda_A$, for B layer: $d_{Bair2} = 712.54\,\text{nm}, \; d_{BSi2} = 209.58\,\text{nm}$

TMM calculation was carried out based on the above values, the obtained transmittance spectra is shown in Fig.5.10.

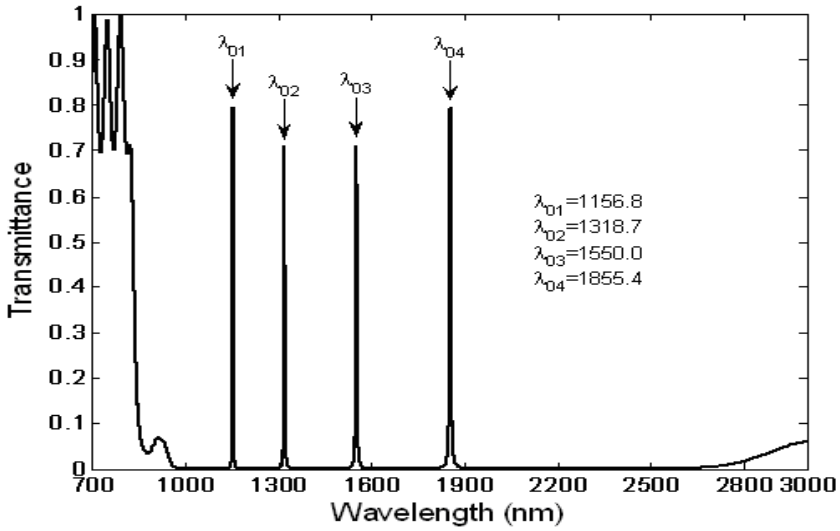

Fig.5.10 TMM calculated spectra of transmittance versus wavelength for the thicknesses of air layer to be 356.27nm and Si layer to be 104.79nm with N = 2 and $\Lambda_B=2\Lambda_A$. Four resonant peaks appear at 1156.8, 1318.7, 1550.0 and 1855.4nm, respectively.

The two middle wavelengths of 1318.7nm and 1550.0nm are obtained at the same time in Fig.5.10, instead of the desired 1310 and 1550nm, and an 8.7nm deviation is generated from the required 1310nm. Actually such a wavelength can be predicted by $\Lambda_{A2}/\omega_{03} = 461.06/0.349618 = 1318.7\,\text{nm}$, which agrees with the TMM calculation result in Fig.5.10.

Since the transmission modes strongly depend on the filling factor η [Lee 2002, 2005], where $\eta = d_H / d_L$, and when the condition $n_H d_H = n_L d_L$ is satisfied, η also equals n_L / n_H. Therefore, changing the refractive indices of the two materials can produce equivalent variations in η and change the transmission properties of the proposed 1-D multi- cavity PhC structure in Fig.5.8.

A changing of air refractive index to 1.2 is carried out first with Si index as 3.4, while the assumed air layer thickness is $d_{Aair3} = 362.5\,\text{nm}$, from the equation $n_H d_H = n_L d_L$, the Si layer thickness now becomes $d_{ASi3} = 127.94\,\text{nm}$. For the

defect layers as $\Lambda_B=2\Lambda_A$, $d_{Bair3} = 725.0$ nm and $d_{BSi3} = 255.88$ nm. Fig.5.11 shows the TMM calculation result based on these parameters.

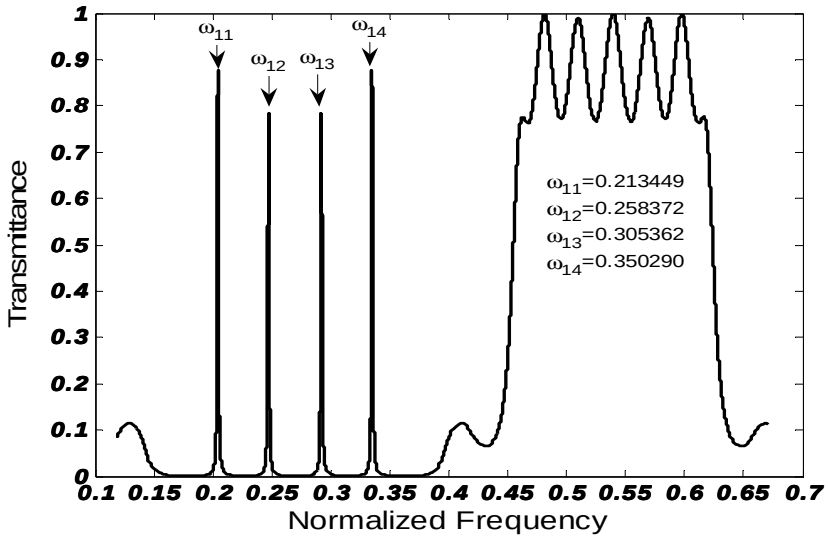

Fig.5.11 TMM calculated transmittance versus normalized frequency ($\omega=\Lambda_A/\lambda$) for the 1-D PhC structure with modified air refractive index of 1.2 and Si of 3.4, as N = 2 and $\Lambda_B=2\Lambda_A$, four resonant peaks appear at 0.213449, 0.258372, 0.305362 and 0.350290, respectively.

Seeing as ω_{12} and ω_{13} correspond to the two middle wavelengths, assuming ω_{12} is the desired 1550nm, another wavelength can be calculated by $(1550\times 0.258372)/0.305362 =$ 1311.5nm, which is close to 1310nm, although a further adjustment is still needed.

Also, a changing of Si refractive index to 3.2 with air index of 1 was considered. The structure parameters become $d_{Aair4} = 362.5$ nm, $d_{ASi4} = 113.28$ nm, $d_{Bair4} = 725$ nm, $d_{BSi4} = 226.56$ nm in the simulation. Fig.5.12 shows the transmission spectra of transmittance versus normalized frequency.

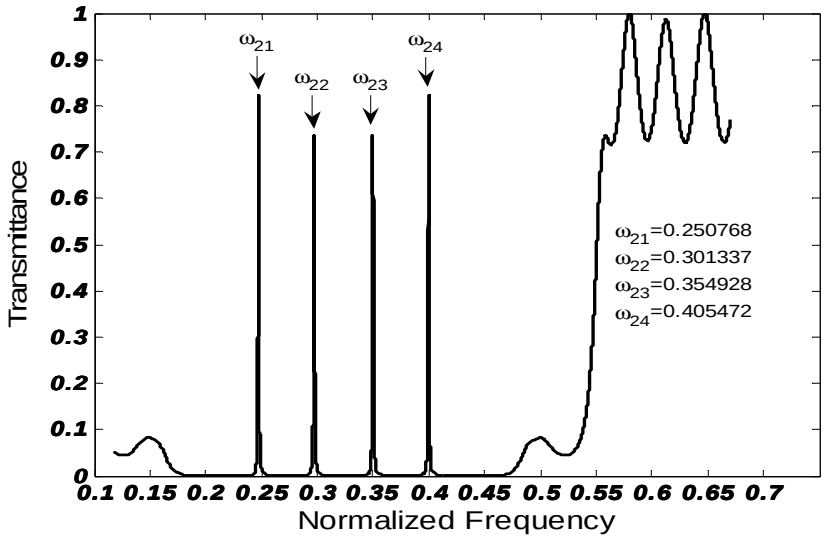

Fig.5.12 TMM calculated transmittance versus normalized frequency ($\omega=\Lambda_A/\lambda$) for the 1-D PhC structure with modified Si refractive index of 3.2 and air of 1, as N = 2 and $\Lambda_B=2\Lambda_A$, four resonant peaks appear at 0.250768, 0.301337, 0.354928 and 0.405472, respectively.

Given that ω_{22} and ω_{23} correspond to the two middle wavelengths, assuming ω_{22} is the desired 1550nm, the wavelength equivalent to the ω_{23} peak can be calculated by $(1550\times 0.301337)/0.354928 = 1316.0$nm, which is closer to the design requirement. It can be concluded that by increasing η value, as $\eta = n_L / n_H$, a beneficial effect is obtained in optimizing the structure to meet the required 1310 and 1550nm multi-wavelength transmission.

Based on the information from Fig.5.11 and Fig.5.12, further trial and error process was carried out to adjust the η value by slightly modifying both the nominal air and Si refractive indices to achieve the ideal 1310 and 1550nm transmission. Finally, a refractive index value of an air layer of 1.189 together with Si layer index of 3.211 is found to be able to create the transmission of 1310.0025 and 1550nm simultaneously. The transmittance versus normalized frequency spectra is shown in Fig.5.13, whilst the parameters used for the simulation are: $d_{Aair5} = 362.5$ nm, $d_{ASi5} = 134.23$nm, $d_{Bair5} = 725$nm, and $d_{BSi5} = 268.46$nm with $n_{air5} = 1.189$ and $n_{Si5} = 3.211$.

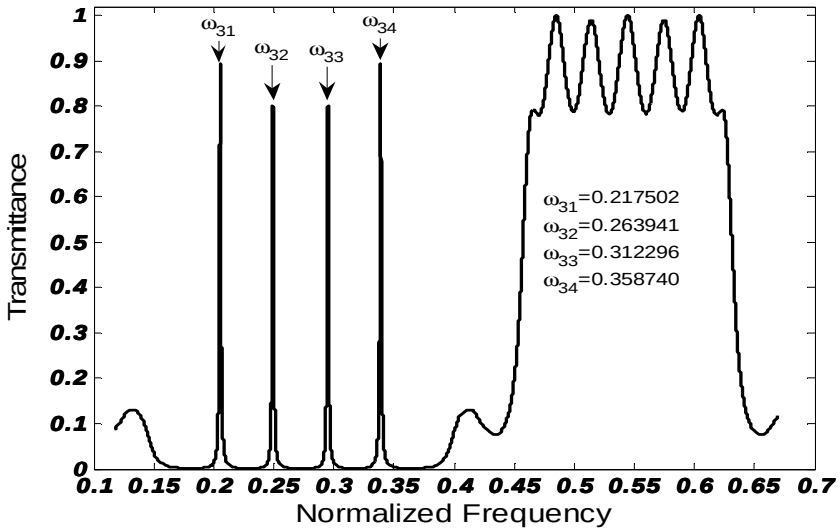

Fig.5.13 TMM calculated transmittance versus normalized frequency ($\omega=\Lambda_A/\lambda$) for the 1-D PhC structure with modified Si refractive index of 3.211 and air of 1.189, as N = 2 and $\Lambda_B=2\Lambda_A$, four resonant peaks appear at 0.217502, 0.263941, 0.312296 and 0.358740, respectively.

As ω_{32} and ω_{33} correspond to the two middle wavelengths, the structure parameters to obtain 1310 and 1550nm transmission are $d_{Aair6} = 298.56$ nm, $d_{ASi6} = 110.55$ nm, $d_{Bair6} = 597.12$ nm and $d_{BSi6} = 221.10$ nm. Fig.5.14 shows the calculated transmittance spectra based on these values with 1310 and 1550nm appearing at the same time.

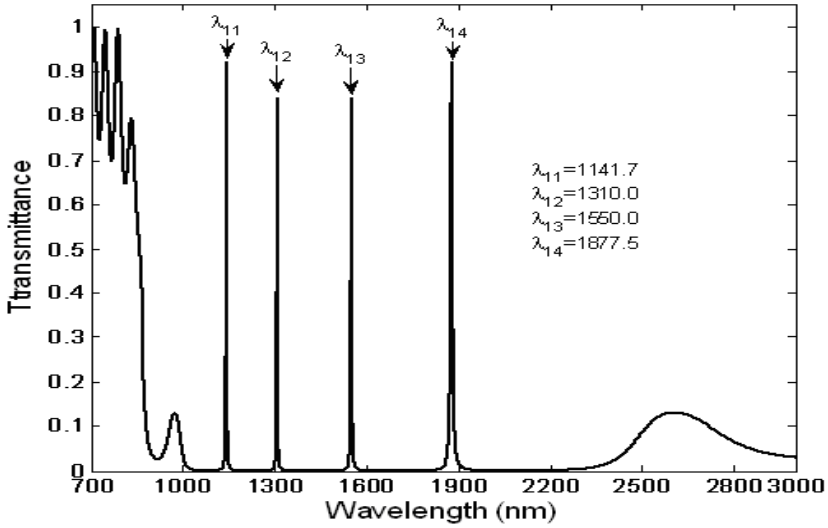

Fig.5.14 TMM calculated spectra of transmittance versus wavelength for the thicknesses of air layer of 298.56nm and Si layer of 110.56nm for the A layers and refractive indices of air layer to be of 1.189 and Si layer of 3.211 with N = 2 and $\Lambda_B=2\Lambda_A$, resonances of 1310 and 1550nm are shown at the same time.

5.4 Fabrication Related Design and Simulation

From the discussions and simulations in section 5.3, for the 1-D multi-cavity PhC structure described in Fig.5.8, by changing the refractive indices of air layer to be 1.189 and Si layer to 3.211, transmission of 1310 and 1550nm is simultaneously obtained, shown in Fig.5.14; this proves the theoretical possibility for achieving the requirement from the optical communication systems to transfer the two broadly used wavelengths at the same time. However, due to the limitations and circumstances in the practical fabrications, some further investigation and modifications are needed.

Based on the ideal structure shown in Fig.5.8, Fig.5.15 demonstrates the sketch of the structure proposed for fabrication,

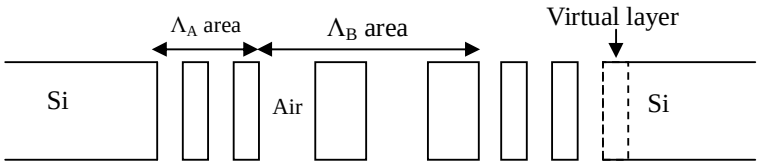

Fig.5.15 Sketch of the proposed 1-D multi-cavity PhC structure for fabrication.

where it can be noticed that a virtual layer has been generated on the border between the PhC region and Si waveguide as the final Si layer of the PhC merges into the Si waveguide, which eventually introduces an extra air layer into the right side of the PhC reflector, and somewhat breaks the symmetry of the reflectors and will affect the agreement between simulation and fabrication; however, this is unavoidable as the PhC region is formed by breaking a small fraction of the Si waveguide. A further simulation is carried out by the structure formation of $2\Lambda_A + 2\Lambda_B + 3\Lambda_A$ based on the same approach for searching for the structure parameters in section 5.3. Fig.5.16 a, b shows the transmittance spectra based on normalized frequency and wavelength for 1310 and 1550nm transmission, the refractive indices of the air layer and Si layer are 1.234 and 3.176, respectively; and the layer thicknesses are: $d_{Aair7} = 287.67$ nm,

$d_{ASi7} = 111.77\,\text{nm}$, $d_{Bair7} = 575.34\,\text{nm}$ and $d_{BSi7} = 223.54\,\text{nm}$.

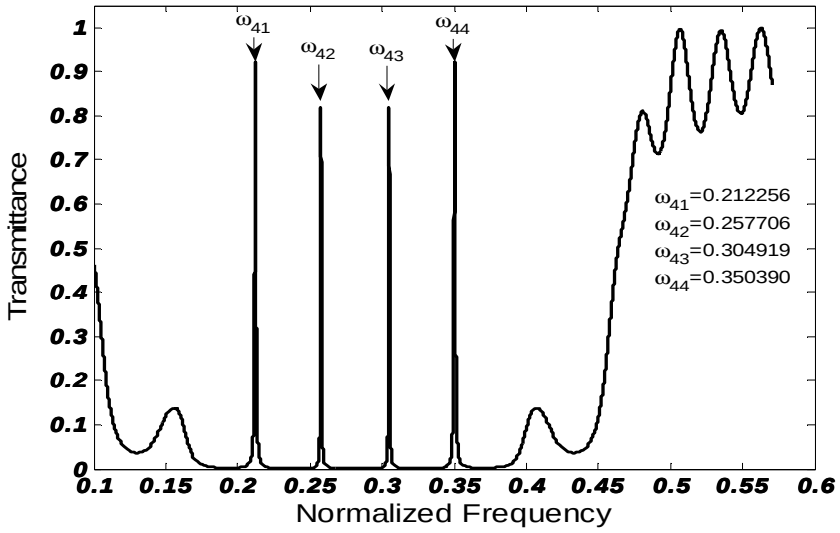

Fig.5.16a TMM calculated transmittance versus normalized frequency ($\omega=\Lambda_A/\lambda$) for the 1-D PhC structure shown in Fig.5.15, with Si layer refractive index of 3.176 and air layer of 1.234, as N = 2 and $\Lambda_B=2\Lambda_A$, four resonant peaks appear at 0.212256, 0.257706, 0.304919 and 0.350390, respectively.

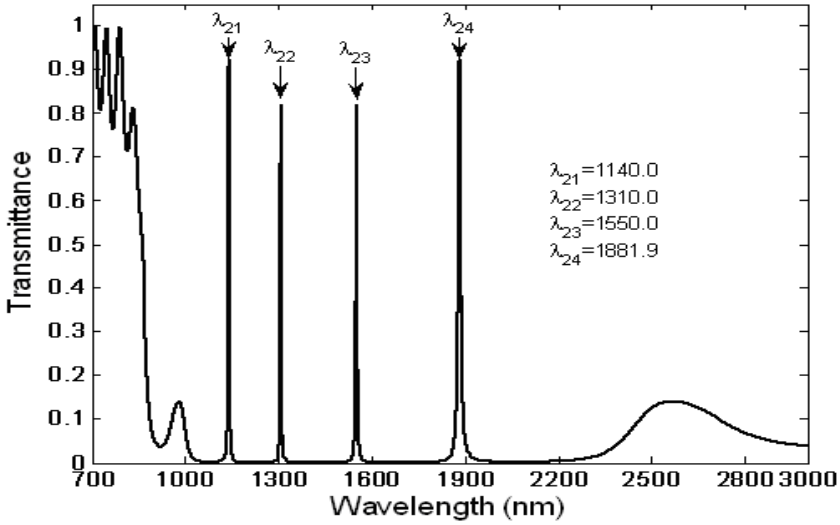

Fig.5.16b TMM calculated spectra of transmittance versus wavelength based on the structure sketch shown in Fig.5.15, for the thicknesses of air layer of 287.67nm and Si layer of 111.77nm for the A layers and refractive indices of air layer of 1.234 and Si layer of 3.176 with N = 2 and $\Lambda_B=2\Lambda_A$, resonances of 1310 and 1550nm are shown at the same time.

The result in Fig.5.16 proves the possibility of obtaining multi-wavelength transmission filter at 1310 and 1550nm simultaneously under the practical structure.

This was achieved by slightly increasing the refractive index of air layer and reducing the index value of Si layer, such trends actually agree with the practical refractive indices changes in real situation. As the air grooves are partially etched in fabrication (described in Chapter 3) and the effective index of the air layer can be expressed by Eq.5.1 with citing Fig.3.8 of the side elevation of the PhC waveguide.

$$n_{aireffective} = \frac{n_{air}H + n_{Si}(D-H)}{D} > 1 \tag{5.1}$$

where $n_{air} = 1$ and $n_{Si} = 3.4$, H is the etched air groove depth and D is the Si layer thickness. However, in practice, H is difficult to measure without destroying the device and, in any case, tended to vary with d_{air} and from device to device. Also, since in Si ridge waveguide, some of the guided optical power will propagate through the low index regions surrounding the waveguide ridge, the effective index can be estimated from propagation constant of the fundamental waveguide mode of the access waveguides [Chiang 1991 1992], the effective refractive index of the rectangular Si waveguide will be lower than the proposed value of 3.4, i.e.

$$n_{Sieffective} < n_{Si} \tag{5.2}$$

here $n_{Si} = 3.4$. Since a two-dimensional mode solver was not available, there was no means of easily verifying the exact effective index value of the Si layer.

In conclusion, based on the fundamental idea and work Lee *et al* reported, TMM simulations were carried out by using trial values of the refractive indices of the air and Si layers to derive spectra in terms of normalized frequency, the structure parameters were then adjusted until two of the wanted transmission peaks coincided with the desired wavelengths. The results and parameters obtained from such TMM simulations guided the fabrication work in section 5.6.

5.5 Additional Wave-Vector Diagram Approach to the Design

A wave-vector diagram method is proposed here as an additional approach for rapid design optimisation for the desired 1-D multi-transmission PhC microcavity devices. The model can be applied to both planar multiple layer structures as well as 1D PhCs etched slab waveguides. The results of this new model are compared with those of the TMM approach and of a more rigorous method that uses the guided modes of a slab to describe a Bloch mode [Gerace 2004].

The new model is then applied to the realisation of a multi-wavelength transmission microcavity formed in a SOI ridge waveguide. Fig.5.17 shows the different types of 1D PhC microcavity considered in the literature, e.g. [Lee 2005] and [Gerace 2004]. Fig.5.17a shows schematically a multiple layer 1-D PhC in which the periodicity varies. The two reflectors at each end and the centre part of the cavity consist of pairs of layers of high refractive index contrast, with period Λ_A in the reflectors and Λ_B in the central section of the cavity ($\Lambda_B = 2\Lambda_A$). In this work, the layer pairs were silicon (dielectric constant ε_{Si} = 11.56 (n_{Si} = 3.4)) and air (ε_{air} = 1). Figs 5.17b and 5.17c show the equivalent structure formed in a planar slab waveguide and a ridge waveguide.

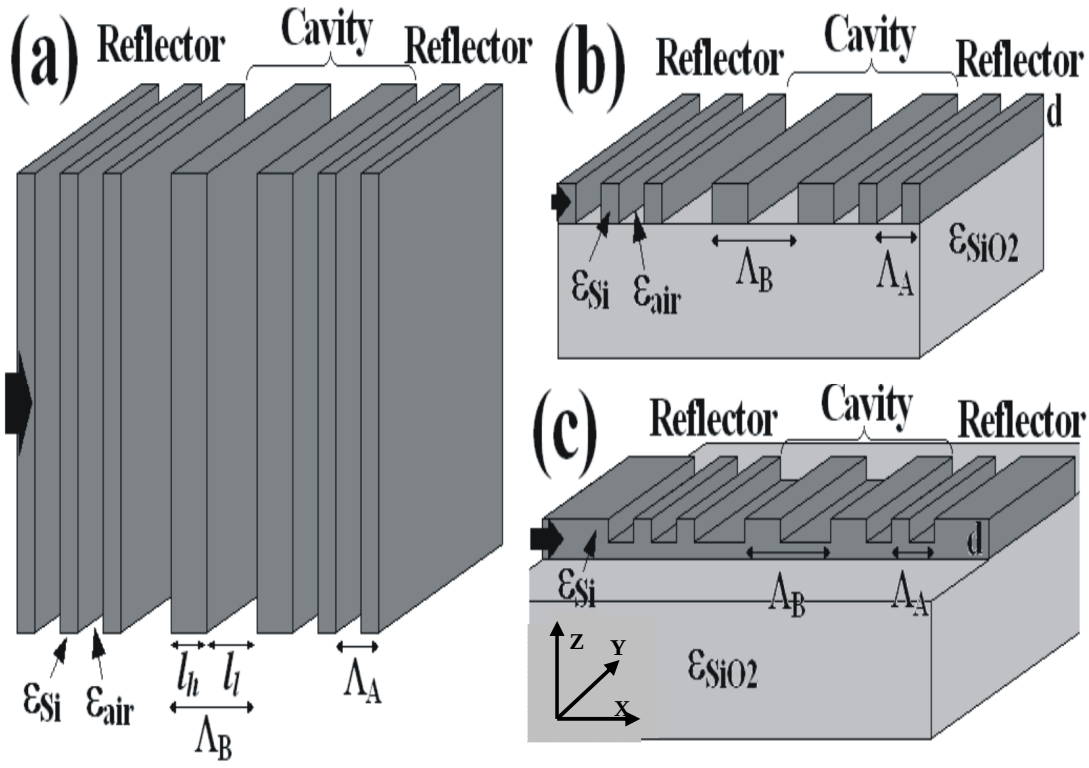

Fig.5.17 Sketches of 1D PhC microcavity structures. (a) multilayer stacks. (b) photonic crystal slabs. (c) planar ridge waveguide on SOI wafers.

Since a ridge waveguide forms a convenient means of coupling light into and from the device, the structure shown in Fig.5.17c is of particular interest in the context of this thesis. However, the field confinement in the Y-direction associated with the waveguide ridge introduces a complication to the analysis. In the practical structure, the air/Si waveguide ridge was wide enough, at ~2.5μm, to support several modes. Whilst the field confinement in the Y-direction is likely to affect the coupling of waveguide modes with the Bloch modes of the PhC device, once light is launched into the latter it has an insignificant effect compared with the confinement in the out-of-plane Z-direction associated with the slab waveguide. Therefore, in the theory that follows the PhC structure is treated like that in Fig.5.17b in which the etched features are assumed to extend laterally over the full range $|Y| \to \infty$.

One other difference between the structures shown in Fig.5.17b and Fig.5.17c is that the air gaps in the latter do not extend through the entire thickness of the Si layer. Incomplete etching of the Si layer helps to control the radiation loss that occurs for

larger air fractions in air/Si PhCs [Gerace 2004] and also changes the effective refractive index of the air layers. However, the remaining Si at the bottom of the air gaps should be thin enough to ensure little effect on the design of a practical multi-wavelength cavity.

The resonant wavelengths are the key factor in designing a multi-wavelength cavity with a PhC central layer, of the type shown in Fig.5.17. For all three structures the resonant condition is given by the universal equation

$$2\pi s = 2(L + L_p)k_s + \pi = 4\pi(L + L_p)\, n_s / \lambda_s + \pi \qquad s = 1, 2, 3 \ldots \qquad (5.3)$$

In Eq. (5.3) k_s, λ_s and n_s are respectively propagation constant, the free space wavelength and the effective modal index of the s-th resonant mode, L is the effective cavity length, L_p is the penetration depth of the resonant mode into the two reflectors. With a PhC replacing the usual homogeneous region in the central section of the cavity, a resonant mode comprises two counter-propagating Bloch modes. One originates from reflections at the interfaces as light passes from high index Si layers to low index Air layers (leftward propagating Bloch modes in Fig.5.17a). The other originates from reflections at the interfaces as light passes from low index air layers to high index Si layers (rightward propagating Bloch modes in Fig.5.17a). The factor π added to the right-hand side of Eq. 5.3 accounts for the phase change associated with the type of reflection.

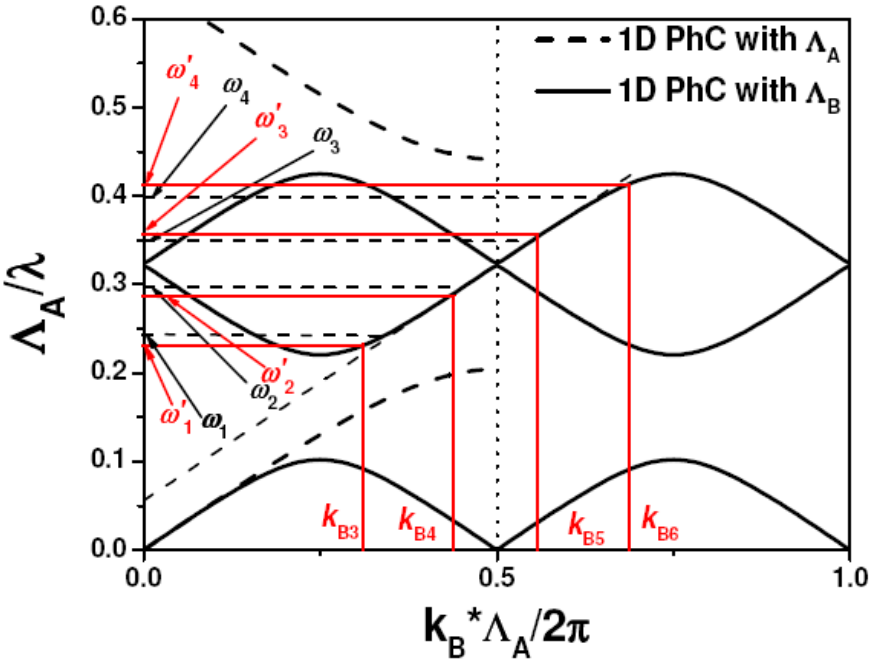

Fig.5.18 Wave-vector diagrams of 1-D PhC stacks with periods of Λ_A (dashed curves) and Λ_B (solid curves). $\Lambda_B = 2\Lambda_A$, $\varepsilon_{Si} = 11.56$, $\varepsilon_{air} = 1$, with both PhCs satisfying the equal optical length condition ($n_h l_h = n_l l_l$). The Bloch wave vectors (k_{B3}, k_{B4}, k_{B5}, and k_{B6}) from Eq.5.3 with the corresponding normalized frequencies ω'_1 (0.232764), ω'_2 (0.286847), ω'_3 (0.357014) and ω'_4 (0.411923) and the normalized frequencies ω_1 (0.248500),ω_2 (0.297456), ω_3 (0.349618) and ω_4 (0.398571) from TMM calculations of Fig.5.9 are both indicated. Close fittings between the black dashed lines (TMM results) and the red solid lines (wave vector approach) can be observed, which indicate the good matching between TMM and wave-vector calculations.

The use of Bloch wave vector diagrams reveals the advantage of using a PhC in the central section of the cavity [Russell 2003(2)]. Fig.5.18 shows the Bloch wave-vector diagrams for the two 1-D periodic stacks Λ_A (dotted lines) and Λ_B (solid lines) and $\Lambda_B = 2\Lambda_A$. Both sets of bi-layers satisfy the equal optical length condition, $n_h l_h = n_l l_l$, where $n_{h,l}$ and $l_{h,l}$ are respectively the refractive index and thickness of the high (low) index layers. Fig.5.18 also shows by vertical solid red lines the Bloch wave vectors (denoted k_{B3}, k_{B4}, k_{B5} and k_{B6}) of the3rd, 4th, 5th, and 6th order resonant modes and their corresponding normalized frequencies calculated from Eq. 5.3 with neglecting

the penetration depth (i.e. with $L_p = 0$).

In the case of a 1-D PhC microcavity of the type shown in Fig.5.17a, the resonant normalized frequencies can be calculated using the transfer matrix method (TMM). The corresponding values are also shown as horizontal black dashed lines in Fig.5.18 and are labeled ω_1, ω_2, ω_3 and ω_4. If the two methods for calculating the resonant condition are entirely equivalent, the vertical and horizontal lines would intersect on the appropriate branches of the wave vector diagrams. Close agreements between the two calculation methods are obtained and further comparison is indicated in Table 5.4, which can be ascribed to a large degree to the neglecting of the penetration depth in Eq. 5.3. This close agreement demonstrates that Eq. 5.3 and the TMM can be used interchangeably to calculate the resonant wavelengths of a complex multiple slab-layer 1-D PhC microcavity, provided the validity of one or other method can be established.

Whilst the TMM additionally provides a rigorously accurate calculation of the band gaps of the 1-D PhC microcavity stack structure, the wave vector diagram approach enables rapid optimisation of the PhC central section of multi-wavelength microcavities of the type shown in Fig.5.17. The wave-vector diagrams of the stack Λ_B can be tuned by varying the air fraction and the refractive index contrast of the periodic structure until its pass band lies within the first band gap of the 1-D PhCs of period Λ_A used to form the reflectors. Since the transmission wavelengths are adjustable with several degrees of freedom, Eq. 5.3 provides a straightforward tool for designing a multi-wavelength transmission filter. Another merit of the wave-vector diagram model is its scope for application to more complicated 1-D PhC slab structures. However, in order to use this model, it is necessary first to test the results obtained from wave-vector diagrams of the 1-D PhC slab lattices against the band structures predicted by more rigorous approaches.

In Gerace's work [Gerace 2004], the authors studied 1-D PhC slabs by expanding the

electromagnetic field in terms of a finite basis set comprising the guided modes of the equivalent slab waveguide of dielectric constant equal to the weighted average of the low and high index regions of the 1-D PhC. The interactions between the expansion components give rise to the band splitting in wave-vector diagrams, whilst the vertical field confinement leads to a blue shift. (The total wave-vector diagram moves towards the short-wavelength region.) Here a simplified treatment is adopted for incorporating these two effects and to show the approximate Bloch wave-vector diagrams.

Firstly, it is assumed that the band splitting effect derives from an assumed infinitely wide multi-layer Si/air stack, with the wave-vector function expressed as $f_0(k)$, where f_0 is the corresponding frequency. Secondly, the vertical confinement effect is treated as an effective homogeneous slab waveguide, as shown in Fig.5.19. The effective slab dielectric constant is assumed to be the spatial average value, ε_{av}, over the 1-D pattern as in Gerace's work [Gerace 2004].

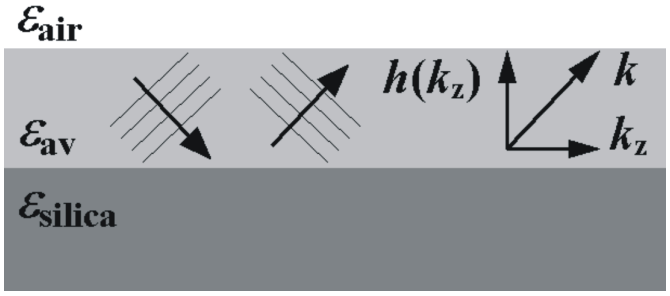

Fig.5.19 Schematic of a plane wave guided in a slab waveguide and its component wave vectors.

The vertical wave vector inside the effective slab, $h(k)$, is calculated and converted into the frequency form. Finally, these two perpendicular components are empirically incorporated into a phenomenological dispersion relationship via

$$f(k) = \{ f_0{}^2(k) + \frac{[h(k)c/2\pi]^2}{\varepsilon_{av}} \}^{1/2} \approx \{ \frac{c^2 h^2(k_z)}{(2\pi)^2 \varepsilon_{av}} + f_0^2(k_z) \}^{1/2} \qquad (5.4)$$

where c is the vacuum light speed.

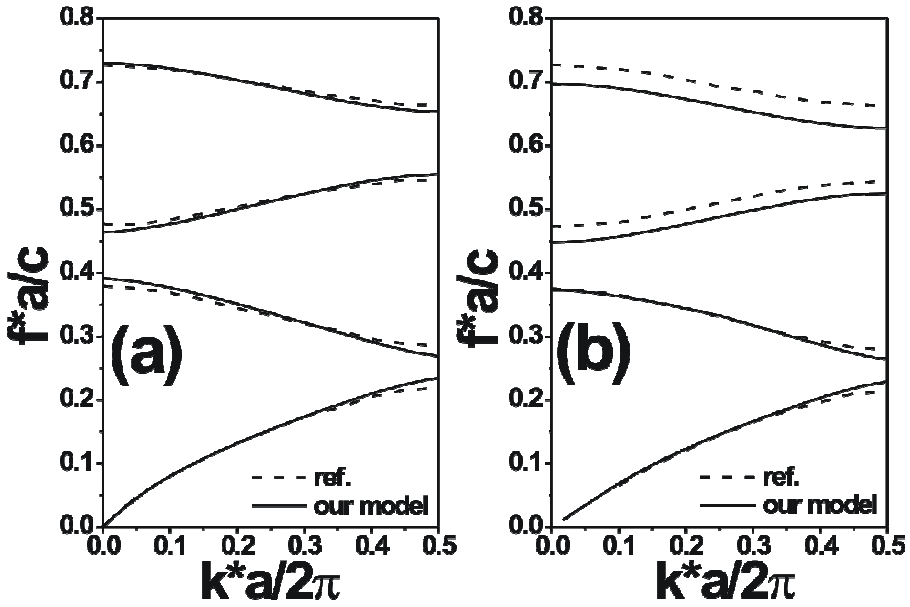

Fig.5.20 Calculated TE wave-vector curves of PhC silicon slabs using the approximate method of Eq. (5.4) (solid lines) and the rigorous method in ref. [Gerace 2004] (dashed lines). Only TE modes are calculated, whilst the obtained TM modes do not match well. The overlap layers are air. The substrate layers in (a) and (b) are air and silica respectively. The thickness of the slab is 0.4 times the period, the air fraction is 0.3. The parameters for the wave-vector calculations are $\varepsilon_{Si} = 12, \varepsilon_{air} = 1,$ and $\varepsilon_{silica} = 2.1$; these values were used for consistency with the values Gerace and Andreani used in their work in order to prove the validity of the wave-vector method.

Fig.5.20 compares the approximate wave vector curves from Eq. 5.4 (solid lines) with the rigorous results taken from Gerace's work [Gerace 2004] (dashed lines) for (a) a symmetric slab waveguide surrounded by air and (b) with a silica buffer layer and an air overlay. The slab thickness is 0.4 times the period and the air fraction is 0.3. It is important to note that in deriving data shown in Fig.5.20, the values of dielectric constant used were $\varepsilon_{Si} = 12, \varepsilon_{air} = 1,$ and $\varepsilon_{silica} = 2.1$[Gerace 2004]. The values of Si and silica differ from those used elsewhere in this thesis and were used here purely for consistency with work of Gerace and Andreani [Gerace 2004] that forms the basis of the comparison shown in Fig.5.20. Fig.5.20 shows that, for TE polarization, there is good agreement between the two sets of results for the first two bands and reasonable agreement for the two higher bands. This proves the viability of using wave-vector diagram for TE polarization for planar ridge waveguide structures. This approximate Bloch wave-vector diagram approach underpinned the

design of the multiple wavelength filter and forms the basis for explaining the close match between the measurement and calculation described in the next section. For TM polarization, the match between the results of Eq.5.4 and the method of Gerace and Andreani is not so good, possibly as a result of the different confinement factors of TE and TM polarization to the slab waveguides.

5.6 Fabrication and Measurements

Silicon-on-insulator wafers with 350 nm thick silicon cladding are again adopted as the starting material, the proposed sketch in Fig.5.15 was used as the pattern for the fabrication. The fabrication procedure essentially followed that described in Chapter 3.

The simulation and discussion in section 5.3 and also the wave-vector diagram approach guided the fabrication. Devices were made with a range of structure parameters close to those identified by the simulations. The fabricated samples were characterized by a super-continuum light source (wavelength range 700-1700nm) consisting of a piece of endlessly single mode photonic crystal fibre [Wadsworth 2004]. The so called endlessly single mode fibre supports only one guided mode over all wavelengths[Birks 1997, 1999]. Table 5.1 shows the parameters of the multi-transmission filter that performed most closely to requirement and its measured resonant wavelengths and transmittance values.

Structure Parameters(nm)				Measured resonant wavelengths(nm) and transmittance values		
d_{Aair}	d_{ASi}	d_{Bair}	d_{BSi}	λ_1 (T_1)	λ_2 (T_2)	λ_3 (T_3)
331	**158**	**697**	**291**	**1168,(0.17)**	**1321, (0.12)**	**1562, (0.11)**

Table 5.1, Structure parameters of the multi-transmission filtering responded PhC waveguides with the measured resonant wavelengths and transmittance values.

Fig.5.21a,b show scanning electron microphotographs (SEM) of the PhC integrated waveguide detailed in Table 5.1.Looking from left to right of Fig.5.21b, the structure consists of a two-cycle PhC reflector of period Λ_A, a microcavity core comprising a two-cycle PhC of period Λ_B , followed by a second reflector formed by two and half-cycles of a PhC of period Λ_A.

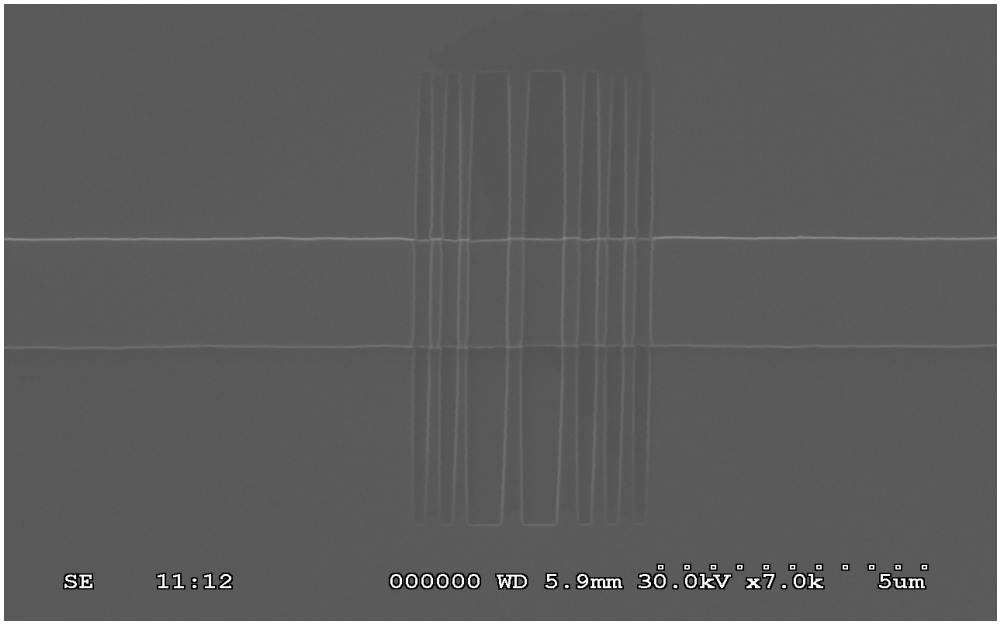

Fig.5.21a, SEM image of the fabricated 1-D PhC multi-transmission optical filter integrated Si waveguide.

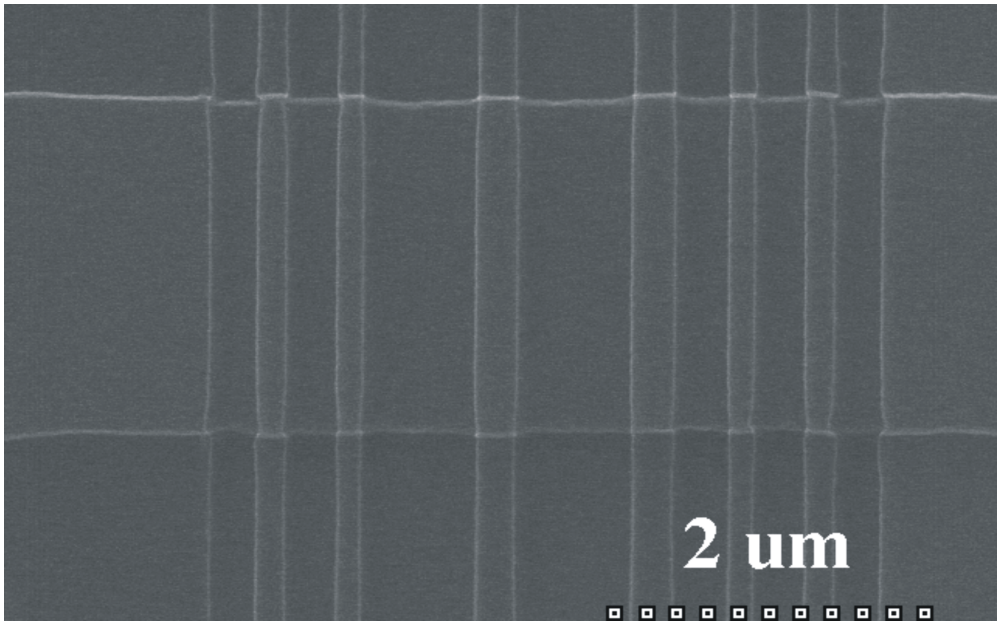

Fig.5.21b SEM image of the magnified 1-D PhC multi-transmission optical filter pattern of Fig.5.21a.

Fig.5.22a shows the transmission spectrum of the waveguide based PhC filter measured by an optical spectral analyzer and the super-continuum light source. Three transmission peaks occur at wavelengths of 1168 nm, 1321 nm and 1562 nm, the fourth one is not shown due to the wavelength range limitation of the light source. Further, a laser stepping measurement with a step of 0.01nm was used to quantify the behaviour around the 1562nm wavelength resonance, the result is shown in Fig.5.22c, the obtained quality factor value was 230 with a transmittance value of 0.11.

Fig.5.22b shows the calculated wave-vector curves of a 1-D PhC slab with a period of Λ_A = 489nm, Λ_B = 988nm. Values of the resonant wave-vectors, k_B, found from Eq. 5.4, with L_p = 0, and the measured transmission frequencies, $\omega = \Lambda_A/\lambda$, taken from Fig.5.22a, are also indicated on the wave vector curves. Good agreement between the measured and calculated results is achieved and detailed comparison is listed in Table 5.2. This agreement justifies the use of the wave vector diagram approach in designing multi-channel-transmission PhC microcavity structured slab filters of the type desired here.

Normalized frequencies from resonant wavelengths(Λ_A/λ)	Wave-vector (Fig.5.22b)	Measurement (Fig.5.22a)	Error
ω_1	0.307874	0.313060	1.68%
ω_2	0.383262	0.370174	-3.41%
ω_3	0.431041	0.418664	-2.85%

Table.5.2 Comparison of the normalized frequencies between measurement and wave-vector calculations.

On the other hand, the transmittance values found by measurement deviate significantly from those predicted by the TMM. This is because TMM does not take losses into account. However, the near equality of the height of the transmittance peaks formed at 1321nm and 1562nm for the fabricated structure complies with the prediction of the TMM. From this, it can be concluded that, in practice, the losses for

radiation in the 1310nm and 1550nm wavelength bands are essentially independent of wavelength for the type of multi-wavelength filter presented here. This is potentially an advantage in meeting system requirements where simultaneously filtering of data encoded on 1310nm and 1550nm wavelength carriers is desired.

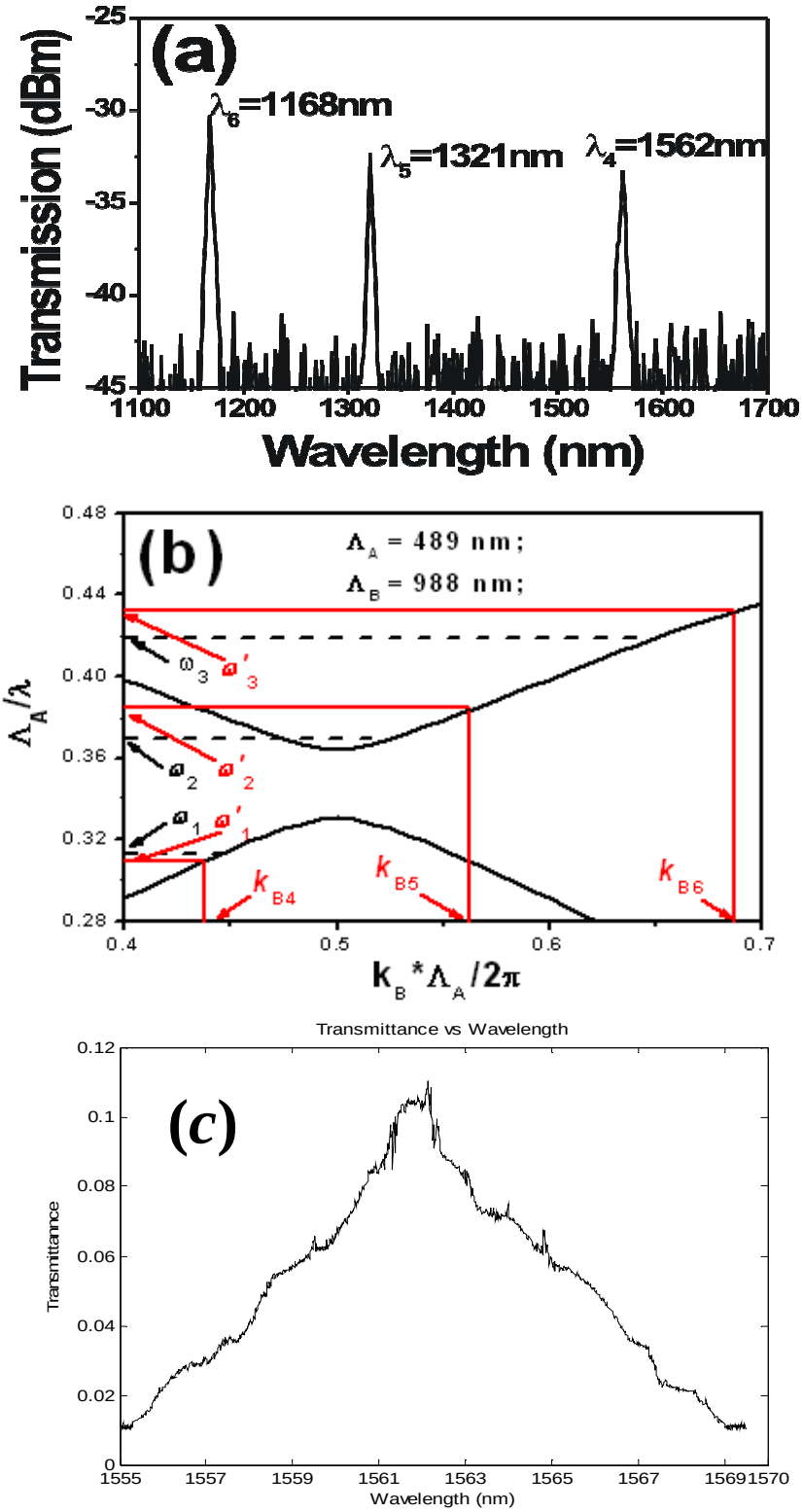

Fig.5.22 (a) Transmission spectrum of the fabricated multi-channel-transmission planar ridge waveguide filter. (b) Comparison of the measured and calculated resonant wavelengths in the wave-vector diagram. ω_1 (0.313036), ω_2 (0.370174) and ω_3 (0.418664) indicate the normalized frequencies from measured results and ω'_1 (0.307874), ω'_2 (0.383262) and ω'_3 (0.431041) from the wave-vector approach based on planar slab waveguide structure calculated from Eq.5.4. (c) Laser stepping measurement of the 1562nm resonance peak.

5.7 Conclusions

The work of design, fabrication and characterization of a multi-transmission optical filter based on a one-dimensional PhC are performed in this chapter, to cater for the requirement from modern WDM optical transmission systems and make progress towards highly integrated optical circuits; the best performed structure was obtained with measured resonances of 1168, 1321, and 1562nm, and transmittance values of 0.17, 0.12 and 0.11, respectively. Since the TMM was used to guide the design, it is instructive to show the comparison between the results of the TMM and those of the optimum fabricated structure.

The reasonable agreement between the two justifies the use of the TMM application in 1-D PhC microcavity design and parameter prediction, despite its limited validity. It is suggested here that this arises because, as the TMM predicts resonant wavelengths for multi-layer stacks, and for the ridge waveguide structures, the deviation may mainly derive from the applicability of TMM to such a specific structure, and also the agreement between the assumed layer refractive indices and the practical values of the air and Si layers. However, if coupling from Bragg modes to radiation modes is low in the PhCs, as will likely happen in carefully fabricated structures, the lateral field distribution perpendicular to the direction of propagation will be more nearly invariant, and the underlying assumption of TMM would be achieved. This would enable the application of TMM for the ridge waveguides structures, as in the design and fabrication procedure in this chapter.

Table 5.3 compares the normalized frequencies between TMM and wave-vector for the 1-D PhC stack structure; very close matches have been obtained, demonstrating the validity of applying the wave-vector approach to the design of multi-wavelength transmission PhC microcavities on the stack structures.

Normalized frequencies from resonant wavelengths(Λ_A/λ)	TMM calculation (Fig.5.9)	Wave-vector (Fig.5.18)	Error
ω_1	0.248500	0.232764	-6.33%
ω_2	0.297456	0.286847	-3.57%
ω_3	0.349618	0.357014	2.12%
ω_4	0.398571	0.411923	3.35%

Tab.5.3 Comparison of the normalized frequencies between TMM and wave-vector calculations.

Table 5.2 presents the comparison of the normalized frequencies between wave-vector calculation of planar slab waveguide structure and measurement; good agreement has also been obtained, which proves the applicability of the wave-vector method to practical structures and its viability in rapid optimization of compact PhC filters for practical applications.

Chapter 6. Experimental Investigation of the Enhancement of the Quality Factor of One Dimensional Photonic Crystal Microcavities

6.1 Introduction

Optical microcavities are characterised by two main quantities: the modal volume V and the quality factor Q. In many applications, high Q values and small V's are highly desirable for the high finesse required for laser and filter applications and for the high Purcell factor [Purcell 1946] required for controlling the spontaneous emission of atoms placed in resonance with the microcavity mode [Yokoyama 1995]. In conventional Bragg gratings, the refractive index contrast is low, and a large number of small reflections over a long propagation distance is needed to produce high reflectivity. Thus, high Q values are achieved at the expense of large V's. Alternatively, periodic microstructures deeply etched into a semiconductor waveguide offer high refractive index contrast and much shorter penetration lengths in the mirrors. However, for strong refractive index variations, the Bragg mirror cannot be considered as a perturbation of the uncorrugated waveguide [Peyrade 2002]. Radiation losses in the claddings are inevitable, and the Q factor is lowered. Thus high Q values and small V's appear to be two conflicting objectives. However, the results of Chapter 4 show that PhC microcavities with high Q and small V can be fabricated in SOI waveguides using the techniques developed in this work. Other researchers have also reported the realisation of PhC microcavities with high Q and small V [Lalanne 2003]. Such high Q, small V cavities are often accompanied by a high transmittance at the resonant wavelength not predicted by conventional Fabry-

Perot resonant theory [Lalanne 2004]. These results have led to several investigations of enhanced Q in PhC microcavities [Cao 2002, Peyrade 2002, Sauvan 2004], especially the very recently reported work from Velha *et al* [Velha 2006].

Theoretically, two approaches which lead to extremely high Q values are known. The first one has motivated the concept of the three-dimensional photonic crystal, the famous "photon cage" [Yablonovitch 1987]. The second refers to a subtle engineering of the core and cladding materials of the waveguide stack, so that minimal mode profile mismatch occurs when propagating through the different waveguide sections [Ctyroky 2001].

For the practical integration of 1-D PhC to SOI ridge waveguides with high Q values, approaches like "radiation recycling,"[Lalanne 2004] which has been discussed in Chapter 4 and the use of mode converting features have been reported [Cao 2002, Peyrade 2002, Lalanne 2004, Sauvan 2004]. These two methods are both applicable to 1-D PhC microcavities etched into ridge waveguides. This chapter describes a systematic practical investigation of the incorporation of mode-matching features into 1-D PhCs in order to enhance the value of Q in small volume waveguide micro-cavities. The effect of mode matching features on transmission, T, is also considered.

6.2 Engineering the PhC Mirrors

It is known that when light propagates in a periodic structure, its mode of propagation is described by Bloch modes which have a periodicity equal to that of the physical structure in the absence of illumination. The Bloch-mode vector can be denoted by $|B\rangle = \begin{bmatrix} E_t \\ H_t \end{bmatrix}$, where E_t and H_t are the transverse components of the electric and magnetic fields, and can be written in the form

$$|B\rangle = |B'(x, y, z)\rangle \exp(jk_0 nx) \tag{6.1}$$

where $|B'(x+\Lambda, y, z)\rangle = |B'(x, y, z)\rangle$. In Eq (6.1) k_0 is the modulus of the free-space wave vector and the quantity n represents the effective index of the Bloch mode. It is defined as the modulus of $2\pi/k_0\Lambda$.

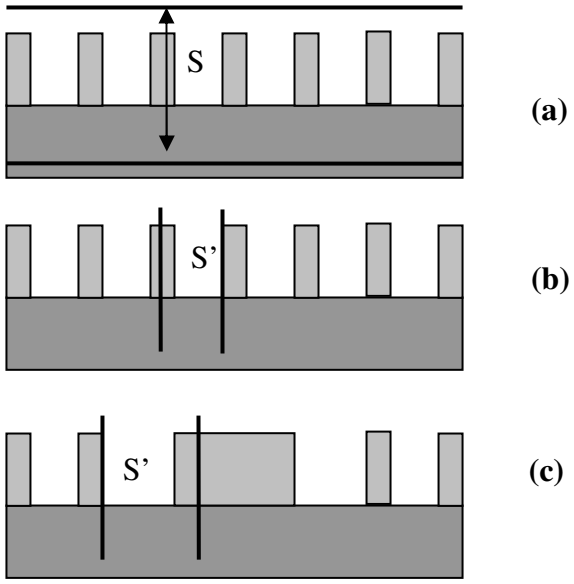

Fig.6.1 Different approaches for Bloch-mode calculation of a periodic waveguide. (a) Grating approach: the Bloch modes are calculated as the complex pole of a "transverse" scattering matrix S. (b) Waveguide approach: the Bloch modes are calculated as the eigen-states of a "longitudinal" scattering matrix S'. (c) The same Bloch modes can be formally identified in a complex and non-periodic waveguide structure.

Two different approaches are usually used to calculate the Bloch modes. As shown in Fig.6.1 (a), one way is to calculate the Bloch modes as the complex poles of the determinant of a "transverse" scattering matrix S that relates the electromagnetic field components in the substrate and in air. Alternatively, one may also calculate the Bloch modes as the eigen-states of a "longitudinal" scattering matrix S' relating the electromagnetic fields between two planes separated by one period, as in Fig.6.1 (b). These two approaches are mathematically equivalent. Clearly, the first approach emphasizes the periodic nature of the Bloch modes, whereas the second approach refers to some locality: the Bloch modes are seen as the eigenstates of the scattering matrix associated with a specific segment [Happ 2001, Mekis 2001, Lalanne 2002]. This segment may correspond to a single period of a periodic structure, as shown in Fig.6.1 (b), or may be embedded into a more complex and nonperiodic patterned waveguide, as shown in Fig.6.1 (c). For the fabrication of the mode-matching structures in this chapter, the second approach provides the basic theoretical support.

By engineering the PhC mirror geometry, that is finely adjusting the dimensions of its component layers or sections, it is possible in principle to drastically reduce the

losses at the interface between a Bragg mirror and a normal waveguide [Lalanne 2003]. This reduction is achieved by a gradual variation of the mirror geometry aimed at tapering the incident guided mode into the fundamental Bloch mode of the mirror. In integrated optics, gradual variation of patterned waveguides has previously been investigated for mode transformation. Tapered segmented waveguides which rely on a progressive transformation of the so-called "quasi-modes" have been proposed and implemented for independently controlling the vertical and lateral confinements in optical waveguides [Lee 2002, Peyrade 2002, Lalanne 2004]. More recently, short tapers for coupling into photonic crystal waveguides have also been proposed and implemented [Talneau 2002].

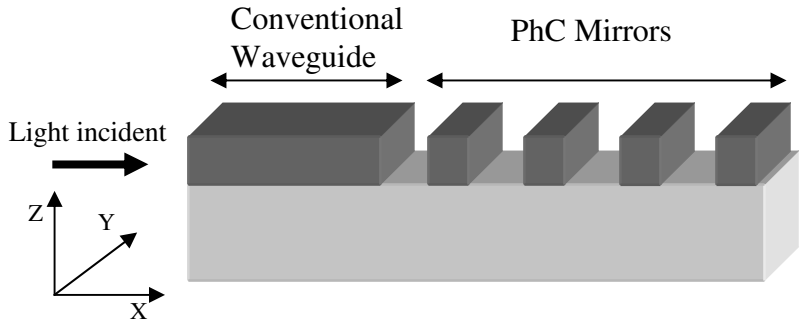

Fig.6.2 Waveguide composed of Conventional Waveguide and normal PhC Mirrors

A physical interpretation for the origin of the loss that occurs at the interface between a classical waveguide and a semi-infinite Bragg mirror was first proposed by Palamaru [Palamaru 2001] and Cao [Cao 2002]. The interpretation relies on a semi-analytical model in which the losses originate from an impedance mismatch between the fundamental guided mode of the x-invariant waveguide and the fundamental Bloch mode of the Bragg mirror. More specifically, the losses are understood as resulting from a triple scattering process as follows. First, the incident guided waveguide is scattered into the fundamental half-Bloch wave propagating into the positive x direction. Then, this wave is coupled back into the conventional waveguide. Provided that the fundamental Bloch mode is a genuine non-leaky guided mode, the back-coupling occurs with unit efficiency, and the radiation losses only result from a mode mismatch. These losses, L, vary linearly with the square of the overlap integral, ξ, between the fundamental guided and the half-Bloch wave

associated with the fundamental Bloch mode of the Bragg mirrors, L = 1 $-\xi^2$ [Palamaru 2001,Cao 2002].

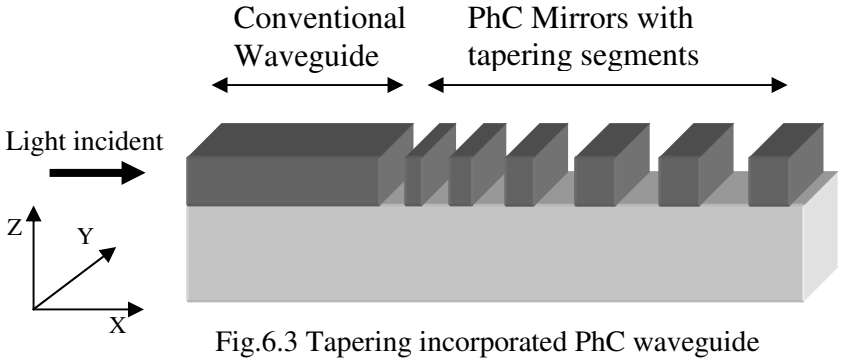

Fig.6.3 Tapering incorporated PhC waveguide

The impedance mismatch problem shows the advantage of designing mirrors which incorporate modal conversion to reduce the radiation losses. Following the numerical work Cao *et al* reported [Cao 2002], the segmented tapers are formed by a series of etched air gaps of feature dimensions that vary progressively. A mirror incorporating a taper between the x-invariant waveguide and the semi-infinite periodic Bragg mirror is shown in Fig.6.3. Here the taper comprises three sections of Si of shorter length than in a regular period of the photonic crystal structure separated by air gaps that are also shorter than those within the regular period of the photonic crystal. The art of obtaining nearly lossless short mirrors lies in tapering the guided mode of the un-patterned waveguide into the fundamental Bloch mode of the Bragg mirror. From the numerical results of Cao's work [Cao 2002], it is clearly shown that after inserting the tapering segments, the mirror losses decrease with increasing number of segments. This is especially stringent at the designed wavelength. Relative to the classical Bragg mirror, a loss reduction by more than a factor of 200 can be achieved for the three-segment engineered mirrors [Xu 2000, Happ 2001, Mekis 2001, Khoo 2005].

6.3 Engineering the Microcavity

From the discussion in section 6.2, it is expected that when tapered segments are inserted between conventional waveguide and PhC mirrors, the transmittance of the mirror could be enhanced. Given that the defect layer or central part of a waveguide microcavity is formed from a section of conventional waveguide, it is also expected the Q and T of the microcavity as a whole will be boosted by inserting additional mode-matching sections between the mirrors and the cavity itself, as shown schematically in Fig.6.4 and Fig.6.5. Peyrade *et al* [Peyrade 2002] have demonstrated practically and from simulation an enhancement of Q in similar 1-D PhC microcavities etched into SOI ridge waveguides using tapered PhCs comprising 16.5 periods (period = 290nm) with air gaps of linearly increasing and then decreasing width (40nm to 80nm and 80nm back to 40nm) either side of a single period with a 90nm air gap. These authors reported an increase of measured Q to 200, compared with Q = 110 for a control microcavity comprising un-tapered 3.5 period (period = 290nm) mirrors with fixed 90nm air gaps.

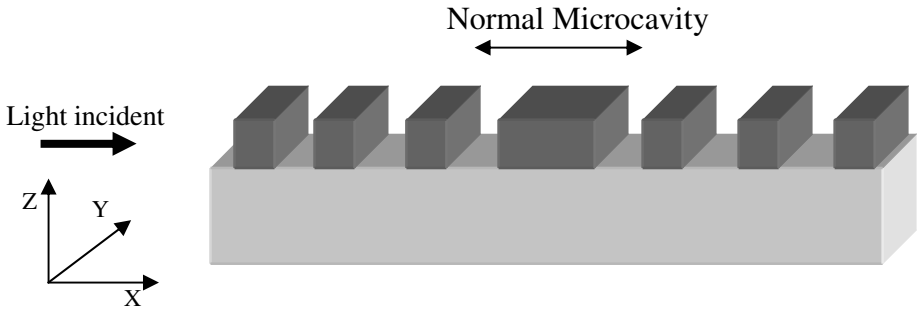

Fig.6.4 Normal microcavity formed by inserting a short monomode waveguide section between two identical Bragg mirrors.

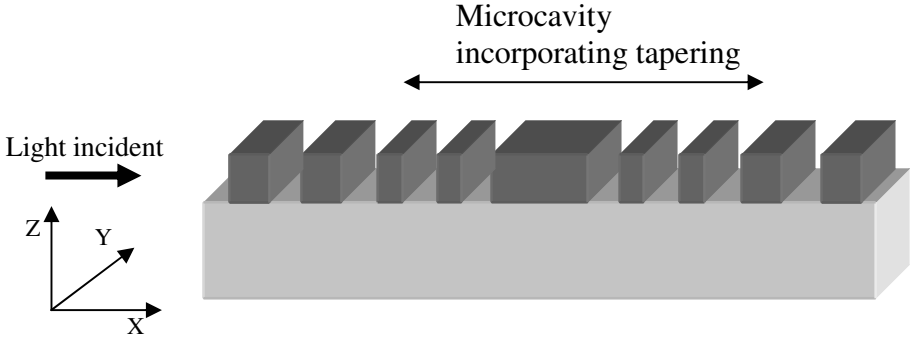

Fig.6.5 Microcavity with tapering between the central section and the Bragg mirror.

In order to investigate the applicability of TMM to the 1-D PhC structure with tapers, based on the structure parameters Peyrade proposed, some TMM simulations are performed to compare the results with Peyrade's work [Peyrade 2002]. Fig.6.6 compares the spectral variation in the reflectivity calculated by TMM of a) 4 periods of period 290nm Si/air Bragg mirror with fixed 90nm wide air gaps—"Mirror 1", b) 11 periods of 290nm period Si/air Bragg mirror with fixed 90nm wide air gaps—"Mirror 2", and c), 11 periods of Si/air bilayers in which the air gap linearly increase from 40nm to 90nm in steps of 10nm—"Mirror 3", whilst the refractive indices of Si is 3.4 and air is 1, band gaps or quasi-band gaps can be observed.

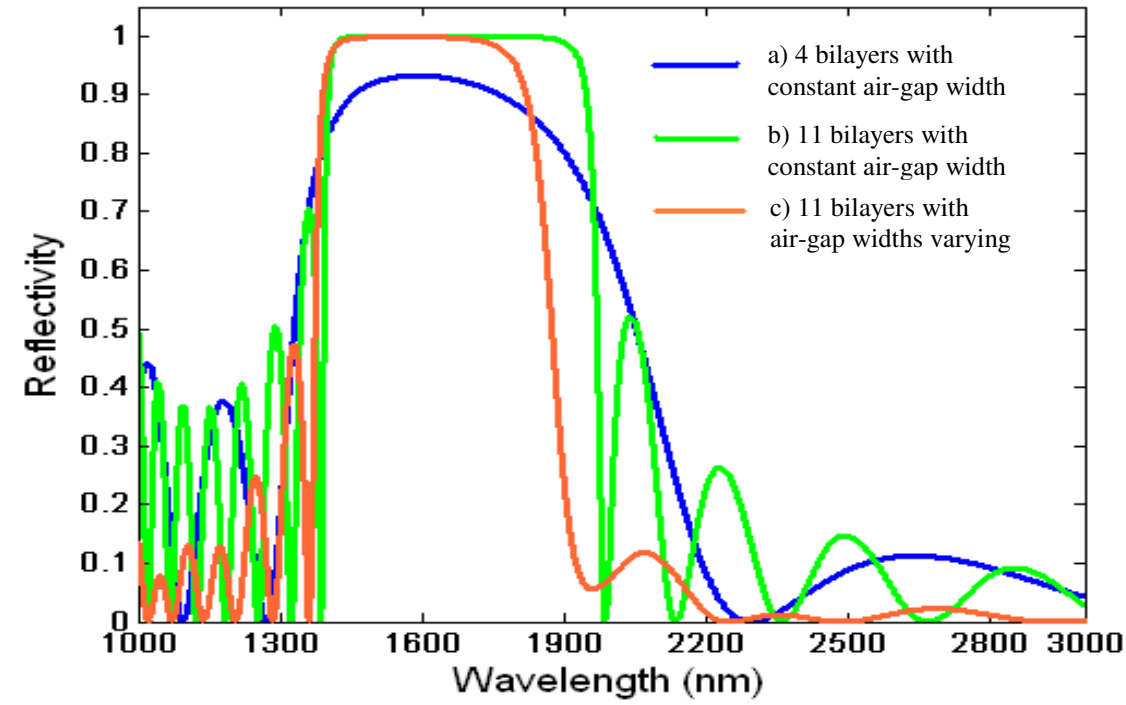

Fig.6.6 Reflectivity comparison of a) 4 periods of 290nm period Si/Air bilayers with fixed 90nm wide air gaps, b) 11 periods of 290nm period Si/air bilayers with fixed 90nm wide air gaps and c), 11 periods of Si/air bilayers in which the air gap linearly increase from 40nm to 90nm in steps of 10nm. The refractive indices of Si and air are 3.4 and 1, respectively.

Fig.6.7 compares the resonant behaviour of three planar microcavities made from the three types of mirrors considered in Fig.6.6 with the same Si defect layer width of 227.94nm in each case; such structures agree with the work Peyrade reported and enables the comparison. The obtained Q values are listed in Table.6.1

Mirror1-Defect-Mirror1	Mirror2-Defect-Mirror2	Mirror3-Defect-Mirror3
247	3648	673

Table 6.1 Comparison of the Q values of the cavity formed by three types of mirrors.

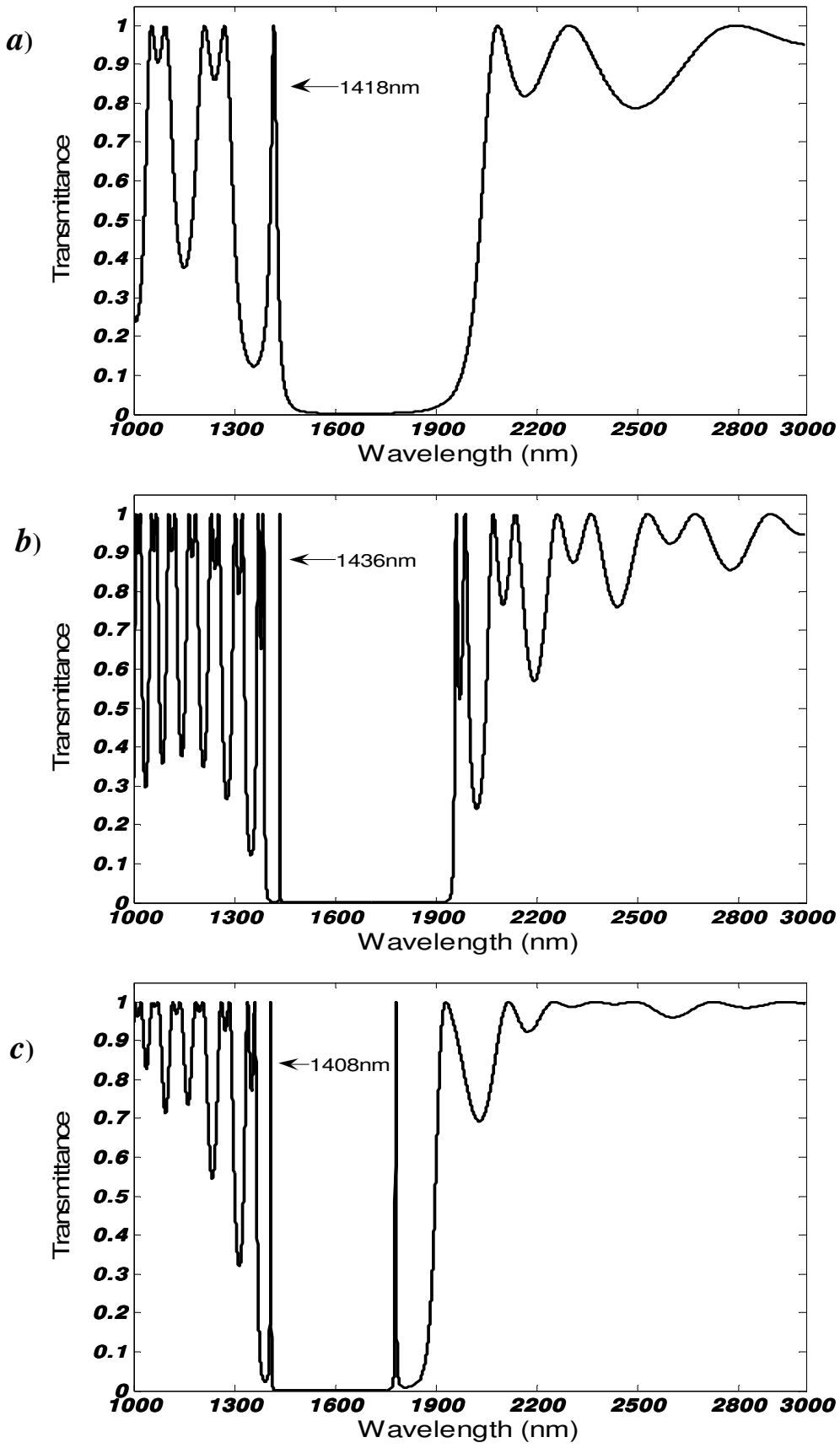

Fig.6.7, Resonance behaviour calculated by TMM of microcavities formed by the mirrors described in Fig.6.6: (*a*) mirror1-defect-mirror1, (*b*) mirror2-defect-mirror2, (*c*) mirror3-defect-mirror3.

The fact that Q of the tapered structure calculated by TMM is lower than the 11 period structure without tapers and therefore is in contradiction to the proposed and demonstrated work by Peyrade *et al* [Peyrade 2002] shows that the TMM is not valid for modelling the integrated tapering structures. The reason is that the basic theory of mode matching is more complicated than the foundation of TMM. To accurately calculate the situation of the mode matching and tapering effects for boosting up the Q values requires advanced simulation work or software. However, the fabrication work is this chapter was guided by the theoretical and numerical works presented by Palamaru and Lalanne [Palamaru 2001, Lalanne 2004].

Very recently, Velha *et al* have reported measurements of greatly enhanced Q values of small volume microcavities formed in SOI ridge waveguides by 1-D PhC mirrors incorporating mode matching features between the central cavity section and 1-D PhC mirrors in the form of a single row of holes etched through the 340nm thick Si core of a 540nm wide ridge waveguide supported by a SiO_2 buffer layer [Velha 2006]. Fig.6.8 shows schematically the basic structure considered by Velha *et al*.

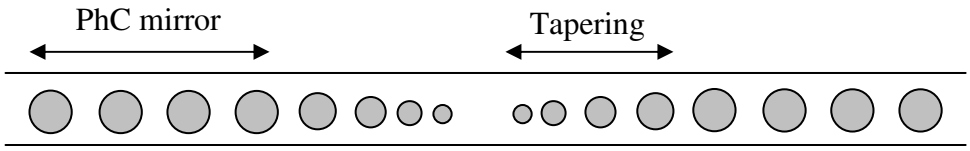

Fig.6.8 Sketch of the tapering inserted PhC microcavity reported by Velha et al, which created the Q value of 8900.

Their tapers comprised, starting from the central cavity section, a short sequence of etched holes with progressively increasing diameter and separation until the geometry complied with the hole geometry and periodicity of the 1-D PhC. Table.6.2 reproduces the measured Q values reported by Velha *et al* and compares these with earlier measurements of Q values for the type of microcavities shown in Fig.6.8.

Q Values	2500	265	360	370	460	**2010**	**3240**	8900
Reported Time	1997	1997	1999	2002	2003	**2005**	**2006**	2006

Tab.6.2 the reported measured Q values in chronological order. The highlighted value and time are the results obtained in this work..

Table 6.2 shows that the Q values obtained for the waveguide microcavity with 5 periods without any mode matching features described in Chapter 4 are indeed competitive with the best reported in the literature to date and are exceeded only in the structures very recently reported by Velha. *et al* [Velha 2006] that incorporate mode matching features between the cavity and the mirror to reduce the loss associated with the mismatch between the cavity mode and the dominant Bloch modes of the mirrors.

Two questions emerge from this comparison. First, can a similar enhancement of Q be obtained in practice for the type of rectangular blocks and slots of 1-D PhCs and microcavities developed in this work, as predicted by Lalanne and Hugonin [Lalanne 2003, 2004]? Second, a mode mismatch also occurs between the guided modes of the access waveguides and the Bloch modes of the PhC mirrors, contributing an additional end-to-end loss. It is assumed that the planting of mode matching features between these two sections could possibly reduce the loss. A new consideration here is the possibility that the mode conversion may not be instantaneous but occurs over a small but finite distance. Consequently, mode-conversion loss will be distributed and potentially will contribute to degrading of the microcavity Q. If indeed this occurs, further enhancement of Q can be expected from incorporating mode matching tapers between the mirrors and the access waveguides.

The remaining sections of this chapter describe a systematic practical investigation of the effect of incorporating mode matching tapers into ridge waveguide based on 1-D PhC microcavities. The 1-D PhC structures and tapers considered are of the block and gap form shown schematically in Fig.6.3 and Fig.6.5. The range of microcavity structures considered is illustrated in Fig.6.9.

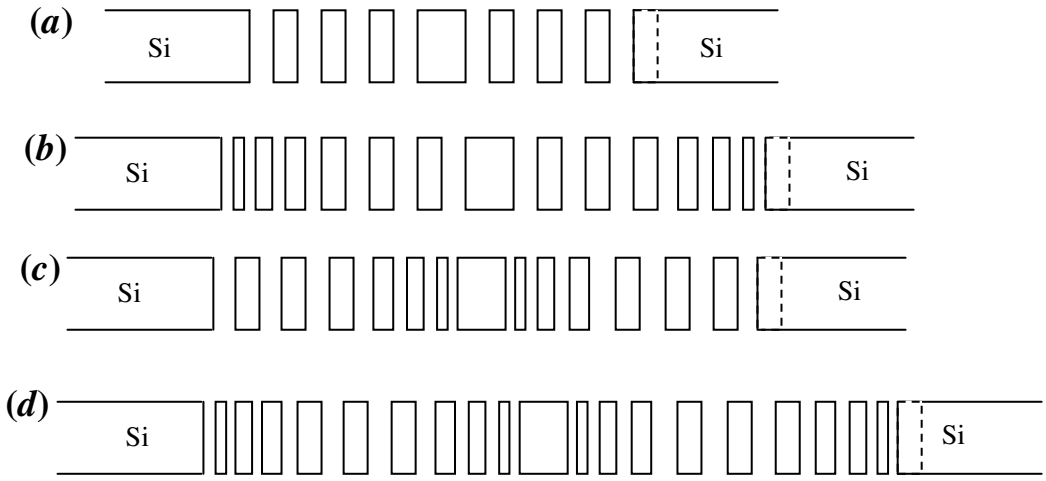

Fig.6.9, Sketches of the four structures to be fabricated: (a) no tapers, (b) tapers inserted between the access guides and the Bragg mirrors, (c) tapers inserted between the defect and the Bragg mirrors and (d) tapers on both sides of each Bragg mirror.

6.4 Fabrication of the Tapering PhC Filters

In order to investigate systematically the effects of incorporating mode matching tapers on the one-dimensional PhC microcavities, four types of the PhC microcavity structures have been fabricated: the normal structure (Fig. 6.9a), the structure with taper between access waveguide and PhC mirrors (Fig. 6.9b), the structure with tapering between PhC mirrors and defect (Fig. 6.9c), and finally the structure with tapering in both regions (Fig. 6.9d). The design parameters of the basic PhC structure satisfies the equation: $n_{Si}d_{Si}=n_{air}d_{air}=\lambda_0/4$, where λ_0 is assumed to be 1550nm and n_{si} and n_{air} are 3.4 and 1, respectively. The width of the defect layer is designed to be twice that of the Si layers of the PhC. Such a design should produce a resonance transmission peak at 1550nm. Based on the taper design shown schematically in Fig.6.9, the intended three air gap widths of the taper are 60nm, 80nm and 100nm, while the three intervening Si blocks progressively vary as 30nm, 50nm and 70nm. These layer widths should be compared with d_{Si} = 113.97nm and d_{air} = 387.5nm in the PhC mirror itself.

The much smaller feature sizes in the tapers compared with those in the PhC described in earlier chapters meant that the electron beam energy and current had to be carefully optimised to ensure accurate definition of the PMMA resist features

after exposure and development. This required further extensive process development.

To obtain a groove of width above 100nm with a deviation of around 20nm, the normal electron beam dose is around 300 units, where dose is defined as the sensitivity of the photo resist (for PMMA it is in the order of 100μAs/cm^2). Normally, the unit of dose is expressed in pixels where one pixel corresponds to the distance between exposure spots. Entering a step size value in μm, the related pixel step size will be calculated by the following equation:

$$\frac{step\_size[\mu m]}{writefield\_width} = \frac{step\_size[pixel]}{65536} \tag{6.2}$$

The entire writefield size is divided into 2^{16} = 65536 pixels. Eq. (6.2) also shows the relation between writefield size, area stepsize in μm and in pixels. In all the work described so far, an electron beam dose equivalent to 10 pixels was used.

However, to obtain a dimension that is under 100nm, this low dose, high pixel approach did not work well due to poor feature definition in the PMMA after exposure and development. Table 6.3 summarises the investigation of measured feature width for different design widths for two electron dose units. As can be seen from the obtained data, vast resist spread occurred for low dose exposure, while high dose confined the spread to significantly closer to the expected dimensions. The combination of high dose, low pixel has the effect of reducing the resist spread after exposure and development, especially for very small dimensions. Fig.6.10 shows a SEM image of a test pattern that reveals the effect of dose for creating features of width under 100nm.

Designed Width (nm)	Dose 300	Dose 1800
10	~100	30～40
20	100～120	35～50
30	100～120	45～70
50	100～120	65～80
70	110～130	80～95

Table 6.3 Comparison of exposure and develop results between electron beam dose 300 and 1800.

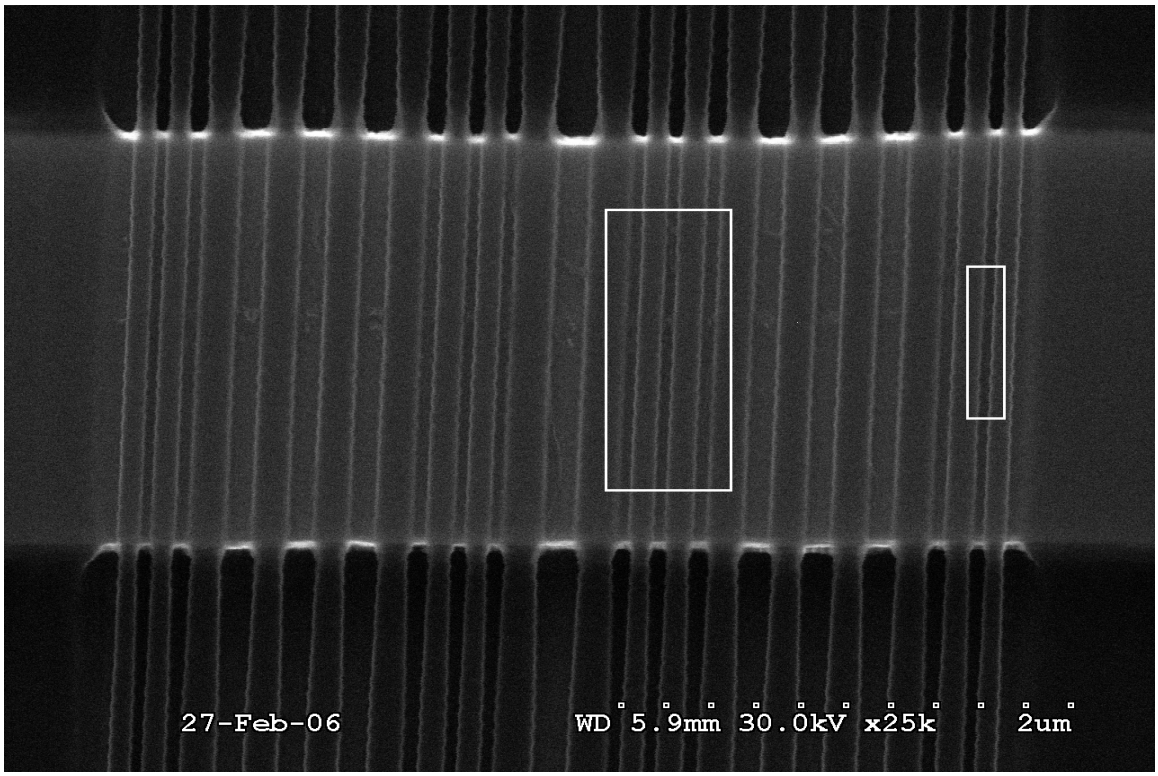

Fig.6.10 SEM image of a text pattern (on PMMA). The larger highlighted area shows the progressive changing of the layer dimensions while the smaller highlighted area shows the smallest width of about 30～40nm that was obtained. The lighter grey sections are exposed and developed areas.

Following the optimisation of the exposure dose, the PhC patterns was created in the PMMA layer. Next, ICP etching was performed to transfer the pattern into the Si ridge waveguide. Owing to the very narrow features in some areas, it is expected that the etch depth will vary in different air gaps of the nanostructure. This arises from aspect ratio dependent etching (ARDE). As the width of the area of the surface exposed by the resist pattern for etching decreases, the rate of transport of etch species to the exposed area and of etch bi-products away from it drops off. Fig.6.11

illustrates this effect for ICP etching of SiO_x [Collins 2006]. In the case of very narrow windows through the etch mask (PMMA in this work), ARDE will have a significant effect. Further, as the widths of the narrow windows vary, as in the case of the required tapers, the etch depth will vary along the taper and it is believed that the sketch in Fig.6.12 represents the real final construction of the whole microcavity.

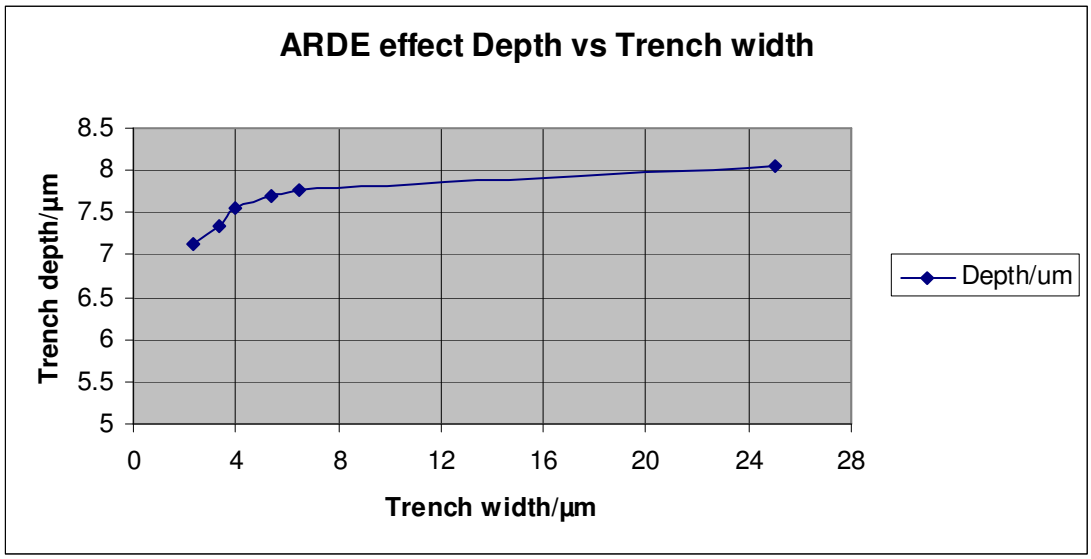

Fig.6.11 Aspect Ratio Dependent Etching (ARDE) effect for SiOx core etching [Information from Oxford Istrument Ltd, manufacturer of the ICP etching machine].

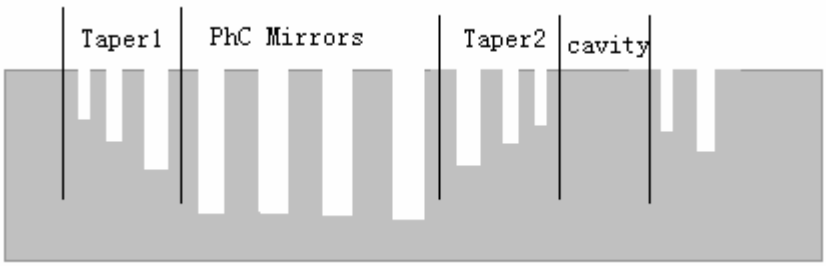

Fig.6.12 Cross Section of the tapering planted PhC cavity (half side)

The SEM microphotographs shown in Fig.6.13b and Fig.6.13c demonstrate that the depths of the air gaps were indeed significantly less in the tapers than in the regular PhC mirror. The limited resolution of the SEM available prevented quantification of the variation of air gap depth with width in the tapered regions. The progressive increase in the depth of the air gaps with their width should in principle enhance the effect of the taper [Johnson 2002, Kuang 2002, Sauvan 2004] and therefore could be advantageous.

Fig.6.13 and Fig.6.14 show respectively the angled and vertical SEM microphotographs of the structures considered in this investigation. In all cases, the main PhC mirror comprised 4 periods. Fig.6.14a shows a normal PhC cavity structure without any tapering. This forms the control sample. Fig.6.14b demonstrates a taper incorporated between the access waveguides and the PhC mirrors on both sides of the cavity in order to improve the coupling efficiency from Si waveguides and the microcavity. Fig.6.14c shows the tapers inserted between the PhC mirrors and the defect layer with the aim of boosting the quality factor of the intrinsic cavity. Finally, Fig.6.14d shows tapers inserted on all sides of the mirrors to create a high transmittance, high Q value cavity.

The taper design was limited by device processing. Table 6.4 shows the consequent intended design and compares this with the dimensions achieved in practice from analysis of high resolution SEM micrographs in Fig.6.15. Excellent fabricated dimensions were achieved in comparison to the design, as can be observed from Table 6.4.

	Design-Fabrication (Taper1)	Design-Fabrication (Taper2)	Design-Fabrication (Taper3)	Design-Fabrication (Mirror)	Design-Fabrication (Defect)
d_{Si}(nm)	30--38	50--54	70--76	113.97--122	227.94--242
d_{air}(nm)	60--48	80--79	100--96	387.5--376	

Table 6.4Comparison of the designed and fabricated dimensions of the tapered 1-D PhC structure.

The electron beam lithography machine used in this work has a theoretical limit of line-width of 10nm. However, in practice, due to all the factors that could have a detrimental affect to the exposure result, the practical limit is estimated to be about 30nm. The fabrication effort needed to make the tapers challenged this limit and impacted on the performance of the final devices. As can be observed from Table 6.4, the intended feature dimensions could not be replicated exactly. The deviation from the design was unsurprisingly largest for the smallest air gap and Si block in the taper, the fabrication error being ~±25%. It is possible that reduced air fraction due to ARDE, manifest in the high resolution SEM microphotograph shown in Fig 6.15, to some extent offsets this limitation. As the size of the features increases, the deviation between the measured and design widths decreases to the 1-10% range, representing

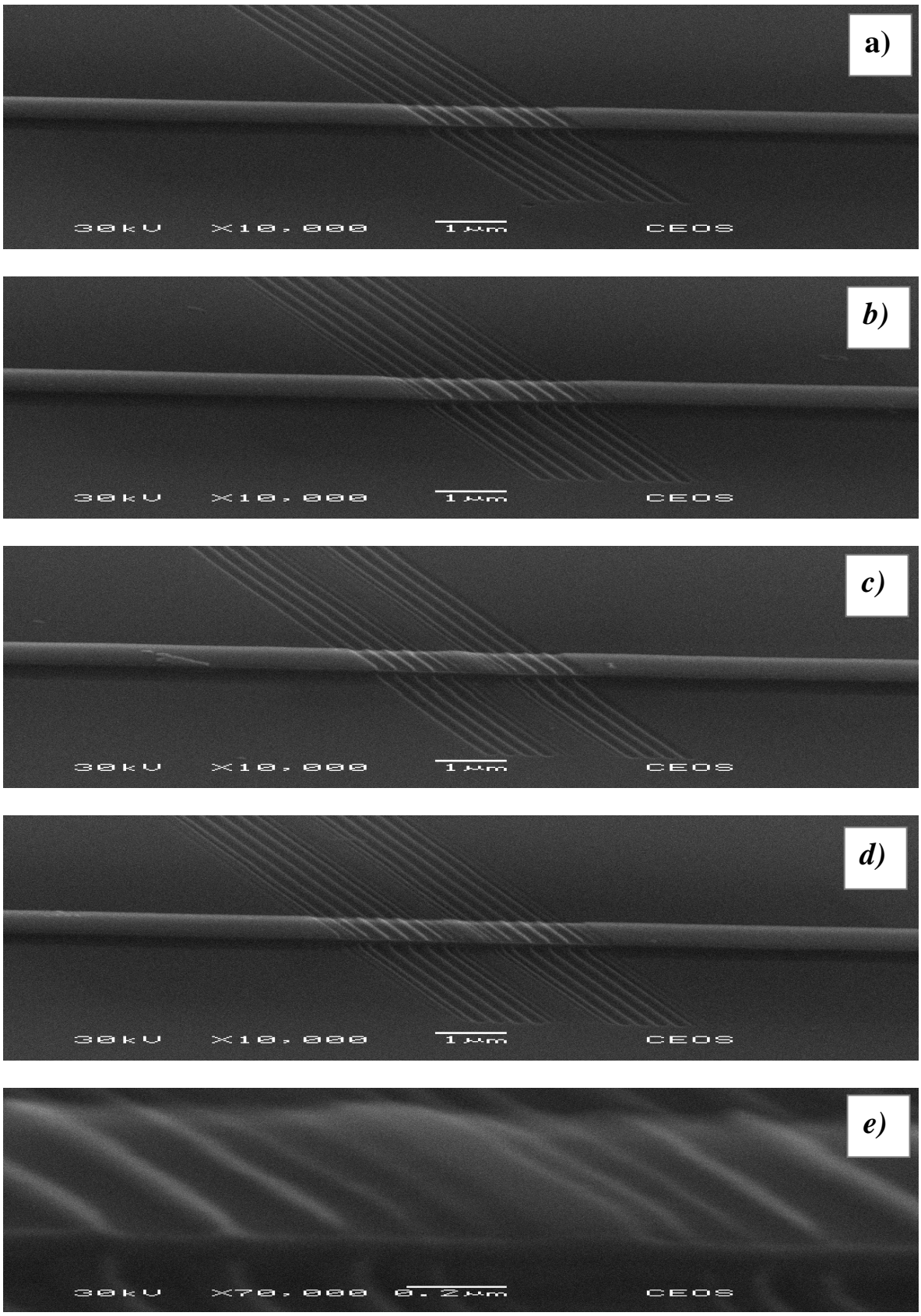

Fig.6.13 Angled SEM images. (a) a PhC structure without tapering; (b) a PhC structure with tapering from waveguide to mirrors; (c) a PhC Structure with tapering from mirrors to cavity; (d) a PhC Structure with tapering in both areas; (e) magnified SEM image of the cavity area with surrounding tapering. Both width and depth progressively vary in the layers around the cavity.

good process control for such demanding device geometries. Overall, the structures incorporating the desired taper features have been fabricated with designs informed by Palamaru and Lalanne's theoretical and modelling work [Palamaru 2001], combining the benefit of the etch depth variation, but not formally based on their work. The final designs used took into account the practical limits on the feature sizes achievable using the electron lithography system available.

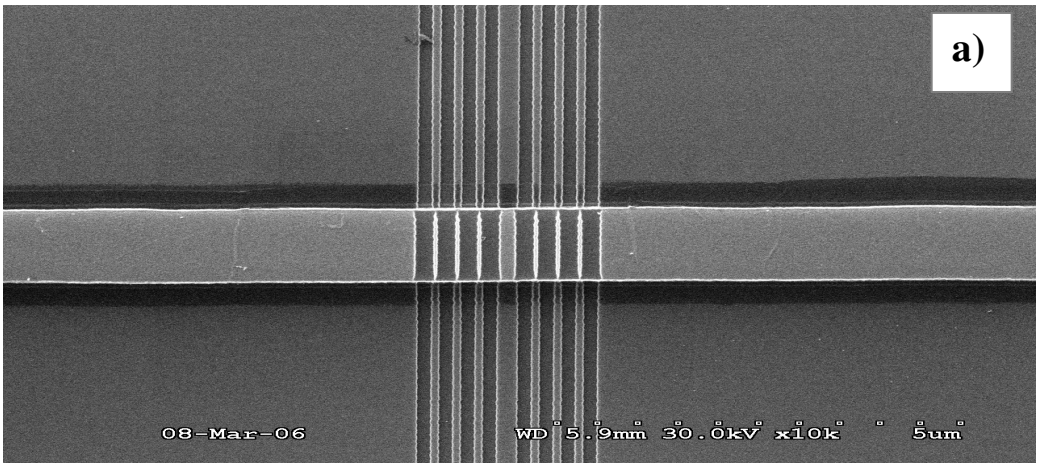

Fig.6.14a Vertical SEM image of the PhC structure without tapering. The microcavity volume is 2.33μm

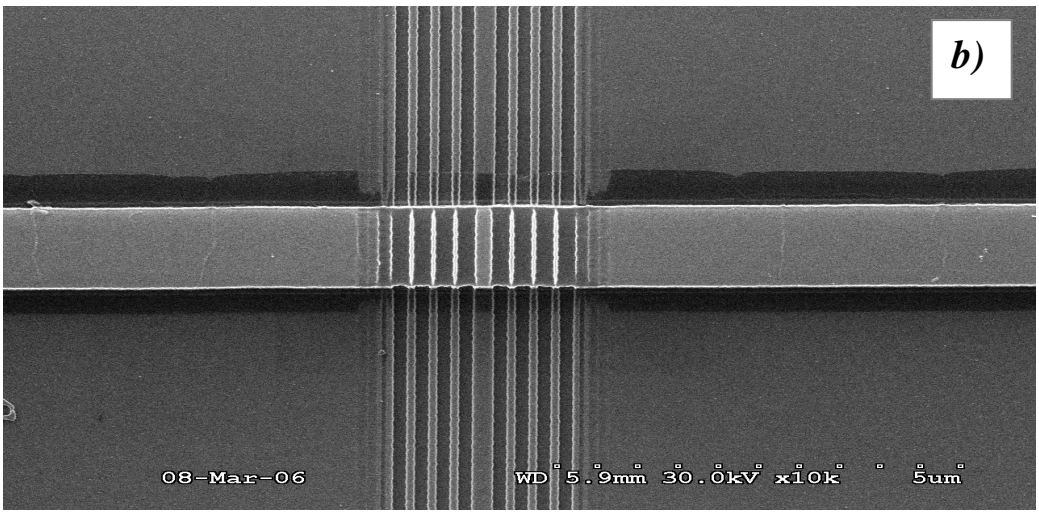

Fig.6.14b Vertical SEM image of the PhC structure with tapering from waveguide to mirrors. The microcavity volume is 3.12μm.

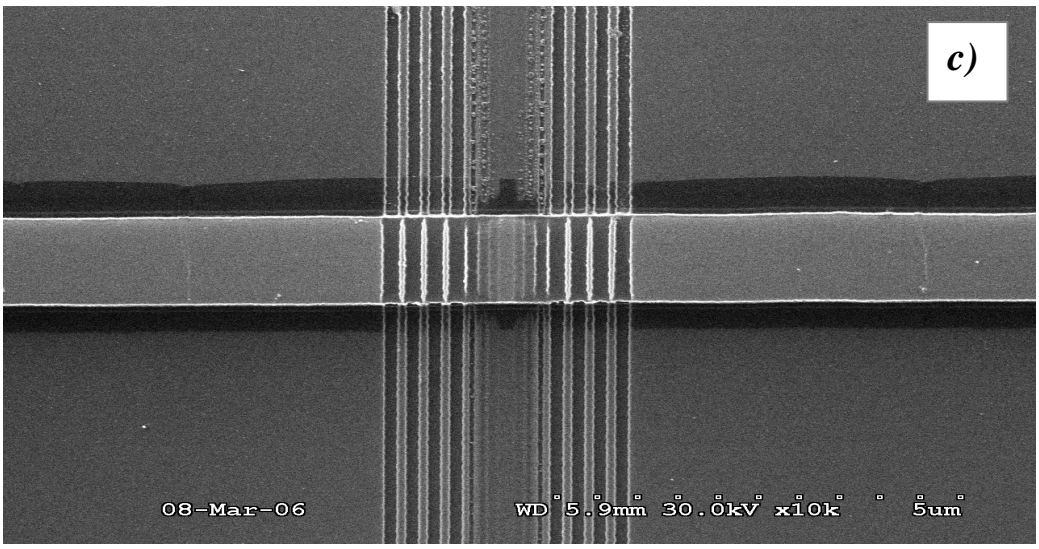

Fig.6.14c Vertical SEM image of the PhC Structure with tapering from mirrors to cavity. The microcavity volume is 3.09μm.

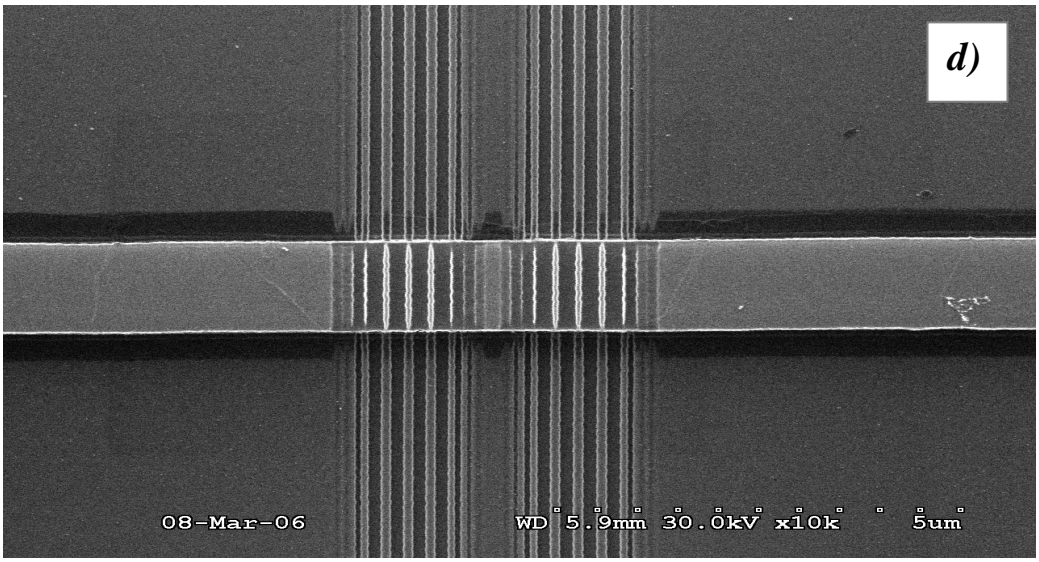

Fig.6.14d Vertical SEM image of the PhC Structure with tapering in both areas. The microcavity volume is 4.06μm.

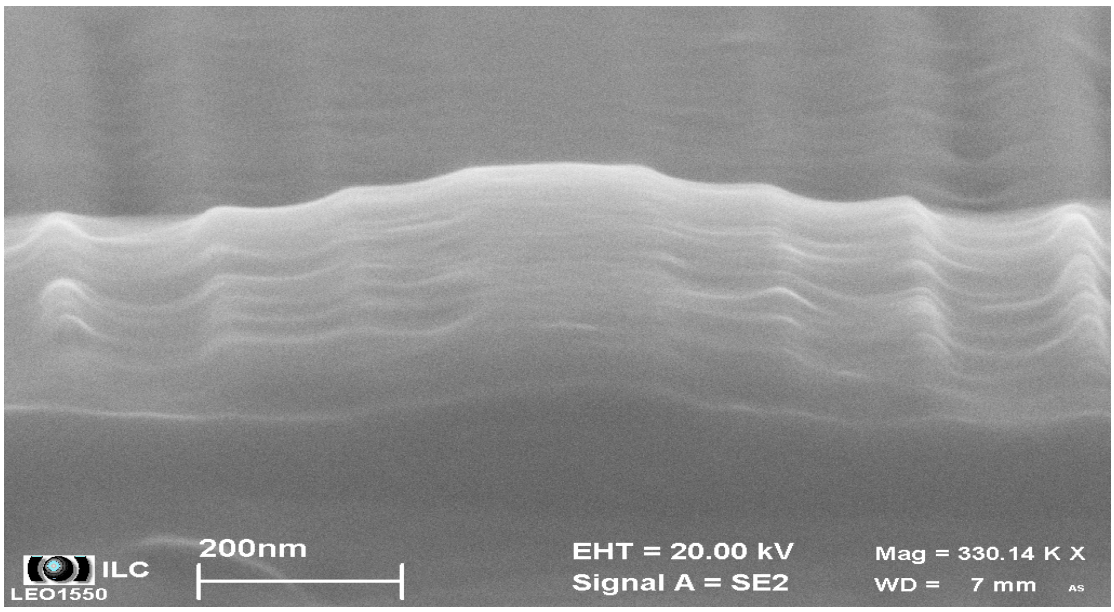

Fig.6.15 An ultrahigh magnification SEM micrograph of the tapering around the defect cavity. The Si segments width and etching depth variations can easily be observed. [SEM microphotograph kindly provided by A. Satka of the International Laser Center, Bratislava, Slovak Republic].

As can be concluded from the magnified SEM image of the tapering feature and from the angled and vertical micrographs, the mode matching features inserted around the 1-D PhC microcavities were successfully fabricated. Compared to the previous fabrication of the conventional microcavities, a high dose and small pixel exposure was used in this work to obtain tapers with features of progressively varying width. Samples were then thinned and cleaved as before to produce good waveguide facets.

6.5 Measurement of the Optical Characteristics of Tapering Structures

The samples were measured using both the conventional laser wavelength stepping method and sideband measurement method described earlier. Resonances were observed in all microcavities, without and with tapers in the various configurations. Fig.6.16 shows the transmission spectra of the four structures with Table 6.5 detailing the measured resonant wavelengths, quality factor and peak transmittances.

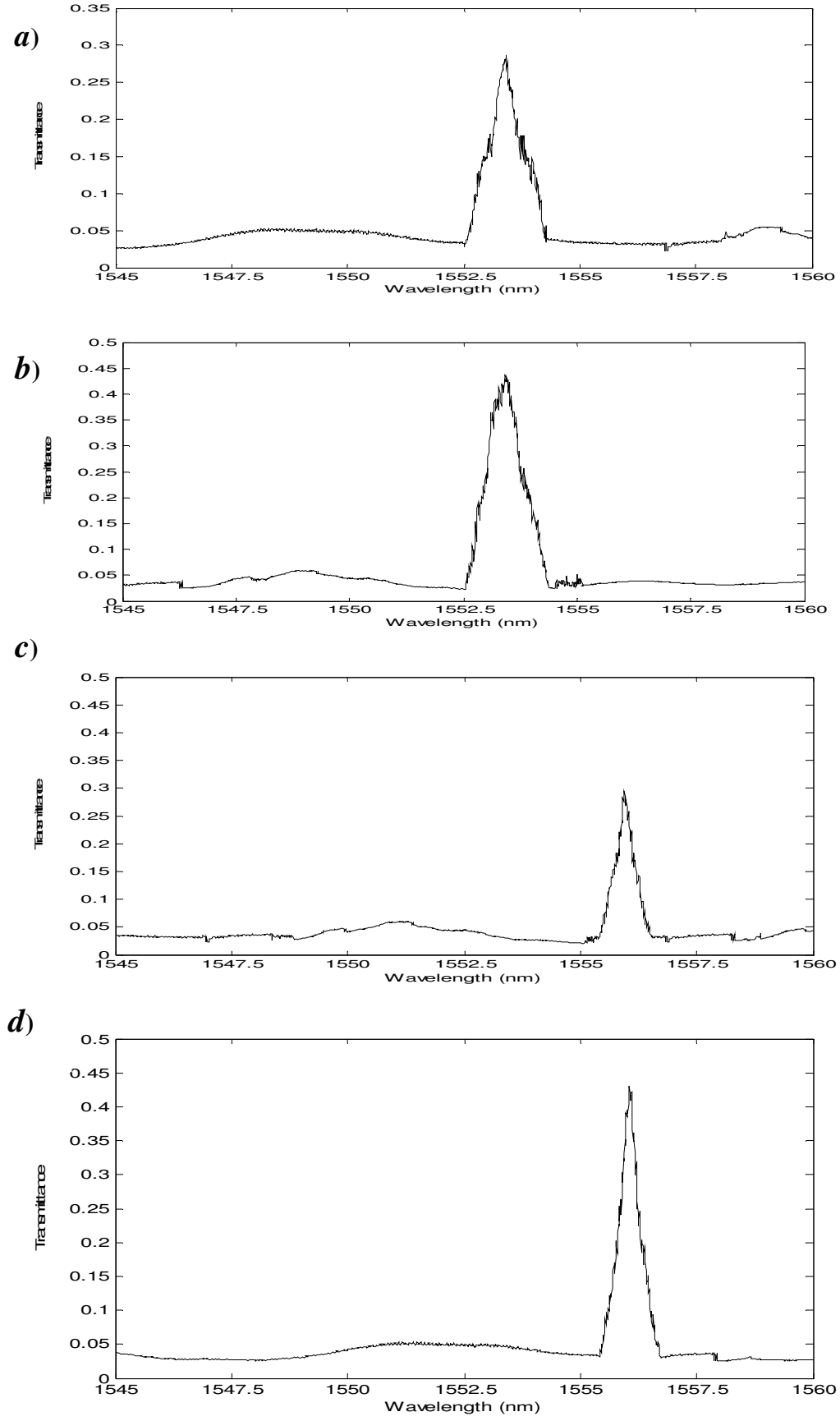

Fig. 6.16, Resonant part of the transmission spectra measured for each microcavity: (a), no taper; (b),taper from access waveguide to PhC; (c),taper around cavity and (d), tapers from access waveguide to PhC and around cavity.

	No Taper	Taper from WG to PhC	Taper around Cavity	Both Tapered
Resonance Wavelengths (nm)	1553.41	1553.42	1555.95	1556.05
Q Value	1600	1700	3100	3200
T Value	0.29	0.44	0.29	0.43

Table 6.5 Measured Q and T values of the fabricated PhC Structures.

The data from Table 6.5 validates the proposal of Lalanne [Lalanne 2004]. The tapers created between conventional Si access waveguides and PhC mirrors reduce the mode mismatch between the Bloch wave of the periodic structure and planar wave of normal ridge waveguides, to improve the transmittance of the whole structure. Further, inserting the tapers between the Bragg mirrors and the cavity improved the mode matching between the Bloch modes of the PhCs and the cavity modes of the defect layer. In this situation, the tapers reduced the internal loss of the microcavity, doubling the Q values, but leaves T largely unchanged. Whilst the increase in Q was not as dramatic as that observed by Velha *et al* [Velha 2006] for their probably more optimised structures, this result nonetheless provides clear confirmation of the theory of Lalanne *et al* [Lalanne 2004].

Finally, it is shown that inserting tapers at each end of the Bragg mirrors results in simultaneous improvement in both Q and T. Indeed, there is a small further increase in the Q values of the microcavity with both sides tapered. A possible reason could be that the internal loss is distributed through the Bragg mirrors and not just confined to the layers adjacent to the defect, as a result of the Fabry-Perot modes penetrating, at least partially, the PhC reflectors. In general, tapers formed by a series of blocks and gaps whose feature dimensions vary progressively, provide low insertion losses over a broad spectral interval. Because of their sub-wavelength scale, the segments of the taper support genuine non-leaky Bloch modes that offer much lower loss mode matching.

6.6 Conclusions

In this chapter, a systematic experimental investigation of the effect of mode matching tapers in one-dimensional photonic crystal microcavity structures has been described. The tapers, which were systematically positioned between the access Si waveguides and PhC waveguides, or around the cavity, were observed to have significant impact on the microcavity resonant performances: both the quality factor and peak transmittance value were improved. Inserting the tapers between the Bragg mirrors and the defect resulted in a doubling of Q, whilst inserting the tapers between the mirrors and the access waveguides increased T by nearly 50%. Inserting tapers at both ends of each mirror resulted in simultaneous improvement in Q and T. This practical work proved the theoretical assumption and numerical calculations reported in the literature [Palamaru 2001, Cao 2002, Peyrade 2002, Jugessur 2003, Lalanne 2003 2004], and it seems reasonable to expect that the progressively adaptive geometries in the form of tapers will play a significant role in the future development of integrated PhC optical circuits.

Chapter 7. Pass Band Optical Filter Based on One Dimensional Photonic Crystal Structures

7.1 Introduction

Wavelength Division Multiplexing (WDM) is the name given to the optical communications technique in which several baseband-modulated channels are transmitted along a single fibre but with each channel located at a different wavelength [Keiser 2003]. The advantage of using WDM derives from the increase in data carrying capacity through a single optical fibre by transmitting information encoded separately at the same bit rate on to several light beams of different wavelengths. The use of spectrum in WDM is shown in Fig.7.1. Here it is assumed each carrier wave has undergone amplitude modulation by a lower frequency sinewave signal. The WDM channels are separated sufficiently in wavelength to avoid crosstalk when they are multiplexed or demultiplexed by a non-ideal optical filter. The signals at different wavelengths can be individually routed through a network or individually recovered by wavelength-selective components. WDM enables the utilisation of a significant portion of the available fibre bandwidth by allowing many independent signals to be transmitted simultaneously on one fibre, with each signal located at a different wavelength [Bayspec.com].

In modern dense WDM (DWDM) systems, characterised by small channel spacing and high bit rates, selective band pass filters are a key component for the implementation of fundamental functions, such as channel add-drop, channel selection, demultiplexing, multichannel filtering, and interleaving [Keiser 2003]. The required characteristics are high selectivity (the ability to separate two adjacent channels), high out-of-band rejection in order to guarantee a low crosstalk between channels, a flat in-band response, and, preferably, a low insertion loss.

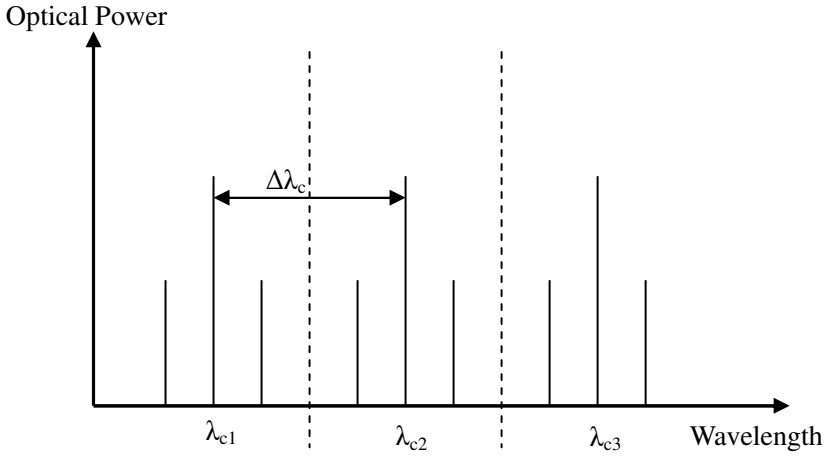

Fig.7.1 Utilisation of the optical spectrum in WDM. The channel spacing $\Delta\lambda_c$, must be wide enough to prevent the side bands of one channel lying in the same wavelength range on the sidebands of an adjacent sideband to prevent crosstalk.

Fibre Bragg gratings (FBGs) [Zengerle 1995, Wei 1997], arrayed waveguide gratings (AWGs)[Keiser 2003], and cascaded Mach-Zehnder filters [Madsen 1999] are excellent devices for the purpose of WDM filtering, but their complexity or dimensions strongly increase with the number of channels for applications in high-density WDM systems. As an example, reflective Bragg gratings often require expensive and bulky circulators, whereas AWGs are difficult to realise when channels are closely spaced in wavelength. In advanced systems, filters based on coupled resonators are more attractive thanks to their smaller dimensions, integrability, optical performances, and flexibility [Lan 2001(2),2002(1,2), Nishikawa 2002, Costa 2003, Jugessur 2004].

For the further and practical application of such coupled resonator structures in optical filters, it is desirable to have a structure that can give light a flat or quasi-flat transmission in the spectral range of the resonance peaks, in order to satisfy the requirement from WDM systems. To achieve this goal, defect coupling method has been introduced and investigated, since coupling of localized defect modes in PhCs in principle will provide important functions which cannot be achieved with a single defect [Kaliteevski 1998, Beggs 2004,Lan 2001(2), 2002(2)].

Theoretical investigations by Beggs *et al* [Beggs 2004] and experimental work by Jugessur *et al* [Jugessur 2004] have revealed that narrow pass bands can be achieved using coupled 1-D PhC microcavities. Beggs *et al* used a transmission matrix approach similar to that described in Chapter 2 to analyse the spectral response of coupled microcavities made from 1-D PhC stacks to show that the width, roll-off and flatness of the pass band can be adjusted by varying the number of microcavities coupled together, the number of periods in *a*) the outer Bragg reflectors and *b*) in the Bragg reflectors in between the cavity layers [Beggs 2004]. Jugesser *et al* considered pairs of coupled microcavities formed by etching circular holes in a single mode AlGaAs/GaAs ridge waveguide both by finite difference time dimensions (FDTD) simulation and experimental demonstration [Jugessur 2004]. These authors also demonstrated the role of the ratio of the number of periods in the outer Bragg reflectors to the number in the inner Bragg reflector in optimising the flatness and roll-off of the pass band. However, the pass bands of the 1550nm wavelength considered by Jugesser *et al* were $>$50nm, too large for WDM application where the channel spacing should be $\leqslant$0.8nm to meet the ITU specification.

The first aim of the work reported in this chapter is to investigate whether or not a coupled 1-D PhC microcavity filter can be designed to meet the specification of the ITU wavelength grid of standard wavelengths for WDM optical transmission systems. The second aim is to demonstrate practically such a filter using the Si/air PhC etched into a SOI ridge waveguide technology developed in this thesis.

7.2 Investigation of Defects Coupling in 1-D PhC Structures

7.2.1 Coupling of Two Identical Microcavities

The work of Lan *et al* [Lan 2001(1,2) 2002(1,2)] and Beggs *et al* [Beggs 2004] inspired and guided the theoretical and simulation work in this chapter. Lan *et al* demonstrated the formation of photonic band gaps in the impurity bands of photonic crystals by the 1-D coupled cavity structure [Lan 2001(1)] and further investigated the formation of the pass band based on 1-D and 2-D coupled cavity PhC structures [Lan 2001(2) 2002(1,2)]. Beggs *et al* [Beggs 2004] developed an analytical approach for the design of optical filters, and presented that in the case of the two coupled cavities, the closest similarity of the transmission peak to a square shape (pass band), while retaining maximum transmission equal to one, is achieved at the point of the strong-weak coupling threshold.

In this section an investigation of the coupling behaviour of two identical cavities is described based on the work Lan *et al* [Lan 2002(2)] and Beggs *et al* [Beggs 2004]. The assumed structure consisting of two coupled microcavities is shown in Fig.7.2.

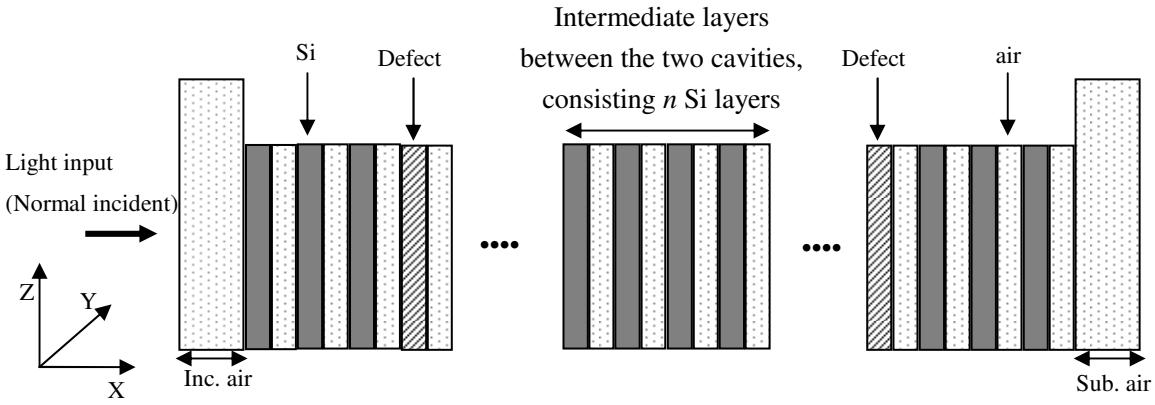

Fig.7.2 Schematic show of the 1-D PhC structure formed by two identical coupled cavities with varying the intermediate Si layers between the cavities, the assumed incident and substrate materials are air to obtain symmetry for the whole structure.

The refractive indices used in the modeling are n_{Si} = 3.4 and n_{air} = 1, in agreement with the values used in other part of this thesis, as guide by the work of Lan *et al* [Lan 2002(2)], the thicknesses of Si and air layers are chosen to be equal and selected randomly to be 360nm, i.e. $d_{Si} = d_{air} = 360\,\text{nm}$, which yields the thickness of a bilayer to be $\Lambda_1 = d_{Si} + d_{air} = 720\,\text{nm}$. The defect layers are formed by the relation of $d_{defect} = 0 \bullet d_{Si}(d_{air})$, and located at the position with three outer Si layers on each side, shown in Fig.7.2. TMM calculations were performed with varying the number of Si layers in the intermediate part between the two cavities and retaining the outer part unchanged; the obtained spectra are presented in Fig.7.3, note the x-axis ranges are slightly modified from spectrum to spectrum to have the best view of the coupling behaviour.

It can be observed from Fig.7.3 that as *n*, the number of the intermediate Si layers increases, the two Lorentzian shape resonant peaks move closer towards the centre frequency, and begin to merge together as *n* further increases. Notably, when *n* = 6, as shown in Fig.7.3(*e*), a flat top band pass filter has been obtained. A magnified view of the top region shown is shown in the inset. However, when *n* reaches 7, shown in Fig.7.3(*f*), a non-unity transmission quasi-Lorentzian shape resonance appears at the same normalized frequency. Kalittevski [Kaliteevski 1998] first

studied the interaction of localized photon states in a structure consisting of two coupled microcavities, which resulting in splitting of the optical modes of the system, and he also developed an analytical expression for the splitting [Appendix 3].

Beggs *et al* also studied the case and had the conclusion that the coupling of two identical microcavites through a central Bragg mirror leads to the splitting of the cavity modes, where the size of the splitting is proportional to the transmission of the separating mirror. Two distinct cases can be identified. In the strong coupling regime, where the splitting is larger than the width of the cavity modes, there are two separated resonant peaks in the transmission spectra. In the weak coupling regime, where the splitting is smaller than the width of the cavity modes, the two lines merge together, and a quasi-flat top pass band is obtained at the point of the strong-weak coupling threshold [Beggs 2004]; however, the influence of the number of the outer Si layers was not considered in their work; from the discussion in Lan *et al*'s work [Lan 2001(2)] and the simulation results shown in Figs.7.5, 7.6, and 7.7, it can be concluded that a stronger confinement in the outer layer, which can be obtained by big number of the outer Si layers, will lead to a increasing of the intermediate Si layer numbers in order to obtain a flat or quasi-flat pass band.

The spectra shown in Fig.7.3 and the analysis from Kaliteevski [Kaliteevski 1998] and Beggs *et al*s' [Beggs 2004] work guided the further simulation and fabrication work in this chapter.

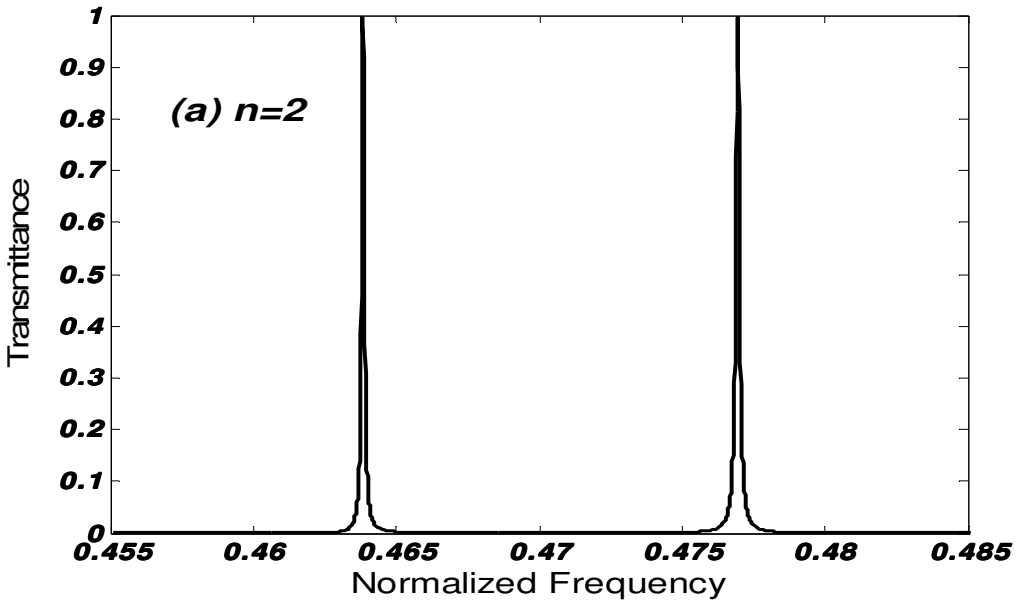
(a) n=2
Transmittance
Normalized Frequency
0
0.1
0.2
0.3
0.4
0.5
0.6
0.7
0.8
0.9
1
0.455
0.46
0.465
0.47
0.475
0.48
0.485

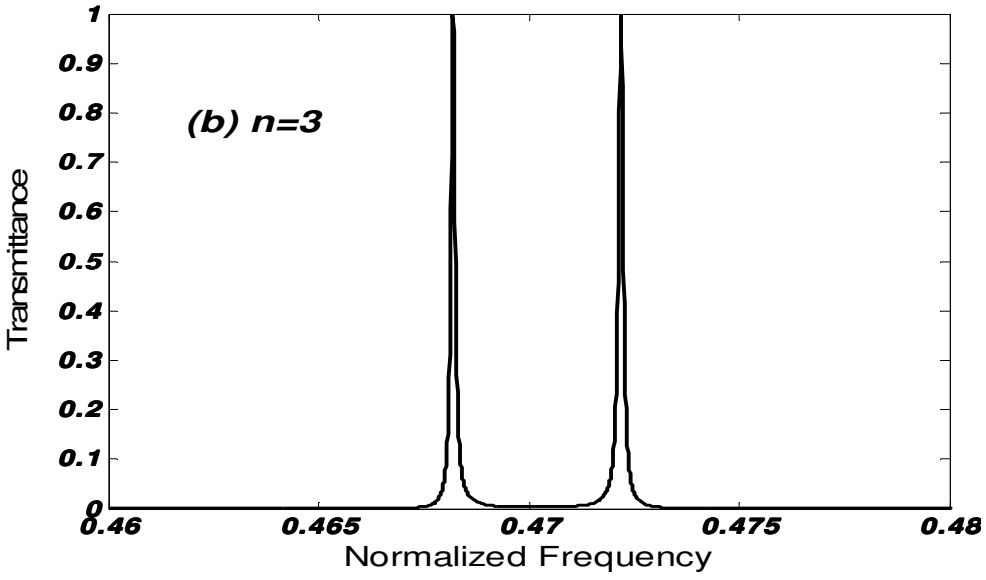
(b) n=3
Transmittance
Normalized Frequency
0
0.1
0.2
0.3
0.4
0.5
0.6
0.7
0.8
0.9
1
0.46
0.465
0.47
0.475
0.48

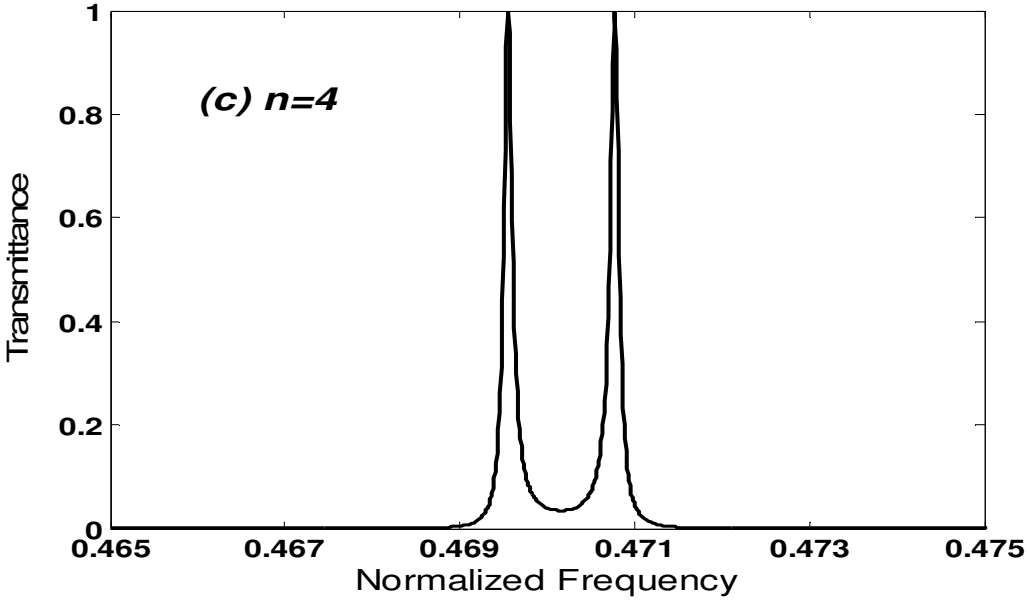
(c) n=4
Transmittance
Normalized Frequency
0
0.2
0.4
0.6
0.8
1
0.465
0.467
0.469
0.471
0.473
0.475

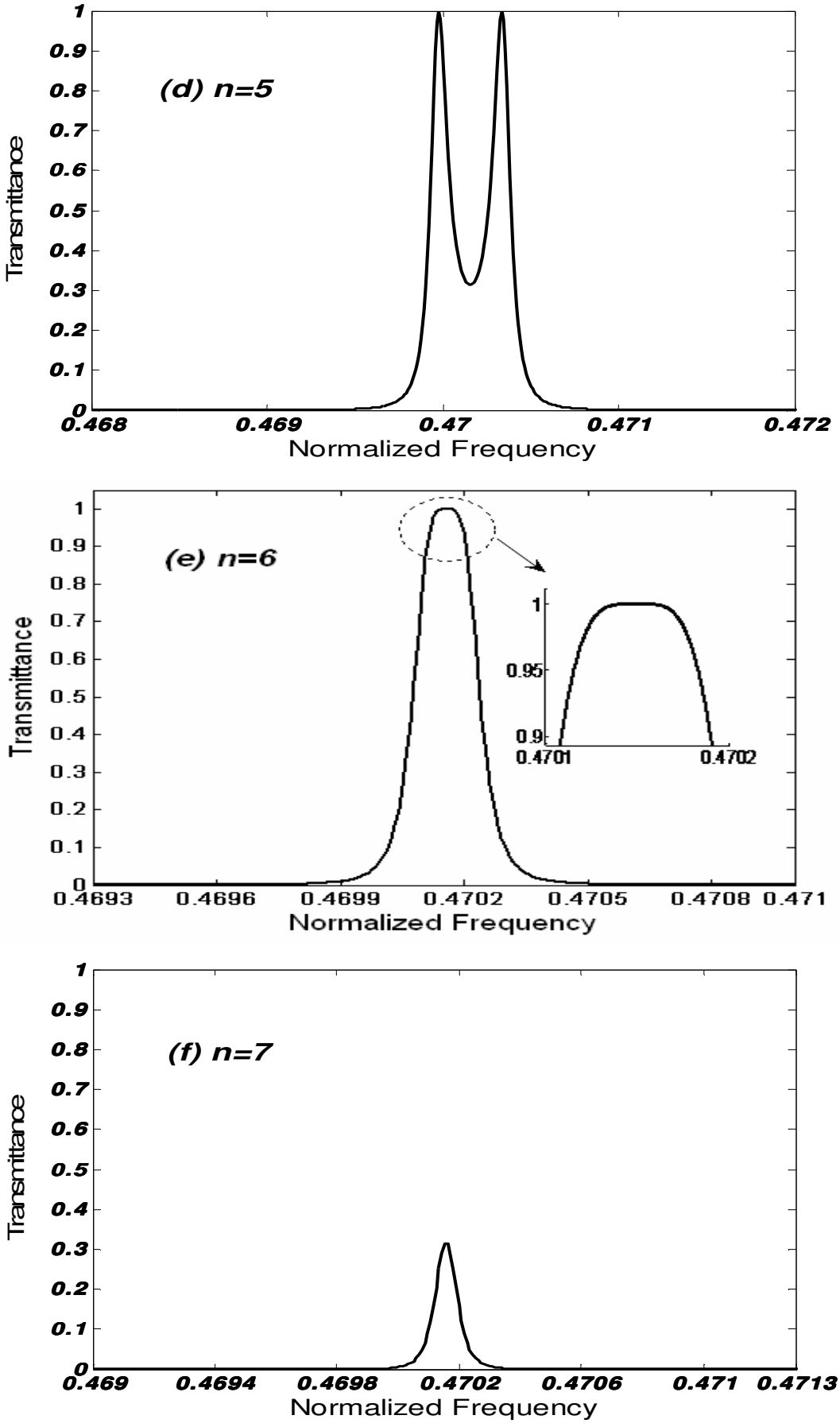

Fig.7.3 Transmittance versus normalized frequency (Λ_1/λ) spectra for two identical coupled microcavities with varying the number of Si layers, *n*, in the intermediate mirrors between the two microcavities. Notably in (*e*), a flat top pass band has been obtained as *n* equals 6.

7.2.2 Investigation of the Coupling Behaviour of Multi-cavities

It has been reported by Lan *et al* [Lan 2001(2)] that in the case of a finite chain of microcavities the spectral shape of the pass band depends on the number *N* of the coupled microcavites. Fig.7.4 shows the basic one-dimensional coupled cavity waveguide (CCW) structure with *N* coupled microcavities distributed with equal space in the structure while the defects are introduced by changing the thickness of the Si layers.

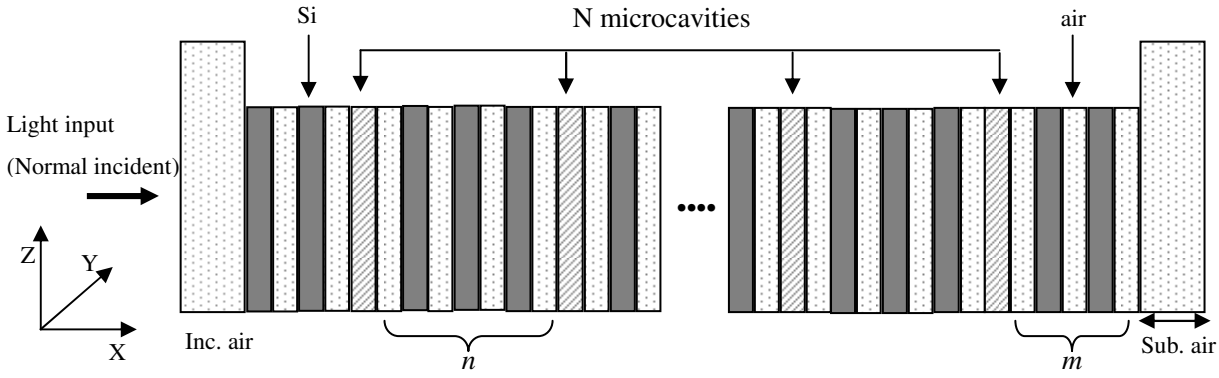

Fig.7.4 Schematic diagram of the coupled cavity waveguide, where *N* is the number of defects or microcavities, *n* is the number of Si layers in the inner PhC mirrors and *m* is the number of Si layers in the outer PhC mirrors, and *d* is the width of each layer, either Si or air.

Compared with the design of the single or multi transmission resonant structures, where the equal optical length condition, $n_A d_A = n_B d_B = n_X d_X / 2 = \lambda / 4$, was applied, the thicknesses of the high and low index layers are assumed to be equal in the CCW structures in this chapter, shown as in Fig.7.4; furthermore, the width of the defect is designed to be a portion of *d*, which was guided by the theoretical analysis from Lan *et al* [Lan 2001(2)].

To investigate the effects of the number of the outer and inner Si layers to the transmission spectra, a structure is constructed by choosing layer thickness to be 360nm, i.e. $d_{Si} = d_{air} = 360\,\text{nm}$, $\Lambda_1 = d_{Si} + d_{air} = 720\,\text{nm}$, and the defect layers are formed by the relation of $d_{defect} = 0 \bullet d_{Si}(d_{air})$.Based on the schematic and

parameter definitions shown in Fig.7.4, N is chosen to be 6 and n to be 3 and 4 in the inner Bragg mirrors with varying m to be 1, 2, 3, 4 in the outer ones, respectively. The simulation results are shown in Figs.7.5, 7.6 (*a-d*).

For m = 1, no quasi-flat transmission band can be seen, and surprisingly only four resonances appear in both transmission bands; which agrees with Lan *et al*'s work [Lan 2001(2)]; in their simulation, the same 1-D CCW structure with N = 10, n = 4, and m = 1 was calculated and eight resonances were observed, although in a general sense that six (ten in Lan's work) should be obtained. The reason for this unusual phenomenon is that under the situation of m = 1, the first and last cavities are much different from the others, they are asymmetric and the confinement is weak compared to those inner cavities, which means the coupling of these two cavities with the others is weak, therefore two resonant modes are missing and only four resonances are seen.

For m = 2, the expected six resonances appear in Fig.7.5(*b*), and a quasi-flat transmission band is obtained in Fig.7.6(*b*), with the condition $n = 2m$ has been satisfied.

For m = 3, six resonances can be seen in Figs 7.5(*c*) and 7.6(*c*), while the coupling strength between each resonance in Fig.7.5(*c*) is weaker than in Fig.7.6(*c*) owing to the smaller n values used in obtaining the data shown in Fig.7.5.

For m = 4, six individual resonances are revealed in both Figs 7.5(*d*) and 7.6(*d*); from the result and discussion of Fig.7.3 and the conclusion in Beggs *et al*s' work [Beggs 2004], it can be concluded that the splitting between each cavity is larger than the width of the cavity mode, i.e. in the strong coupling regime, so six separated Lorentzian peaks appear.

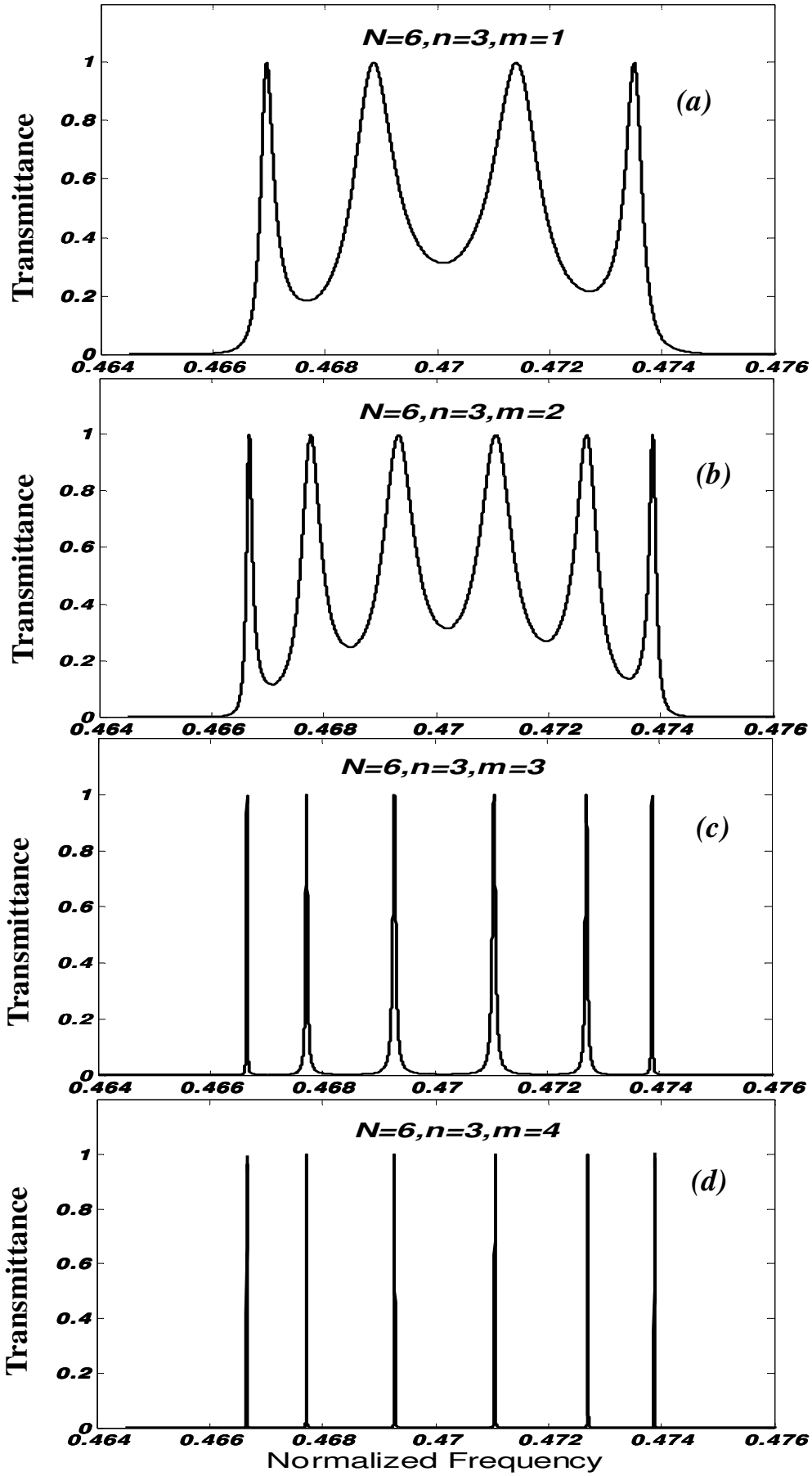

Fig.7.5 Transmittance versus normalized frequency (Λ_1/λ) spectra of 1-D CCWs with N=6, n=3 and m varies of 1, 2, 3, and 4, no quasi-flat pass band has been obtained for which n = 3 is an odd number.

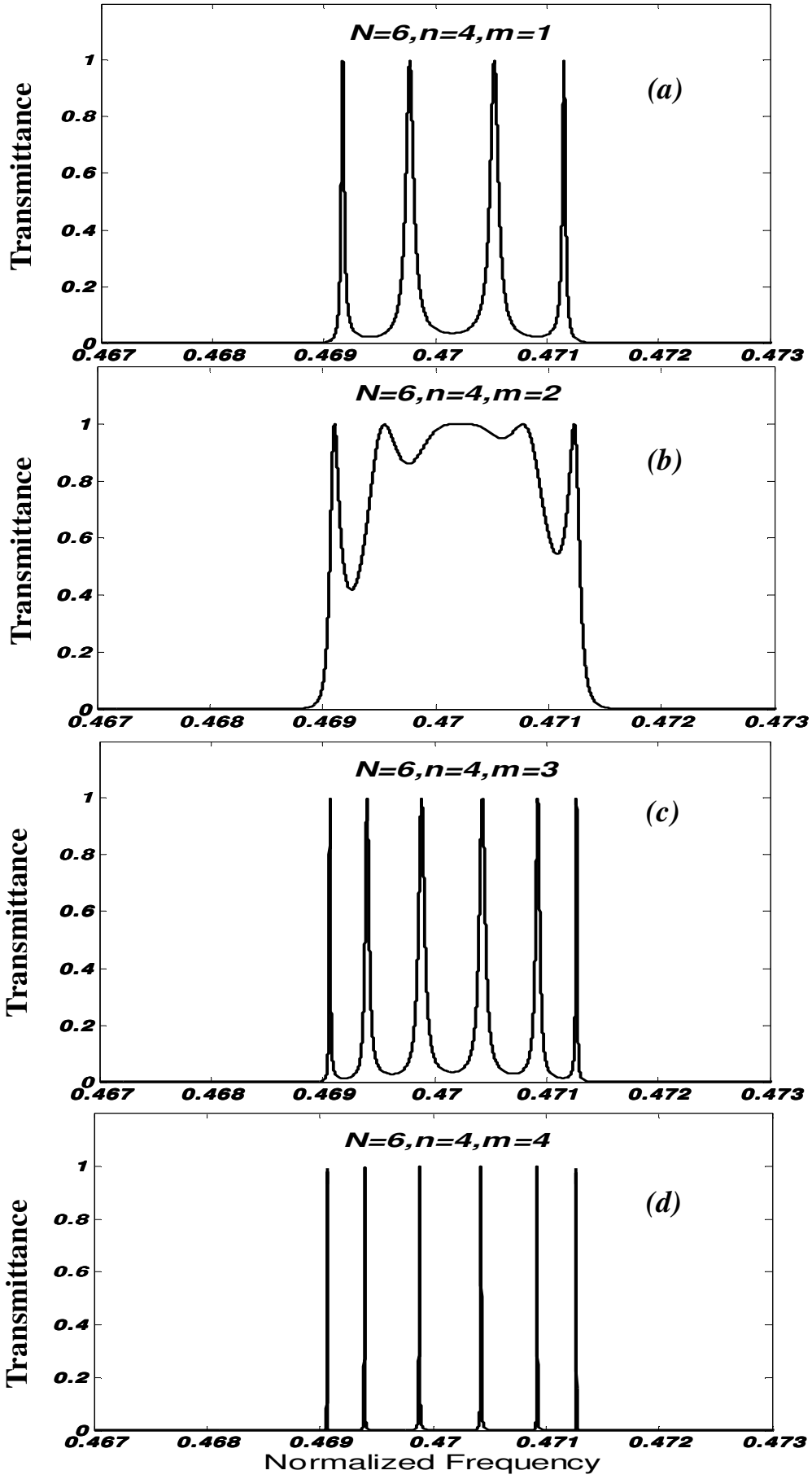

Fig.7.6 Transmittance versus normalized frequency (Λ_1/λ) spectra of 1-D CCWs with N=6, n=4 and m varies of 1, 2, 3, and 4, a quasi-flat pass band has been obtained in (*b*) when m=2, which satisfies the condition $n = 2m$.

From the above simulation results and the discussion in the work by Beggs *et al* and Lan *et al*, some conclusions can be made for the coupling behaviour of 1-D PhC coupled cavity structures based on the number of the mirror layers between cavities (indicated by *n* in this chapter) and the number of mirror layers on the two outer region (indicated by *m* in this chapter).

First, to obtain a quasi-flat transmission pass band, a condition of $n = 2m$ must be satisfied, this is due to the strict requirement of symmetry for the formation of the quasi-flat transmission pass band; the two very outer cavities cannot be equalized with the other inner ones if such a condition is not fulfilled. Second, unusual coupling behaviours have been observed, i.e. only four resonances appear in some of the structures although six were expected, this could possibly be explained by the weak confinement introduced by small value of *m*. Third, it can be observed from the simulation results that for the same *n* value, increasing *m* will lead to stronger contrast of the resonances and the linewidth of each resonance narrows significantly apart from the quasi-flat band situation, while for the same *m* value, increasing *n* will change the coupling strength between each cavity as previously demonstrated and discussed under the situation of the two cavities.

To investigate the influence of the number of the cavities to the structure, TMM simulations were carried out with the evolution of the number (*N*) of the coupled cavities based on the schematic shown in Fig.7.4, where the structure parameters are $d_{Si} = d_{air} = 360$ nm, which yields the thickness of a bilayer of $\Lambda_1 = d_{Si} + d_{air} = 720$ nm and the defect layers form by the relation of $d_{defect} = 0 \bullet d_{Si}(d_{air})$. Cavity numbers $N = 2, 4, 8$ with unchanged $n = 4$ and $m = 2$ are investigated, the obtained spectra are shown in Fig.7.7(*a-d*).

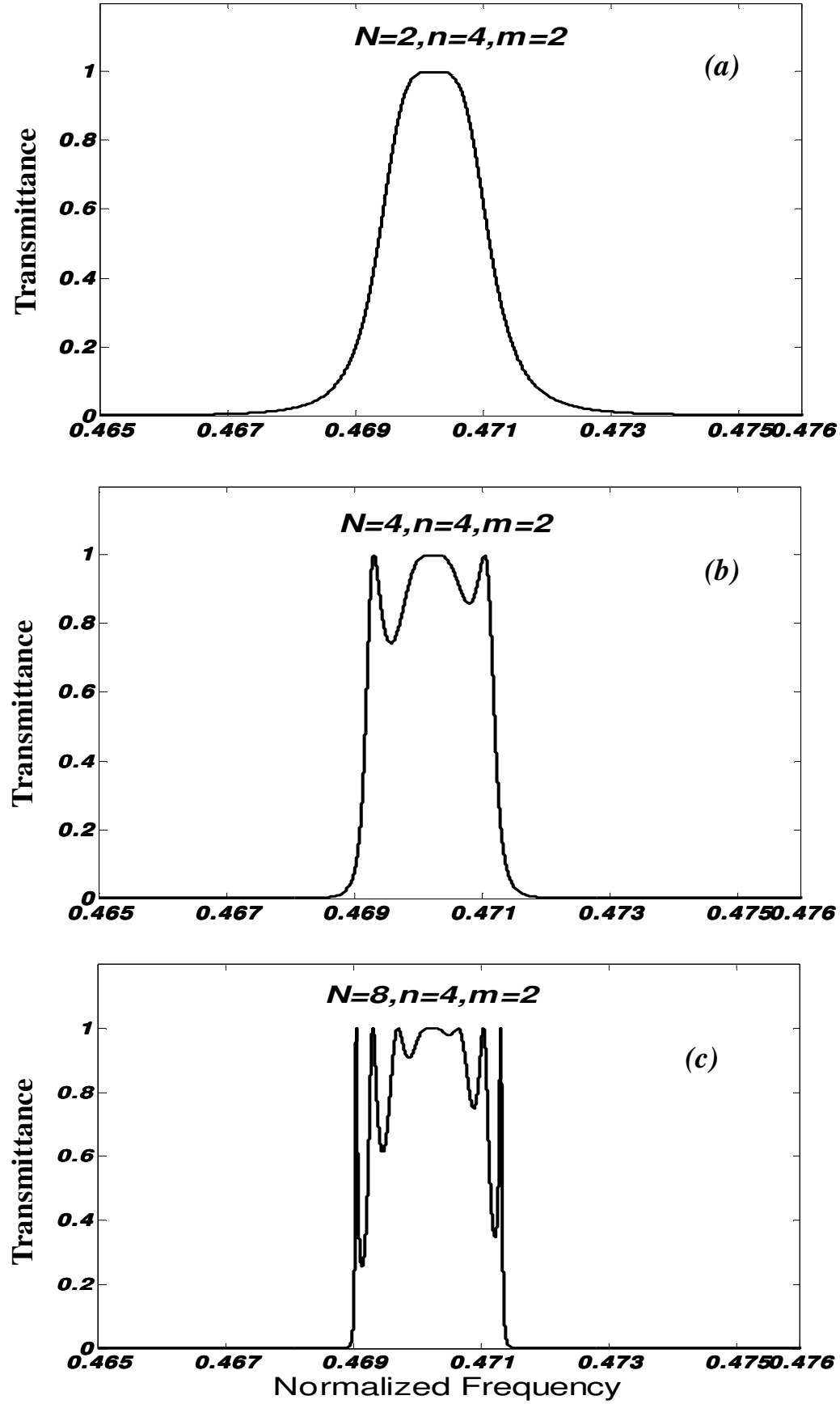

Fig.7.7 Transmittance versus normalized frequency (Λ_1/λ) spectra of 1-D CCWs with retaining n=4 and m=2 and N varies of 2, 4, and 8, quasi-flat transmission band appear in all the spectra, as the condition $n = 2m$ stands.

The simulation results obtained in Fig.7.7 agree with Beggs *et al*'s [Beggs 2004] work. Increasing *N* leads to the appearance of fringes within the transmission band, and the band edges become sharper and sharper as *N* values increase. To obtain a flat or quasi-flat top transmission band without fringes, or say a "clean" flat top, a two cavity structure is the ideal candidate, which can be proved by both Fig.7.3(*e*) and Fig.7.7(*b*).

In conclusion, from the simulation work in this chapter, the elements which govern the coupling behaviour of the 1-D PhC multi-cavity structure are the number of the inner and outer reflectors and the number of the coupled cavities. Most importantly, it has been revealed that to obtain a quasi-flat pass band a condition of $n = 2m$ must be satisfied, while once more than two cavities are introduced into the structure, fringes appear in the pass band, and the two coupled cavity structure has been found to be ideal for the proposed WDM requirement in this chapter.

7.3 Structure Definition for Fabrication

Based on the above theory and simulations, further work was carried out to optimize the design for the device to be fabricated. ITU DWDM Grid Specification [Bayspec.com] was used as reference, where the structure should satisfy the standard 100 GHz channel separation plus 50GHz offset with a central wavelength defined to be 1550.12nm (193.40 THz). A two coupled cavity structure has been chosen for fabrication; Fig. 7.8 shows the schematic layout of the structure. Fig. 7.9(*a-c*) shows the results of TMM simulations using the structure parameters in Table 7.1. It can be seen that the structure has a pass band width of ~0.5nm at a wavelength of 1550nm, thereby satisfying the ITU standard. The equivalent bandwidth is defined from the following equation

$$\Delta f = \frac{C}{\lambda^2}\Delta\lambda \tag{7.1}$$

Here C is the speed of light in vacuum. The obtained Δf is 62.39GHz while λ is

1550nm. Also, from the optimisation process for finding this ideal transmission peak, it can be concluded that the flat resonance is very sensitive to the width, the position and the refractive indices of each layer. Any small deviation could have a deleterious influence on the desired result.

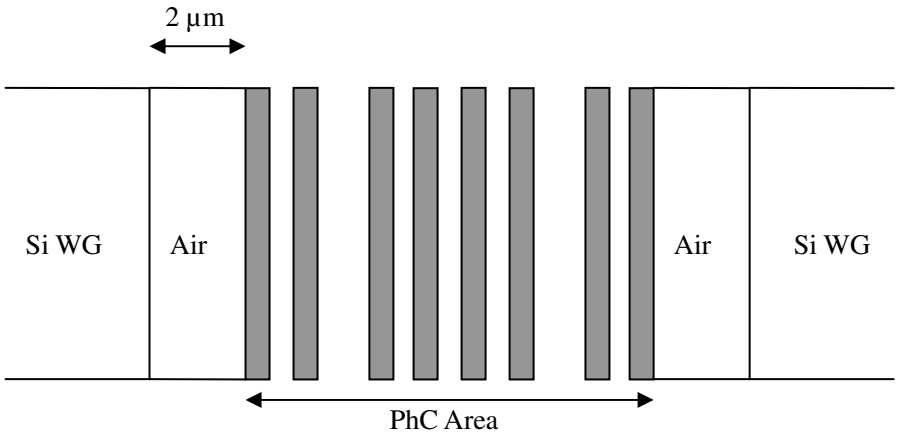

Fig.7.8 The defined structure for fabrication. Two air gaps of 2μm wide are incorporated on each side of the PhC area to achieve the symmetry requirement of the band pass structure.

Referring to the discussion in Section 7.2 and Fig.7.4, the parameters of the structure for fabrication are listed in Table 7.1.

n_{Si}	n_{air}	d_{Si}	d_{air}	d_{defect}	N	n	m
3.4	1.0	364.415nm	364.415nm	0• d_{Si}	2	4	2

Table 7.1 Specification of the optimized coupled microcavity structure.

Especially, as shown in Fig.7.8, when the defects were assigned to be air, once the light is launched from a Si waveguide and goes into another Si waveguide, the two outer Si reflector layers merge into the access waveguides, breaking the symmetry of the whole structure. The introduction of a 2μm wide air gap at the outer edges of the PhC area overcomes this problem and regains the symmetry for the whole coupled microcavity structure although at the cost of a likely reduction in transmittance owing to high loss in attempting to couple light across the 2μm wide air gaps.

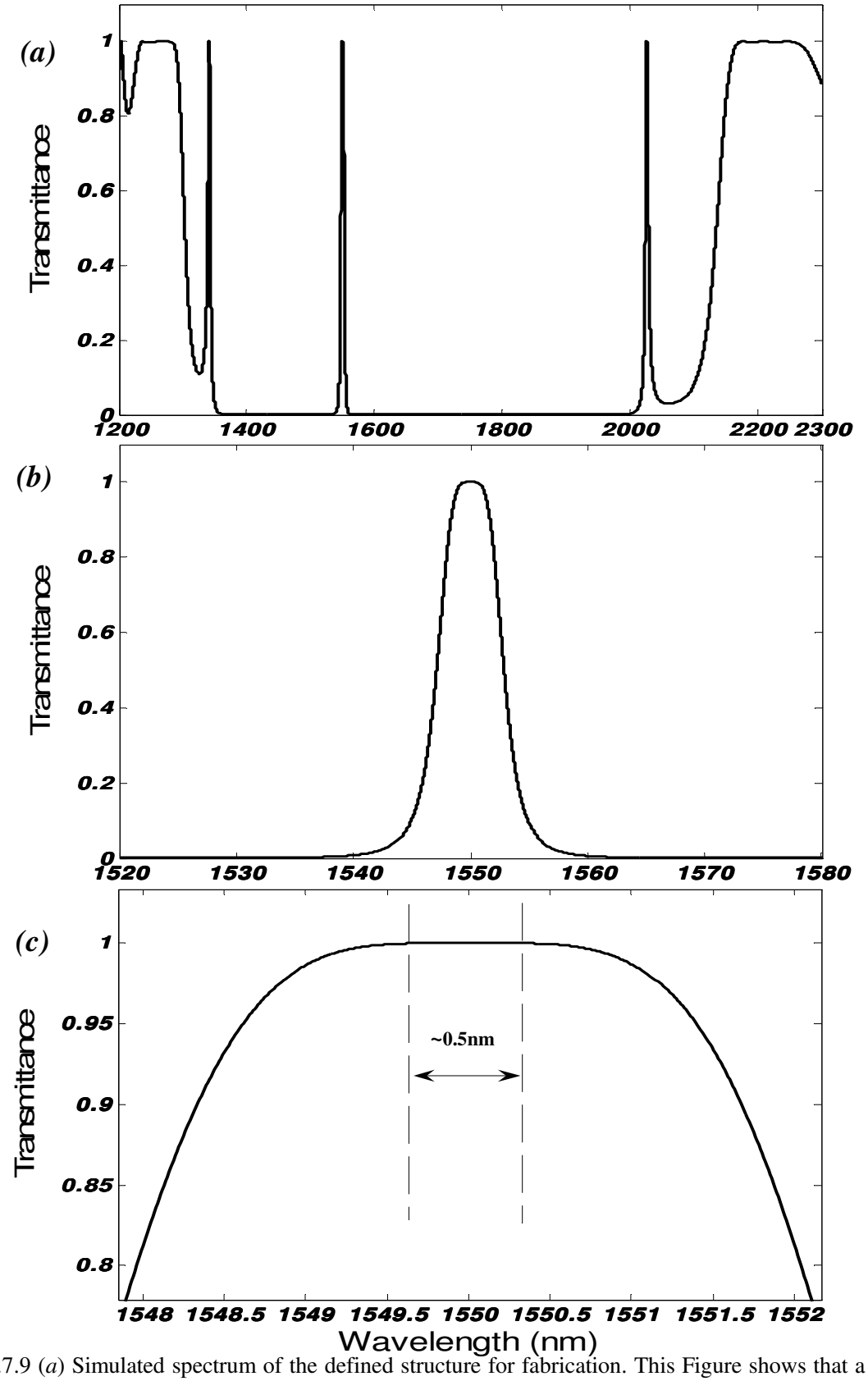

Fig.7.9 (*a*) Simulated spectrum of the defined structure for fabrication. This Figure shows that a resonance peak appears inside a clear band gap at a wavelength of 1550nm. (*b*) Whole spectrum of the pass band. (*c*) Enlarged view of the top of the resonance peak showing a quasi-flat transmission with width of ~0.5nm. For the central wavelength of 1550nm, the frequency expansion of this width is 62.39GHz, which satisfies the ITU DWDM standard,1550.12nm (193.40THz), 100GHz Grid + 50GHz offset [Bayspec.com].

7.4 Fabrication and Measurement of the 1-D Coupled Cavity PhC Integrated Waveguides

The coupled microcavity integrated waveguide was fabricated using the process described in Chapter 3. Its spectral response was measured using both the laser stepping method and the side-band measurement method.

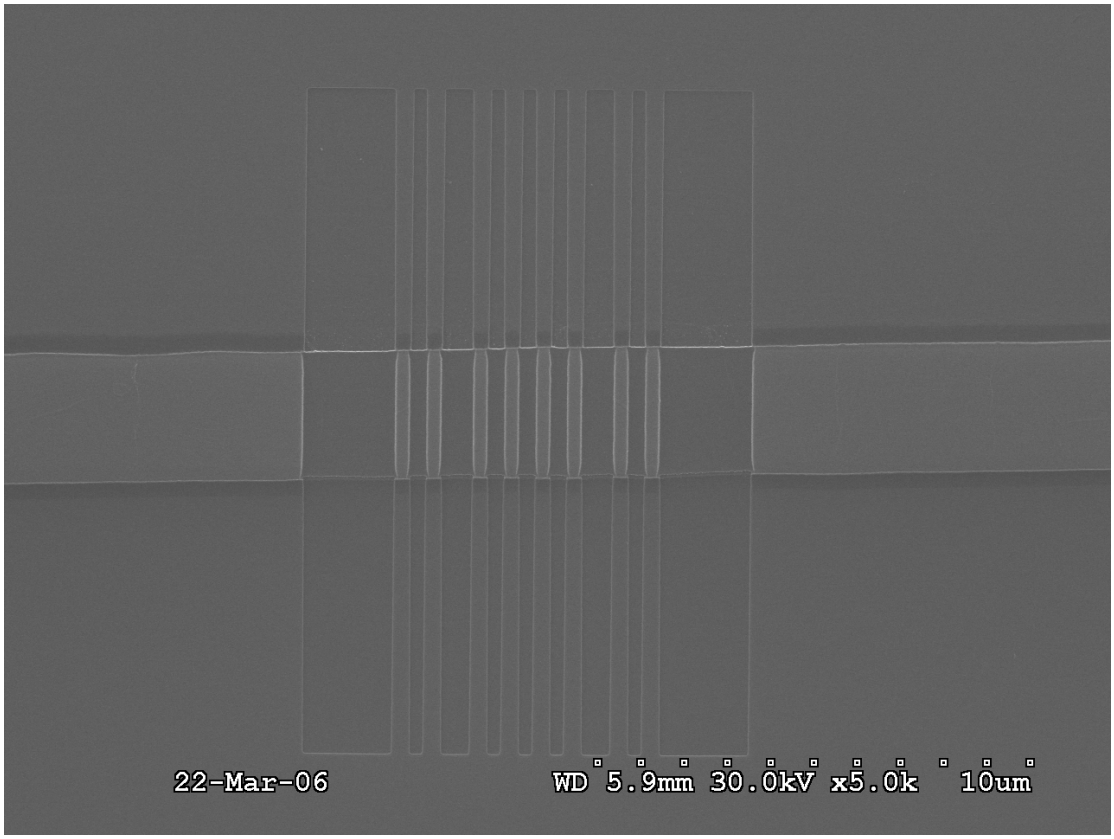

Fig. 7.10 SEM image of the fabricated passing-band structure under 5.0K magnification.

Fig. 7.10 shows an SEM image of the fabricated 1-D PhC coupled microcavity structure integrated Si waveguide. As can be clearly observed, both the edge of the waveguide and the PhC layers have smooth sidewalls. After measuring the dimensions of the fabricated structure, the width of the Si layers in the PhC are 330nm ±5nm, the air layer is 370nm ±5nm, and the defect layer is 760nm ±5nm. Based on these measured dimensions, the transmission spectra of the structure has been recalculated using the TMM method. Fig. 7.11(*a-c*) shows the results.

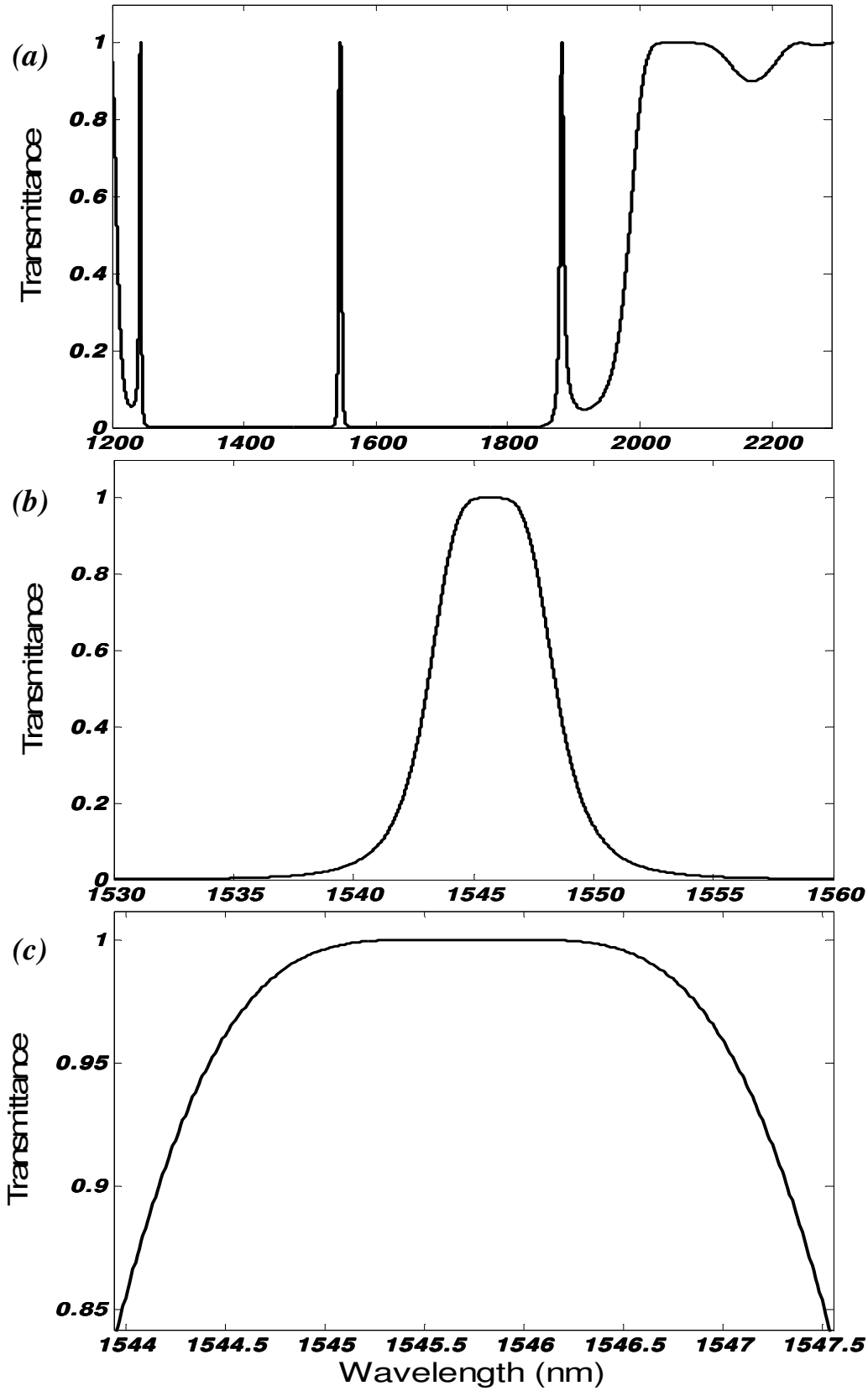

Fig.7.11 TMM simulated results based on the measured dimensions of the fabricated device. (*a*) the whole spectra of the transmission band, (b) Whole spectra of the pass band, (c) Enlarged view of the top of the of the pass band. Compared with the spectra in Fig.7.9, it can be seen that the shape of the spectra remains, but with the centre wavelength of the pass band is at about 1545.75nm, with a deviation of less than 5nm from design.

From the simulation results in Fig.7.11 (*a-c*), the shape of the pass band remains unchanged but with the centre wavelength shifted to be about 1545.75nm, which represents a deviation of only less than 5nm from the design, indicating that the pass band specification is unlikely to be compromised too severely by the fabrication tolerance, apart from a small deviation of the centre wavelength.

The transmission spectrum measured by stepping the tunable diode laser is shown in Fig.7.12. A pass band of spectral width of about 4nm centered on a wavelength of ~1540nm is observed. Fig.7.13 shows the top of the pass band measured by the side

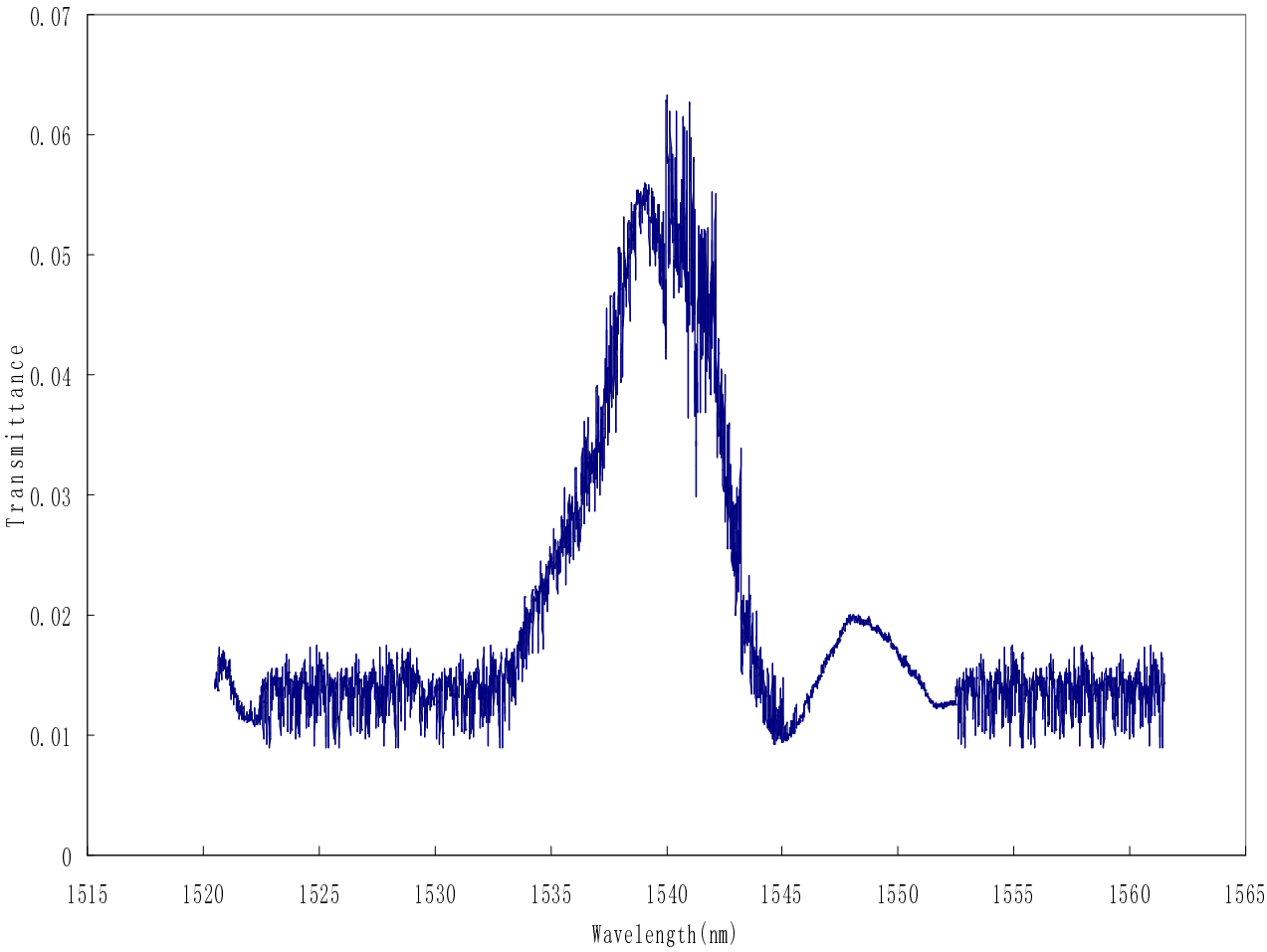

Fig.7.12 Measured Spectrum of the pass band PhC coupled microcavity structure

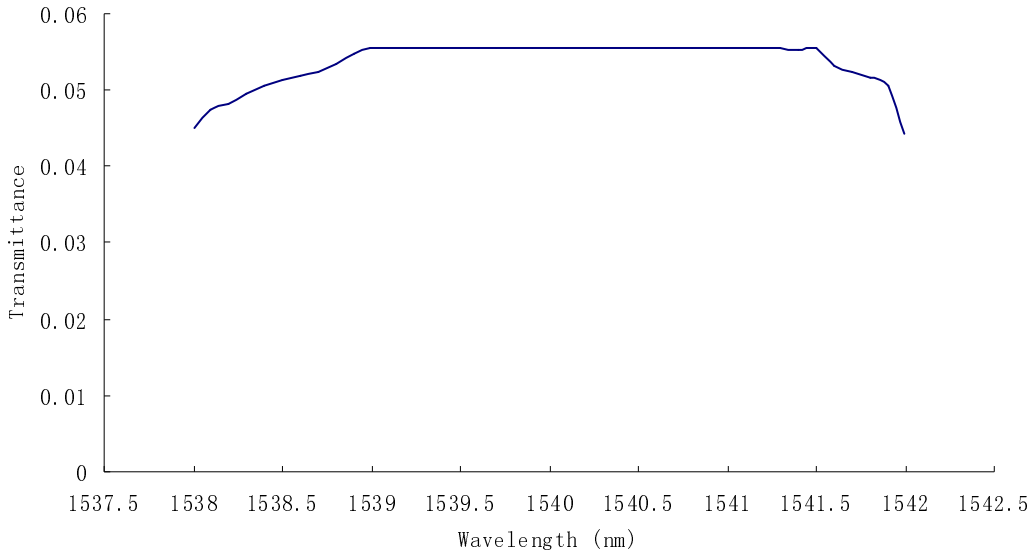

Fig.7.13 Transmission spectrum at the top of the pass band, measured by the side band method.

band method over a spectral range from 1538nm to 1542nm. The pass band is almost flat topped over a spectral range from 1539nm to 1541.5nm, with marked roll-off occurring at ~1538nm and 1542nm. The result in Fig.7.13 confirms the pass band is close to ~ 4nm. This is in reasonable agreement with the pass band of broadened resonance (Fig.7.9(*b*), Fig.7.11(*b*)) observed in the TMM simulations. The main discrepancy with simulation lies in the displacement of the measured central wavelength (λ_{Cmeas} = 1540nm) of the real device and the predicted values in Fig.7.9 for the optimum design (λ_{Coptim} = 1550nm), and in Fig.7.11 for the simulations based on the measured device dimensions ($\lambda_{Cpractical}$ = 1545.75nm). The cause of the discrepancy is likely to be the limited validity of the TMM and the dimension deviations of each reflector layer of the coupled microcavity from fabrication, since the central wavelength is very sensitive to the width of each reflector. However, a deviation of only less than 6nm between the measured spectra and the TMM calculation, based on practical dimensions, indicates a high fabrication accuracy and also the promising viability of transferring the 1-D coupled cavity PhC structure from stacks to integrated waveguides, which promotes the practical application of such a structure in future highly integrated optical circuits for DWDM system. The large 2μm air gaps between the access waveguides and the Bragg reflectors are likely to give rise to far greater mode spreading between the two sections of the structure

than that which occurs with narrower air gaps, causing low transmittance, as observed. The basis of this is shown in Fig.7.14.

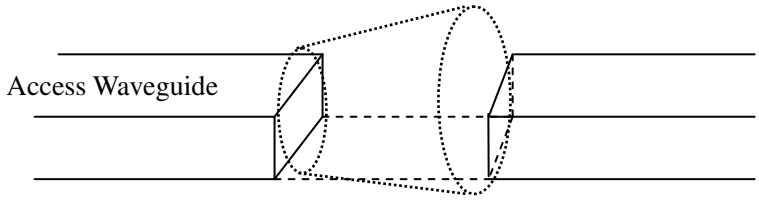

Fig.7.14 Schematic diagram of the mode profile expansion across air gap between sections of waveguides.

As light radiates from the aperture of the access guide, it spreads out in a cone in which the vertical and horizontal angles of the diverging beam made with the direction of propagation differ. This occurs as a result of the greater width of the waveguide ridge compared to its height, an effect well-known in diode lasers [Yariv 1989]. This is likely to be the case in the 2μm wide air gaps between the two sides of the PhC area, resulting in significant radiation loss in coupling light to and from the access waveguides.

The 4nm width of the measured pass band can be compared with the 7nm band width reported by Jugessur *et al* [Jugessur 2004] for a 1-D PhC coupled cavity filter centred on a wavelength of 820nm, and the absence of a clearly defined narrow pass band in the structures designed for 1550nm wavelength operation reported by these same authors. Also it can be claimed that the result obtained in this chapter in terms of narrowness and flatness of the pass band probably advances the state-of-the-art in accelerating the development of coupled cavity structures towards real applications compared to the work reported in journals. Whilst the measured width of the pass band, at ~4nm, exceeds the target of 0.5nm for application in WDM optical networks operating at 100GHz + 50GHz offset channel spacing, the predicted narrow band behaviour is observed, seemingly for the first time in the technologically important 1550nm wavelength range in SOI based microcavity devices.

7.5 Conclusions

The design, simulation, fabrication and characterization of a coupled 1-D PhC microcavity waveguide filter are described in this chapter. The practical needs for operation in a WDM system inspired the design of the filter. The implemented device was shown to have the quasi-flat transmission peak required for WDM, whilst the measured pass band at 4nm is a step closer to meeting the requirements of the ITU wavelength grid. Basic theoretical consideration and TMM simulations of coupled microcavities resulted in a simple design that was straightforwardly implemented using the fabrication technology developed in this thesis. Reasonable agreement between the width of the measured pass band and that found by the TMM was obtained and explained. Agreement between the measured and simulated centre wavelengths of the pass bands was not so good, but the discrepancy (~10nm) was sufficiently small not to undermine the use of the TMM for the initial design stage of narrow, flat top pass band structures. With the ITU grid, placement of the centre wavelengths needs to be exact for WDM applications. Therefore, the design of fully engineered WDM coupled cavity waveguides will require exact modeling.

It can be concluded from this work that the crucial elements in achieving a flat narrow pass band at a specific centre wavelength are the width and refractive indices of the mirror layers; the number, position, width, refractive index of the defect layers and also the symmetry of the whole structure. After careful design and simulation work, a flat top pass band with expected width and position can be obtained. It is expected that such filters fabricated in SOI could contribute to progress in both DWDM technology and photonic integration.

Chapter 8. Conclusions and Future work

Based on the fundamental understanding of the theory of photonic crystals (PhCs) and the numerical and experimental progress in this area, the work in this thesis focuses on detailed experimental investigations of PhC structures for light filtering applications. The primary goal of the project is to improve the performances of optical filters based on 1-D PhC structures. The realization of multi-transmission of the broadly used 1310 and 1550nm wavelength filter, taper implemented microcavity structures to boost up the quality factor and transmission and flat top pass band filters can be presented as the new findings of this PhD project.

8.1 Conclusions

Chapter 1 reviewed the history and development of PhCs and gave the definition of a PhC as periodically structured electromagnetic media, generally possessing photonic band gaps. Photonic band gaps are defined as ranges of frequency in which light cannot propagate through the structure. Owing to their property of controlling light transmission, PhCs are expected to have wide possibilities for application in optics and photonics. The concept of a defect in a PhC was introduced and the properties of defects reviewed. Until now, PhC structures have been broadly investigated as a means of improving the performance of optical waveguides and for creating optical microcavities. So called photonic crystal fibres are, to date, the most successful application of PhCs. As both the theoretical understanding and practical capability are expanding, it is reasonable to expect that PhCs will play a significant role in the

future optical and photonic area.

Chapter 2 dealt with the design and simulation of the 1-D PhC dielectric stacks, to create a theoretical and numerical foundation for the fabrication work described in the following chapters. For structures without defects, good agreement has been obtained between the Kronig-Penny model and TMM; for the defects introduced quarter-wave stacks, resonant peaks have been observed at 1550nm in the band gap of all the structures with different parameters.

Chapter 3 described the fabrication process. Starting from a raw silicon-on-insulator (SOI) chip, conventional photolithography and dry etching were carried out for creating the ridge waveguides. For both alignment of finding the positions of the PhC patterns and the writing field, the deposition of markers are necessary. These were formed by photolithography again with a special marker mask and thermal evaporation of Ti and Au. When the waveguides and markers are created on the sample, it is ready for forming the PhCs. Electron beam lithography (EBL) played a critical role in the whole fabrication process. With the aid of the E-Beam resist PMMA, the definition of the process could achieve feature resolution down to less than a hundred nano-meters with a deviation of about 20-30nm. During the development of the fabrication process, much work was done on optimising the parameters that could affect the dimensions of the critical device features, such as dose of the electron beam, the exposure time, the developing time and even the temperature of the PMMA. Systematic trials revealed the right combination of the parameters to create various types of PhC structures. The PhC patterns in the PMMA could then be transferred to the Si by ICP etching. After thinning and cleaving of the starting chip, the samples are ready for measurement.

Chapter 4 described the methods for characterising the PhC structures, notably their effect on light transmission. A special test bed composed of a computer controlled laser source and multi-meter, NanoMax TS 3-axis flexure stages and an optical

microscope were set up. The butt coupling method was used for light launching and collecting. With fine adjustment of the nano-flexure-stages, good alignment was achieved. The laser could then be stepped via GPIB control and the transmitted power recorded for each wavelength. The obtained transmission spectrum agreed closely with the simulation work. Also in this chapter, a novel method for accurately measuring the pass band of high Q microcavities was reported, based on using the sidebands of an AM optical signal as a tunable probe of the filter response. A 27% improvement in accuracy was achieved.

Chapter 5 presented the fabrication and characterisation of a multi-transmission optical filter based on a 1-D PhC and a new wave-vector method was proposed for predicting the resonance wavelengths. As the structure was created by replacing the homogeneous cavity layer with a multi-layered cavity, multi-wavelength transmission can be obtained. Progressive and detailed TMM simulations to find out the structure parameters for 1310 and 1550nm transmission were executed, and fabrication work was done based on the information from such simulations. Normalized frequencies of the resonant wavelengths were used as criterion to judge the agreement between TMM simulation and fabrication, TMM simulation and wave-vector approach and wave-vector approach and fabrication; reasonable agreement has been obtained in the first set and good agreement in the latter two sets, which demonstrate the validity of applying TMM and the wave vector approach to the design of multi-wavelength transmission PhC microcavities.

Chapter 6 focused on a systematic experimental investigation of the tapering effects on one-dimensional photonic crystal microcavity structures. The tapers, which were inserted between the Si access ridge waveguides and PhC waveguide or around the cavity, were observed to have an impact on the microcavity performances. Both the quality factor and transmittance were improved. This practical work proved the theoretical assumptions and numerical calculations described in the literature. It seems reasonable to expect that the progressive adaption of the geometries will play

a significant role in the future application of integrated PhC optical circuits.

Chapter 7 described the work of design, simulation, fabrication and characterisation of coupled cavity photonic crystal waveguides (CCW). The practical needs of 1550nm wavelength DWDM systems inspired the design of the CCW structure, which could provide a quasi-flat transmission top in the resonance peak. In this chapter, basic theoretical investigations and TMM simulations of the performance of CCWs have been described. The fabrication and measurement were based on a design of a simple and effective structure and good agreement between calculation and fabrication was achieved. It can be concluded from this work that in order to obtain a flat, narrow pass band at a specific central wavelength, the crucial elements are the width and refractive index of the mirror layer, the number, position, width, refractive index of the defects layer, and, also, the symmetry of the whole structure.

In summary, various types of 1-D PhC structures were fabricated and tested. Reasonably good agreement between TMM simulation and experiments weas obtained, a new measurement method developed and theoretical explanations of the observed practical results proposed.

8.2 Future Work

The author has been immersed in practical research into photonic crystals and the nano-fabrication area for nearly three years, and wishes to propose new research topics based on the work reported in this thesis.

From the work of realization of the multi-transmission filter and the pass band filter, it can be expected that a investigation of the combination of these two structures, i.e. a multi-channel pass band filter, will indeed push the application of 1-D PhC integrated Si waveguides towards real WDM system.

As it can be concluded that inserting tapers into 1-D PhC integrated waveguides will not only improve transmittances but also boost up the quality factors of the microcavities, such a method can be applied to enhance the performances of the microcavities which can be fabricated in such a way.

Generally speaking, investigation in the area of photonic crystals is expanding and a great number of research results have appeared in the last two decades, although the most successful practical application of PhCs is only photonic crystal fibres, much work still focuses on improving the property performance of PhCs; however, the author does believe that PhCs will thrive in the future optics and photonics owing to their unique properties of controlling light transmission. To achieve this target, from a fabricator's point of view, the control of fabrication accuracy plays a vital role, nowadays a process deviation of about 20-30nm represents the frontier of the fabrication facilities, but it can be expected that the forthcoming new methods or technologies will reduce such deviation to be a few nano-meters and finally bring PhCs from labs to factories.

Appendix 1

Transfer Matrix Method for the Structure Calculations

Electromagnetic Treatment

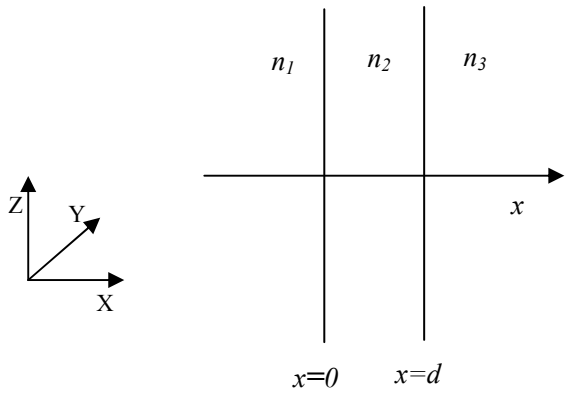

Fig.A.1 A thin homogeneous layer of dielectric material.

Referring to Fig.2.1, consider the reflection and transmission of electromagnetic waves at a thin dielectric layer between two semi-infinite media. It is assumed that all the media are homogeneous and isotropic, so that the whole structure can be described by

$$n(x) = \begin{cases} n_1, x < 0 \\ n_2, 0 < x < d \\ n_3, d < x \end{cases} \quad \text{A.1}$$

If it is also assumed that the plane of incidence is the *xz* plane, the electric field vector of a general plane-wave solution of the wave equation takes the form

$$E(x)\exp[i(\omega t - \beta z)] \quad \text{A.2}$$

since the medium is homogeneous in the *z* direction.

The parameter β is the *z* component of the propagation wave vector. Since the field vectors must satisfy the boundary conditions at the interfaces, β must have

the same value in all the layers so that similar to the case of a single interface, Snell's law is obeyed at each interface. With reference to Fig. 2.1, it is assumed that a plane wave is incident from the left, and the electric field vector *E(x)* can be written as

$$E(x)=\begin{cases} Ae^{-ik_{1x}x}+Be^{ik_{1x}x}, & x<0 \\ Ce^{-ik_{2x}x}+De^{ik_{2x}x}, & 0<x<d \\ Fe^{-ik_{3x}(x-d)}, & d<x \end{cases} \qquad \text{A.3}$$

where it is assumed that the electric field vector is *s* polarized (i.e., perpendicular to the plane of incidence). The complex amplitudes *A, B, C, D*, and *F* are constants, and k_{1x}, k_{2x}, and k_{3x} are the *x* components of the wave vectors:

$$k_{ix}=[(\frac{n_i\omega}{c})^2-\beta^2]^{1/2}=(\frac{\omega}{c})n_i\cos\theta_i, i=1,2,3 \qquad \text{A.4}$$

where θ_i is the ray angle measured from the *x* axis. The constant *A* is the amplitude of the incident wave. The constants *B* and *F* are amplitudes of the reflected and transmitted waves, respectively.

The boundary conditions on the tangential components of the electric, *E*, and magnetic, *H*, field vectors require that E_y, E_z, H_y, and H_z must be continuous at the interfaces *x=0* and *x=d*. Using these boundary conditions, it is possible to obtain the amplitudes *C, D, B*, and F in terms of *A*. In applying these boundary conditions, one must consider the *s*(TE) wave and the *p*(TM) wave separately. These two components of the electromagnetic wave are independent of each other. There is no coupling between these two components through the medium since every part of the medium is isotropic and homogeneous.

For the case of the *s* wave, the boundary conditions require that E_y and H_z be continuous at the interface. The electric field *E(x)* is *yE(x),* with *E(x)* given by Eq.(1.3). The *z* component of the magnetic field is obtained by using $H_z=(i/\omega\mu)(\partial E/\partial x)$ and is given by

$$H_z(x)=\begin{cases}\dfrac{k_{1x}}{\omega\mu}(Ae^{-ik_{1x}x}-Be^{ik_{1x}x}), x<0\\ \dfrac{k_{2x}}{\omega\mu}(Ce^{-ik_{2x}x}-De^{ik_{2x}x}), 0<x<d,\\ \dfrac{k_{3x}}{\omega\mu}Fe^{-ik_{3x}(x-d)}, d<x,\end{cases} \quad \text{A.5}$$

where μ is the magnetic permeability constant.

Imposing the continuity of E_y and H_z at the interfaces $x=0$ and $x=d$ leads to

$$A+B=C+D \quad \text{A.6}$$

$$k_{1x}(A-B)=k_{2x}(C-D), \quad \text{A.7}$$

$$Ce^{-ik_{2x}d}+De^{ik_{2x}d}=F \quad \text{A.8}$$

$$k_{2x}(Ce^{-ik_{2x}d}-De^{ik_{2x}d})=k_{3x}F \quad \text{A.9}$$

These four equations can be used to solve for *B, C, D,* and *F* in terms of *A*. After a few steps of algebraic manipulation, the following result is obtained

$$F=A\frac{4k_{1x}k_{2x}e^{-ik_{2x}d}}{(k_{1x}+k_{2x})(k_{2x}+k_{3x})+(k_{1x}-k_{2x})(k_{2x}-k_{3x})e^{-2ik_{2x}d}} \quad \text{A.10}$$

and

$$B=A\frac{(k_{1x}-k_{2x})(k_{2x}+k_{3x})+(k_{1x}+k_{2x})(k_{2x}-k_{3x})e^{-2ik_{2x}d}}{(k_{1x}+k_{2x})(k_{2x}+k_{3x})+(k_{1x}-k_{2x})(k_{2x}-k_{3x})e^{-2ik_{2x}d}} \quad \text{A.11}$$

Here *C* and *D* can be written in terms of *F* as

$$C=\frac{1}{2}F(1+\frac{k_{3x}}{k_{2x}})e^{ik_{2x}d} \quad \text{A.12}$$

and

$$D = \frac{1}{2} F(1 - \frac{k_{3x}}{k_{2x}}) e^{-ik_{2x}d}, \quad \text{A.13}$$

respectively.

Recalling that $k_{ix} = (\omega / c) n_i \cos\theta_i$ [see Eq(A.4)], one can write the Fresnel reflection and transmission coefficients of the dielectric interfaces for *s* waves as

$$r_{12} = \frac{k_{1x} - k_{2x}}{k_{1x} + k_{2x}}, \quad \text{A.14}$$

$$r_{23} = \frac{k_{2x} - k_{3x}}{k_{2x} + k_{3x}}, \quad \text{A.15}$$

and

$$t_{12} = \frac{2k_{1x}}{k_{1x} + k_{2x}}, \quad \text{A.16}$$

$$t_{23} = \frac{2k_{2x}}{k_{2x} + k_{3x}} \quad \text{A.17}$$

respectively. Using these formulas, the transmission and reflection coefficients can be written as

$$t \equiv \frac{F}{A} = \frac{t_{12} t_{23} e^{-i\phi}}{1 + r_{12} r_{23} e^{-2i\phi}} \quad \text{A.18}$$

and

$$r \equiv \frac{B}{A} = \frac{r_{12} + r_{23} e^{-2i\phi}}{1 + r_{12} r_{23} e^{-2i\phi}}, \quad \text{A.19}$$

respectively. The parameter ϕ in the above equations is given by

$$\phi = k_{2x} d = \frac{2\pi d}{\lambda} n_2 \cos\theta_2 \quad \text{A.20}$$

and is proportional to the thickness *d* and index n_2 of the layer.

Transmittance, Reflectance, and Absorptance

Reflectance is defined as the fraction of energy reflected from the dielectric structure and is given by

$$R = |r|^2. \tag{A.21}$$

Reflectance is meaningful only when medium 1 is nonabsorbing. In addition, if medium 3 is also nonabsorbing, transmittance is given by

$$T = \frac{n_3 \cos\theta_3}{n_1 \cos\theta_1} |t|^2 \tag{A.22}$$

where the factor $n_3 \cos\theta_3 / n_1 \cos\theta_1$ corrects for the difference in phase velocity. Both formulae can be used regardless of whether the layer is absorbing. Absorptance, which is defined as the fraction of energy dissipated, is given by

$$A = 1 - R - T. \tag{A.23}$$

For dielectric structures with real n_1, n_2, and n_3, it can be shown using the expressions for r and t that $R + T = 1$, which agrees with the conservation of energy.

Appendix 2

Special Electron Beam Lithography Skills Developed in this Project

As electron beam lithography (EBL) plays a vital role in the whole fabrication process of this project, and also is the steepest and most important technique in nano-fabrications, the author would like to share his experiences obtained from the three years' PhD working with EBL, or so called "special skills" as stated in the above title, in order to benefit future users.

1. Alignment

Alignment can be realized as a preliminary and crucial step in the EBL operation, which can be divided into two stages: Field Alignment and Writing-field Alignment.

1.1 Field Alignment

Field alignment calibrates the positions of every single point on the sample surface and sets up an independent coordinate for the following operations. The initial coordinates are the stage coordinates *x*-*y*, which describe the physical positions of the sample carrier and do not give any information regarding the position on the sample. The filed alignment is therefore to set up a second coordinate system *u*-*v*, which is sample related, and also to find the relation between *x*-*y* and *u*-*v* with respect to shift, scaling and rotation, in order to perform a permanent coordinate transformation between the two systems. Referring to Figs.3.3 and 3.5 in Chapter 3, the logic of field alignment can be explained by the schematic layout in Fig.A.2.

The yellow squares in Fig.A.2 indicate the gold markers which were used for the alignment, shown by SEM image by Fig.3.3. To set up a *u*-*v* coordinate, which is independent from the physical *x*-*y* coordinate, three markers were chosen, with marker *a* being the very bottom gold square of the very left column in the marker area, and *b* being the very top one of the very left column, finally *c* is the one in the

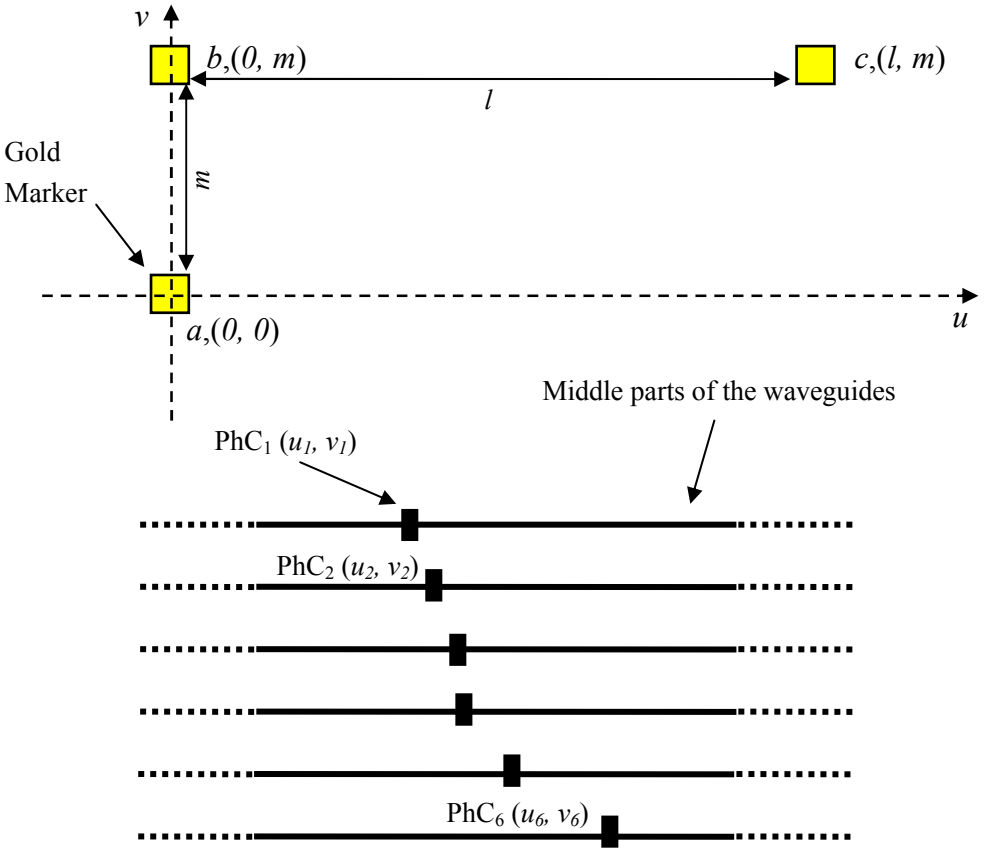

Fig.A.2 Layout shown of the field alignment logic

very middle of the top row and on the same line as *b*, the distances between *a* and *b*--*m*, *b* and *c*--*l*, are physically defined by the mask used to create the markers and will never change.

After the Si ridge waveguides and the marker area have been created, the SOI wafer is ready for the preliminary alignment. The wafer is sent into the EBL machine chamber without coating PMMA for the first time, after adjusting the focus and ensuring that a good image of the wafer surface is showing, the three markers described above *a*, *b*, and *c* are picked up and at the same time a *u*-*v*

coordinate value is assigned to each of them, which are *a(0, 0)*, *b(0, m)* and *c(l, m)*, respectively, now a *u-v* coordinate system has been set up. So that the positions where the PhC pattern will be generated (shown by black dots in Fig.A.2) on the waveguides will have their *u-v* coordinate values, it is necessary to record these six coordinate data for using in the next step; once these six values are read and recorded, the wafer can be taken out for further processing.

The wafer re-entered the chamber for formal exposure to generate the PhC patterns after PMMA coating, and this time the same three markers need to be selected and an identical *u-v* coordinate is built in the way described above. The E-beam gun needs to be switched off at this stage, for in EBL operations viewing an area means exposing it by electron beam, and a formal exposure must be executed without viewing that part of PMMA at all, this actually forms the necessity of such an alignment procedure. As the six position values for the PhC patterns have been obtained, enter the values one by one to drive the sample to the wanted positions under the E-beam gun to expose the PMMA resist for the pattern formation.

1.2 Writing-field Alignment

Writing-field alignment calibrates the dimensions of the writing-field which is used to create the PhC patterns; this is a very crucial operation to obtain nano-structures with accurate features.

The logic of writing-field alignment is schematically shown in Fig.A.3, while Fig.3.4 in Chapter 3 shows a real gold marker used for writing-field alignment. The marker was made to be a $16\times16\mu m^2$ square, by adjusting the middle point of it to be (*0, 0*) the three relative corners will have the coordinates (*-8, -8*), (*-8, 8*) and (*8, 8*), shown in Fig.A.3, and ideally they should be the very exact points of the corners; however, in practice, finding these three very exact points and assigning

them the coordinate values stimulate the process of writing-field alignment.

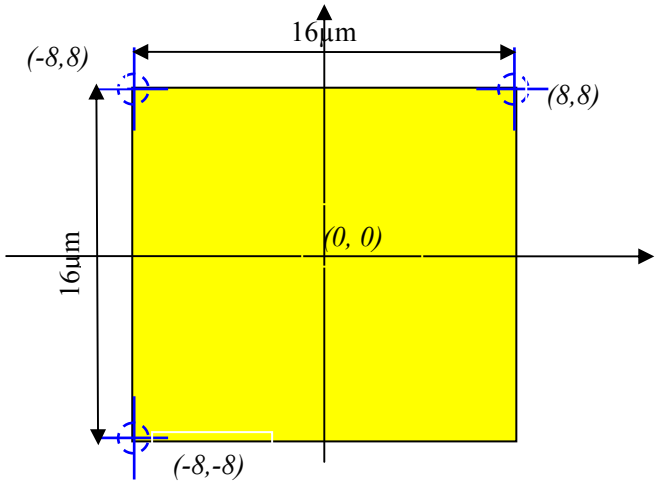

Fig.A.3 Layout shown of the writing-field alignment logic

The writing-field alignment is actually an iterative process to place the crosshairs, shown in Fig.A.3, into the very corner points of the marker; the writing-field is calibrated by doing this and the logic can be understood as the fitting of a virtual 16μm with a real 16μm.

2. Creating very fine nano-structures

Apart from the fabrication process described in Chapter 3 and the method of obtaining very small features described in Chapter 6, the author also would like to share his experiences of fabricating very fine nano-structures which were not mentioned in the above contents, or were too trivial to mention.

2.1 PMMA temperature

Normally PMMA is kept in a fridge at about 5°C for longer shelf life, and it has been revealed that using of cold PMMA has a negative influence on the feature formations after exposure and develop. As cold PMMA is stickier than that at room temperature, spin coating of such PMMA will make uneven layer thickness, and more importantly, in the subsequent pre-exposure baking, the solvent in the PMMA solution cannot be fully evaporated, which has unpredictable influence on the exposure result. Taking the PMMA out of the fridge about 1 to 2 hours before coating is recommended in order to avoid such influence.

2.2 Develop time

In addition, compared to the exposure dose used for creating good nano-features, develop time also plays an important role, and a good combination of these two factors is a vital point for the generation of very fine features. A good method of controlling develop time is to check the pattern under microscope by a 5 seconds step, for develop time varies even for the same exposure dose.

Appendix 3

Dispersion Relations of Two Coupled Microcavities

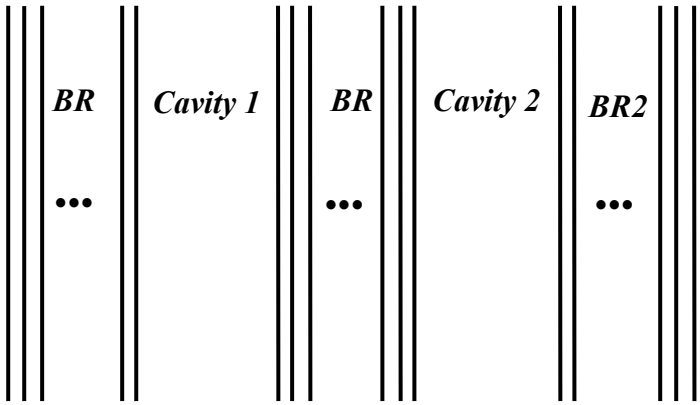

Fig.A.4 Diagram of the two coupled cavity structure

Fig.A.4 shows a diagram of a structure in which the interaction of localized photon states can occur. In consists of two microcavities sharing a common central Bragg reflector (*BR*). The *cavities 1* and *2* are located on each side of the common reflector. The structure is bounded on the exterior sides by Bragg reflectors *BR1* and *BR2*. The photon modes localized in *cavities 1* and *2* can interact via tunneling through the common reflector.

The interaction will be most efficient in the case when the free-state characteristic frequencies ω_1 and ω_2 of cavities 1 and 2, determined under normal incidence of light by the equations

$$Arg(R_1) + Arg(r) + 2\Phi_1 = 2\pi N, \qquad \text{A.24a}$$

$$Arg(R_2) + Arg(r) + 2\Phi_2 = 2\pi M, \qquad \text{A.24b}$$

are equal to each other. Here N and M are integers; r is the amplitude reflection coefficient of the common reflector; $R_{1(2)}$ is the amplitude reflection coefficient of the outer mirror of the first (second) cavity; $\Phi_{1(2)}$ are the phases acquired by the light as it passes through the first (second) cavity, which are determined by the expression

$$\Phi_{1(2)} = n_{c1(2)} L_{1(2)} \omega_{1(2)} / c, \qquad \text{A.24c}$$

where $n_{c1(2)}$ are the refractive indices of the cavities, $L_{1(2)}$ are cavity thicknesses, $\omega_{1(2)}$ are the characteristic frequencies of the first (second) cavity, and c is the speed of light in vacuum.

According to the approach set forth in Ivchenko *et al*'s work [Ivchenko 1996], the dispersion relation for the characteristic modes of the structure shown in Fig.A.4 can be written in the form

$$\begin{aligned}&(t^2 - r^2) R_1 R_2 \exp(i(\Phi_1 + \Phi_2)) - \exp(-i(\Phi_1 + \Phi_2)) \\ &+ r(R_1 \exp(i(\Phi_1 - \Phi_2)) + R_2 \exp(i(\Phi_2 - \Phi_1))) = 0\end{aligned} \qquad \text{A.25}$$

For a symmetric structure with $R_1 = R_2 = R$, $\Phi_1 = \Phi_2 = \Phi$, and $L_1 = L_2 = L$ one can rewrite Eq.(A.25) in the form

$$R^2 (t^2 - r^2) \exp(2i\Phi) + 2Rt \exp(i\Phi) - 1 = 0 \qquad \text{A.26}$$

which can be represented as a product of two cofactors corresponding to two characteristic modes of the system of coupled cavities

$$[R(r + t) \exp(i(\Phi + \varphi)) - 1] \times [R(r - t) \exp(i(\Phi + \varphi) - 1] = 0 \qquad \text{A.27}$$

where φ is the phase of the reflection coefficient of the exterior reflectors [Savona 1995], which satisfies the relation

$$\varphi = \frac{\pi n_1 n_2}{(n_2 - n_1) n_c} \frac{\omega - \omega_B}{\omega_B} \qquad \text{A.28}$$

where n_1 and n_2 are the refractive indices of the cavity forming layers, and ω_B is the Bragg interference frequency of the reflector.

It should also be noticed [Kaliteevskii 1995] that near the Bragg interference

frequency of the reflector the phase of the amplitude reflection and transmission coefficient differ by $\pi/2$ when the reflector contains an odd number of layers, i.e., in the case of the symmetric structure

$$Arg(\frac{t}{r}) \approx \frac{\pi}{2} \qquad \text{A.29}$$

which becomes an exact equality at the Bragg interference frequency.

When assuming that $t/r \langle\langle 1$, i.e. the reflection coefficient of the common reflector is quite large. Substituting expressions (A.28) and (A.29) into Eq.(A.27), one can obtain an equation for the mode splitting $\Delta\omega$

$$\Delta\omega(\frac{n_c L}{c} + \frac{2\pi n_1 n_2}{\omega_B (n_2 - n_1) n_c}) \approx 2\frac{t}{r} \qquad \text{A.30}$$

if the Bragg interference frequency ω_B of the reflector equals the frequency ω_0 of the characteristic mode of a single microcavity, as determined by Eqs.(A.24), then Eq.(A.30) can be rewritten in the form

$$\Delta\omega \approx \frac{\omega_0 |t|}{\pi(\frac{n_c L}{\lambda_0} + \frac{n_1 n_2}{(n_2 - n_1) n_c})} \qquad \text{A.31}$$

where $\lambda_0 = 2\pi c/\omega_0$ is the wavelength of light in vacuum, corresponding to the characteristic frequency of the microcavity.

List of References

Adachi, S., "Model dielectric constants of Si and Ge," *Physical Review B*, vol. 38, No. 18, pp.12966-12977, 1988.

Baba, T., N. Fukaya and Y. Yonekuva, "Observation of Light propagation in Photonic Crystal optical Waveguides with bends," *Electronic Letters*, vol. 35, No. 8, pp. 654-655, 1999.

Baba, T., N. Fukaya, and A. Motegi, "Clear correspondence between theoretical and experimental light propagation characteristics in photonic crystal waveguides," *Electronics Letters*, vol. 37, No. 12, pp. 761-762, 2001.

Beggs, D. M., M. A. Kaliteevski, S. Brand and R. A. Abram, "Optimization of an optical filter with a square-shaped passband based on coupled micocavites," *Journal of Modern Optics*, vol. 51, No. 3, pp. 437-446, 2004.

Benisty, H., C. Weisbuch and D. Labilloy, "Optical and confinement properties of two-dimensional photonic crystals," *Journal of Lightwave Technology*, vol. 17, No. 11, pp. 2063-2077, 1999.

Birks, T. A., D. M. Atkin, G. Wylangowski and P. St. Russell, "2D Photonic Band Gap Structures in Fiber Form," *Photonic Band Gap Materials*, *NATO ASI Series*, Series E: Applied Science, vol. 315, pp. 437-444, 1995.

Birks, T. A., J. C. Knight, and P. St. J. Russell, "Endlessly single-mode photonic crystal fibre," *Optics Letters*, vol. 22, pp. 961-963, 1997.

Birks, T. A., D. Mogilevtsev, J. C. Knight, P.St.J. Russell, J. Broeng, P.J. Roberts, J.A.

West, D.C. Allan, and J.C. Fajardo, “The analogy between photonic crystal fibres and step index fibres,” *Optical Fibre Conference*, Paper FG-4-1, pages 114-116, Friday, February 26 1999.

Biswas, R., C. T. Chan, M. Sigalas, C. M. Soukoulis, and K. M. Ho, “Photonic Band Gap Materials,” *Photonic Band Gap Materials*, *NATO ASI Series*, Series E: Applied Sciences, vol. 315, pp. 23-40, 1995

Brown, R. and O. Mcmahon, “Large electromagnetic stop bands in metallodielectric photonic crystals,” *Applied. Physics Letters*, vol. 67, pp.2138-2140, 1995.

Busch, K., C. T. Chan and C. M. Soukoulis, “Techniques for Bandstructures and Defect States in Photonic Crystals,” *Photonic Band Gap Materials*, *NATO ASI Series*, Series E: Applied Science, vol. 315, pp. 465-486, 1995.

Cao, Q., Ph. Lalanne, and J. P. Hugonin, “Stable and efficient Bloch-mode computational method for one-dimensional grating waveguides,” *Journal of the Optical Society of America A*, vol. 19, No. 2, pp. 335-338, 2002.

Cassagne, D., C. Jouanin and D. Berton, “Hexagonal photonic band gap structures,” *Physical Review B*, vol. 53, pp. 7134-7142, 1996.

Chan, C. T., K. M. Ho and C. M. Soukoulis, “Photonic band-gaps in experimentally realizable periodic dielectric structures,” *Euro-physics Letters*, vol. 16, pp. 563-568, 1996.

Chen, K. M., A. W. Sparks and H. C. Luan, “SiO2/TiO2 omnidirectional reflector and microcavity resonator via the sol-gel method,” *Applied Physics Letters*, vol. 75, No. 24, pp. 3805-3807, 1999.

Cheng, C. and A. Scherer, “Fabrication of photonic band gap crystals,” *Journal of Vacuum Science technology B*, vol. 10, pp. 296-302, 1993.

Chiang, K. S., “Performance of the effective-index method for the analysis of dielectric waveguides,” *Optics Letters*, Vol. 16, No. 10, pp. 714-716, 1991.

Chiang, K. S., “Analysis of rectangular dielectric waveguides: effective-index method with built-in perturbation correction,” *Electronic Letters*, vol. 28, No. 4, pp. 388-390, 1992.

Chigrin, D. N., A. V. Lavrinenko and D. A. Yaroksty, “Observation of total omnidirectional reflection from a one-dimensional dielectric lattice,” *Applied Physics, A: Materials Science & Processing*, vol. 68, No. 1, pp. 25-28, 1999(1).

Chigrin, D. N., A. V. Lavrinenko and D. A. Yaroksty, “All-dielectric one-dimensional periodic structures for total omnidirectional reflection and partial spontaneous emission control,” *Journal of Lightwave Technology*, vol. 17, No. 11, pp. 2018-2024, 1999(2).

Chung, C-K., “Geometrical pattern effect on silicon deep etching by an inductively coupled plasma system,” *Journal of Micromechanics and Microengineering*, vol. 14, pp. 656-662, 2004.

Chutinan, A., S. Noda, “Waveguides and waveguide bends in two-dimensional photonic crystal slabs,” *Physical Review B*, vol. 62, No. 7, pp. 4488-4492, 2000(1).

Chutinan, A., S. Noda, “Analysis of waveguides and waveguide bends in photonic crystal slabs with triangular lattice,” *Japanese Journal of Applied Physics Part 2-Letters*, vol. 39, No. 6B, pp. 595-596, 2000(2).

Collins, R. E., *SiO_x Etching process from Oxford Instrument*, provider of the ICP etching machine in the Bath clean-room 2006.

Costa, R., A. Melloni, and M. Martinelli, "Bandpass Resonant Filters in Photonic-Crystal Waveguides," *IEEE Photonic Technology Letters*, vol. 15, No. 3 pp. 401-403, 2003.

Cregan, R. F., B. J. Mangan, and J. C. Knight, "Single-mode photonic band gap guidance of light in air," *Science* 285 (5433), pp. 1537-1539, 1999.

Ctyroky, J., "Photonic bandgap structures in planar waveguides," *Journal of the Optical Society of America A*, vol. 18, No. 2, pp. 435-441, 2001.

Davies, P., *Final Year Project*, Department of Electronic Engineering, University of Bath, 2005.

De La Rue, R. M., and T. F. Krauss, "Strategies for the fabrication of photonic microstructures in semiconductors," *Microcavities and Photonic Bandgaps: Physics and Applications*, *NATO ASI Series*, Series E: Applied Science, vol. 324, pp. 175-192, 1995.

Earnshaw, M. P., Quantum Well Electrorefraction materials and devices, *PhD Thesis*, Department of Electronics, University of York, pp. 83, 1999.

Edward, D. P., "Handbook of Optical Constants of Solids," Academic Press, INC., 1985.

Edward, D. P., "Handbook of Optical Constants of Solids ," Academic Press, INC., 1998.

Fan, S., P. Villeneuve, R. Meade and J. Joannopoulous, “Design of three-dimensional photonic crystals at aubmicron lengthscales,” *Applied Physics Letters*, vol. 65, pp.1466-1468, 1994.

Fan, S., P. Villeneuve and J. Joannopoulos, “Large omnidirectional band gaps in metallodielectric photonic crystals,” *Physical Review B*, vol. 54, pp.11245-11251, 1996.

Fan, S., P. R. Villeneuve and J. D. Joannopoulos, “High extraction efficiency of spontaneous emission from slabs of photonic crystals,” *Physical Review Letters*, vol. 78, no. 17, pp. 3294-3297, 1997.

Fan, S., P. R. Villeneuve, J. D. Joannopoulos and H. A. Hans, “Channel Drop Tunneling through Localized States,” *Physics Review Letters*, vol. 80, pp.960-963, 1998.

Fan, S., S. G. Johnson and J. D. Joannopoulos, “Waveguide branches in photonic crystals,” *Journal of the Optical Society of America B Optical Physics*, vol. 18, No. 2, pp. 162-165, 2001.

Fan, S., and J. D. Joannopoulos, “Analysis of guided resonances in photonic crystal slabs,” *Physical Review B*, vol. 65, No. 23, Art. No. 235112, 2002.

Foresi, J. S., P. R. Villeneuve, J. Ferrera and J. D. Joannopoulos, “Photonic-bandgap microcavities in optical waveguides,” *Nature*, 390 (6656), pp. 143-145, 1997.

Gerace, D. and L. C. Andreani, “Gap maps and intrinsic diffraction losses in one-dimensional photonic crystal slabs”, *Phys. Rev. E*, vol. 69, pp. 056603, May 2004.

Ghosh, G., “Dispersion equation coefficients for the refractive index and birefringence of Calcite and quartz crystals,” *Optics Communications*, vol. 163, pp.95-102, 1999.

Gruning, U., V. Lehmann, S. Ottow and K. Busch, “Macroporous silicon with a complete two-dimensional photonic band gap centered at 5μm,” *Applied Physics Letters*, vol. 68, No. 6, pp. 747-749, 1996.

Happ, T. D., M. Kamp, and A. Forchel, “Photonic crystal tapers for ultracompact mode conversion,” *Optics Letters*, vol. 26, No. 14, pp. 1102-1104, 2001.

Hattori, T., N. Tsurumachi and N. Muroi, “Enhancement of optical nonlinearity in one-dimensional photonic crystals,” *Progress in Crystal growth and characterization of materials*, vol. 33, No. 1-3, pp. 183-186, 1996.

Hattori, T., N. Tsurumachi and H. Nakatsuka, “Analysis of optical nonlinearity by defect states in one-dimensional photonic crystals,” *Journal of the optical Society of America B Optical Physics*, vol. 14, No. 2, pp. 348-355, 1997.

Herzberger, M. and C. D. Salzberg, “Refractive Indices of Infrared Optical Materials and Color Correction of Infrared Lenses,” *Journal of the Optical Society of America*, vol. 52, No.4, pp.420-427, 1962.

Ho, K. M., C. T. Chan, C. M. Soukoulis, “Existence of a photonic gap in periodic dielectric structures,” *Physical Review Letters*, vol. 65, pp.3152-3155, 1990.

Ho, K. M., C. T. Chan, C. M. Soukoulis, R. Biswas and M. Sigalas, "Photonic band-gap in three-dimensional new layer-by-layer periodic structures," *Solid State Communications*, vol. 89, pp. 413-416, 1994.

http://www.bayspec.com/pdf/ITU-DWDM.pdf

Inoue, K., M. Wada, K. Sakoda, A. Yamanaka, M. Hayashi and J. W. Haus, "Fabrication of two-dimensional photonic band structure with near-infrared band gap," *Japanese Journal of Applied Physics*, vol. 33, No. 10B, pp. L1463-L1465, 1994.

Inoue, K., M. Wada, K. Sakoda, M. hayashi, T. Fukushima and A. Yamanaka, "Near-infrared photonic band gap of two-dimensional triangular air-rod lattices as revealed by transmittance measurement," *Physical Review B*, vol. 53, pp. 1010-1013, 1996.

Ivchenko, E. L., M. A. Kaliteevski, A. V. Kavokin, and N. A. Nesvihzskii, "Reflection and absorption spectra from microcavities with resonant Bragg quantum wells," *Journal of the Optical Society America B*, vol.13, pp.1061-1068, 1996.

Ji, J., F. E. H. Tay, J. Miao and J. Sun, "Characterization of Silicon Isotropic Etch by Inductively Coupled Plasma Etcher for Microneedle Array Fabrication," *Journal of Physics:* Conference Series 34, pp.1137-1142, International MEMS Conference, 2006.

Jin, C. J., B. Y. Cheng and Z. L. Li, "Two dimensional metallic photonic crystal in the THz range," *Optics Communications*, vol. 166, No. 1-6, pp. 9-13, 1999(1).

Jin, C. J., B. Y. Cheng and B. Y. Man, "Two dimensional metallodielectric photonic

crystal with a large band gap," *Applied Physics Letters*, vol. 75, No. 9, pp. 1201-1203, 1999(2).

Jin, C. J., B. Y. Cheng and B. Y. Man, "Band gap and wave guiding effect in a quasiperiodic photonic crystal," *Applied Physics Letters*, vol. 75, No. 13, pp. 1848-1850, 1999(3).

Jin, C. J., Z. W. Sun and B. Y. Cheng, "Microcavities composed of point defects and waveguides in photonic crystals," *Optics Communications*, vol. 188, No. 5-6, pp. 255-260, 2001.

Joannopoulos, J. D., R. D. Meads and J. N. Winn, "Photonic Crystals: Molding the Flow of Light" Princeton University, Princeton, N.J. 1995.

Joannopoulos, J. D., P. R. Villeneuve and S. Fan, "Photonic Crystals: Putting a new twist on light," *Nature*, 386 (6621), pp. 143-149, 1997(1).

Joannopoulos, J. D., P. R. Villeneuve and S. Fan, "Photonic Crystals," *Solid State Communications,* vol. 102, No. 2-3, pp. 165-173, 1997(2).

John, S., "Strong localization of photons in certain disordered dielectrics superlattices," *Physical Review Letters*, vol. 58, No. 23, pp. 2486-2489, 1987.

John, S., "Localization of Light: Theory of Photonic Band Gap Materials," *Photonic Band Gap Materials*, *NATO ASI Series*, Series E: Applied Science, vol. 315, pp. 563-666, 1995.

Johnson, S. G., P. R. Villeneuve, S. H. Fan, "Linear waveguides in photonic-crystal

slabs," *Physical Review B*, vol. 62, No. 12, pp. 8212-8222, 2000.

Johnson, S. G., S. Fan and A. Mekis, "Multipole-cancellation mechanism for high-Q cavities in the absences of a complete photonic band gap," *Applied Physics Letters*, vol. 78, No. 22, pp. 3388-3390, 2001.

Johnson, S. G., P. Bienstman, M. A. Skorobogarity *et al*, "Adiabatic theorem and continuous coupled-mode theory for efficient taper transitions in photonic crystals," *Physical Review E*, vol.66, pp. 066608 (1-15), 2002.

Johnson, S. G., *MIT MRS Chapter,2003 IAP*, http://ab-inito.mit.edu/mpb.

Jugessur, A. S., P. Pottier and R. M. De La Rue, "One-dimensional periodic photonic crystal microcavity filters with transition mode-matching features, embedded in ridge waveguides," *Electronics Letters*, vol. 39, No. 4, pp. 367-369, 2003.

Jugessur, A. S., P. Pottier and R. M. De La Rue, "Engineering the filter response of photonic crystal microcavity filters," *Optics Express*, vol. 12, No. 7, pp. 1304-1312, 2004.

Kaliteevskii, M. A., and A.V. Kavozhin, "Effect of interband and exciton light absorption on the optical properties of Bragg reflectors," *Physics of the Solid State*, vol. 37, pp. 1497-1500, 1995.

Kaliteevskii, M. A., "Optical properties of a system of two coupled vertical microcavities," *Technical Physics*, vol. 43, pp. 565-568, 1998.

Keiser, G., "Optical Communications Essentials" McGraw-Hill, 2003.

Khoo, E. H., A. Q. Liu, and J. H. Wu, "Nonuniform photonic crystal taper for

high-efficiency mode coupling," *Optics Express*, vol. 13, No. 20, pp. 7748-7759, 2005.

Khorasani S and B. Rashidian, "Analysis of Kronig-Penny photonic crystals by modified transfer matrices", *Proceedings of SPIE*, vol. 4655, pp. 260-266, 2002.

Kitson, S.C., W.L. Barnes and J.R. Sambles, "Full Photonic band gap for surface modes in the visible," *Physical Review Letters*, vol. 77, pp. 2670-2673, 1996.

Knight, J. C., J. Broeng, T. A. Birks and P. S. Russell, "Photonic band gap guidance in optical fibers," *Science*, 282 (5393), pp. 1476-1478, 1998.

Konotop, V. V., "Waveguides in Periodic Structures with Smoothly Varying Parameters," *Photonic Band Gap Materials*, *NATO ASI Series*, Series E: Applied Science, vol. 315, pp. 547-554, 1995.

Kosaka, H., T. Kawashima, A. Tomita and S. Kawakami, "Photonic-crystal spot-size converter," *Applied Physics Letters*, vol. 76, No. 3, pp. 268-270, 2000.

Krauss, T.F., Y. P. Song, S. Thoms, C.D.W. Wilkinson and R.M. De La Rue, "Fabrication of 2-D photonic bandgap structures in GaAs/AlGaAs, *Electronic Letters*, vol. 30, pp. 1444-1446, 1994.

Krauss, T.F., R.M. De La Rue and S. Brand, "Two-dimensional photonic band gap structure operating at near-infrared wavelengths," *Nature*, 383, pp. 699-702, 1996.

Krauss, T.F., B. Vögele, C.R. Stanley and R.M. De La Rue, "Waveguide microcavity based on photonic microstructures," *IEEE Photonic Technology Letters*, vol. 9, pp.

176-178, 1997.

Kuang, W., C. Kim, A. Stapleton, and J. D. O'Brien, "Grating-assisted coupling of optical fibers and photonic crystal waveguides," *Optics Letters*, vol. 27, No. 18, 2002.

Labilloy, D., H. Bensity and C. Weisbuch, "Demonstration of cavity mode between two-dimensional photonic crystal mirrors," *Electronics Letters*, vol. 33, No. 23, pp. 1978-1980, 1997.

Lalanne. Ph. and A. Talneau, "Modal conversion with artificial materials for photonic-crystal waveguides," *Optics Express*, vol. 10, No. 8, pp. 354-359, 2002.

Lalanne, P. and J.P. Hugonin, "Bloch mode engineering for high-Q small-V microcavities," *IEEE Journal of Quantum Electronics*, vol. 39, pp. 1430-1438, 2003.

Lalanne, P., S. Mias, and J.P. Hugonin, "Two physical mechanisms for boosting the quality factor to cavity volume ratio of photonic crystal microcavities," *Optics Express*, vol. 12, No. 3, pp. 458-467, 2004.

Lan, S., S. Nishikawa, and O. Wada, "Leveraging deep photonic band gaps in photonic crystal impurity bands," *Applied Physics Letters*, vol. 78, No. 15, pp. 2101-2103, 2001(1).

Lan, S., S. Nishikawa, O. Wada and H. Ishikawa, "Design of impurity band-based photonic crystal waveguides and delay lines for ultrashort optical pulses," *Journal of Applied Physics,* vol. 90, No. 9, pp. 4321-4327, 2001(2)

Lan, S., and H. Ishikawa, "Coupling of defect pairs and generation of dynamical band gaps in the impurity bands of nonlinear photonic crystals for all-optical

switching," *Journal of Applied Physics*, vol. 91, No. 5, pp. 2573-2577, 2002(1)

Lan, S., S. Nishikawa, Y. Sugimoto, N. Ikeda, K. Asakawa, and H. Ishikawa, "Analysis of defect coupling in one- and two-dimensional photonic crystals," *Physical Review B*, vol. 65, pp.165208, 2002(2)

Lau, W. T. and S. H. Fan, "Creating large bandwidth line defects by embedding dielectric waveguides into photonic crystal slabs," *Applied Physics Letters*, vol. 81, No. 21, pp. 3915-3917, 2002.

Laude, V., and P. Tournois, "Superluminal asymptotic tunneling times through one-dimensional photonic bandgaps in quarter-wave-stack dielectric mirrors," *Journal of the Optical Society of America B – Optical Physics*, vol. 16, No. 1, pp. 194-198, 1999.

Lee, H-Y., H. Makino, T. Yao and A. Tanaka, "Si-based omnidirectional reflector and transmission filter optimized at a wavelength of 1.55μm," *Applied Physics Letters*, vol. 81, No. 24, pp.4502-4504, 2002.

Lee, H-Y., S. J. Cho, and G. Y. Nam, "Multiple-wavelength-transmission filters based on Si-SiO_2 one-dimensional photonic crystals", *Journal of Applied Physics*, vol. 97, No. 10, Art No. 103111, 2005.

Leung, K. M., "Diamondlike photonic band-gap crystal with a sizable band gap," *Physical Review B*, vol. 56, No. 7, pp. 3517-3519, 1997

Lin, S. Y., E. Chow, V. Hietala and J. D. Joannopoulos, "Experimental Demonstration of Guiding and Bending of Electromagnetic Waves in a Photonic Crystal," *Science*, vol. 282, No. 5387, pp. 274-276, 1998.

Liu, Y. F., K. M. Leung and L. Carin, “Dispersion-Curves and transmission spectra of a 2-Dimensional Photonic band-gap crystal – theory and experiment,” *Journal of Applied Physics*, vol. 77, No. 8, pp. 3631-3636, 1995.

Loncar, M., D. Nedeljkovic, T. Doll, J. Vuckovic, A. Scherer and T.P. Pearsall “Waveguiding in Planar Photonic Crystals,” *Applied Physics Letters*, vol. 77, No. 13, pp. 1937-1939, 2000(1).

Loncar, M., T. Doll and J. Vuckovic, “Design and Fabrication of Silicon Photonic Crystal optical Waveguides,” *Journal of Lightwave Technology*, vol. 18, No. 10 1402-1411, 2000(2).

Lourtioz, J.-M., H. Bensity, V. Berger, J.-M. Gerard, D. Maystre, A. Tchelnokov, “Photonic Crystals, Towards Nanoscale Photonic Devices,” Springer 2005

Lousse, V., W. Suh, O. Kilic and S. Fan, “Angular and polarization properties of a photonic crystal slab mirror,” *Optics Express*, vol. 12, No. 8, pp. 1575-1582, 2004.

Madsen, C.K., and J. H. Zhao, “Optical Filter Design and Analysis: A signal processing approach,” New York: Wiley 1999.

Martorell, J., and N. M. Lawandy, “Observation of inhibited spontaneous emission in a periodic dielectric structure,” *Physics Review Letters*, vol. 65, pp. 1877-1880, 1990.

Meade, R. D., K. D. Brommer, A. M. Rappe, and J. D. Joannopoulos, “Existence of a photonic band gap in two dimensions,” *Applied Physics Letters*, vol. 61, No. 4, pp. 495-497. 1992

Mekis, A., J. C. Chen and I. Kurland, “High transmission through sharp bends in

photonic crystal waveguides," *Physical Review Letters*, vol. 77, No. 18, pp. 3787-3790, 1996.

Mekis, A. and J. D. Joannopoulos, "Tapered Couplers for Efficient Interfacing Between Dielectric and Photonic Crystal Waveguides," *Journal of Lightwave Technology*, vol. 19, No. 6, pp. 861-865, 2001.

Nishikawa, S., S. Lan, N. Ikeda, Y. Sugimoto, H. Ishikawa, and K. Asakawa, "Optical characterization of photonic crystal delay lines based on one-dimensional coupled defects," *Optics Letters*, vol. 27, No. 23, pp. 2079-2081, 2002.

Ohtera, Y., T. Sato, T. Kawashima and S. Kawakami, "Photonic crystal polarisation splitters," *Electronics Letters*, vol. 35, No. 15, pp. 1271-1272, 1999.

Ojha, S.P., S.K. Srivastava, N. Kumar, "Design of an optical filter using photonic band gap material," *Optik* 114, No. 3. pp.101-105, 2003.

Olivier, S., M. Rattier and H. Benisty, "Mini-stopbands of a one-dimensional system: The channel waveguide in a two-dimensional photonic crystal," *Physical Review B*, vol. 63, No. 11, Art, No. 113311, 2001(1).

Olivier, S., H. Benisty and M. Rattier, "Resonant and nonresonant transmission through waveguide bends in a planar photonic crystal," *Applied Physics Letters*, vol. 79, No. 16, pp. 2514-2516, 2001(2).

Olivier, S., H, Benisty, C. Jm. Smith, "Transmission properties of two-dimensional photonic crystal channel waveguides," *Optical and Quantum Electronics*, vol. 34, No. 1-3, pp. 171-181, 2002.

Ortowski, A., M. Rusek and J. Mostowski, “Localization of light in 2D random media,” *Microcavities and Photonic Bandgaps: Physics and Applications*, *NATO ASI Series*, Series E: Applied Science, vol. 324, pp. 165-174, 1995.

Ozbay, E., E. Michel, G. Tuttle, R. Biswas, M. Sigalas and K.M. Ho, “Micromachined millimeter-wave photonic band gap crystals,” *Applied Physics Letters*, vol. 64, pp.2059-2061, 1994.

Painter, O., R. K. Lee, A. Scherer, A. Yariv, J. D. O’Brien, P. D. Dapkus and I. Kim, “Two Dimensional photonic band gap defect mode laser,” Science, 284, pp. 1819-1821, 1999.

Palamaru, M. and Ph. Lalanne, "Photonic crystal structure waveguides: out of plane losses and adiabatic modal conversion," *Applied Physics Letters.* vol. 78, pp.1466-1468, 2001.

Patrini, M., M. Galli, M. Belotti, L.C. Andreani, G. Guizzetti, G. Pucker, A. Lui and P. Bellutti, “Optical response of one-dimensional $(Si/SiO_2)_m$ photonic crystals,” *Journal of Applied Physics*, vol. 92, No.4, pp.1816-1820, 2002.

Pechstedt, R. D., P. St. Russell and T. A. Birks, “Dispersion, Tunability and Applications of Defect Modes in Photonic Band-gap Structures,” *Photonic Band Gap Materials*, *NATO ASI Series*, Series E: Applied Science, vol. 315, pp. 445-452, 1995.

Peyrade, D., E. Silberstein, P. Lalanne, A. Talneau, Y. Chen, “Short Bragg mirrors with adiabatic modal conversion,” *Applied Physics Letters*, vol. 81, pp.829-831 2002.

Purcell, E. M., “Spontaneous emission probabilities at radio frequencies,” *Physical Review*, vol. 69, No. 11-1, pp. 681-681, 1946.

Rattier, M., H. Benisty and C. Jm. Smith, “Performance of waveguide-based two-dimensional photonic-crystal mirrors studied with Fabry-Perot resonators,” *IEEE Journal of Quantum Electronics*, vol. 37, No. 2, pp. 237-243, 2001.

Robertson, W. M., G. Arjavalingam, R.D. Meade, K.D. Brommer, A.M. Rappe and J.D. Joannopoulous, “Measurement of Photonic Band Structure in a Two-dimensional Periodic Dielectric Array,” *Physical Review Letters*, vol. 68, pp. 2023-2026, 1992.

Rosenberg, A., R.J. Tonucci, H.B. Lin and A.J. Campillo, “Near-infrared two-dimensional photonic band-gap materials,” *Optics Letters*, vol. 21, pp. 830-832, 1996.

Ripin, D.J., K-Y. Lim, *et al*, “One-Dimensional Photonic Bandgap Microcavities for Strong Optical Confinement in GaAs and GaAs/Al_xO_y Semiconductor Waveguides,” *Journal of Lightwave Technology*, vol. 17, No. 11, pp.2152-2160, 1999.

Ripin, D.J., K-Y. Lim, *et al*, “Photonic band gap airbridge microcavity resonances in GaAs/AlxOy waveguides,” *Journal of Applied Physics*, vol. 87, No.3, pp.1578-1580, 2000.

Russell, P., and T. A. Birks, “Bloch Wave Optics in Photonic Crystals : Physics and Applications,” *Photonic Band Gap Materials*, *NATO ASI Series*, Series E: Applied Science, vol. 315, pp. 71-91, 1995.

Russell, P., “Photonic crystal fibers”, *Science*, vol. 299, pp. 358-362, 2003(1).

Russell, P. St. J., "Designing photonic crystals", *Electron and Photon Confinement in Semiconductor Nanostructures*, IL Nuovo Cimento (editor), Amsterdam: IOS Press, pp. 79-103, 2003(2).

Sauvan, C., G. Lecamp, P. Lalanne and J. P. Hugonin, "Modal-reflectivity enhancement by geometry tuning in Photonic Crystal microcavities," *Optics Express*, vol. 13, No. 1, pp. 245-255, 2004.

Savona, V., L. C. Andereani, P. Schwendimann, and A. Quatropani, "Quantum well excitons in semiconductor microcavities: Unified treatment of weak and strong coupling regimes," *Solid State Communications*, vol. 93, pp. 733-739, 1995.

Smith, C. J. M., H. Benisty, S. Olivier, "Low-loss channel waveguides with two-dimensional photonic crystal boundaries," *Applied Physics Letters*, vol. 77, No. 18, pp. 2813-2815, 2000.

Smith, C. J. M., R. M. De La Rue and M. Rattier, "Coupled guide and cavity in a two-dimensional photonic crystal," *Applied Physics Letters*, vol. 78, No. 11, pp. 1487-1489, 2001.

Snyder, A.W. and J. D. Love, "Optical Waveguide theory," Chapman and Hall, N.Y., 1983.

Soljacic, M., S. G. Johnson and S. H. Fan, "Photonic-crystal slow-light enhancement of nonlinear phase sensitivity," *Journal of the Optical Society of America B Optical Physics*, vol. 19, No. 9, pp. 2052-2059, 2002.

Soljacic, M., C. Luo, J. D. Joannopoulos and S. Fan, "Nonlinear photonic crystal microdevices for optical integration," *Optics Letters*, vol. 28, No. 8, pp. 637-639,

2003.

Souzuer, H.S. and J.W. Haus, “Photonic bands simple-cubic lattice,” *Journal of the Optical Society of America B*, vol. 10, pp. 296-302, 1993.

Srinivasan, K., P.E. Barclay, O. Painter, J. Chen, A.Y. Cho and C. Gmachl, “Experimental demonstration of a high quality factor photonic crystal microcavity,” *Applied Physics Letters*, vol. 83, No. 10, pp. 1915-1917, 2003.

Talneau, A., P. Lalanne, M. Agio and C.M. Soukoulis, “Low-reflection photonic-crystal taper for efficient coupling between guided section of arbitrary widths,” *Optics Letters*, vol. 27, No. 17, pp.1522-1524, 2002.

Taniyama, H., “Waveguide structures using one-dimensional photonic crystal,” *Journal of Applied Physics*, vol.91, No.6, pp.3511-3515, 2002.

Temelkuran, B., and E, Ozbay, “Experimental demonstration of photonic crystal based waveguides,” *Applied Physics Letters*, vol. 74, No. 4, pp. 486-488, 1999.

Tokushima, M., H. Kosaka, A. Tomika and H. Yamada, “Lightwave propagation through a 120 degrees sharply bent single-line-defect photonic crystal waveguide,” *Applied Physics Letters*, vol. 76, No. 8, pp. 952-954, 2000.

Tsurumachi, N., S. Yamashita, N. Muroi and H. Nakatsuka, “Enhancement of Nonlinear Optical Effect in One-Dimensional Photonic Crystal Structures,” *Japanese Journal of Applied Physics*, vol. 38, pp.6302-6308, 1999(1).

Tsurumachi, N., M. Abe and M. Arakawa, “Time response of one-dimensional photonic crystals with a defect layer made of semiconductor quantum dots,”

Japanese Journal of Applied Physics Part 2 Letters, vol. 38, no. 12A, pp. L1400-L1402, 1999(2).

Velha, P., J. C. Rodier, P. Lalanne, D. Peyrade and J.P. Hugonin, "Ultracompact silicon-on-insulator ridge-waveguide mirrors with high reflectance," *Applied Physics Letters*, vol. 89, No. 17, Art No. 171121-3, 2006.

Villeneuve, P. R. and M. Piche, "Photonic band gap in two-dimensional square and hexagonal lattices," *Physical Review B*, vol. 46, pp. 4969-4972, 1992.

Villeneuve, P. R., S. Fan, J. D. Joannopoulos, K-Y. Lim, G. S. Petrich, L. A. Kolodziejski, and R. Reif, "Air-bridge microcavities," *Applied Physics Letters*, vol. 67 (2), pp.167-169, 1995(1).

Villeneuve, P., S. Fan and J. D. Joannopoulos, "Microcavities in photonic crystals," *Microcavities and Photonic Bandgaps: Physics and Applications*, *NATO ASI Series*, Series E: Applied Science, vol. 324, pp. 133-152, 1995(2).

Wadsworth, W. J., N. Joly, J. C. Knight, T. A. Birks, F. Biancalana, and P. St.J. Russell, "Supercontinuum and four-wave mixing with Q-switched pulses in endlessly single-mode photonic crystal fibres", *Optics Express*, vol. 12, pp. 299-309, 2004**.**

Wang, Y. Q., C. J. Jin and S. Z. Han, "Defect modes in two-dimensional quasiperiodic photonic crystal," *Japanese Journal of Applied Physics Part 1-Regular Papers short notes & review papers*, vol. 43, No. 4A, pp. 1666-1671, 2004.

Wei, L., and J. W. Y. Lit, "Phase-Shifted Bragg Grating Filters with Symmetrical Structures," *Journal of Lightwave Technology*, vol. 15, pp. 1405-1410, 1997.

Xu, Y., R. K. Lee, and A. Yariv, “Adiabatic coupling between conventional dielectric waveguides and waveguides with discrete translational symmetry,” *Optics Letters*, vol. 25, No. 10, pp. 755-757, 2000.

Yablonovitch, E., “Inhibited spontaneous emission in solid-state physics and electronics,” *Physical Review Letters*, vol. 58, No. 20, pp. 2059-2062, 1987.

Yablonovitch, E., T. Gmitter and K. Leung, “Photonic band structure: The face-centred-cubic case employing nonspherical atoms”, *Physical Review Letters*, vol. 67, No. 17, pp. 2295-2298, 1991.

Yamada, K., A. Shinya, C. Takahashi, and M. Notomi “Improved line-defect structures for photonic-crystal waveguides with high group velocity,” *Optics Communications*, vol. 198, no. 4-6, pp. 395-402, 2001.

Yamada, K., M. Notomi, A. Shinya and C. Takahashi, “Singlemode lightwave transmission in SOI-type photonic-crystal line-defect waveguides with phase-shifted holes,” *Electronics Letters*, vol. 38, No. 2, pp. 74-75, 2002.

Yariv, A., “Quantum Electronics,” 3rd Edition, Wiley, 1989.

Yeh, P., “Optical Waves in Layered Media,” John Wiley & Sons, 1988.

Yokoyama, H. and K. Ujihara, “Spontaneous emission and Laser Oscillation in Microcavities,” Boca Raton, FL: CRC Press, 1995.

Zengerle, R., and O. Leminger, “Phase-shifted Bragg-Grating Filters with improved Transmission characteristics,” *Journal of Lightwave Technology*, vol. 13, pp. 2354-2358, 1995.

Zhang, J. P., D. Y. Chu, S. L. Wu, W. G. Bi, R. C. Tiberio, R. M. Joseph, A. Taflove, C. W. Tu and S. T. Ho, "Nanofabrication of 1-D photonic bandgap structures along a photonic wire," *IEEE Photonic Technology Letters*, vol. 8, pp. 491-493, 1996.

Zhang, X. D., Z. Q. Zhang and L. M. Li, "Enlarging a photonic band gap by using insertion," *Physical Review B*, vol. 61, no. 3, pp. 1892-1897, 2000.